DOCTOR OF PHILOSOPHY

Electromechanical characterisation of PP EMFi

Fernández, Oscar

Award date:
2004

Awarding institution:
Bangor University

Electromechanical Characterisation of PP EMFi

By Oscar Fernández

A thesis submitted in candidature for the degree of

Doctor of Philosophy

School of Informatics

University of Wales, Bangor (2004)

To María Angeles

She knows why

Contents

List of Figures

List of Tables

Acknowledgements

I would like to thank my supervisor, Professor Martin Taylor to whom I am very much indebted for the needed support and guidance during the three years of this project. I would also like to express my gratitude to Professor John Lewis for his helpful suggestions and kind support in the conferences in Toulouse and Boulder. Thanks also to VTT Chemical Technology for the material supply.

Thanks are also due to Professor José Antonio de Saja for allowing me to use the equipment used for DSC, TGA, TMA and DMA at the University of Valladolid and to Dr Miguel Angel Rodríguez for his helpful discussions regarding these measurements.

Thanks also to my colleague Dr Pablo Marin-Franch for his assistance, helpful suggestions and specially for creating always an incredibly good atmosphere at work. Also thanks to the members of the group, James, Nacho, Penny, David, Stephen, Hmoud and Paco. Special mention is deserved for José Luís for his help and always interesting conversations during the otherwise unbearably hot Spanish summers of 2002 and 2003.

My gratitude to the technicians in the mechanical and electrical workshops, to the Homer J Simpson Computing Laboratory and to the administrative staff. I would also like to thank John Cambridge for the excellent SEM micrographs presented in this work.

I would also like to express my gratitude to my parents, Alipio and María Angeles and to my brothers, Raúl and Edgar for their constant support and for being always there in the hardest moments.

And last but not least, I specially thank my wife, María Angeles, for her infinite love during these twelve years and for her never-ending tolerance, especially during the writing up of this thesis.

Summary

This thesis describes a study into Electromechanical Film (EMFi) of polypropylene (PP). The reported results were obtained from an extensive investigation which included the characterisation of the polypropylene itself, its cellular structure as well as the mechanical, electrical and piezoelectric properties of the material. In particular, the study investigated the dependence of these properties on temperature.

Based on cross-section SEM micrographs, the cellular structure was characterized in terms of the associated magnitudes such as anisotropy ratios (R_{12} =1.69, R_{13} =7.96 and R_{23}=4.71) and cell wall thickness.

Thermo-mechanical analysis (TMA) revealed thickness-mode Young's modulus, Y_3, ranging from $\sim$ 0 to $\sim$ 50 KPa which is unusually low for close-cell foams suggesting that a significant leakage of gas out of the foam occurs when the foam is compressed. TMA also revealed the low thermo-mechanical stability of the material whose cellular structure starts to collapse at $\sim$ 60°C.

Charge stability was also investigated using the Thermo stimulated current (TSC) technique. The TSC curves showed the depolarisation of the material starting at 60°C and the inital rise method yielded an activation energy of $\sim$ 2 eV suggesting that the depolarisation arises from the charge detrapping.

The piezoelectric nature of the foam was investigated in terms of the piezoelectric d_{3j} coefficients and resonator parameters such as electromechanical coupling factors, acoustic absorptions and sound velocities, obtained by fitting the measured values of the complex capacitance to the theoretically predicted expression close to the piezoelectric resonances. Especial emphasis was placed on the thermal instability of the piezoelectric property.

The Young's moduli, Y_1, Y_2 and Y_3 for the foam, extracted from the resonator parameters were observed to reversibly decrease with increasing temperature because of softening of the polymer. It was also observed that the values of the moduli measured after annealing increased irreversibly for anneal temperatures above 60°C suggesting the collapse of the cellular structure.

Based on the obtained results, we propose that the thermal instability of the foam relies on both the depolarisation of the material by charge detrapping and the thermal instability of the cellular structure which leads to a collapse of the voids.

Chapter 1

INTRODUCTION

A variety of piezoelectric materials has been used over many years to convert mechanical energy into electrical energy (sensors) and vice versa (actuators). Typical piezoelectric materials include single crystals, ferroelectric polycrystalline ceramics and polymers.

Some ferroelectric ceramics, *e.g.*, lead zirconate titanate (PZT), display good piezoelectric properties, *i.e.*, high values of the piezoelectric d_{ij} coefficient and electromechanical coupling factor [28][29]. Single crystals, *e.g.*, quartz (SiO_2), generally have lower piezoelectric coefficients than ferroelectric ceramics [29]. However they possess a very sharp resonance frequency. For this reason quartz has been widely used as a frequency controller.

Ceramics and single crystals are in general very fragile, which makes them unsuitable for use under extreme mechanical conditions. In addition, the usual high cost of these materials makes them inappropriate when large samples are required.

Polymers are good candidates for covering this range of applications due to their flexibility and ruggedness, their availability as thin films and low cost [8]. However, piezoelectric coefficients, d_{ij}, as well as electromechanical coupling factors are normally much lower than those of ceramics and crystals.

Ceramic-polymer composites have been investigated for applications where there is a need to combine the piezoelectric properties of ceramics (electro-active material) and mechanical properties of polymers [30]. However, the piezoelectric properties of piezo-

electric composites critically depend on the amount of ceramic and on the connectivity [30].

In the last decade, a promising material was developed by VTT Chemical Company (Tampere, Finland). The material is microporous polypropylene (PP) with a nominal thickness of 70 μm and a highly anisotropic cellular structure, which becomes piezoelectric after poling. The material exhibits very interesting properties such as low density, high flexibility and high thickness mode piezoelectric coefficient, d_{33}.

The raw material (PP) is one of the cheapest polymers and, due to its flexibility, it can be easily foamed. The resulting foam is even more flexible so that it can be poled and electroded in a continuous mannner. As a result, large samples can be produced without increasing the final cost of the material.

All these advantages are very attractive and the material has been the subject of many publications in the last few years [5-14].

However, it is well known that the main drawback of PP foam is that its thermal stability is limited to around 60°C, when the magnitudes of the piezoelectric properties start to decrease [9,10,13]. This instability is generally attributed solely to the material depolarisation by charge detrapping [9,10,15].

The piezoelectric effect is, however, a coupling between mechanical and electrical properties. Consequently, a detailed study of a piezoelectric material requires the study of both the mechanical and electrical properties. This is especially necessary for polymer foams where most magnitudes cannot be viewed as constant, even in a first approximation.

For example, thickness strongly depends on temperature and on the applied mechanical stress. Therefore, determining the thermal expansion coefficient and Young's modulus is indispensable. In addition, since the two phases have very different properties, a variation in thickness strongly affects other properties such as density, relative dielectric permittivity, Young's modulus, etc. This introduces an additional complexity which needs to be considered if true piezoelectric characterisation of the foam is to be

pursued.

However, to date, the mechanical properties of PP foam have been poorly investigated. The mechanical response of a foamed polymer depends on the mechanical properties of the polymer and on the cellular structure. Both effects were investigated in this work.

Chapter 2

Polymers

2.1 Historical Overview

A *polymer* is a large molecule constructed from many smaller structural units called-*mers*, covalently bonded together in any conceivable pattern [1]. The word comes from the Greek *poly* (many) and *meros* (parts).

The term *macromolecule* is often used synonymously for *polymer* and vice versa. Other common names frequently used for polymers are derived from the properties and/or appearance of these materials in solid form: *plastics*(from *plastikos*, the Greek term for mouldable) and *resins*.

If it is desired to lay down a boundary between macromolecular and low molecular weight compounds, the substances with a molecular weight greater than ten thousand, *i.e.*, the molecules which consist of one thousand and more atoms, may be classified as macromolecular. Beyond roughly this size, characteristic macromolecular properties occur [31].

Polymers can be classified into many different groups depending on the criteria for the division. Thus, according to their origin they can be classified into *natural* and *synthetic* polymers.

Natural polymers are those that can be encountered in nature without human intervention. Examples of these are wool, cotton, flax, resins, wood (cellulose), leather

(collagen)-, etc. and they all have played a decisive role in all civilizations and cultures since the beginning of history. Structural proteins in the form of leather were used to make sandals, belts, shields and later on, parchments [32]. Amber, a high-molecular-weight resin was worn by the Greeks as a jewel and the use of asphalt as an adhesive is mentioned in the Bible [20]. Hardened wood and strongly tanned leather were the first offensive and defensive weapons, and later, catapults and artillery were placed in position on wooden carriages drawn by horses or men using cellulosic ropes [19].

Another natural polymer is rubber. Pietro Martyre d'Anghiera in 1511 [33] described a bouncy ball used by Aztec Indians in their favourite game after Columbus returned from his second voyage (11 June 1496), bringing back those playing balls made by the Aztecs who obtained it from the *Hevea trees* (Columbia encyclopedia, Sixth Edition). Its empirical formula C_5H_8 was established by Faraday (1791-1867) in 1826 [34] [35] and confirmed in 1904 by Harries (1866-1923) [36].

In 1860, Williams (1829-1910) isolated the most preponderant species (C_5H_8) and called it isoprene [37] [38]. It would be the rubber material on which the young plastics industry would base its activity in the 1800's [39]. The uses of rubber were enhanced by the discovery of the vulcanization process by Goodyear (1800-1860) in 1851.

The idea of producing synthetic polymers is a very old dream. The first ideas reach back to the 17th century, the main focus being to find a substitute for silk. In 1664 Hooke (1635-1703) [40] made the first attempts to microscopically explore the structure of silk. Later, in 1734, Reaumur wrote: "Silk is only liquid rubber that has been dried. Couldn't we produce silk from rubber or resin ourselves?". In 1839 Payen isolated cellulose from wood. By then, the most important step toward the production of synthetic fibres was to find a process where cellulose could be converted into a "spinnable" solution.

The first step had been taken in 1833 by Braconnot (1780-1855) who obtained cellulose nitrate by treating cellulose with nitric acid [41]. In 1846 Schönbein discovered a practical method for obtaining cellulose nitrate by treating cellulose with a mixture of

nitric and sulfuric acids. In 1885, Audemars applied for a British patent (British patent 283) for the production of artificial fibres by the treating of bast fibres from mulberry twigs with nitric acid, dissolving the product in a mixture of alcohol and ether together with rubber and, from this viscous mass, drawing fibers with a steel needle.

In 1868 the first synthetic plastic was invented by Hyatt (1837-1920) when seeking a substitute for ivory (then used to make billiard balls). He made solutions of cellulose nitrate in camphor (plastification) and produced celluloid. In 1893 Fisher (1852-1919) proposed a structure for natural cellulose. He considered cellulose to contain a chain of glucose units [42]. Celluloid was used as a base for the first films still used in photography and in the early motion pictures.

Kekule (1829-1896) in 1877 proposed that natural organic substances consist of very long chains. By that time, the term polymerization had been already introduced by Berthelot (1827-1907) [43].

Like the natural rubber industry, the man-made fibres industry had its origins in the use of natural polymers. After Ozama in 1862 constructed the first spinning jets and Swan (1828-1914) in 1883 (who was experimenting with producing high-capacity threads for electric bulbs) developed a chemical process to denitrate the filaments and convert them into cellulose hydrate, the way was open for Count L. M. Hilaire Bernigaud de Chardonnet (1839-1924) to obtain a patent in 1885 and to establish the base for the step from laboratory to plant production by simplifying and coordinating four steps: nitration, dissolution, spinning and regeneration. In 1890, the "Societe Anonyme pour la fabrication de la soie de Chardonnet", the first factory to make nitro silk from cellulose, was established.

In 1909 Baekeland (1863-1944) invented phenol formaldehyde resins (Bakelite) [44]. He was searching for a synthetic material by reacting phenol with formaldehyde to form a hard resin and then dissolving the resin in a suitable solvent. Although he could not find a proper solvent, he realized that some of the hard, solvent-resistant resins were valuable in themselves because they were easy to machine and maintained their

shape. In addition they were good electrical insulators and resistant to heat and many chemicals. He announced his development of Bakelite at a meeting of the New York Section of the American Chemical Society.

Hyatt and Baekeland invented their plastics by trial and error [42] but the age of synthetic polymers is usually accepted to start some years later, in the 1920's when Staudinger (1881-1965) proposed linear structures for polystyrene, polyoxymethylene and natural rubber that are still accepted today [45].

Staudinger's ideas were not widely accepted. Difficulties originated years before when, in 1861 Graham (1805-1869) noted an unusual property of some organic compounds such as starches and cellulose [46]. When dissolved, they could not pass through fine filters. He called them colloids (from the *kolla*, the Greek term for glue) and stated that they were formed by a large number of structurally simple molecules held together "by association". The nature of the forces responsible for this association were unknown at that time. Graham and the so-called *micellar* or *colloid* theory influenced two generations of chemists, among which Karrer was the most conspicuous.

The strength of the opposition to Staudinger's ideas at that time is clear in the advice that he received [47]:

> *Dear colleague, Leave the concept of large molecules well alone; organic molecules with a molecular weight above 5000 do not exist. Purify your products, such as rubber then they will crystallize and prove to be lower molecular weight substances.*
>
> *Organic molecules with more than 40 carbon atoms do not exist.*
>
> *Molecules cannot be larger than the crystallographic unit cell, so there can be no such thing as a macromolecule.*

Staudinger's ideas were shared by Meyer (1883-1952) and Mark (1895-?) although they disagreed on specific details. Staudinger proposed incorrectly that chains were rigid rods while Mark and his group (Kuhn and Guth) in the German chemical firm I.G. Farben, opposed this view and suggested correctly that polymer molecules had

considerable flexibility. They also formulated in 1934 the entropy-driven elasticity in terms of conformational states.

According to Mark [48] there were three main factors that favoured Staudinger's idea of macromolecules. First, the improvement and refinement of X-Ray diffraction methods allowed Katz [49] to demonstrate the fibre-like diagram for stretched rubber. Sponsler and Dore [50] [51] after similar experiments demonstrated that the diffraction patterns obtained from cellulose fibres were consistent with a chain formula composed of an indefinitely large number of units. Meyer and Mark [52] also proposed a semicrystalline structure for long-chain molecules in cellulose.

On the other hand, the use of the new methods for determining molecular weights and weight distributions, *e.g.*, dilute solutions [53] and ultracentrifugation [54] resulted in the determination of a narrow weight distribution for proteins, which was difficult to explain in terms of the colloid theory [55].

Finally, the definitive experimental support for long-chains was obtained by Carothers (1896-1937) and co-workers in the Experimental Station of the Du Pont Company (U.S.A). They deduced evidence of very-long chains from their extensive work in the qualitatively analytical determination of end groups by studying polycondensation reactions [56] [57]. Their studies resulted in the production of the first synthesised aliphatic polyesters 6,6 (nylon). A few years after the discovery of nylon 66, Shlack at Badise Anilin und Soda Fabril (BASF, Germany) commenced the synthesis of the aliphatic polyamide, nylon 6, whose commercial production started in 1943 [58].

In the 1930's, with the basic structure of polymers clarified, polymer science began its explosive growth as a new discipline. From then on, a vast amount of polymers were developed due, among other factors, to the increasing knowledge of the properties of macromolecules. The commercial introduction of polymers had proceeded through three time-stages giving rise to three generations of polymers[1].

The first generation was introduced before 1950 and is listed in Table 2.1. As men-

[1]When two dates appear, the first refers to the discovering and the second to the commercial production.

Polymer Name	*Year*	*Discovered by*	*Nationality*
Polystyrene	1911	Matthews	U.K.
Poly (vinyl chloride)	1912, 1938	Ostromislensky	Russia
Polyethylene (low density)	1933, 1939	Fawcett (Imperial Chemical Industries)	U.K.
Polytetrafluorethylene (Teflon)	1941, 1950	Plunket	U.K.
Polyurethane	1937, 1950	Bayer	Germany
Polyamide (nylon 66)	1930, 1935	Carothers (DuPont Company)	U.S.A.
Polyethylene terephthalate	1941	Whinfield and Dickinson	U.K.
Polyamide (Nylon 6)	1943	BASF Company	Germany
Silicon	1936, 1943	Rochow	U.S.A.
Ethylene vinyl alcohol	1945		
Epoxy	1936, 1946	CastanSwitzerland	

Table 2.1: Historical development of the first generation of industrial polymers.

tioned above, together with the appearance of new materials, there also were important advances in the understanding of macromolecules. In 1937, Flory (1910-1985) -at one time working with the Carothers group- confirmed the Gaussian molar mass distribution for polymers made by step-growth polymerization and the Poisson distribution for those obtained by anionic polymerization [59]. The same year, Kuhn, Mark and Guth found evidence that polymers in solution were flexible; the viscosity in solution was related to the molar mass of the polymer [60]. In 1934, the statistical theory for rubber elasticity was first formulated by Kuhn, Guth and Mark and some years later, in 1941, Guth and James formulated the first stress-strain relation based on statistical mechanics. In 1942 Flory and Huggins presented, independently, the thermodynamic theory for polymer solutions.

The second generation of polymers was introduced during the period from 1950 to 1965 and includes a number of commodity and engineering plastics (Table 2.2).A very

Polymer Name	*Year*	*Discovered by*	*Nacionality*
Polyethylene (high density)	1950's	Hogen Phillips Petroleum Co.	U.S.A.
Polypropylene (Isotactic)	1954, Hoechst AG	Natta	Italy
Polycarbonates	1958	Schnell and Fox	U.K.
Polyetherketoneketone	1962		
Polysulfone	1965		

Table 2.2: Historical development of the second generation of industrial polymers.

important achievement during these years was the discovery by Ziegler (1898-1973) that organic compounds, such as aluminium alkyl enabled polyethylene to polymerize at room temperature and atmospheric pressure [61]. In 1954 Natta (1903-1979) announced the synthesis of stereoregular polypropylene (see section 2.3), poly-α-butylene and polystyrene [62][63] demonstrating for the first time that it was possible for man to mimic nature and make polymers with stereospecific structures like those of cellulose and proteins[2]. Also in this period (1955), the growth of a single crystal was first reported [64].

The third generation, after 1965, consisted mainly of highly processed polymers with complex chemical structures. Some representative examples are poly(phenylene sulphide), polyaryletherketone and polyimides. Also, polyethylene was improved by the process of crosslinking.

The use of differential thermal methods introduced by Le Chatelier (1850-1936) [65][66] in an investigation of constitution of the clays [67] gave rise to the development of Differential Scanning Calorimetry (DSC) first published by Watson *et al.* in 1964 [68] and subsequently exploited by DuPont and Perkin-Elmer who released highly sensitive

[2]Just one year before, in 1953, Staudinger wrote in the Nobel Lecture: *"In deriving macromolecular natural substances from vegetable and animal material the original macromolecules are in many cases modified to a greater or lesser extent by isolation and purification, and thus the macromolecules examined are not the same as those formed by Nature"* [31].

instruments so that thermal methods started to be widely applied to polymers [69][70].

In 1969, Kaway [71] reported the piezoelectric character of poly (vinylidene fluoride) and, in 1971, Nakamura and Wada [72] reported its pyroelectric character.

In 1972, Pierre-Gilles de Gennes presented the reptation model which describes the diffusion of a chain molecule in a matrix of similar chain molecules as an improvement of the Rouse model [73]. The evidence for reptation in an entangled polymer was reported in 1978 by Klein [74].

In 1973, Juhfuss and Jackson, from Eastman Kodak, patented the first well-characterized thermotropic polymer (a copolyester of p-hydroxybenzoic acid and ethylene terephthalate). In 1976 they reported the discovery of its liquid crystalline behaviour.

In 1977 MacDiarmid (1927-), Heeger (1936-) and Shirikawa (1936-) developed the first conductive polymer by exposing polyacetylene to bromine vapour which acted as a dopant [75].

In 1990's a new polymerization reaction using a metallocene catalyst was used in the production of polyolefines (see section 2.5) with a uniform molecular structure and narrow molar mass.

2.2 Classification of Polymers

Any attempt to classify polymers into different categories tends to be somewhat arbitrary. One useful way is to place them into groups displaying similar properties which has the advantage of reflecting the underlying molecular structure [76]. These groups will be reviewed in the following sections.

2.2.1 Organic and Inorganic Polymers

Polymers are usually composed of carbon, hydrogen, nitrogen and oxygen and are therefore called *organic polymers*. Examples can be encountered among natural polymers such as proteins, polysaccharides, polyaminoacids, etc. and also among synthetic poly-

mers such as polyethylene, polypropylene, polycarbonate, etc. Chlorine, fluorine, boron, silicon, phosphorous and sulphur are involved in some polymers. Thus, polytetrafluorethylene -Teflon®- contains fluorine, poly (vinyl chloride) -PVC- contains chlorine and vulcanized rubber contains sulphur.

However, it is customary to refer to this group as organic polymers [48] and, at a molecular level, their characteristic feature is the chain of tetravalent carbon atoms which form strong bonds with atoms of other elements or other carbon atoms [77].

The term *inorganic polymer* is reserved for those containing elements of the second and higher rows of the periodic table in the backbone. Examples of inorganic polymers are polyphosphacenes, polysiloxanes or polysilanes. Polysilanes are widely used as components of photoresist because of the light-sensitive silicon-silicon bonds.

2.2.2 Homo- and Copolymers

In section 2.1 the importance of polymeric materials was discussed in terms of answering specific needs. Sometimes, however, no known polymer fulfils the required properties because they lie somewhere between the properties of two (or more) known polymers. Unfortunately, it is quite likely that in a polymer resulting from the mixture of the two, i.e., the *blend*, the poorer qualities of each will become exaggerated [1]. Besides, two polymers are most of the time incompatible [32]. The desired synergistic effect is often achieved when the two monomers are on the same polymer chain giving rise to a *copolymer*. It is easy to see that the potential number of polymers is increased by a factor $(n-1)$ where n is the number of the available monomers.

The properties of copolymers are usually determined by the particular arrangement of the forming monomers on the polymer chain. Even for the simplest case of two different monomers, five kinds of copolymers can exist, random, alternating, block, graft[3] and stereoblock copolymers which are schematised in Fig.2.1.

[3]Block and graft copolymers are obtained from two consecutive and separated reactions and so they are sometimes called *multistep copolymers*.

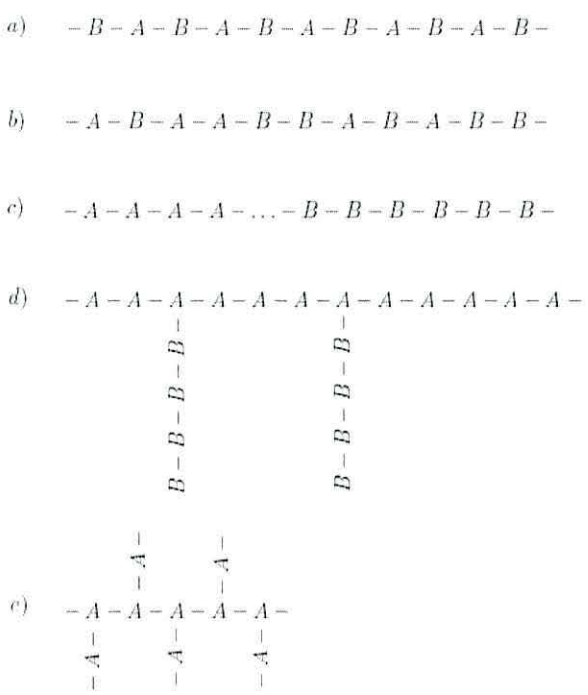

Figure 2.1: Schematical representation of copolymers. a) alternating, b) random, c) block, d) graft and e) stereoblock, the monomer is the same A, but with different tacticities.

2.2.3 Chemical Bonding

As mentioned in section 2.2.1 the different atoms in polymeric chains are held together by covalent bonds. It is worth noting, however, that a certain ionic character arises when two (or more) different atoms -especially when the difference in electronegativities is appreciable- participate in the bond. Pure ionic bonds are not found in polymers, except those appearing between divalent ions and carboxyl groups acting as crosslinking agents in natural resins.

In condensed phases, some forces are still present between molecules. These forces are generally termed *intermolecular* or *secondary* forces and are of great importance in many physical properties of condensed phases in general and in polymers in particular. Although the nature is electrostatic, the origin is diverse. Thus, in dipolar substances, dipole-dipole interactions give rise to electrostatic forces that, at molecular distances may be of great intensity. Moreover, the directional character of dipole-dipole

	Bond	*Bond Length* ($\AA$)	*Dissociation Energy* ($KJ\ mol^{-1}$)
Primary bonds	$C-C$	1.54	347
	$C=C$	1.34	611
	$C-H$	1.10	414
	$C=O$	1.46	360
Secondary bonds	Dipolar		8 - 25
	Induced		10
	Dispersion		< 8
	H. Bond	2.4 - 3.2	12 - 40

Table 2.3: Typical primary and secondary bond lengths and energies [18][19].

interactions results in a high dependence of these forces on the mutual orientation of the molecules involved and therefore, on thermal agitation, *i.e.*, on temperature. In addition, the charge distribution in a molecule is more or less altered by the presence of an electric field. The presence of an electric field, created by a dipolar molecule may therefore induce other dipoles in the surrounding molecules resulting in an interaction (*induction interaction*) between the permanent and induced dipoles. The magnitude of the resulting force depends, of course, on the capability of the molecule to become polarized -polarizability- and on the dipolar moment of the permanent dipole.

Finally, the characteristic interactions in a non-dipolar condensed molecular compound are due to the so-called *dispersion*, *London* [78] or *Van der Waals* [79] forces and arise from the interaction between instantaneous dipolar moments which do not vanish even in non-polar molecules. These are almost independent of temperature [19][18] and are present in all kinds of compounds representing the major part of the intermolecular forces unless a large dipolar force exists.

Polyethylene chains are nonpolar and all the interactions are due to dispersion forces

which, added to the low flexibility gives polyethylene its relatively low melting point and rigidity as well as easy solubility. In polyformaldehyde however, the rotation about the $C-O$ bond is not as inhibited as the rotation about $C-C$. Furthermore, the dipole character of the aldehyde group produces polar forces between adjacent chains, which act over longer distances and are stronger than dispersion forces resulting in a higher melting point and higher rigidity than polyethylene [48].

An important case of dipolar forces is that in which a hydrogen atom is covalently bonded to a highly electronegative atom, *e.g.*, fluorine, nitrogen, oxygen and chlorine (in order of increasing energy). As a result of the difference in electronegativity, the system becomes polar. If there is another group with the same characteristics in the same or another molecule, there will appear a high dipolar force between the hydrogen of one group and the accompanying atom of the other group called a *hydrogen bond.* Hydrogen bonds together with sulphur-sulphur bonds are responsible for the tertiary structure of proteins [80], for example.

The high melting point of nylon 66 results from the combination of dispersion and dipolar forces as well as hydrogen bonding between polyamide chains [19].

2.2.4 Entanglement Effects

In addition to the primary and secondary forces, the presence of *entangled* chains -which can slip over each other but cannot cross each other [81]- are also of great importance in the properties of polymeric materials. Thus, although paraffin wax and high density polyethylene are similar, the chains in paraffin wax are too short to allow entanglement effects and hence it lacks the strength of high density polyethylene [19].

2.2.5 Molecular Architecture

So far we have implicitly accepted the one dimensional character of the polymer backbone. This is the case in some polymers such as polyethylene and polyformaldehyde which are then classified as *linear* polymers (Fig.2.2 a)). In some cases, however,

polymers have branched chains although they keep their discrete character. They are referred to as *branched* polymers. The longest chains are called *main* chains and the rest, *branched* chains. When main and branched chains are not formed by the same monomer, the term *graft copolymer* is used. Most of the time, branching is due to imperfections in the polymerization reaction but sometimes it is intentionally induced. When the length of branched chains increases, some of them can connect two (or more) main chains. If the frequency of long branched chains increases so that all molecules are connected, the whole polymer converts into a huge molecule and is referred to as a *crosslinked* or *network* polymer (Fig.2.2 c)). Crosslinking can be obtained in the polymerization reaction -vulcanization- or after, by chemical treatment -curing- or by exposure to radiation.

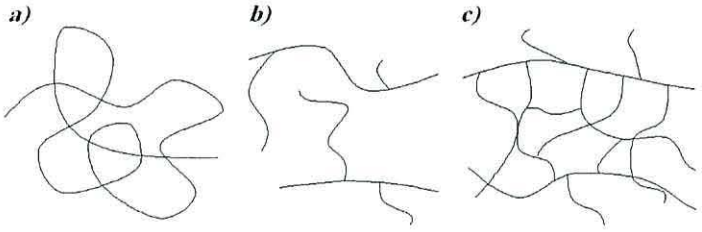

Figure 2.2: Schematic representation of a) linear, b) branched and c) crosslinked polymers.

2.2.6 Response to Stress and Temperature

Elastomers are polymers that undergo reversible deformation under the application of small stresses, *i.e.*, they are elastic. Natural rubber and styrene butadiene (SBR) (synthetic) are examples of elastomeric materials.

The term plastic is widely used in common life. A plastic is defined as: *"A synthetic material made from a wide range of organic polymers such as polyethylene, PVC, nylon, etc., that can be moulded into shape and then set into a rigid or slightly elastic form."* [82]. For the sake of precision, further division is customary. Thus, plastics can be *thermostable* or *thermosetting* and thermoplastic. Thermostable materials are

those which, once they have been processed, can no longer be changed into any other shape. They are usually crosslinked and the crosslinking is usually performed during fabrication. Epoxy resins are among the most widely used thermosetting materials. A thermoplastic material however, can be moulded into shape when heated above T_g (see section 2.4). Polyethylene, polypropylene and poly (vinyl chloride) -PVC- are examples of thermoplastics.

2.2.7 Tacticity

Many polymers are generated from monomers which, when polymerized, contribute an asymmetric atom to every repeat unit of the chain. In this case, what becomes important is the sequence of absolute configurations along the backbone of the chain. The shortest distinguishable piece of the sequence is the so-called *diad*. If two consecutive configurations have the same absolute configuration (*e.g.*, $R-R$ or $S-S$), the diad is designated a *meso diad* while if they are different (*e.g.*, $R-S$ or $S-R$), the diad is designated a *racemic diad*. Polymer *tacticity* refers to the the diad sequence. The possible cases of tacticity are:

1. *Isotactic* polymers which consist entirely of meso diads. This means that the absolute configuration sequence is either $-R-R-R-R-$ or $-S-S-S-S-$.

2. *Syndiotactic* polymers which consist entirely of racemic diads. The absolute configuration sequence is $-R-S-R-S-R-$. Syndiotactic polymers typically have very different properties from their isotactic analogues.

3. *Atactic* is the most usual configuration. It is neither isotactic nor syndiotactic and corresponds to a random sequence.

   Different tacticities of polypropylene are schematized in Fig.2.3.

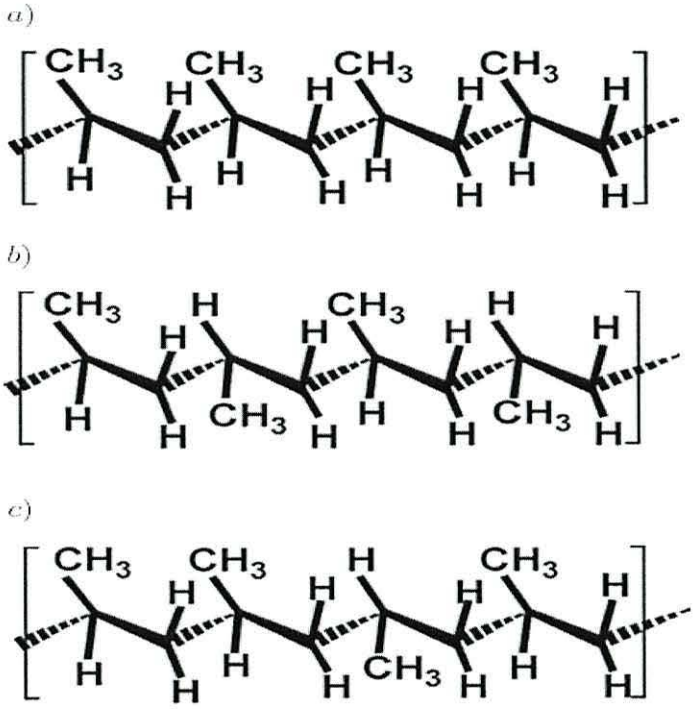

Figure 2.3: Different tacticities of polypropylene. a) isotactic, b) syndiotactic, c) atactic. From [1].

2.3 Crystallization

So far, we have concentrated on the different geometrical structures that chains can adopt (linear, branched or network) and how the repeat units can arrange in different ways to form syndiotactic, atactic or isotactic configurations. Another basic property of chain molecules is that they show a tendency to form crystalline aggregates. Crystallization is a first-order transition and therefore characterized by the discontinuity of the first derivatives of the Gibbs function, *i.e.*, entropy and specific volume.

Crystallinity was first discovery in natural polymers (cellulose, keratin, gelatin, wool and stretched rubber) [83]. As early as 1913 (a year after the discovery of X-Ray diffraction by Von Laue and the same year as the first successful application of X-Ray diffraction to the determination of crystal structure by Bragg), Nishikawa and Ono first demonstrated the semi-crystalline character of cellulose using X-ray measurements [84].

The first semi-crystalline high polymer was reported by Schildknecht in 1948 [85].

Single crystals of α-gutta were reported by Schlesinger in 1953 [86] and soon afterwards, in 1957, single crystals of synthetic polymers with sufficiently regular backbone structure and few or no side groups were grown in several laboratories [87][88][89].

In 1955, Jaccodine reported spiral growth in polymethylene [64]. This unexpected growth was verified by Till [89] in polyethylene single crystals.

2.3.1 Conditions for Crystallization

The tendency of polymers to crystallize is of course related to the composition and structural details of the individual chains, the most important being: structural regularity, chain flexibility, the presence of groups which produce intermolecular forces and bulky substituents which inhibit the chain segments from fitting into a crystal lattice [48].

Linear polymers such as polyethylene and polyformaldehyde can assume, because of their simple structure, planar conformations and therefore, a very simple period which favours the lateral order as required in the crystalline phase. In addition, stereoregularity is also of considerable importance in the formation of crystals. Natta [62][63] demonstrated that stereoregular polymers -isotactic and syndiotactic- are crystallizable whereas atactic specimens do not crystallize under any conditions.

Chain bending is necessary to accommodate long chains within the crystal entity, and is associated with lamellar single crystals [90]. Chain flexibility depends on energy barriers associated with conformational changes in the chain. Therefore, chains formed from single bonds are more flexible than those incorporating double bonds. In the presence of strong stereoregular and intermolecular forces they are likely to crystallise. Furthermore, in the cis form, double-bonds reduce the energy barrier for rotation of adjacent bonds, thereby increasing the tendency of such materials to crystallise as well [48].

Yet, chain stiffness may also enhance crystalline formation by allowing only certain conformations to occur within the polymer chain. Thus p-polyphenylene is a linear

chain that cannot fold over at high temperatures. It is however highly crystalline [19]

It has been found that all groups which carry dipoles, highly polarizable groups, or permit the development of interchain hydrogen bonds favour crystallization [48][19].

The vibrational and rotational mobility of an intrinsically flexible chain can be inhibited by bulky substituents. This is of crucial importance in life. The cholesterol molecule situated between the acids that form the lipidic shell of cells inhibits crystallization thus conserving the flexibility of the cell [80].

The extent of crystallization is measured by the quantityX_c which is given by:

$$X_c = \frac{\rho_c}{\rho}\frac{\rho - \rho_c}{\rho_c - \rho_a} \tag{2.1}$$

where ρ, ρ_c and ρ_a are the densities of the material, the crystalline and the amorphous phases respectively. Several experimental methods can be used to determine X_c among which the most relevant are X-Ray diffraction, specific volume, infrared absorption [18] and differential scanning calorimetry (DSC) [20] (see Chapter 5).

2.3.2 Morphology of Polymer Crystals

Fringed-Micelle Model

Although X-Ray diffraction studies show recognizable features in some high polymers, the Bragg reflections appear diffuse compared to those from well-developed single crystals. Diffraction theory indicates that this can arise from either small crystallites or the presence of defects and/or impurities. Since the diffraction patterns from polymers are usually too weak to permit discrimination between these two possibilities [91], the hypothesis of small crystallites was selected as the most probable. With this assumption, a crystal size no bigger than a few hundred atoms was calculated from the width of the diffraction rings [18] [83], which was many times smaller than chain length.

Hermann, Gerngross and Abitz proposed the so-called *fringed-micelle* model [92] [93] which assumes that chains are parallel to each other in crystalline zones but diverge

into the amorphous zone each running through several crystalline zones, linking them together and therefore acting as crosslinks as schematized in Fig.2.4 a). The theory was also supported by Bunn [94] and Mark [95].

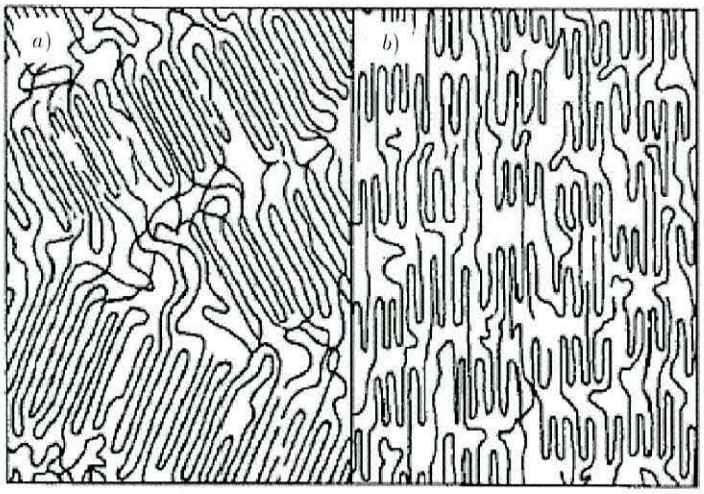

Figure 2.4: Fringed-Micelle model for: a) unstrained and b) stretched polymer

This model explains the observed increase in crystallinity of the polymer when strained [83] (Fig.2.4 b)) as well as the resemblance between highly-crystalline and crosslinked polymers [48].

Lamellar Structures. Folded-Chain Crystallities

The discovery of spherulites [91] and years later of single crystals [64] highlighted inconsistencies of the fringed micelle model. In 1957, Till [89] reported crystals about 100 $\AA$ thick and with lateral dimensions around 50 $\AA$ showing sharp point reflections, suggesting the existence of single crystals. From the interpretation of the electron-diffraction patterns in single crystals of polyethylene, Keller [88] proposed a model in which the direction of chains is normal to the crystal surfaces. Therefore, since polymeric chains are a hundred or thousand times larger than crystal thicknesses, the so-called *lamellar structure* was proposed in which polymeric chains are folded back and forth upon themselves as shown in Fig.2.5.

The idea of chain folding was generally accepted after Keller, although it had been suggested almost twenty years before by Storks after his electron-diffraction experiments in stretched polyethylene and vulcanized gutta-percha [96].

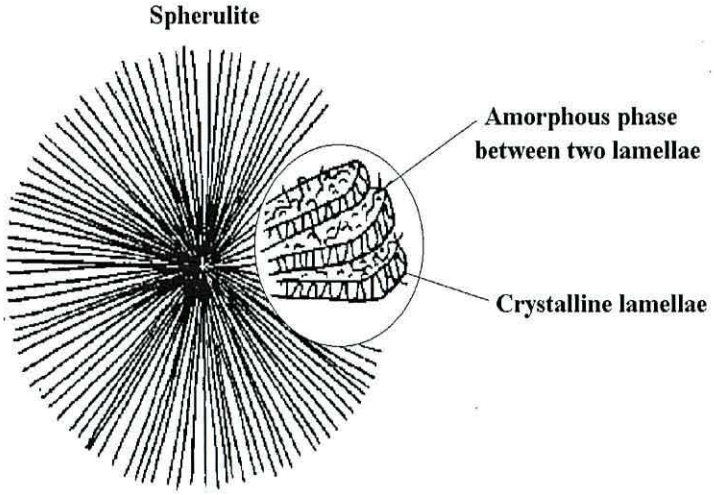

Figure 2.5: Schematic representation of a spherulite and the lamellae crystallity [1].

The chain-folding model is consistent with the structure of highly crystallized polymers such as medium molecular weight polyethylene with $X_c = 0.85$ but it fails to explain the structure of low crystalline polymers such as nylon with $X_c = 0.3$ where contributions to the amorphous phase coming from crystal defects, free ends, tie molecules[4] and uncrystallizable components account for 70% of the sample [83].

In 1962 Flory proposed a modified chain-folded model in which a certain fraction of chains may proceed into the amorphous regions and enter into nearby crystallites providing interconnections between crystallites without which: *"Even the most rudimentary properties of crystalline polymers would be different from those observed"* [97]. Flory also postulated that substantial segments of those chains that re-enter the same crystallite may be expended in amorphous zones before re-entering, in some cases in a sequence other than the one adjacent to its previous passage. The proposed model can be seen as a hybrid between perfect chain-folding and the fringed-micelle model.

[4]Tie molecule is the term used to refer to the part of the chains that act as a link between two discrete crystallites.

2.3.3 SPHERULITES

When crystallization proceeds from the melt a number of polycrystalline structures are formed among which the commonest is the so-called *spherulite*. As already mentioned, the spherulitic structure was first reported by Bunn in 1945 [91] when studying polyethylene crystals. Under a microscope spherulites show a characteristic dark Maltese cross when observed between two crossed polarizers.

This mysterious appearance was solved after the discovery of lamellar crystallites. Lamellar structures were found to be crystalline but anisotropic, and therefore birefringent with optical axes parallel and perpendicular to the fold plane. Assuming that spherulites are composed of lamellar crystallites with spherical symmetry, as shown in Fig.2.5, there are only four regions in which the orientation of the lamellae is perpendicular to both polarizers. These regions will appear dark in the microscope and form the observed Maltese cross pattern (Fig.2.6).

Spherulites often appear with a more complex structure where the Maltese cross is evident but the radial fibrillar appearance is replaced by a series of concentric bands. This is ascribed to the rotation of the crystal orientation around the spherulite radius [2].

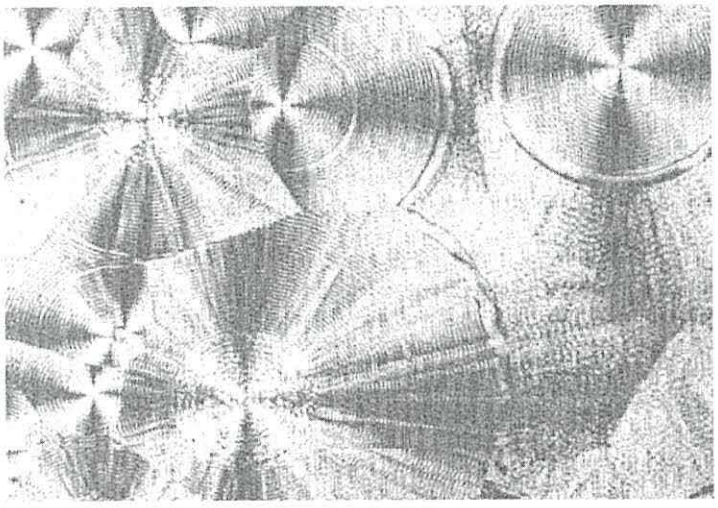

Figure 2.6: Spherulites of poly (trimethylene glutarate) observed in the optical microscope between crossed polarizers, showing the ringed Maltese cross patterns [2].

Other structures have been reported in polymers crystallized from the melt, for

example *extended-chain* crystals in which the dimension of the crystal in the chain direction is approximately that of the chains [98]. The planar conformation corresponds to the minimum energy unless groups cause steric impediments. Polymers in which the extended chain conformation has been seen include polyethylene, poly (vinyl alcohol), poly (vinyl chloride), syndiotactic polymers, most polyamides and cellulose [18].

There are also several crystal structures. In polymers crystallised from dilute solutions, *dendrites* and *shish-kebab* structures are found, resulting from direction-dependent crystallisation. Also seen are *hedrites*, which are polyhedral structures formed by lamellae joined together along a common plane. These structures are typically found in high concentration solutions [1].

2.3.4 CRYSTALLINE STRUCTURES

A wide variety of conformations can be assumed by flexible chains. In principle, since they define the spatial relationship between chains and are dependent on the nature of the chemical bonding (bond length and bond angles) the number of possible conformations is very high. Modelling such a system is therefore complex and is solved using statistical mechanics.

However, when the conditions for crystallization are fulfilled, different chains or segments are aligned parallel to each other so that lateral forces may influence the resulting configuration. This is true where hydrogen bonds or polar forces act over laterally adjacent groups (see section 2.2.3). Thus, for polyethylene, it is known that the energy is minimized in a planar zigzag arrangement which leads to the crystalline structure shown in Fig.2.7. Here, part of the chain inside the parallelepiped produces the crystal by translations and reproduces the so-called *unit cell.*

However, in polymers with bulky substituents, the planar zigzag represents a high energy due to the repulsion interactions between the substituents [32]. This interaction is avoided quite often by the formation of the so-called *helical conformation* since it allows the substituents to pack closely without appreciable distortion of the chain

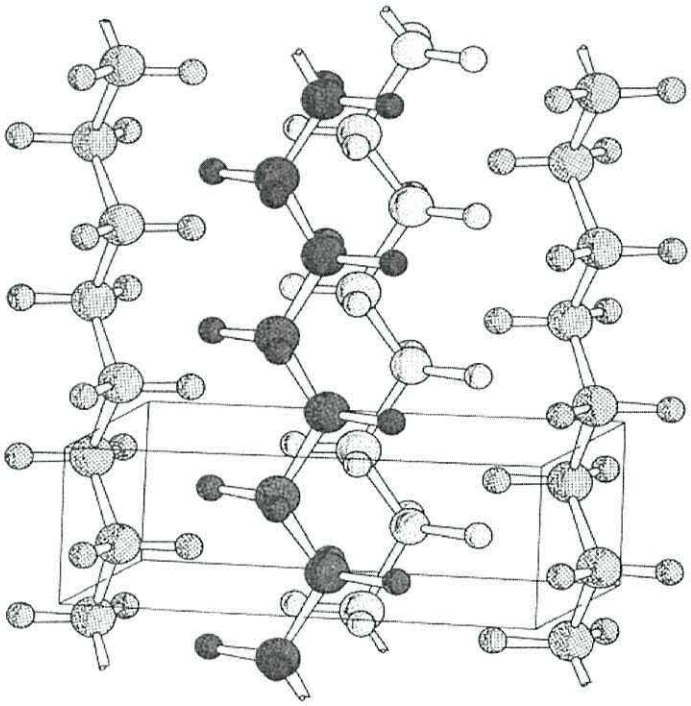

Figure 2.7: The crystal structure and unit cell of polyethylene [3].

bonds [18]. This conformation is typical in most isotactic polymers, as well as in isobutylene, polytetrafluoroethylene and polypeptides and is represented in Fig.2.8.

Helical structures are represented with the notation n_m where n is the number of carbons per helix turn and m, the number of carbons in the monomeric unit. The helical conformation implies the existence of a *subcell* which is represented by one turn of the helix and which gives rise to short-range periodicity that is, of course, detected by the same methods as the long-range periodicity arising from the existence of the unit cell.

It can be shown mathematically that solids can only exist in seven crystalline systems. In crystalline polymers, the nature of intra- and intermolecular forces are such that the cubic system is excluded. However, all the rest (hexagonal, tetragonal, rhombohedral, orthorhombic, monoclinic and triclinic) are all possible.

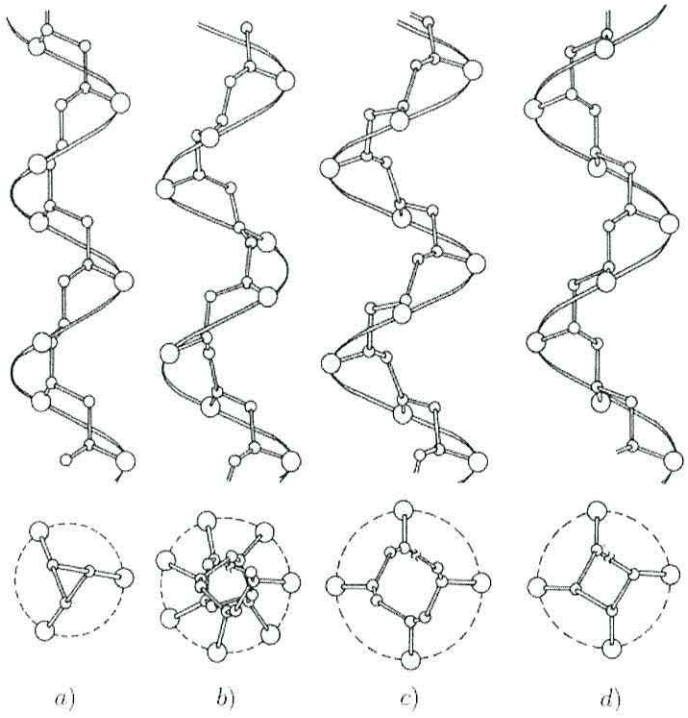

Figure 2.8: Helical conformations of isotactic polymers [4].

2.4 Phase Transitions

Polymers can exhibit a number of conformational changes each accompanied by differences in their properties. Generally, the resulting transitions are designated in alphabetical order, α, β, γ, etc., with decreasing temperature, irrespective of their molecular origin [77][99].

Low-temperature relaxations are associated with the conformational changes, chiefly rotations, of elements around covalent bonds of the backbone and are principally controlled by the intramolecular contribution to the rotational potential [99]. Where these conformational changes involve large elements of the chain, the relaxation is volume-dependent and is termed a *glass-transition* [58][76][99]. The segmental movements above T_g allow large-scale reorganization in response to an externally impressed stress [77] thus influencing the mechanical response of the polymer.

Glass-transitions often occur in a very short temperature range and then it is meaningful to refer to a single *glass-transition temperature*, T_g [99]. As mentioned

above, the rotations around the covalent bonds of the backbone are highly affected by the intramolecular interactions. For example in polyethylene $(-CH_2 - CH_2-)_n$, T_g has been found to lie in the range (140-270) K (see below) while in poly (p-xylene) $(-CH_2 - p - phenylene - CH_2-)$ the p-phenylene rings in the polyethylene chain impede the rotational movements and stiffen the backbone chain [76]. As a result a much higher value of T_g of 353 K is found in poly (p-xylene). The nature of the side-groups does also influence the chain flexibility, *i.e.*, the glass-transition process. In general, the bulkier the side-group the higher T_g which reflects both the larger barrier to internal rotation and the steric impediments [76][99].

The glass-transition process is accompanied by a change in the second derivatives of the Gibbs function, *i.e.*, thermal expansion coefficient and specific heat. As a result it is often classified as a second-order phase transition, a fact which has been a matter of controversy since the amorphous phase is a non-equilibrium state.

In semicrystalline polymers, the crystalline-amorphous regions may experience some slight onset of segmental motions above the glass-transition but movements of polymer chains in the crystalline phase are impeded by the strong intermolecular forces arising from the closer packing in this phase. Therefore, the glass-transition is related to the amorphous phase. The determination of the glass-transition temperature is therefore a difficult task for highly-crystalline polymers such as polyethylene for which values of T_g have been quoted between 140 and 270 K [76].

In crystalline phases however, a higher temperature transition is observed, the so-called *melting transition* which is the reverse of crystallization. Although it is present in all crystalline materials, melting of polymers is a complex process; its nature is highly dependent on the thermal and mechanical conditions during the formation of the crystal structure, on the thermal history of the crystalline samples, and even on the testing parameters, *e.g.*, heating rate, used for melting [100]. The most widespread technique for studying polymer melting is calorimetry. Calorimetric melting curves provide valuable and exact information about the thermal (T_m) and structural (degree

of crystallinity) parameters [101].

The melting transition is, as crystallization, a first-order transition characterized by a discontinuity in the first derivatives of the Gibbs function. The factors which influence the melting process are the same as those which influence the glass-transition. In fact, it has been observed that for many semicrystalline polymers T_g is around (0.5-0.8) times T_m [102].

In addition to the above mentioned transitions, it is well-known that polymers undergo other *secondary* or *subsidiary* transitions. Some of these secondary relaxations are related to movements of short elements in the backbone. For example, a relaxation due to the movement of short segments (10-20 carbon atoms) of the main chain in polyethylene has been reported [103]. Other relaxations are associated with the movement of specific molecular groups. Poly(methylmethacrylate) shows three relaxations below T_g associated with the side-chain motion of the ester group (α) [104], and methyl groups attached to the main chain (γ) and to the side chain (δ) respectively [99].

Secondary relaxations can also be ascribed to the crystalline phase and amorphous-crystalline interface. For example, diffusion of defects in the crystalline phase [105][106] as well as localized movements in the amorphous-crystalline interface [107] have been suggested as the molecular origins for the γ relaxation in polyethylene. Secondary relaxation of polypropylene are discussed in section 4.6.

2.5 POLYPROPYLENE

Polypropylene is an organic polymer that belongs to the family of olefins[5]. Its chemical formula is presented in Fig.2.9.

It was first synthetised in 1954 by G. Natta by means of the so-called *Ziegler-Natta polymerization* route [63]. The resulting polymer was a hard, highly crystalline thermoplastic. Natta's group determined that its crystallinity comes from its stereoregularity

[5]Olefins or alkenes are the family of polymers formed from the monomer with general formula $CH_2 = CHX$ where X is composed exclusively of carbon and hydrogen.

$$\left[-CH_2-\underset{\displaystyle CH_3}{\underset{|}{CH}}-\right]_n$$

Figure 2.9: Chemical formula of polypropylene.

and reported an helical structure with three monomeric units per turn [63]. It can be made in isotactic, syndiotactic and atactic forms which are shown in Fig.2.3. The polypropylene chains form helices with three monomer units to a full turn, *i.e.*, 3_1 helix [63] with a different crystalline system associated with each tacticity (see Table 2.4). These three phases correspond to various packagings of 3_1 helices.

Form	*Units in the Unit Cell*	*Lattice Constants* (Å) *a*	*b*	*c*	*Crystalline System*
Isot. (α form)	12	6.65	20.96	6.50	Monoclinic
Isot. (β form)	?	6.47	10.71	?	Pseudohexagonal
Isot. (γ form)	3	6.38	6.38	6.33	Triclinic
Syndiot.	8	14.50	5.81	7.3	Orthorhombic

Table 2.4: Lattice Constants and Crystal Forms of Crystalline Polypropylene [20].

In the monoclinic α phase each chain is in contact with three adjacent enantiomorphous and two isomorphous chains [108][109]. The hexagonal β phase corresponds to groups of three isomorphous chains [110]. In the rare triclinic γ phase, the unit cell bears a strong resemblance to that of the α form [108][109]. This unit cell appears to result from the modification of the α form by a simple shear along the a axis [111] and the chain arragement in the two forms is probably analogous [112]. The growth of polypropylene single crystals was first reported by Ranby in 1960 [113].

Low cost and a reasonably good combination of chemical and heat resistance made

Property	*Tacticity*	*Value*
Thermal Expansion[a]		(70-110) 10^{-6} K^{-1}
Crystallinity		$31 - 65$ (%)
Density[a]	Isotactic, Crystalline	910 $Kg\ m^{-3}$
	Isotactic, Amorphous	(850-854) $Kg\ m^{-3}$
Melting point	Isotactic	186^oC
	Syndiotactic	138^oC
Glass transition temperature		-18^oC
Specific heat	Isotactic	(1.8-1.92) $KJ\ Kg^{-1}\ K^{-1}$
Young's modulus at 20^oC[a)]		(1.2-1.7) GPa
Dielectric constant (1 KHz)[b)]		2.2
Dielectric loss factor (1 KHz)[b)]		< 0.02
Breakdown voltage[b)]		640 $V\ \mu m^{-1}$

Table 2.5: Properties of polypropylene [21]. a) [15] b) [22].

polypropylene of great commercial importance [42]. Other physical properties of polypropylene are summarized in Table 2.5.

The commercial types of polypropylene usually contain additives, among which, the most usual are calcium carbonate ($CaCO_3$) [114][115] and talc [116][117].

Chapter 3

Dielectrics in Electric Fields

3.1 Historical Overview

We know about electrostatics at least from as early as 600 B.C. when the ancient Greeks observed that rubbed amber could attract light objects [118][119]. Electricity has also been used in medicine since the days of the Romans. In 46 B.C. Scribonius Largus recommended the discharge of the electric torpedo fish for relief of pain [120]!.

Since then, no research activity seems to have been done until 1600 when W. Gilbert (1544-1603) a physician to Queen Elizabeth I and after her death to James I, published his book *De Magnete* [121][122]. He introduced the term *electrics*[1] to dielectric materials. In opposition, those that did not show this effect were termed *non electrics*. He also distinguishes the attraction due to amber and the attraction due to lodestone.

Important contributions followed such as the invention of the Leyden jar which is attributed to Musschenbroek (1692-1761) and his assistant Cunaeus in 1746 although von Kleist (1700-?), Dean of the cathedral at Kammin reported it in 1745 [123].

Another contribution is given to Gray whose study of electricity appeared in 1732 [119] where he wrote about his *"enquiry whether there might not be a way found to make the property of electrical attraction more permanent in bodies"* [124], which represents the first idea of long-lasting electrification -electrets. For this purpose he experimented

[1] From *elektron*, the Greek term for amber.

with various materials like rosin, shellac, sulphur, etc. which he melted and allowed to cool and solidify. He reported that materials so formed appeared as strongly electrified [125][126]. His studies in molten dielectrics were continued by Johann K. Wilcke (1703-1770), a professor ordinarius of Latin and Greek by that time and later professor ordinarious of physics at the University of Leipzig [127][128], who gave the name *spontaneous* to the electricity produced during solidification [119].

In the 1740's Franklin (1706-1790), an American editor and statesman, became interested in electrical experiments. Working with the Leyden jar he realized that grounded pointed bodies had the property of discharging charged bodies. Experiments led Franklin to represent electricity as a natural quantity of bodies so that when a body loses some he would call it electrically negative, or minus and if it gains some he would call it positive or plus. Franklin also postulated the conservation of charge, since if one or more bodies gain electrical fire, some other or others must lose it.

In 1748 Franklin started a series of experiments on the Leyden jar which would be later known as a *dissectible capacitor*. The first result he announced was that a Leyden jar always contains charges of opposite sign on the two conductors and that these charges are of the same magnitude. After that, Franklin started wondering whether the electric power of the Leyden jar was in the water or in the glass itself. The fact that when the water of a charged Leyden jar was decanted into a non-charged Leyden jar this did not show any electric effect at all made Franklin consider two possibilities: the charge was lost during the decanting process or it remained behind in the glass. The latter was proved to be the case after observing electric effects in the Leyden jar filled with non electrified water. Franklin had discovered *dielectric absorption*.

Franklin's experiments were continued by Priestley (1733-1804), famous for the discovery of oxygen, who used two pith balls which were entirely inside an electrically charged cup and found that the balls remained inmobile until a grounded conductive susbtance touched them. In this case, the balls immediately separated, being attracted to the sides of the cup (reference (7) in [129]).

In the meantime, in 1758 Aepinus (1724-1802) had published his *Tentament*, the first reasoned, fruitful exposition of electrical phenomena based on the principle of action-at-a-distance [130]. He stated the presence of three forces: a repulsion between the particles of electric fluid, an attraction between them and the corpuscles of common matter and a repulsion between the corpuscles. He also used a variation of these forces on the square of distance in one of his calculations but he left the question open. With this model he showed the existence of all the stages between insulators and conductors [131].

Two years later, in 1769 Robinson (1739-1805) determined the law of force between electric charges by direct observation. As a result of the experiments he performed, he concluded that [129]:

> *...the mutual attraction of two spheres, electrified positively or negatively, was very nearly in the inverse proportion of the squares of the distance of their centers, or rather a proportion somewhat greater, approaching to* $1/r^{2.06}$".

In 1773 Cavendish (1731-1810) demonstrated the inverse square law of forces, including the precision of his data. He also introduced the concept of *degree of electrification*, (the *electric potential*), and the idea that when two charged objects are set into contact, they redistributed their charges in order to attain the same degree of electrification [129].

Since Cavendish determined not to publish his findings they were unknown for almost a century. Thus, the inverse squares law is usually attributed to de Coulomb (1736-1806) who, using a torsion balance from his invention, demonstrated the inverse square distance dependence of electric forces [132].

In the meantime, Poisson (1781-1840) using the inverse square law as a fundamental postulate and taking advantage of the mathematical methods developed by Lagrange (1736-1813) and Laplace (1749-1827) for gravitation, introduced a function $\phi(x_1, x_2, x_3)$ [2] whose partial spatial derivatives $\partial\phi/\partial x_i$ equal the corresponding components of the

[2] Called *potential function* by Green fifteen years later.

electric force at the considered point (x_1, x_2, x_3) as long as it is not occupied by a charge. Two years later he extended the model for the case of points occupied by charges [133]:

$$\sum_{i=1}^{3} \frac{\partial^2 \phi}{\partial x_i^2} = -4\pi\rho \tag{3.1}$$

which is known as *Poisson's equation* and where ρ is the volume density of charge and whose integral counterpart was established in 1813 by Gauss (1777-1855):

$$\oint_S \vec{E} \cdot d\vec{S} = \int_V \vec{\nabla} \cdot \vec{E} dV \tag{3.2}$$

where S is a closed surface bounding the volume V and $\vec{E}$ is a vector with first derivatives in a region containing V. When equation 3.2 is applied to the electric case, where $\vec{E}$ varies with the inverse of the distance, it converts into *Gauss' Theorem*:

$$\int_S \vec{E} \cdot d\vec{S} = 4\pi\rho. \tag{3.3}$$

Some years later, in 1820 Ampère (1775-1836) [134] published his achievements where he made the following assertion:

> *The currents of which I speak self accelerate until inertia of the electric fluids and resistance that they encounter due to imperfections in even the best conductors cause equilibrium with the electromotive force, after which they continue indefinitely at a constant speed such that this force remains at a constant intensity; but cease at the instant that the circuit is interrupted.*

first introducing a clear definition of electric current and the cause-effect relation between potential and current. He also invented an instrument for measuring electric current which he called a *galvanometer* in honour of Galvani.

In 1837 Faraday (1791-1867) reported his investigations of the dielectric absorption [35] on shellac using a spherical dissectible capacitor. He found that immediately after the capacitor was discharged, the dielectric exhibited an electrification whose polarity was opposite to that of the capacitor and therefore requiring more primary charge

to maintain the same voltage, *i.e.*, rediscovering the fact that a dielectric located between capacitor plates increases its capacitance which had been discovered by Cavendish years before. This polarization state quickly disappeared followed by a *reversal of polarity* of the dielectric so that the surface in contact with the positive conductor during charging now appeared positive and the opposite surface appeared negative. After the polarity reversal, the apparent charges of the dielectric gradually increased in intensity for some time. Faraday measured what is now termed *relative dielectric constant* for a variety of insulators. He also established a link between electricity and magnetism [35]:

> *The particles of an insulating dielectric whilst under induction may be compared to a series of small magnetic needles, or more correctly still to a series of small insulated conductors.*

an analogy from which Faraday established a link to Poisson's successful theory of magnetism [135] by replacing $\vec{M}$, the magnetic polarization vector in Poisson's theory by $\vec{P}$ the dielectric polarization vector leading to:

$$\phi = \oint_S \frac{\vec{P} \cdot d\vec{S}}{r} + \int_V \frac{-\vec{\nabla} \cdot \vec{P}}{r} dV \tag{3.4}$$

where S is the external surface of the body and V its volume. Faraday [136] was also the first to use the concept of lines of force, a concept he took from the observation of the disposition of iron filings in the neighorhood of a permanent magnet. However, Faraday was not a mathematician, and his concepts of the field did not immediately appeal to the mathematicians. They were still thinking in terms of inverse-square laws [137] as was, for instance, the eminent Astronomer Royal, Sir George Biddel Airy (1801-1892) who declared [129] that he could:

> *hardly imagine anyone who knows the agreement between observation and calculation based on action at a distance to hesitate an instant between this simple and precise action on one hand and anything so vague and varying as lines of force on the other.*

In 1847 Mossotti [138] and Clausius (1822-1888) in 1879 [139] tried to establish the relation between the dielectric constant and the volume fraction of conducting particles in the dielectric, arriving at the so-called *Clausius-Mossotti equation* (see section 3.3)

Following Faraday, the Italian physicist Matteucci [140] performed a series of experiments of dielectric absorption. After contact charging a long sulphur rod with a Leyden jar and by subsequent slicing he determined the charge distribution inside the rod and demonstrated, in accord with the Franklin and Faraday experiments, the conduction of charge from the electrode to the dielectric.

In 1854 Kohlraus [141][142] reported the analogy between the phenomenon of dielectric absorption and elastic recovery of strained bodies (known as Creep; see Chapter 3)[3] concluding that the electric effects could be explained in terms of molecular interactions in a similar fashion as elastic effects had been explained. He also introduced the concept of dipolar polarization, *i.e.*, the polarization due to the aligment of electrical dipoles under the action of an electric field and suggested that it would be predominant in the long-lasting polarization of dielectrics.

Two years later, Maxwell (1831-1879) [144] by defining a line of force as a curve in space whose direction at each point is that of the force on a positive charge and further imagining the space as completely filled with such lines he wrote:

> *We should thus obtain a geometrical model of the physical phenomena, which would tell us the direction of the force, but we should still require some method of indicating the intensity of the force at any point. If we consider these curves not as mere lines, but as fine tubes of variable section carrying an incompressible fluid, then, since the velocity of the fluid is inversely as the section of the tube, we may make the velocity vary according to any given law, by regulating the section of the tube, and in this way we might represent the intensity of the force as well as its direction by the motion of the fluid in these tubes.*

[3] A comparision between elastic effects and electric phenomena can be seen in reference [143] (Chapter 1).

and with this model in mind he showed that all results obtained for static charges or permanent magnets using action-at-a-distance formulas, were also obtainable in terms of Faraday's lines of force.

Maxwell also developed Kohlrausch ideas [145] and by calculus of the polarization of heterogeneous dielectrics he showed that in such dielectrics the residual charge can be a result of charge accumulation on interfaces between regions occupied by different components of the dielectric with different conductivities and dielectric constants, the so-called *Maxwell-Wagner-Sillars effect* which was quantitatively studied by Wagner [146] and extended by Sillars [147].

The phenomenon of dielectric relaxation was reported in 1864 by Siemens [148] who observed that the conductivity of a capacitor was several times larger than its measured dc value. A year later Maxwell [149] introduced the concept of dielectric displacement as the quantity of interest in dielectric phenomena in the presence of matter.

A few years after Drude's results were published, Pellat[4] [150][151] introduced the concept of a *relaxation time* τ as the time at which the step-response function decays by a factor of e. The frequency dependence of the resulting complex dielectric constant, $\tilde{\varepsilon}(\omega)$ is given by:

$$\tilde{\varepsilon}(w) = \varepsilon_\infty + \frac{\varepsilon_s - \varepsilon_\infty}{1 + \imath w\tau}. \tag{3.5}$$

where ε_S and ε_∞ are the static and inmediate responses.

After the experimental realization of electromagnetic waves by Hertz [152] in 1887, Drude [153] determined that some substances absorb part of the energy of low-frequency electromagnetic waves.

In 1913, von Schweidler [154] introduced a discrete set of relaxation times $g(\tau)$ for different parts of the orientation polarisation and a year later, Wagner [155] extended the method to a continuous distribution of relaxation times.

In the same year Debye made a major contribution relating the effect of the molec-

[4]In some texts the author is referred to as Pellet.

ular structure to the resulting dielectric loss [156]. He considered a model based on spherical dipoles of volume V rotating in a viscous medium of viscosity η under the effect of an electric field. Using the relation obtained by Stokes [157] that governs the movement of spherical particles in a viscous fluid, Debye obtained an expression for the permittivity of the form:

$$\tilde{\varepsilon}(\omega) = \varepsilon_\infty + \frac{\varepsilon_s - \varepsilon_\infty}{1 + \imath\omega\tau} \tag{3.6}$$

and a relaxation time of:

$$\tau = \frac{3\eta V}{k_B T} \tag{3.7}$$

where η is the viscosity, V the volume of the spheres, k_B the Boltzmann's constant and T the temperature.

Equation 3.7 is valid only for spherical molecules since, if molecules are not spherical the process of orientation by rotation about different axes requires a distribution of relaxation times [158].

In 1885 Heaviside theorized over the possibility of producing permanently polarized bodies [159] and also included a proposal of a method which basically consisted in locating a dielectric in an electric field as long as necesary for absorption to take place, covering it with conducting electrodes for the neutralization of its intrinsic polarization and removing the coating which led to the reappearance of the electric field around the electret of opposite polarity to that first observed due to the surface charges.

He introduced the term *electret* by analogy to their magnetic counterparts *magnets*. However, it would not be until 1919 that the Japanese Eguchi [125] actually made electrets using a mixture of carnauba wax and resin[5] upon which he applied the thermal method used by Gray and Heaviside although without being aware of Heaviside's work.[6]

[5] A disk 20cm in diameter and 1cm thick of an Eguchi electret is preserved at the Science Museum in Tokyo [160].

[6] In his first papers Eguchi still used the term *electrophorus* a term which he changed to electret in subsequent papers.

By the same time, the theories of polarization had also begun with the work of Lorentz, Lorenz, Debye, Onsager, Kirwood and Fröhlich among others. These theories will be reviewed later in section 3.8.

3.2 Phenomenological Relations

The energy of a charged particle is altered by the presence of an electric field. Since materials are composed of charged particles, their energy will be affected by the presence of electric fields. The natural trend of physical systems towards the minimum energy (allowed by the constraints) will then become manifest as the material is set under an electric field. In a conductor there are no spatial constraints to the movement of electrons inside the physical limits of the material so that they can migrate under the field effect giving rise to an induced electric field inside the material equal in magnitude and of opposite sign to that externally applied, completely compensating the effect of the external and leading to a zero-field inside the conductor (*screening effect*).

In insulators, however, charge flow is limited. In such a situation the external field can only be partially screened resulting in the presence of an electric field throughout the material. Therefore, the term *dielectric*, is often used to refer to these materials. The existence of an electric field in the interior of dielectrics gives rise to new phenomena from the possible effects of the field on the constituents of the material. These phenomena are collectively termed *dielectric polarization* and will be commented upon in the next section.

A complete description of the effects of electric fields on dielectrics would require knowledge of the charge density $\rho(\vec{r})$ which depends on the positions of many ($N_A \sim 10^{23}$ mol^{-1}) charges which fluctuate in space over small (interatomic) distances and in time due to thermal agitation. Fortunately, under some approximations, the problem can be treated.

Historically, the first approximation was made by Kelvin [161] and Maxwell [162] who considered matter as a continuum inside which cavities can be made. Electric

fields could then be defined in the usual manner:

$$\vec{E}(\vec{r}) = \lim_{q' \to 0} \frac{\vec{F}(\vec{r})}{q'} \tag{3.8}$$

Other approaches consist in picturing the atomic structure of matter as a set of point charges in space [163][164][165][166] averaging the microscopic field $E_{av} \equiv < \vec{E} >$ over spatial and time intervals large enough so as to contain a representative number of charges but differential in the sense that all the operations of the integro-differential calculus can be performed without risk of appreciable error [167] and therefore considering matter as quasi-continuous[7]. Following Mazur [164][165] and Groot [166] we can imagine a dielectric being composed of point charges forming clusters. Using the index ik to label the i-th charge in the k-th cluster, e the electrical charge, m the mass and $\vec{r}$ the vector position, the centre of gravity of the k-th cluster $\vec{r}_k$ is given by:

$$\vec{r}_k \sum_i m_{ki} = \sum_i m_{ki} \vec{r}_{ki} \tag{3.9}$$

and now, defining the monopolar, e, dipolar, m and quadrupolar, Q, moments of the clusters with respect to their centre of gravity:

$$e_k = \sum_i e_{ki} \tag{3.10}$$

$$\vec{m}_k = \sum_i e_{ki} \vec{l}_{ki}; \qquad \vec{l}_{ki} = \vec{r}_{ki} - \vec{r}_k \tag{3.11}$$

$$\vec{Q}_k = \frac{1}{2} \sum_i e_{ki} l_{ki}^2. \tag{3.12}$$

We can express the potential $\phi(\vec{r})$ as :

[7] In covalent insulators this approach must be taken carefully since a great part of the charge resides on the bonds, and then, its response cannot be inferred from a model of isolated particles [168]. See section 3.8.

$$\phi(\vec{r}) = \sum_k \sum_i \frac{e_{ki}}{|\vec{r}_{ki} - \vec{r}|} \tag{3.13}$$

and the electric field $\vec{E}(\vec{r}) = -\nabla\phi(\vec{r})$ is then given by:

$$\vec{\nabla} \cdot \vec{E} = 4\pi\rho(\vec{r}) \tag{3.14}$$

where:

$$\rho(\vec{r}) = \overbrace{\sum_k e_k \delta(\vec{r}_k - \vec{r})}^{\text{real charge}} + \overbrace{\vec{\nabla} \cdot \sum_k m_k \delta(\vec{r}_k - \vec{r})}^{\text{dipolar term}} + \overbrace{(\vec{\nabla})^2 \sum_k \vec{Q}_k \delta(\vec{r}_k - \vec{r})}^{\text{quadrupolar term}} + \text{Higher Terms.} \tag{3.15}$$

In the case of charge neutrality, the first or *monopolar* term vanishes and the second or *dipolar* term does not depend on the chosen origin [169]. In addition, in most cases, the contribution due to the third, *quadrupolar*, and higher terms in equation 3.15 is small so that their contributions can be neglected [170] [169]. Equation 3.15 simplifies then to:

$$\rho(\vec{r})_{dip} = \vec{\nabla} \cdot \sum_k m_k \delta(\vec{r}_k - \vec{r}) = -\vec{\nabla} \cdot \vec{P} \tag{3.16}$$

where $\vec{P}$ is referred to as the *polarization vector*. For a continuum distribution of charges $\rho(\vec{r})$, the equivalent expression is [169] [171]:

$$P = \int_v \rho_{dip}(\vec{r})\vec{r}dv \tag{3.17}$$

which, integrated over a volume element between two surface areas each at one side of the dielectric surface, gives:

$$\sigma_{dip}(\vec{r}) = \vec{P}(\vec{r}) \cdot \vec{n}(\vec{r}) \tag{3.18}$$

where σ is the superficial charge density and $\vec{n}$ the unit vector in the normal direction

of the surface at each point. A medium in which $P \neq 0$ is said to be *polarized.*

In view of equations 3.15 and 3.14:

$$\vec{\nabla} \cdot \vec{D}(\vec{r}) = \rho_r(\vec{r}) \tag{3.19}$$

where:

$$\vec{D} = \varepsilon_0 \vec{E} + \vec{P} \tag{3.20}$$

where ε_0 is the dielectric permittivity of vacuum and $\vec{D}$ is the so-called *electric induction* or *electric displacement vector*

Considering that the interatomic fields are of the order of $10^7 Vm^{-1}$ [172], fields attainable in the laboratory represent a small perturbation so that a linear relation between field and polarization can be used without great error. Then, it is usual to write:

$$\vec{P} = \chi \vec{E} \tag{3.21}$$

where χ is the so-called *dielectric susceptibility tensor.* For isotropic solids and cubic crystals, χ is independent of direction, *i.e.*, it is a scalar. In these cases by virtue of equations 3.20 and 3.21:

$$\vec{D} = (1 + 4\pi\chi)\vec{E} = \varepsilon \vec{E} \tag{3.22}$$

where ε is the so-called *dielectric permittivity.*

The internal energy associated with polarization in a dielectric can be written as (see for instance [171]):

$$dU = TdS + \vec{E} \cdot d\vec{D} \tag{3.23}$$

where T is the temperature, and dU and dS are respectively the differential internal

energy and entropy of the system per unit volume.

3.3 Polarization Mechanisms

Several mechanisms can be distinguished by means of which a dielectric becomes polarised. Firstly, the electronic densities around nuclei distort leading to a separation of the centers of gravity of positive and negative charge distributions and consequently induced dipole moment. The term *electronic polarizability* is often used although atomic polarizability can be found in some texts [168][8]. In ionic solids we must also expect a contribution to the polarization from the movement of individual ions in response to the applied field, the resulting polarization being termed *ionic polarization.* In polar substances, the orientations of permanent dipoles have also to be considered.

Quantification of the effects of the above mechanisms on the polarization clearly requires a microscopic model of matter. It is usually accepted, as a first approximation [167], that for low fields, the dipole moment is proportional to the so-called *local field*, that is, the actual field acting over the considered microscopic region of the material, *i.e.*, electron, ion, dipole, etc. Therefore, it is usual to write:

$$\vec{p}(\vec{r}) = \vec{\alpha}\vec{E}_{loc}(\vec{r}) \tag{3.24}$$

where α is the so-called *polarizability tensor.* In amorphous solids and cubic crystals, α is a scalar.

The relation between the macroscopic dielectric behaviour and the microscopic structure is then given by the relation between the polarizability and the dielectric constant and therefore, between macroscopic and local fields. One of the first attempts to correlate the dielectric constant to the structure was made in 1847 by Mossotti [138] and in 1879 by Clausius [139] who, following Faraday, considered a dielectric to be

[8] The term atomic polarizability is also referred to as the movement of atomic nuclei even in non-ionic solids [158]. In polymers the movements of nuclei result from structural transformations of the molecule such as isomeric transitions, rotation of groups, vibrations, etc. [143].

composed of conducting spheres embedded in a non-conducting medium. They proceeded to determine the effect of the volume fraction occupied by these spheres on the dielectric permitivity.

In 1880, Lorentz [163] introduced the concept of a local field and derived the relation between the macroscopic and local fields in a system of neutral, non-polar particles in a completely disordered system. The relation:

$$\vec{E}_{loc} = \vec{E} + \frac{1}{3\varepsilon_0}\vec{P} \tag{3.25}$$

is known as the *Lorentz relation.* Developing equations 3.22, 3.24 and 3.25, it is readily shown that:

$$\frac{\varepsilon - 1}{\varepsilon + 2} = \frac{1}{3\varepsilon_0}\sum_j N_j\alpha_j \tag{3.26}$$

where N_j and α_j are the concentration and polarizabilities of the atoms. If the concentration of particles is assumed proportional to the density ρ, the Lorentz relation transforms into:

$$\frac{M}{\rho}\frac{\varepsilon - \varepsilon_0}{\varepsilon + 2\varepsilon_0} = \frac{N_A\alpha}{3\varepsilon_0} \tag{3.27}$$

where M is the mass of the particles and N_A is Avogadro's number. Equations 3.26 and 3.27 are known as the *Claussius-Mossoti* relations[9]. About a decade before Lorentz introduced the concept of local field, Maxwell had published his unified theory of electromagnetism [145][173] including the so-called *Maxwell relation*[10] $\varepsilon = n^2$, where n is the *refractive index* which when substituted into the Clausius-Mossotti relations gives:

[9] Some authors (see for instance [158]) attributed the derivation of the local field in equation 3.25 to Mossotti and therefore call it the Mossotti field. However, although the Claussius-Mossoti relations were derived first by Mossotti [138] and Clausius [139] they did not make use of the local field concept but derived them by the use of a general potential function.

[10] This relation fails when the dielectric has important losses since the dielectric permittivity has to be considered as having a complex nature as we will see later in this chapter.

$$\frac{n^2-1}{n^2+2} = \frac{1}{3\varepsilon_0}\sum_j N\alpha \tag{3.28}$$

which is known as the *Lorenz-Lorentz* [174][175] equation. Lorenz-Lorentz and Clausius-Mossotti relations fail at low frequencies. However, the former is applied in the optical region where permanent dipoles are unable to react to the alternating electric field. A quantitative theory including the effect of the permanent dipoles was introduced in 1912 by Debye [176] who applied the theory developed by Langevin [177][178] for the orientation of magnetic dipoles of constant dipolar moment μ in a magnetic field, to the case of electric dipoles. By assuming that the electric dipoles were in a Lorentz local field he arrived at the relation:

$$\frac{\varepsilon-\varepsilon_0}{\varepsilon+2\varepsilon_0} = \frac{1}{3\varepsilon_0}N\left(\alpha+\frac{\mu^2}{3k_BT}\right). \tag{3.29}$$

Equation 3.29 is known as the *Debye equation.* The Debye equation gives good agreement with the experimental results for polar gases and dilute solutions[11] [170][179] but fails for pure polar liquids and concentrated solutions [167]. In 1936 Onsager [180] improved the Debye model by introducing the so-called *reaction field.* The field acting over the considered dipole is the sum of that acting if the particle under consideration was not polar, the *internal field* plus that taking into account the polarization exerted by the dipole over the surrounding medium, the *reaction field.* For equal spherical particles and applying the Langevin calculation following Debye and considering that the energy term must not include the reaction effect[12], it can be shown that: (for a detailed calculation see [167][181]):

$$\varepsilon-\varepsilon_0 = \frac{Ng}{1-\alpha f}\left[\alpha+\frac{\mu^2}{3(1-\alpha f)k_BT}\right] \tag{3.30}$$

which is the *Onsager equation.* Here:

[11] Debye responses have only been experimentally observed in some ferroelectrics [170][179].

[12] The reaction field is in the same direction as that of the creating dipole so that the former does not contribute to the orientational energy of the later. See for instance references [167][181].

$$f = \frac{2N}{3\varepsilon_0}\frac{\varepsilon - \varepsilon_0}{2\varepsilon + \varepsilon_0} \tag{3.31}$$

and N is the dipole concentration:

$$N = \frac{3}{4\pi R^3} \tag{3.32}$$

where R is the radius of the cavities assumed to be equal to the particle radius. The Onsager model was extended by Scholte [182] to ellipsoidal particles.

In all the models presented above, the interaction between each particle and the rest in the dielectric is obtained by assuming a continuum character for the dielectric surounding the considered particle. In such an isotropic medium, $\cos\phi$ (ϕ is the dipole-dipole angle) averages to zero as does the dipole-dipole interaction energy. In some materials however, molecules associate with one another to form aggregates or chains (for example polymers) giving the material an anisotropic nature for which the dipole-dipole interaction does not average to zero. In these cases the molecular structure must be explicitly considered, which requires the use of statistical theories. The statistical approach will be briefly commented upon later in section 3.8.

3.4 Time Response Function

An interesting property of dielectric materials is their response to time-dependent electric fields. The characterization of the time response requires knowledge of $\vec{D}(t)$ as a function of $\vec{E}(t)$ in the time interval under consideration. To obtain this relation, it is assumed that equation 3.22 holds for a time-dependent dielectric constant. Thus:

$$\vec{D}(t) = \varepsilon(t)\vec{E}(t) \tag{3.33}$$

so that the problem reduces to the determination of $\varepsilon(t)$ in the considered time interval. To find an expression for $\varepsilon(t)$ we will try to find the response of a dielectric material to

an impulse of electric field $\vec{E} = \vec{E}_0\delta(t - t_0)$ occurring at t_0, with a width $\delta(t_0)$. It can be expressed as a superposition of two step pulses $\vec{E}_1$ and $\vec{E}_2$ of the form:

$$\vec{E}_1(t) = \vec{E}_0\Gamma(t - t_0) \tag{3.34}$$

$$\vec{E}_2(t) = -\vec{E}_0\Gamma(t - t_0 - dt_0) \tag{3.35}$$

where:

$$\Gamma(x) = \begin{cases} 1 & \text{if } x \geq 0 \\ 0 & \text{otherwise} \end{cases} \tag{3.36}$$

so that, the dielectric displacement can be expressed as[13]:

$$\vec{D}(t) = \vec{D}_1(t) + \vec{D}_2(t) \tag{3.37}$$

where $\vec{D}_1(t)$ and $\vec{D}_2(t)$ are the responses associated with $\vec{E}_1(t)$ and $\vec{E}_2(t)$. We can express the displacement vector as the sum of two terms corresponding to induced and orientational polarization:

$$\vec{D}_{ind}(t) = \varepsilon_{ind}\vec{E}_1 + \varepsilon_{or}\vec{E}_1 \tag{3.38}$$

Since induced polarisation takes place almost inmediately, while it takes longer for the permanent dipoles to orientate we can consider ε_{ind} as the value of the permittivity at very-high frequencies and represented by ε_∞. Thus, ε_{or} will be considered as being $\varepsilon_s - \varepsilon_\infty$ where ε_s is the static permittivity, *i.e.*, the permitivitty when all the mechanisms take place. Then, we can write $\vec{D}_1(t)$ and $\vec{D}_2(t)$ as:

$$\vec{D}_1(t) = \varepsilon_\infty\vec{E}_0\Gamma(t - t_0) +$$

[13]The superposition principle is admitted.

$$+ (\varepsilon_s - \varepsilon_\infty)\vec{E}_0 f(t - t_0) \tag{3.39}$$

and:

$$\begin{aligned} \vec{D}_2(t) = & -\varepsilon_\infty \vec{E}_0 \Gamma(t - t_0 - dt_0) - \\ & - (\varepsilon_s - \varepsilon_\infty)\vec{E}_0 f(t - t_0 - dt_0) \end{aligned} \tag{3.40}$$

where, in both equations, the first term represents the response of the induced polarization and the second the orientational polarisation. The latter is described by a temporal function $f(t)$ equal to zero at $t = 0$ and tending to unity as time increases[14]. The total displacement will then be:

$$\begin{aligned} \vec{D}(t) &= \vec{D}_1(t) + \vec{D}_2(t) = \varepsilon_\infty \vec{E}(t)[\Gamma(t - t_0) - \Gamma(t - t_0 - dt_0)] + \\ &+ (\varepsilon_s - \varepsilon_\infty)\vec{E}_0 \, [f(t - t_0) - f(t - t_0 - dt_0)]. \end{aligned} \tag{3.41}$$

In the considered interval:

$$\Gamma(t - t_0) - \Gamma(t - t_0 - dt_0) = 1 \tag{3.42}$$

and:

$$df(t - t_0) = \lim_{dt_0 \to 0} \frac{f(t - t_0 - dt_0) - f(t - t_0)}{dt_0} \tag{3.43}$$

so that, for short pulses ($dt_0 \to 0$), the displacement vector can be expressed as:

$$D(t) = \varepsilon_\infty \vec{E}(t) + (\varepsilon_s - \varepsilon_\infty)\vec{E}_0 \dot{f}(t - t_0) dt_0 \tag{3.44}$$

where $\dot{f}$ stands for the time derivative. The function $\Xi(t) = \dot{f}(t)$ is the so-called

[14] It is assumed that for long times the polarisation reaches the saturation value.

response function of the dielectric. Now, any field can be expressed as a sum of short pulses, and then, since we are assuming that the superposition principle holds, the total response will be the sum of the responses to each pulse. On the other hand, if the time interval of the application of the field $(t - t_{in})$ is high in comparison with the duration of the pulses, the sum can be replaced by an integral leading to:

$$\vec{D}(t) = \varepsilon_\infty \vec{E}(t) + (\varepsilon_s - \varepsilon_\infty) \int_{t_{in}}^{t} \Xi(t - t_0)\vec{E}(t_0)dt_0 \tag{3.45}$$

In the previous description we assumed that no perturbation had been made over the sample before t_{in} or that, if any, their effects over the sample were no longer noticeable at t_{in}. However, a more precise treatment would require that the displacement vector be expressed as:

$$\vec{D}(t) = \varepsilon_\infty \vec{E}(t) + (\varepsilon_s - \varepsilon_\infty) \int_{-\infty}^{t} \Xi(t - t_0)\vec{E}(t_0)dt_0 \tag{3.46}$$

which, after the change $\eta = t - t_0$ transforms into:

$$\vec{D}(t) = \varepsilon_\infty \vec{E}(t) + (\varepsilon_s - \varepsilon_\infty) \int_{0}^{\infty} \Xi(\eta)\vec{E}(t - \eta)\ d\eta. \tag{3.47}$$

Then, the dielectric response for a step function $\vec{E}_0\Gamma(t)$ is:

$$\vec{D}(t) = \varepsilon_\infty \vec{E}_0\Gamma(t) + (\varepsilon_s - \varepsilon_\infty) \int_{0}^{\infty} \Xi(\eta)\vec{E}_0\Gamma(t - \eta)\ d\eta. \tag{3.48}$$

On the other hand we have:

$$\frac{d\vec{D}}{dt} = \frac{\partial \vec{D}}{\partial t}dt + \frac{\partial \vec{D}}{\partial x}\frac{dx}{dt} + \frac{\partial \vec{D}}{\partial y}\frac{dy}{dt} + \frac{\partial \vec{D}}{\partial z}\frac{dz}{dt} =$$

$$= \frac{\partial \vec{D}}{\partial t} + \vec{\nabla} \cdot (\vec{D} \cdot \vec{r}) \tag{3.49}$$

so that:

$$\int_V \frac{d\vec{D}}{dt}\, dV = \int_V \frac{\partial \vec{D}}{\partial t}\, dV + \int_V (\vec{\nabla} \cdot \vec{D})\vec{v}\, dV \tag{3.50}$$

where $\vec{v}$ is the time derivative of the spacial coordinates *i.e.*, the velocity. Accordingly with equation 3.20:

$$\int_V (\vec{\nabla} \cdot \vec{D})\ \vec{v}\ dV = \int_V \rho_r \vec{v}\ dV = \int_V \vec{J}_c\ dV \tag{3.51}$$

where $\vec{J}_c$ is the current density associated with the *real* movement of free charges. Then, we see that a temporal variation of $\vec{D}$ gives way to a conduction current $\vec{J}_{con}$ plus a term:

$$\vec{J}_{pol} = \frac{\partial \vec{D}}{\partial t} \tag{3.52}$$

that represents the so-called *polarization current*, which, by virtue of equation 3.48, can be expressed as:

$$\vec{J}_{pol}(t) = \varepsilon_{ind}\vec{E}_0 \frac{\partial \Gamma(t)}{\partial t} +$$

$$+ (\varepsilon_s - \varepsilon_\infty) \int_0^\infty \Xi(t - t_0)\vec{E}_0 \frac{\partial \Gamma(t-\eta)}{\partial t}\, d\eta. \tag{3.53}$$

Here $\Gamma(t)$ only changes at time t and that change takes place in an infinitely small period of time *i.e.*:

$$\frac{\partial \Gamma(t)}{\partial t} = \delta(t') = \begin{cases} \infty & \text{when } t' = t \\ 0 & \text{otherwise} \end{cases} \tag{3.54}$$

with the additional condition:

$$\int_{-\infty}^{\infty} \delta(t)\ dt = 1 \tag{3.55}$$

where δ is the so-called *Dirac function* which satisfies the condition:

$$\int_0^\infty f(t-t_0)\delta(t_0)\,dx = f(t-t_0). \tag{3.56}$$

Combining equations 3.53, 3.54 and 3.56:

$$\vec{J}_{pol}(t) = \varepsilon_\infty \vec{E}_0 \delta(t) + (\varepsilon_s - \varepsilon_\infty)\vec{E}_0 \Xi(t) \tag{3.57}$$

which gives the relation between the polarization current and the response function of the dielectric. This is usually referred to in the literature as the (charging) *transient current.* The delta function is not measurable so that we can conclude that the polarization current experimentally measured will be proportional to the response function[15]. The last term in equation 3.57 is usually called the *absorption current* and is entirely due to the presence of the dielectric. Analogously, it can be shown that, in the case that the field is suddenly removed instead of being suddenly applied (discharging transient current), the polarization current is again given by equation 3.57 but is opposite in sign and for obvious reasons is called the *depolarization current.* However, consistent with the causality principle, in this case no conduction current will be present. Transient currents are widely used in the study of conduction processes in dielectrics. Typical charging and discharging transient currents for polypropylene films are shown in Fig.3.1 [5].

3.5 Frequency Response Function

In determining equation 3.47, no assumptions were made about the temporal variation of the electric field. For the particular case of an harmonic temporal variation $\vec{E}(\omega,t) = \vec{E}_0\, e^{i\omega t}$ we have:

[15] Although the delta function is not measurable, it has a physical meaning which is the finite polarisation of vacuum. The finite resistance of the external circuit usually transforms it into a decreasing exponential. The first seconds are therefore not taken into consideration in transient currents.

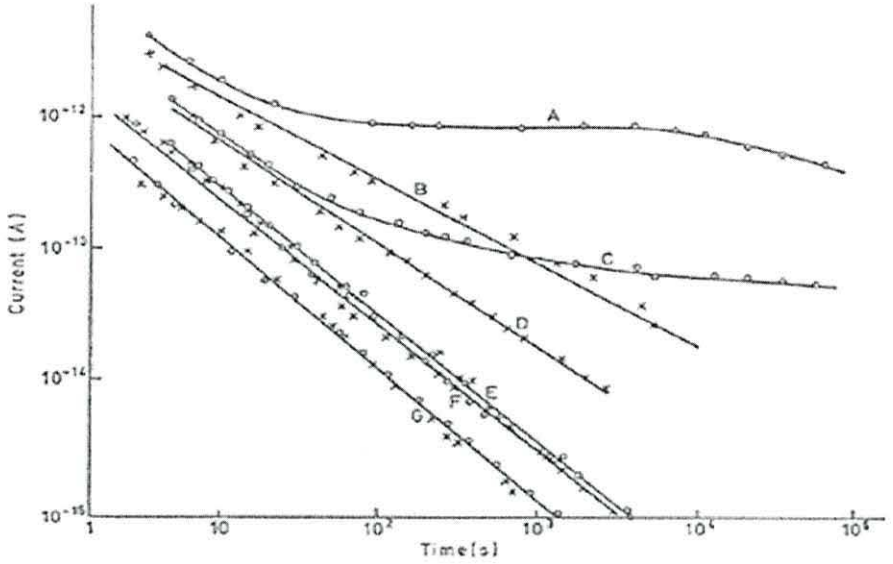

Figure 3.1: Transient currents for PP. Charging (○) and discharging (×) currents in polypropylene over the temperature range 83-373 K at a constant rate of 6.67x10^7 Vm^{-1}. Electrode material: gold; sample thickness: 15 μm. A and B, 373 K; C and D, 341 K; E, 303 K; F, 270 K, G, 83 K. From [5].

$$\begin{aligned}\vec{D}(\omega,t) &= \varepsilon_\infty \vec{E}_0\, e^{i\omega t} + (\varepsilon_s - \varepsilon_\infty)\int_0^\infty \Xi(\eta)\vec{E}_0\, e^{i\omega(t-\eta)}\, d\eta \\ &= \left[\varepsilon_\infty + (\varepsilon_s - \varepsilon_\infty)\int_0^\infty \Xi\, e^{-i\omega\eta}\, d\eta\right]\vec{E}_0\, e^{i\omega t} \\ &= \left[\varepsilon_\infty + (\varepsilon_s - \varepsilon_\infty)\int_0^\infty \Xi\, e^{-i\omega\eta}\, d\eta\right]\vec{E}(\omega,t) \qquad (3.58)\end{aligned}$$

where the integral is the Fourier transform of the function Ξ. The term in brackets is a complex quantity. Thus, we can write:

$$\vec{D}(\omega,t) = \tilde{\varepsilon}(\omega)\vec{E}(\omega,t) \qquad (3.59)$$

where $\tilde{\varepsilon}(\omega)$ is the *complex permittivity* at frequency ω, and may be written as:

$$\tilde{\varepsilon}(\omega) = \varepsilon(\omega) - i\varepsilon''(\omega). \qquad (3.60)$$

Combining equations 3.58, 3.59 and 3.60 gives:

$$\tilde{\varepsilon}(\omega) = \varepsilon_\infty + (\varepsilon_s - \varepsilon_\infty) \int_0^\infty \Xi(\eta) e^{-\imath\omega\eta}\, d\eta \tag{3.61}$$

from which, by comparson with equation 3.57 it can be seen that:

$$\tilde{\varepsilon}(\omega) = \int_0^\infty \frac{\vec{J}_{pol}}{\vec{E}_0} e^{-\imath\omega t}\, dt \tag{3.62}$$

and then, that $\tilde{\varepsilon}(\omega)$ is the Fourier transform of $\vec{J}_{pol}/\vec{E}_0$.

On the other hand, the real part of the displacement vector is:

$$\vec{D}_0 \cos(\omega t) = \varepsilon(\omega)\vec{E}_0 cos(\omega t) + \varepsilon''(w)\vec{E}_0 \sin(\omega t) \tag{3.63}$$

which, in view of the trigonometric identity:

$$\cos(\omega t - \delta(\omega)) = \cos(\omega t)\cos(\delta(\omega)) + \sin(\omega t)\sin(\delta(\omega)) \tag{3.64}$$

can be written as:

$$\vec{D}_0 \cos(\omega t) = \vec{E}_0 \cos(\omega t - \delta(\omega)) \tag{3.65}$$

where:

$$\delta(\omega) = \frac{\varepsilon''(\omega)}{\varepsilon(\omega)}. \tag{3.66}$$

$\delta(\omega)$ is referred to as the *loss tangent* or *tan* δ. Equation 3.65 means that the displacement vector $\vec{D}$ lags behind the applied electric field $\vec{E}$. This lag in phase is given by δ and is due to the slow mechanisms of polarization which require some finite time to manifest themselves.

3.6 KRAMERS-KRÖNIG RELATIONS

It has been seen in the previous section, that the dielectric permittivity is a complex quantity and that it has real and imaginary components. Moreover, we have seen that both arise from the same physical reason, *viz.* the existence of polarization mechanisms. Therefore, there is no reason to consider them as independent of each other. In fact, it can be shown that the real and imaginary parts of the dielectric permittivity are related by the so-called *Kramers-Krönig relations* [183][184]:

$$\varepsilon'(\omega) - \varepsilon_\infty = \frac{2}{\pi} \int_0^\infty \frac{\omega' \varepsilon''(\omega')}{\omega'^2 - \omega^2} \, d\omega' \tag{3.67}$$

$$\varepsilon''(\omega) = -\frac{2\omega}{\pi} \int_0^\infty \frac{\varepsilon'(\omega') - \varepsilon_\infty}{\omega'^2 - \omega^2} \, d\omega'. \tag{3.68}$$

Note that the integrands in equations 3.67 and 3.68 are not defined at the frequency $\omega = \omega'$. However, given that in both cases, the left-hand sides have physical meaning and must have a finite value, it is clear that the integrals will converge in both cases. These integrals must however be understood in the sense:

$$v.p = \lim_{\tau \to 0} \int_0^{\omega - \tau} \frac{\omega' \varepsilon''(\omega')}{\omega'^2 - \omega^2} \, d\omega' + \lim_{\tau \to 0} \int_{\omega + \tau}^\infty \frac{\omega' \varepsilon''(\omega')}{\omega'^2 - \omega^2} \, d\omega \tag{3.69}$$

which is *Cauchy's principal value* and is represented by v.p[16].

3.7 OTHER QUANTITIES THAT CHARACTERIZE THE DIELECTRIC RESPONSE

So far, we have defined dielectric behaviour in terms of the dielectric permittivity. In some circumstances, other magnitudes are helpful in the description of dielectric phenomena. Thus, the *capacitance* between two conductors is defined by:

[16] From French *valeur principale.*

$$C = \frac{Q}{V} \tag{3.70}$$

where Q is the charge that must be transferred from one conductor to the other to change the potential difference V between them. We can now express the current by:

$$I(t) = \frac{dQ}{dt} = C\frac{dV}{dt}. \tag{3.71}$$

When the applied voltage is of the form: $V = V_0 e^{\imath\omega t}$, then:

$$I(\omega) = \imath\omega C(\omega)V. \tag{3.72}$$

When the material has dielectric losses, the capacitance is a complex quantity which, by analogy with the complex dielectric permittivity is written as:

$$\tilde{C}(\omega) = C'(\omega) - iC''(\omega). \tag{3.73}$$

Therefore, the (complex) *admittance* $Y(\omega) = Y'(\omega) - \imath Y''(\omega)$, defined as the ratio between the current I flowing through a sample and the applied voltage V, can be written as:

$$\tilde{Y}(\omega) = \frac{I}{V} = \imath\omega\tilde{C}(\omega) \tag{3.74}$$

so that:

$$Y''(\omega) = -\omega C' \tag{3.75}$$

$$Y'(\omega) = \omega C''. \tag{3.76}$$

The inverse of the (complex) admittance is the (complex) *impedance*, $Z(\omega)$.

3.8 Dielectric Behaviour of Polymers

The assumption of a single relaxation time τ (Debye model), leads to a polarization current of the form:

$$\vec{J}_{pol} = \varepsilon_\infty \vec{E}_0 \delta(t) + (\varepsilon_s - \varepsilon_\infty) \left(\frac{1}{\tau} e^{-t/\tau} \right) \vec{E}_0 \tag{3.77}$$

which, compared to equation 3.57 gives a response function:

$$\Gamma(t) = \frac{e^{-t/\tau}}{\tau}. \tag{3.78}$$

It has been observed that equation 3.77 does not describe the behaviour of many solids. It fact, it has been long-established experimentally [154][185] that the polarization current and the corresponding response functions for many solids are given by[17]:

$$J_{pol} \propto \Xi(t) \tag{3.79}$$

where

$$\Xi(t) \propto t^{-n} \tag{3.80}$$

and n is a constant close to unity [5] but may be as small as 0.7 [186].

Such a deviation from the Debye equation can be caused by many factors. Firstly, we saw in Chapter 2 that the main feature of organic polymers is that carbon atoms are linked by covalent bonds. Therefore, an appreciable electronic charge contributing to the polarisation relies on covalent bonds [168] whose behaviour cannot be inferred from an isolated set of atoms, as assumed in section 3.2.

In addition, it was mentioned in section 3.3 that for anisotropic substances, the dipole-dipole interaction must be explicitly considered so requiring the use of statistical theories. Such an extension of the Onsager model was performed by Kirkwood [187] and developed by Fröhlich [181]. In the *Kirkwood-Fröhlich model* each particle is considered

[17] Deviations for this general behaviour are usually observed at high fields and temperatures. See section 3.12.

to be surrounded by a region of $\mathfrak{N}$ particles explicitly considered whereas the remaining material is treated as continuous. The degree of approximation depends therefore on the value of $\mathfrak{N}$. The short-range order is characterized by an orientational correlation factor for the molecule i, the so-called *Kirkwood factor*:

$$g_i = 1 + (\mathfrak{N} - 1) < \cos\phi_{ij} > \tag{3.81}$$

where [167]:

$$< \cos\phi_{ij} >= \frac{\int \cos\phi_{ij} e^{-U_{w_i,w_j}/k_B T} dw_i dw_j}{\int e^{-U_{w_i,w_j}/k_B T} dw_i dw_j} \tag{3.82}$$

and w_i and w_j denote the orientational coordinates of the corresponding molecule and U_{w_i,w_j}, the orientational intermolecular interaction energy. The integral in equation 3.82 extends over the $\mathfrak{N} - 1$ nearest molecules. A relation between the correlation factor and the permittivity is given by the *Kirkwood-Fröhlich* equation [167] [18] [19]:

$$g\mu^2 = \frac{3k_B T}{N} \frac{(\varepsilon_0^2(\varepsilon_s - \varepsilon_\infty)(2\varepsilon_s + \varepsilon_\infty)}{\varepsilon_s(\varepsilon_\infty + 2\varepsilon_0)^2}. \tag{3.83}$$

One of the major achievements of the Kirwood-Fröhlich equation was predicting the high relative permittivity of water (~80) [188].

The models reviewed in section 3.3 also fail to deal with macromolecules since they treat dipoles as being rigid and therefore, with an associated constant dipolar moment. For polymeric chains this is clearly not the case since the shape of the molecules and, consequently, the total molecular dipole moment changes during thermal motion. Only parts of chains are to be considered, the configurations of which are considered unchanged during thermal motion [143].

Other processes have to be taken into account for an accurate description of some materials. Thus, it has been observed that some materials show reflectance and absorption of photons whose energy lies below the band-gap, where the solid is supposed to be

[18] Note that in reference [167] the cgs system is used while equation 3.83 is expressed in SI.
[19] Note that for $g = 1$, the Kirkwood-Fröhlich equation reduces to Onsager (equation 3.30).

transparent. The photon absorption is accompanied in these cases by the creation of a bound electron-hole pair [189], the so-called *exciton*. Where there is some correlation between atoms, an excited atom (electron-hole pair) can translate the excitation to neighbouring atoms giving rise to a localized or *Frenkel exciton* [190].

Polymeric chains are held by intermolecular forces, whose magnitude depends on the presence of dipolar groups, hydrogen bonds and temperature. These secondary forces strongly influence the nature and extent of the molecular motions, which in turn, affect their dielectric behaviour, charge transport and charge storage [191]. Where the intermolecular forces are strong, *e.g.*, in organic semiconductors, the electron-hole pair may not be in the same atom but correlated by their Coulomb attraction. Such an exciton is termed a *Mott-Wannier exciton* [192]. Nonetheless, for polymer solids and viscoelastic liquids the contribution of exciton states to the permanent dipole moments is not very large so that they can be viewed as a system of not very strongly interacting dipoles [143].

Finally, micro- or macro-heterogeneities of a continuous or discrete nature can lead to interfacial polarization [193]. Crystalline-amorphous interfaces, polymer-electrode interfaces, structural defects or chemical impurities, cracking or voids, traces of monomer, solvent, cross-linking or foaming agents, moisture and additives such as plasticisers or colorants are common examples of interfaces in polymeric materials. Interfacial polarization also plays a crucial role in dielectric breakdown [158][6][194].

The experimentally observed shape of relaxation peaks in solid polar materials does not conform, in most cases, to the Debye model which applies to non-interacting dipoles [195].

In order to account for these deviations, Cole and Cole [196] proposed in 1941 a generalization of equation 3.5 such that:

$$\tilde{\varepsilon}(w) = \varepsilon_\infty + (\varepsilon - \varepsilon_\infty)\frac{1}{1 + (iw\tau_0)^{1-\alpha}}. \tag{3.84}$$

They also suggested a graphical method, the *Cole-Cole method*, which consists in

plotting ε'against ε'' from which it can be seen whether the experimental results for the complex dielectric constant correspond to a single or a distribution of relaxation times [197][20].

Another generalization of equation 3.5 was given by Davidson and Cole [199][200] in 1950[21]:

$$\tilde{\varepsilon}(w) = \varepsilon_\infty + (\varepsilon - \varepsilon_\infty)\frac{1}{(1+iw\tau_0)^\beta} \tag{3.85}$$

and by Havriliak and Negami [201] in 1966 who proposed :

$$\tilde{\varepsilon}(w) = \varepsilon_\infty + (\varepsilon - \varepsilon_\infty)\frac{1}{\left(1+(iw\tau_0)^{1-\alpha}\right)^\beta}. \tag{3.86}$$

Other functions characterizing the dielectric relaxation in terms of experimentally determined magnitudes were given by Fuoss and Kirkwood in 1941 [202] and by Jonscher [203] in 1975.

Even with two-parameter models of dielectric relaxation, it has not been possible to associate the relaxation time distributions deduced from the experimental data with chemical composition, molecular architecture or morphology of various insulating solids [204]. A four-parameter response function, $\phi(t)$, known as the *Universal Response Function* was proposed by Jonscher [170] [179]:

$$\phi(t) = \frac{k}{(t/\tau)^n + (t/\tau)^{m+1}} \tag{3.87}$$

which has been explained within the quantum formalism of many-bodies interactions by Dissado and Hill [205][206][207][208].

[20]The method was modified in 1955 by R. H. Cole [198] by plotting $w\varepsilon''$ against ε/w.

[21] The paramenters introduced in the Cole-Cole, Davidson-Cole and Havriliak-Negami methods can be used in the fitting process for the characterization of dielectric relaxations of the system at a certain temperature and pressure [197].

3.9 Band Model and Localisation

Band theory is a one-electron independent-particle theory which pictures a solid as a gas of (valence) electrons under the influence of the potential of the periodically distributed cores (nucleus plus internal electrons). In addition, because of the lack of periodicity imposed by the physical limits of the solid, cyclic boundary conditions referred to as *Born-von Karman conditions* are imposed. Thus, the electron is under the action of a perfectly periodic potential V.

As a result, the electron wave function will be perfectly periodic. From the properties of periodic functions, *i.e.*, expansion in a Fourier sum, it can be shown that [168]:

$$\phi_n(\vec{k}) = V_{\vec{k}} e^{i\vec{k}\vec{r}} \quad ; \qquad n \equiv \text{ integer} \tag{3.88}$$

which is referred to as the *Bloch theorem.*

In equation 3.88, n is referred to as the *band index* and $\vec{k}$ is the wave vector which has a discrete nature imposed by the continuity of the wave functions at the boundaries (from boundary conditions). For each value of n the number of allowed k-vectors is inversely proportional to the lattice constants (few $\AA$). Therefore, bands can be viewed as continuous states that can accommodate an odd number of electrons.

Perturbation theory to the second order in V applied to the Schrödinger equation leads to [168][189]:

$$\epsilon = \frac{1}{2}\left(\epsilon^0_{\vec{k}} + \epsilon^0_{\vec{k}-\vec{K}}\right) \pm \left[\left(\frac{\epsilon^0_{\vec{k}} - \epsilon^0_{\vec{k}-\vec{K}}}{2}\right) + |V_{\vec{K}}|^2\right]^{\frac{1}{2}}. \tag{3.89}$$

In many cases however, the overlapping of the orbitals is enough to require corrections to the picture of isolated atoms but no so much so as to render the atomic description completely irrelevant [168]. In such a case, *tight binding* or *Bloch approximation* [209] represents a better description of the problem. In the tight binding approximation, the total Hamiltonian is represented as:

$$H = H_{at} + H' \tag{3.90}$$

where H_{at} represents the atomic nature and H' accounts for the overlapping and the crystal periodicity. The crystal states under this approximation are of the form:

$$\varphi = \sum_n e^{\imath \vec{k} \vec{a}_n} \phi_n(\vec{r}) \tag{3.91}$$

where $\phi_n(\vec{r})$ are eigenstates of the atomic Hamiltonian at the positions $\vec{a}_n$. Equation 3.91 is of the form of equation 3.88. The modulation function is given by the atomic orbitals. The energy of crystal states lie in a band of width:

$$B = 2zI \tag{3.92}$$

where z is the coordination number and I, the so-called *transfer integral*:

$$I = \int\int\int \varphi_n H \varphi_{n+1} d\vec{r} \tag{3.93}$$

and is a measure of the overlapping.

Anderson [210] introduced disorder by means of a random potential such as:

$$-\frac{1}{2}V_0 < V < \frac{1}{2}V_0 \tag{3.94}$$

and showed that if V_0/B is larger than a critical value, the solid states are localized states of the form:

$$\varphi \propto e^{-\alpha \vec{r}} \tag{3.95}$$

where α is the so-called *localization depth.*

Mott [211][212] pointed out that if V_0/B lies below a critical value, localized states will nonetheless exist near the extremities of a band, and that an energy E_c must separate energies where states are localized from energies where they are extended, E_c

being called the *mobility edge* by Cohen *et al.* [213].

3.10 Localization and Traps in Polymeric Materials

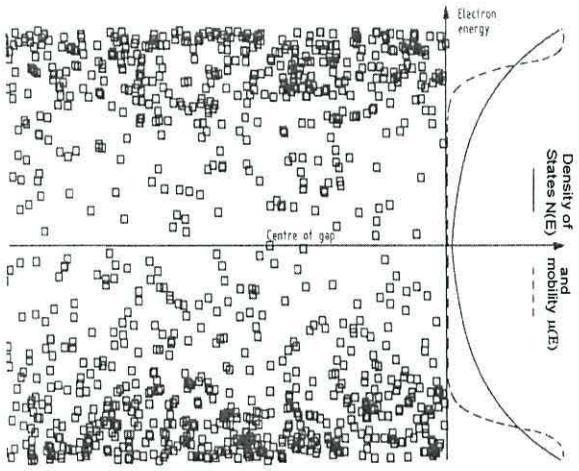

Figure 3.2: A schematic diagram showing localised states in a non-crystalline material (squares) as a function of electron energy together with the density of states, $N(E)$ and the mobility, $\mu(E)$. Although the band edges are ill-defined the effective mobility decreases shaply near the centre of the gap where there is a low concentration of states and it is unlikely that hopping or tunneling can take place between them [6].

Structural disorder must be expected in polymers since, as we saw in Chapter 2, polymer chains are not rigid especially above the glass-transition temperature. Thus, segments of the polymer chains can undergo a variety of conformational changes, a situation of considerable significance for charge storage and conduction [214]. In addition, molecular dispersion (Gaussian or Poisson molecular weight distributions), chain folding and chain ends, localized states from Peierls distortion and double bond formation, low intermolecular forces between chains, voids or residues are some of the common factors leading to structural disorder in polymers [194]. Therefore, we may not expect a band structure of electronic levels but a distribution of localized states (traps) as shown in Fig.3.2. The existence of traps gives rise to space-charge in the form of non-

compensated trapped charge[22]. Chemical traps, originating from chemical impurities may also be present [215].

The disorder has led to the assumption of distributions of traps extending to a depth about 1-2 eV [6][216] from the conduction levels[23].

However, thermally stimulated current (TSC) measurements on polymers such as PE and PE- EVA copolymer [194], polyethylene terephthalalate (Mylar) [217] and PP, show several peaks therefore suggesting discrete traps or *bands of traps.* A typical spectrum for PP is given in Fig.3.3.

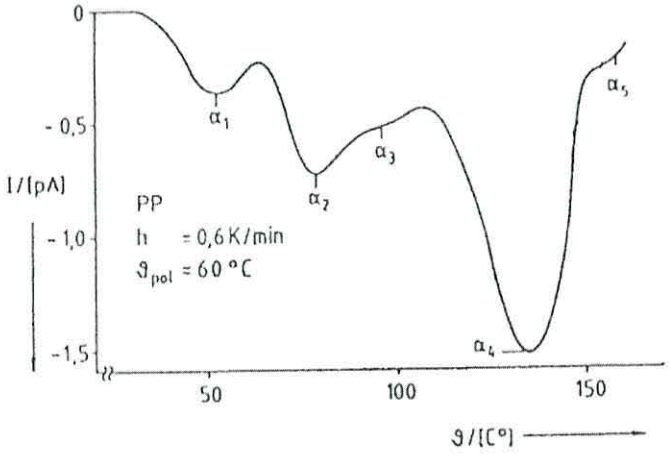

Figure 3.3: TSC spectrum of PP following a high field polarisation. From [7].

Several trapping levels have been suggested by Perlman [218] and Creswell *et al.* [13] in polyolefines. These are believed to be associated with atomic sites on molecular chains (primary level), electrons trapped between groups of atoms in neighbouring molecules (secondary level) and traps in crystalline or amorphous-crystalline regions (tertiary level). Therefore, more realistic representations of the density of states in polymers are as shown in Fig.3.4.

In addition, it may be expected that a solid suface will have different electrical

[22] The existence of traps was somehow proposed by Franklin under the name of *pores.*

[23] Although the existence of any "energy-band" structure is not obvious in disordered materials, if an electron is given sufficient energy it will become free to move through the substance, *i.e.*, is said to exist in a conduction level [216].

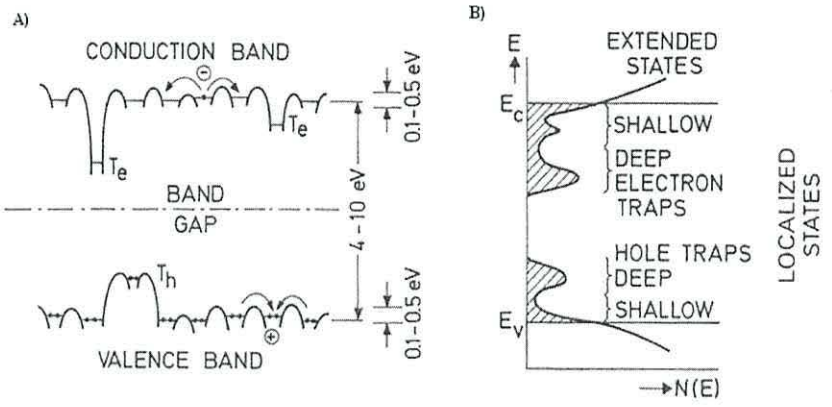

Figure 3.4: A) Energy diagram for a polymer. T_e electron traps, T_h hole traps. B) Density of states $N(E)$ for a polymer. Localized states (traps) are shaded. E_c and E_v mobility edges [8].

properties from the bulk material because of dangling bonds, adsorbed impurities and oxidative and other chemical reactions [219]. These defects are thought to be responsible for the capture of charges in certain cases [220]. Atactic amorphous material concentration near the surface has also been reported [221] which can lead to surface traps.

Permanganic acid treatment has been proved to be successful in removing surface traps in some polymers therefore exposing more crystalline and crystalline-amorphous interfaces, *i.e.*, deeper traps thus improving the charge stability of electrets so formed [222].

The effect of electrode deposition may also influence the surface behaviour. The possible creation of surface defects (traps) during electrode evaporation has been pointed out by Baba [223] while silver paint and colloidal graphite electrodes may also modify the contact surface due to solvent plasticization of the polymer [224].

3.11 ELECTRETS

An *electret* is a dielectric that produces a permanent external field which results from permanent ordering of molecular dipoles, or stable uncompensated surface or space

charges [225]. Surface and volume charge in electrets are stored in trapping levels located in the gap between conduction and valence bands [8].

Space-charge electrets are the most widely used kind. In this case, the stability of the electret is related to the energy of trapping states of electrons (holes) injected into the material during the polarization process [11].

Systematic research into electret properties began in 1919 (see section 3.1) with Eguchi [125][126]. These electrets exhibited polarization whose direction was opposite to the direction of the polarizing field. Over time the polarization of electrets decreased to zero following which there appeared on the electret surfaces a permanent charge whose sign agreed with the polarity of electrodes during their formation. Gemant termed them *hetero-* and *homocharge* respectively [226].

Electrets made from polymer films with electric charge implanted from outside have found widespread applications [11]. Different methods can be used for charge implantation.

In the *electron beam method*, a sample is irradiated in vacuum with a beam of monoenergetic electrons whose maximum range is smaller that the thickness of the dielectric (Fig.3.5). Uniform irradiation is obtained by rapidly deflecting the beam in two perpendicular directions (scanning) [9]. Electron beam charging is hardly suitable for large-scale implementation. However electron-beam charging allows control over charge depth, lateral charge distribution and charge density determined by the energy range of electrons. These advantages have made the electron-beam method suitable for studying the properties related with charge trapping and charge decay in electrets [227][228][229][230][10][231].

Another method of charge injection is the so-called corona charging technique [232][233]. Corona is a widely applied poling method. It is based on the use of an inhomogeneous field to produce a discharge in air at atmospheric pressure. This inhomogeneous field is produced by applying a voltage between a point-shape or a knife-shape upper electrode at a certain distance from one side of the dielectric and a planar back electrode on

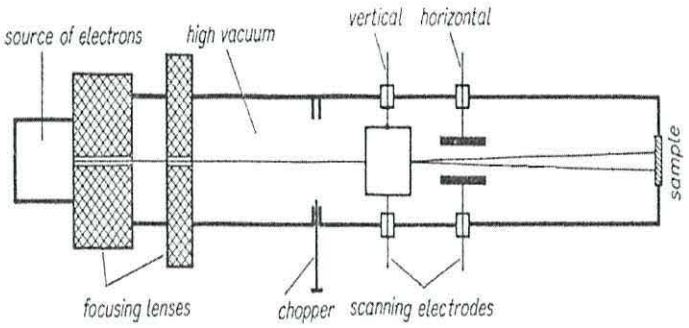

Figure 3.5: Schematics set-up used to obtain film electrets by scanning with a beam of monoenergetic electrons. Modified from [9].

the other side [232][233]. The prefix negative (positive) indicates the polarity of the point-shape electrode.

Locating of a mesh wire at a potential of at least a few hundred volts between offers a control over the the charging process [234]. The mesh controls the current to the sample which has initially a bell-shaped distribution modulated by the "shadows" of the wires. However, the eventual distribution of the deposited charge is generally uniform when the entire sample has assumed a saturation potential which equals the grid potential [8]. A drawback in a setup not using a grid electrode is the relatively large lateral nonuniformity of the charge distribution [8].

An advantage of the corona method is that it can be modified for continuously charging long strips of film. In this method, the polymer film, metallized side down is carried on an aluminium roller some millimeters beneath a knife-edge electrode. The surface charge is monitored with a curved vibrating electrode [217][10] as shown in Fig.3.6.

During negative corona, when sufficient overvoltage is applied free electrons present in the air due to, *e.g.*, cosmic rays acquire the energy necessary to produce an electronic avalanche in the gas phase [235]. These electrons are then driven by the electric field towards the surface of the sample and collide with neutral molecules ionizing them forming negative ions with a thermal energy of about 1eV [236]. In air at atmospheric

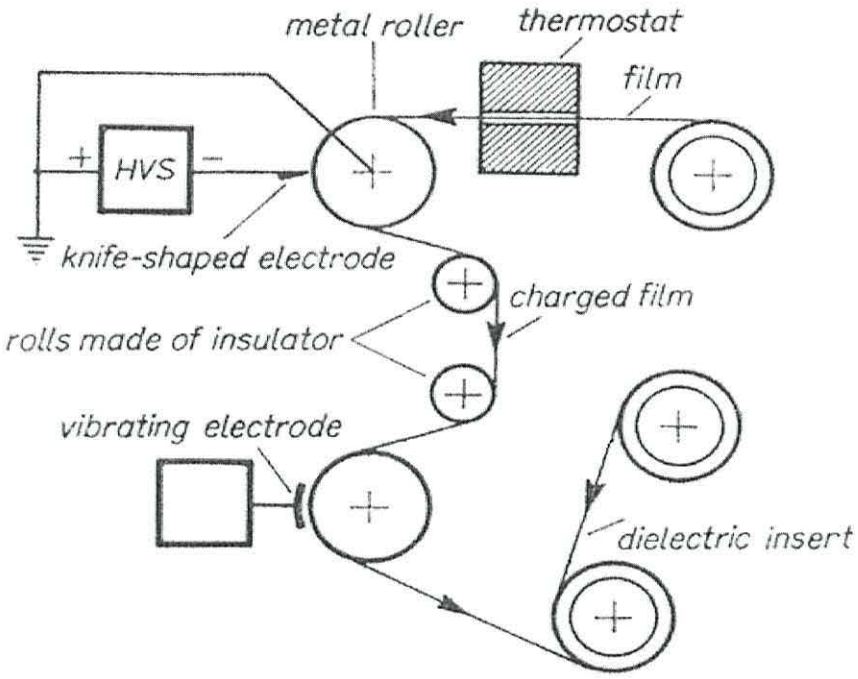

Figure 3.6: Schematic representation of the apparatus to corona-charge dielectric films [10].

pressure, negative carriers are mainly CO_3^- ions [237][238].

In coming up to the surface of the material these ions transfer their electrons to the conduction band. This negative charge becomes trapped on the surface first by deep then by the shallow traps, following which it may be released and transferred into the bulk in the internal electric field related to the injected charge [11]. Due to their small energy, it is likely that molecules do not penetrate into the material and, after transferring the charge, re enter the air. This has been observed on amorphous selenium surfaces [239].

It has been found that, by corona-discharge, double C=C bonds and carboxyl groups C=O are produced in polymers, and they may constitute additional traps for current carriers [240]. The frequency spectrum of corona-charged PP displays a low-frequency relaxation probably due to dipolar groups introduced during corona charging [241]. The presence of corona induced dipoles has also been suggested by Blaise *et al.* [242] from

IR measurements.

Another method for charge injection takes advantage of electric breakdown effects. The procedure was first applied by Perlman *et al.* [243] and further developed by Sessler *et al.* [12] and is shown schematically in Fig.3.7.

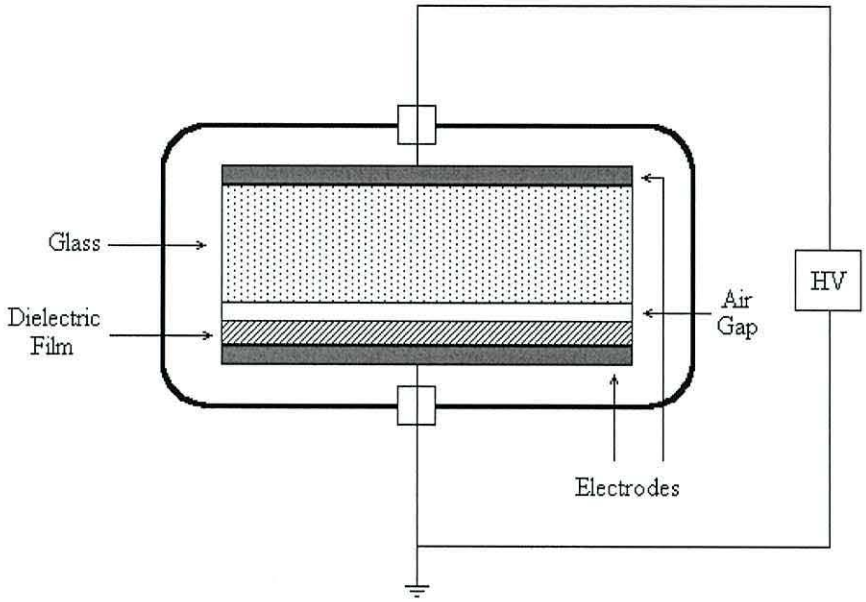

Figure 3.7: Schematic set-up for breakdown poling. Modified from [11].

As a result of the applied voltage small breakdowns in the air layer take place which lead to charge deposition in the dielectric film surface. The breakdown process has the same origin as in corona poling. The charging process finishes when the potential across the air gap reaches a certain value V_{lim} which depends basically on the thickness of the air gap. The dependence of the threshold voltage on the air gap thickness is shown in Fig.3.8.

In order to avoid damaging the film, it is customary to introduce a much thicker dielectric plate with much lower resistivity (typically $10^{10}\Omega$m [11]) which therefore acts as a protective series resistance [8]. In addition, the dielectric insert also allows for the removal of the electret without it becoming discharged [8].

The breakdown charging method is of great importance in this work since it is by

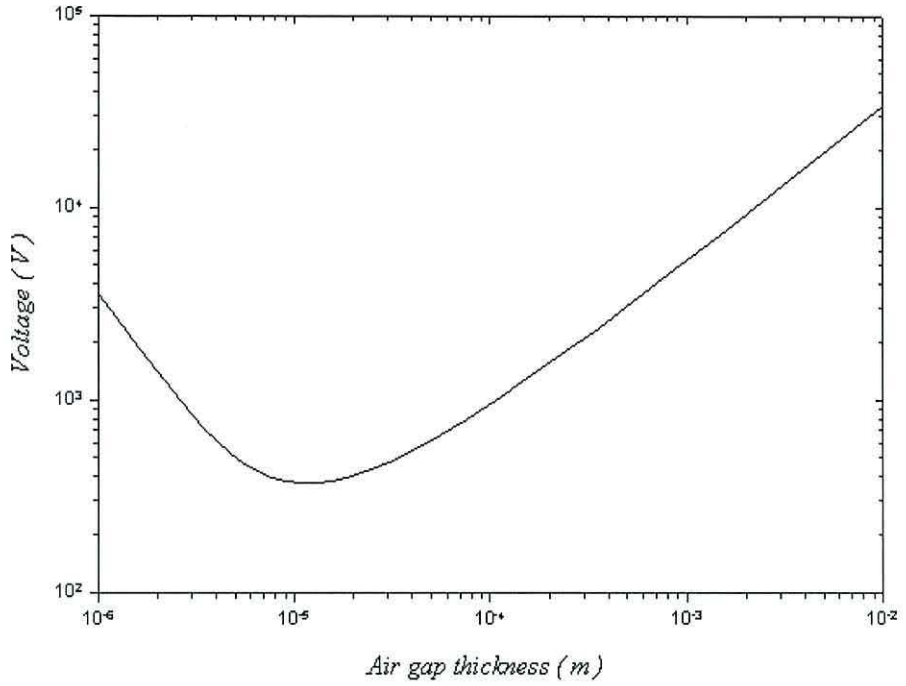

Figure 3.8: Dependence of the threshold voltage for breakdown on the air gap thickness. Modified from [12].

this effect that polypropylene foam becomes piezoelectric as we shall see in Chapter 6.

3.12 Conduction Mechanisms in Polymers

As we saw in section 3.4, the total current in a material is the sum of a rapidly decreasing term due to the finite polarization of vacuum, the absorption current due to polarization of electric dipoles of the material and a term which accounts for the real movement of charges, the conduction current.

Conduction currents in insulating polymers are important since they are related with phenomena such as degradation [244] resulting in the failure of the material. In addition knowledge of conduction mechanisms (as well as polarization mechanisms) can give information about chemical [245] [246] as well as structural properties of materials [247] [194].

Polymeric materials at high fields and/or temperatures often do not follow the Curie-

von Schweidler law (equations 3.79 and 3.80) [248] because measurable conduction currents begin to flow under these conditions. In fact, no known polymer is completely free of electrical conduction [195]. Carriers can be electrons (holes) and/or ions. Ions in polymers can be of intrinsic nature, *e.g.*, from the dissociation of dissociable groups or may be extrinsic, as chemical impurities introduced during manufacture of the polymer or thereafter. Several methods have been proposed to detect ionic conduction in solids (see for instance [194]) and indeed intrinsic ionic conductivity phenomena have been observed in polyamide (Nylon) 6,6 [249] and extrinsic ionic conductivity in various polymers [250]. A situation where electrons may become attached to low molecular weight species thus forming ionic carriers must also be considered [251].

We have seen that aperiodicity causes the available conduction bands to split off into single localised states corresponding to , *e.g.*, single molecules. As a result, the electrons (holes) jump from one molecule to the other in an activated manner. Electronic conduction may exist along polymer chains even in the presence of disorder [252]. However, in actual macromolecular chains we must consider many types of disorder (*e.g.*, chain folds) as well as phonons which influence carrier movement, both of these factors giving rise to traps [253]. Besides, a one-dimensional conductor consisting of an infinitely-long chain of equally-spaced carbon atoms each containing one π electron would be unstable, and Peirl's distortion would produce a bond-alternating polyene with the bond-alternating structure resulting in π localization and a band gap of around 2 eV [6].

In addition, one must also deal with intermolecular transfer of charge. In order to participate in charge transfer an electron (hole) must jump from one chain to another. Therefore we have to deal with two mobilities, *viz.* intra- and inter-chain as first postulated by Hirsch [254]. The intra-trap mobility of electrons (holes) is likely to be quite high ($10^{-4} m^2 V^{-1} s^{-1}$) . The inter-chain transfer of charge does clearly depend on the intermolecular interactions. In polymers, especially when neither dipolar forces nor hydrogen bonds are present, the intermolecular interaction is weak leading to a much lower associated mobility ($10^{-14} m^2 V^{-1} s^{-1}$) [6].

In saturated polymers, the band-gap is usually too high to provide carriers at least at moderate temperatures [253][195]. For example, a band gap as high as 8.8 eV has been reported for polyethylene (PE) [255], pointing to the extrinsic character of conduction in PE and therefore, to the existence of carriers injected directly into the conduction band of the polymer from electrodes or as a result of dissociation of ionized impurities.

Generated carriers, whatever their origin, are thought to undergo inter-chain conduction by *phonon-assisted* or *thermally activated hopping* between adjacent localized states [251]. Although hopping conduction does not involve band conduction but localized states, the thermally activated character of hopping makes it possible to use the concepts of band theory, *e.g.*, trap-modulated mobility, since both mechanisms eventually lead to detrapping via thermally activated processes [11]. Then, the hopping mechanism explains the observed Arrhenius-type dependence of conductivity in polymers.

Contrary to the model of hopping conduction between rigidly localized states, Lowell [256] has pointed out that since in polymeric chains, segments or side groups are mobile (even below the glass transition temperature), trapped charges will be displaced by the action of an electric field although they remain in the trap. These field-induced movements of the segments (traps) may facilitate the interchain transfer of charge because 1) as the groups approach each other, the probability of transfer by tunnelling increases and 2) the relative motion of the charges and the empty states results in fluctuations of the energy difference which in fact controls the transfer probability via the conservation of energy principle.

Interchain conduction enhanced by iodine I_2 has been reported for some polymers, *e.g.*, PE [257][258], PVF [259] and PP [260] among others. Iodine is a strong electron acceptor through its empty d-orbitals which results in its high electronegativity. It has been suggested by Swan [257] that the transfered electrons can be retained by the iodine molecules acting thus as ions[24].

[24]This effect is known to happen in I_2-piridine compounds where ionic bonds are formed between iodine and piridine molecules [261].

3.13 Electrical Properties of Polypropylene

PP is widely used as a dielectric because of its high rigidity and low dielectric losses [262] [241] arising from the lack of dipolar groups [22][5]. The observed, small dielectric loss may arise from the existence of a small dipole moment as suggested by Anderson *et al.* [263]. The experimental value found for the loss tangent (~ 0.01) [5] is in reasonable agreement with the value of 0.081 D obtained by Curtis [264] for the dipole moment of propane.

PP has also proved to be a good electret [241][265]. Figure 3.9 shows the temperature dependence of surface charge density for electrets formed from various polymers by corona charging [13].

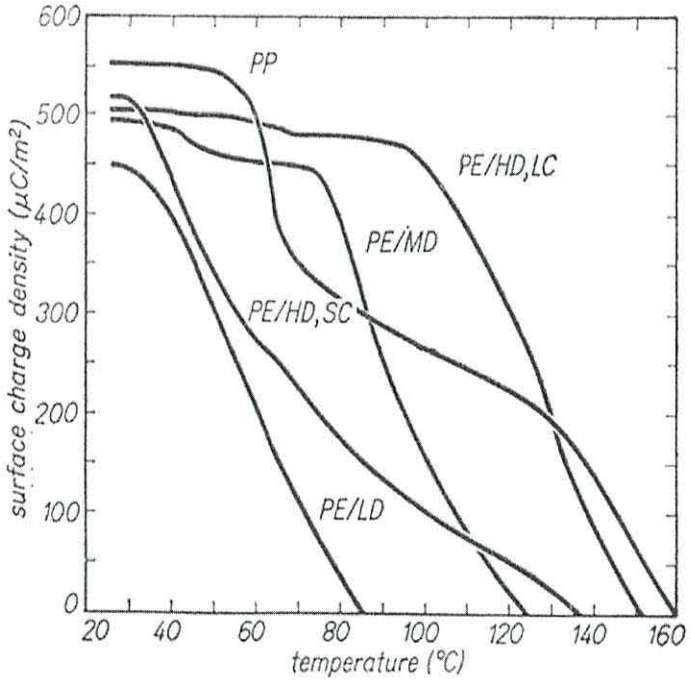

Figure 3.9: Temperature dependence of surface charge density for electrets formed from various films by corona charging. Heating rate 1°C min^{-1}. PE/HD, LC -polyethylene with high density and large size of crystallites, PE/HD, SC -polyethylene with high density and small size of crystallites, PE/LD -low density polyethylene, PE/MD -medium density polyethylene, PP -polypropylene [13].

TSC (Thermally Stimulated Currents) (see section 7.1.1) is a useful method to mea-

sure the energy distribution of trapped charge in a polymer [227]. TSC experiments on polypropylene under different poling conditions have been widely studied. Comparison of TSC results on corona- and electron-beam-charged PP has been useful in showing the difference in behaviour between surface and bulk-trapped charge [236][266].

By comparing corona- and electron-beam-charged PP, Yang [267] attributed the open-circuit TSC peaks (~70°C) and (~100°C) to surface and bulk traps respectively.

In addition, comparison between open and short circuit TSC has also been used to distinguish between surface and bulk traps. Thus, Yang [267] suggested, by performing open- and short-circuit TSC on electron-beam-charged PP samples, that the presence of a high-temperature peak (~150°C) is due to surface traps. The same procedure was used by Singh *et. al.* [268] in negatively corona-charged samples. They reported three peaks (~50, ~90 and ~120°C) arising from bulk traps and a high temperature peak (~145°C) due to surface traps.

By recording short-circuit TSC at different temperatures and polarization fields, Datt *et al.* [269] reported surface traps (~60 and ~100°C peaks) and bulk traps (~120°C) on voltage-poled PP samples.

Activation energy is also useful for determining the origin of a certain TSC peak. Thus, an open-circuit TSC peak ~ 77°C has been reported by Motyl [270] for positively corona-charged PP. The calculated activation energy of ~ 1.7 eV suggests that this peak arises from charge detrapping.

The effect of the morphology on electret behaviour of PP has also been studied by several authors.

Krause *et al.* [271][272] compared Thermally Stimulated Fourier Transformed Infrared Spectroscopy TS-FTIR and TSC on voltage-polarized PP samples. This comparison led them to distinguish between relaxation in the amorphous phase (TSC peak at ~80°C) and a high-temperature relaxation (TSC peak at ~150°) explained as a separation of charge carriers from the helix molecules in the crystalline structures of the polymer. An increase of charge storage with crystallinity has been reported by Nath *et*

al. [273].

Two (open-circuit) TSC peaks (~70 and ~140°C) have been reported by Baba *et al.* [274] on positively corona-charged samples. They attributed the low-temperature peak to shallow traps in the strained amorphous phase and the high-temperature peak to deep traps in the crystalline phase (inside the spherulites). This was further confirmed by Ikezaki *et al.* [275] by direct observation, under an optical microscope, of charged samples treated with photoionized dye particles, in good agreement with Krause *et al.* [271][272].

Despite the usefulness of the TSC technique, all the different data and the conclusions extracted found in literature indicate that the mechanism of charge storage is not fully understood yet.

Chapter 4

Mechanical Properties

The characterisation of the mechanical response of a material when subjected to a mechanical excitation, *i.e.*, the mechanical characterisation, is, as we will see in Chapter 5, needed for understanding the piezoelectric effect. In this chapter we present the basic concepts and magnitudes related to the mechanical properties of materials. These magnitudes will be used in chapters 5 and 11 where we present the basic concepts of piezoelectricity and the piezoelectric properties of PP foam respectively.

The history of mechanics is excellently presented in the book of Love [276]. Therefore, we will not attempt to give it here in a less elegant way.

4.1 Phenomenological Relations

4.1.1 Stress

Matter is composed of discrete entities and is therefore highly inhomogeneous. However, from a phenomenological point of view, it is useful to treat it as a continuum. Under the so-called *continuum approximation*, the material properties can be defined in terms of vectorial fields.

Thus, if in a certain reference system $R \equiv \{O; \hat{x}_1, \hat{x}_2, \hat{x}_3\}$ we denote by $F^{\vec{n}}$ the part of the total force $\vec{F}$ acting on the surface ΔS in the direction of a unit vector $\vec{n}$, the stress $T^{\vec{n}}$ acting on the surface at the point P can be defined as:

$$\vec{T}^{\vec{n}} = \lim_{\Delta S \to 0} \frac{\Delta \vec{F}^{\vec{n}}}{\Delta S} = \frac{d\vec{F}^{\vec{n}}}{dS}. \tag{4.1}$$

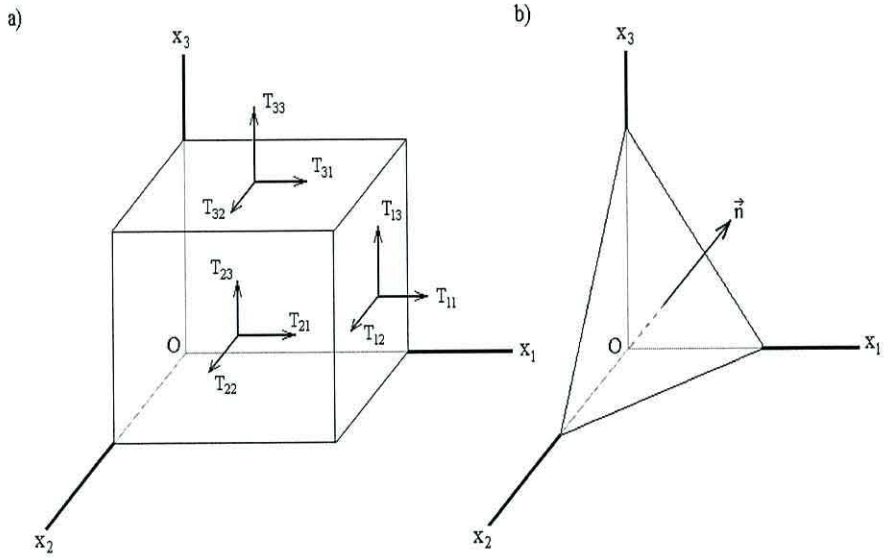

Figure 4.1: a) Notation for stress components. b) Oriented surface of area S with unit normal vector $\vec{n}$.

For the case of the reference vectors $\{\hat{x}_1, \hat{x}_2, \hat{x}_3\}$, the stress vectors $\vec{T}^{\hat{x}_i}$ are defined in terms of their components (Fig.4.1 a)) as:

$$\vec{T}^{\hat{x}_i} = \sum_{j=1}^{3} T_{ij} \hat{x}_j \tag{4.2}$$

where:

$$T_{ij} = \vec{T}^{\hat{x}_i} \cdot \hat{x}_j \tag{4.3}$$

are the components of the $\vec{T}^{\hat{x}_i}$ in the $\hat{x}_j$ directions. These are the components of the so-called *stress tensor*:

$$\mathbf{T} = \begin{pmatrix} T_{11} & T_{12} & T_{13} \\ T_{21} & T_{22} & T_{23} \\ T_{31} & T_{32} & T_{33} \end{pmatrix}. \tag{4.4}$$

It can be proved [277] that for any oriented surface such as that shown in Fig.4.1 b), the stress vector $\vec{T}^{\vec{n}}$ can be expressed in terms of the stress vectors $\vec{T}^{\hat{x}_i}$ as[1]:

$$\vec{T}^{\vec{n}} = T_{ij} n_j \tag{4.6}$$

and therefore, the stress is completely defined by the stress tensor components.

4.1.2 STRAIN

The deformation suffered by a material in a certain time interval $\Delta t = (t - t')$ as a result of the action of an applied force at time t' is given by the position vectors $\vec{R}_p$ and $\vec{r}_p$ (here the subscript p is used to label the *p-th* particle) for all the particles that compose the material. Under the continuous approximation, the subscript p can be removed and the vector $\vec{r}$ used to "label" the particle. Thus, the vector $\vec{R}$ is taken as a dependent variable ($\vec{R}(\vec{r})$). It is usual to define the so-called *strain tensor* η as [277]:

$$\eta_{ij} = \frac{1}{2}\left(\frac{\partial R_i}{\partial r_i}\frac{\partial R_i}{\partial r_k} - \delta_{jk}\right) = \frac{1}{2}\left(\frac{\partial h_j}{\partial r_k} + \frac{\partial h_k}{\partial r_j} + \frac{\partial h_i}{\partial r_j}\frac{\partial h_i}{\partial r_k}\right) \tag{4.7}$$

where, by h_i we denote the components of the so-called *displacement vector*:

$$\vec{h} = \vec{R} - \vec{r}. \tag{4.8}$$

4.1.3 EQUATION OF MOTION

Since the velocity, $\vec{v}$, is the linear momentum, $\vec{p}$, per unit mass, we can write:

$$\frac{d\vec{p}}{dt} = \int_V \rho \frac{d\vec{v}}{dt}\, dV \tag{4.9}$$

[1] The notation $T_{ij}n_j$ is used to indicate:

$$\sum_j T_{ij} n_j \vec{x}_j. \tag{4.5}$$

which, from Newton's second law when only stresses are considered[2] can be written as:

$$\int_V \rho \frac{d\vec{v}}{dt}\, dV = \oint_S \vec{T}\, dS. \tag{4.10}$$

Since the two terms in the equation above identically equal each other, the integrands must be identically equal, *i.e.*,

$$\rho \frac{d\vec{v}}{dt} = \vec{T}\, dS. \tag{4.11}$$

Now, with the help of Gauss' theorem:

$$\rho \frac{dv_i}{dt} = \frac{\partial T_{ij}}{\partial r_j}. \tag{4.12}$$

4.2 THERMODYNAMICAL RELATIONS

The stress state of a body has been defined in terms of the dimensions of the stressed body while the strain has been defined with respect to the unconstrained state. It follows that the differential work per unit mass[3], dW' done by the application of the stress in straining the body, does not satisfy the relation:

$$dW' \propto T_{ij} d\eta_{ij}. \tag{4.13}$$

On the contrary, dW' is given by [277][278]:

$$dW' = \rho_0^{-1} t_{ij} d\eta_{ij} \tag{4.14}$$

where ρ_0 is the unstrained density. In addition, in the case of non-dissipative stresses, the so-called *thermodynamic tensions*, t_{ij}, are given by [277][278]:

[2]We distinguish between body forces, which are proportional to the mass of a volume element dV and surface forces (stresses), which act on its surface.

[3]Pure translation is not considered.

Thermodynamic Potential	*Exact Differential*
Internal Energy $U(\eta_{ij}, S)$	$dU = t_{ij}d\eta_{ij} - TdS$
Enthalpy $H(t_{ij}, S)$	$dH = -\eta_{ij}dt_{ij} - TdS$
Helmholtz Free Energy $A(\eta_{ij}, T)$	$dA = t_{ij}d\eta_{ij} - SdT$
Gibbs Free Energy $G(t_{ij}, T)$	$dG = -\eta_{ij}dt_{ij} - SdT$

Table 4.1: Exact differentials for different thermodynamic potentials. T is temperature and S is entropy.

$$T_{ij} = \frac{1}{det(J)} \frac{\partial R_k}{\partial r_m} \frac{\partial R_m}{\partial r_i} t_{ij} \tag{4.15}$$

where:

$$det(J) = \lim_{dV_0 \to 0} \left(\frac{dV}{dV_0} \right) = \begin{vmatrix} \partial R_1/\partial r_1 & \partial R_1/\partial r_2 & \partial R_1/\partial r_3 \\ \partial R_2/\partial r_1 & \partial R_2/\partial r_2 & \partial R_2/\partial r_3 \\ \partial R_3/\partial r_1 & \partial R_2/\partial r_2 & \partial R_3/\partial r_3 \end{vmatrix}. \tag{4.16}$$

The internal energy per unit volume can therefore be written as:

$$dU = t_{ij}d\eta_{ij} - TdS \tag{4.17}$$

where T and S are the temperature and entropy (per unit volume) respectively. Other thermodynamic potentials are obtained by applying Legendre transformations in equation 4.17 and are shown in Table 4.1.

4.2.1 THERMODYNAMIC COEFFICIENTS

ELASTIC STIFFNESS AND COMPLIANCE COEFFICIENTS

The so-called *elastic stiffness coefficients* are defined as the partial derivatives of the thermodynamic tensions with respect to the strain tensor components, *i.e.*:

$$c_{ijkm}^{S,T} = \left(\frac{\partial t_{ij}}{\partial \eta_{km}}\right)_{S,T} \tag{4.18}$$

where the subscripts S, T stand for derivation at constant entropy and temperature respectively. Using the exact differential of the thermodynamic potentials A and U in Table 4.1 we have respectively:

$$c_{ijkm}^{T} = \rho_0 \left(\frac{\partial^2 A}{\partial \eta_{ij} \partial \eta_{km}}\right)_{T} \tag{4.19}$$

and:

$$c_{ijkm}^{S} = \rho_0 \left(\frac{\partial^2 U}{\partial \eta_{ij} \partial \eta_{km}}\right)_{S}. \tag{4.20}$$

From equation 4.7, it follows that:

$$c_{ijmk}^{S,T} = c_{jimk}^{S,T} = c_{ijkm}^{S,T} = c_{jikm}^{S,T}. \tag{4.21}$$

In addition, considering that the order of differentiation is not relevant, we can write:

$$c_{ijkm}^{S,T} = c_{kmij}^{S,T}. \tag{4.22}$$

Another important set of coefficients are the so-called *compliance coefficients*, defined by:

$$s_{ijkm}^{S,T} = \left(\frac{\partial \eta_{ij}}{\partial t_{km}}\right)_{S,T} \tag{4.23}$$

which follow the same symmetry rules as the elastic stiffness. Compliance coefficients can also be defined in terms of the thermodynamic potentials. In this case, considering the exact differentials of H and G in Table 4.1:

$$s^S_{ijkm} = -\rho_0 \left(\frac{\partial^2 H}{\partial t_{ij} \partial t_{km}} \right)_S \tag{4.24}$$

and:

$$s^T_{ijkm} = -\rho_0 \left(\frac{\partial^2 G}{\partial t_{ij} \partial t_{km}} \right)_T . \tag{4.25}$$

Due to the symmetry properties above, it is customary to introduced the so-called *abbreviated notation*:

$$\begin{aligned} 11 &\sim 1 \quad 23 = 32 \sim 4 \\ 22 &\sim 2 \quad 13 = 31 \sim 5 \\ 33 &\sim 3 \quad 12 = 21 \sim 6. \end{aligned} \tag{4.26}$$

From equations 4.18 and 4.23 with the notation introduced above we write:

$$c^{S,T}_{km} s^{S,T}_{ij} = \frac{\partial t_k}{\partial \eta_m} \frac{\partial \eta_m}{\partial t_j} = \delta_{kj} \tag{4.27}$$

from which:

$$c_{km} = \frac{(-1)^{k+m} \Delta^s_{km}}{\Delta^s} \tag{4.28}$$

and:

$$s_{ij} = \frac{(-1)^{i+j} \Delta^c_{ij}}{\Delta^c} \tag{4.29}$$

where Δ^c, Δ^s are the determinants of the stiffness and compliance tensors respectively and Δ^c_{lh}, Δ^s_{lh} are the determinants of the minor obtained by crossing out the row l, column h. Finally, the thermal expansion coefficient at constant thermodynamic tension is defined as:

$$\alpha_{km} = \left(\frac{\partial \eta_{km}}{\partial T} \right)_t . \tag{4.30}$$

4.3 Linear Theory

4.3.1 Linear Elasticity

For small isothermal or isoentropic deformations, the thermodynamic tensions can be expanded as [277]:

$$t_{ij} = \left(\frac{\partial t_{ij}}{\partial \eta_{km}} \right) \eta_{km} + \ldots = c_{ijkm} \eta_{km} + \ldots . \tag{4.31}$$

In addition, for small deformations, *i.e.*, in the so-called *linear approximation* we have:

$$\frac{\partial h_i}{\partial r_j} \approx 0 \tag{4.32}$$

and then, (see equation 4.7) the strain tensor, η_{ij}, reduces to the classical *infinitesimal strain tensor* or *elongation tensor*, S_{ij}, whose components are given by:

$$S_{ij} = \frac{1}{2} \left(\frac{\partial h_i}{\partial r_j} + \frac{\partial h_j}{\partial r_i} \right) . \tag{4.33}$$

Finally, from equations 4.15 and 4.16, *i.e.*, for non-dissipative stresses, we have:

$$T_{ij} \approx t_{ij} \tag{4.34}$$

by virtue of which, equation 4.31 can be expresed as:

$$T_{ij} = c_{ijkm} S_{km} \tag{4.35}$$

or, using the abbreviated notation in (4.26):

$$T_i = c_{ij} S_j \tag{4.36}$$

where c_{ij} are the elements of the so-called *stiffness matrix*, C_{ij}.

Equation 4.36 is the so-called *generalized Hooke's law*. Analogously:

$$S_i = s_{ij} T_j \tag{4.37}$$

where s_{ij} are the elements of the so-called *compliance matrix*, S_{ij}.

Finally, the internal energy and the equation of motion are given by:

$$dU = \frac{1}{2} T_i dS_j \qquad i, j = 1, \ldots, 6 \tag{4.38}$$

and

$$\rho \frac{\partial^2 h_i}{\partial t^2} = \frac{\partial T_{ij}}{\partial r_j}. \tag{4.39}$$

The thermal expansion coefficient in equation 4.30 is, in the linear approximation:

$$\alpha_i = \left(\frac{\partial S_i}{\partial T_i} \right)_T. \tag{4.40}$$

In view of equations 4.22 and 4.36 or 4.37 we see that 21 parameters are required to describe the relation between the stress and strain states of a body. However, for almost all symmetries the number of independent elements reduces. Hence, for *orthotropic* symmetry[4], the compliance matrix, S_{ij}, is given by [15]:

[4]We say that a material has orthotropic symmetry when the material structure has three mirror planes [15].

$$S_{ij} = \begin{pmatrix} \frac{1}{Y_1} & -\frac{\nu_{21}}{Y_2} & -\frac{\nu_{31}}{Y_3} & 0 & 0 & 0 \\ -\frac{\nu 12}{Y_1} & -\frac{1}{Y_2} & -\frac{\nu_{32}}{Y_3} & 0 & 0 & 0 \\ -\frac{\nu_{13}}{Y_1} & -\frac{\nu_{23}}{Y_2} & \frac{1}{Y_3} & 0 & 0 & 0 \\ 0 & 0 & 0 & s_{44} & 0 & 0 \\ 0 & 0 & 0 & 0 & s_{55} & 0 \\ 0 & 0 & 0 & 0 & 0 & s_{66} \end{pmatrix} \tag{4.41}$$

where Y is the so-called *Young's modulus* and ν_{ij}, the so-called *Poisson's coefficient*, defined as:

$$\nu_{ij} = -\frac{S_j}{S_i} \tag{4.42}$$

where the stress is applied in the direction $\vec{x}_i$,

Furthermore, where non-dissipative stress is considered, the elastic energy is a thermodynamical potential. Under such conditions, it can be shown that [276] $s_{ij} = s_{ji}$, and then:

$$\frac{\nu_{ij}}{Y_i} = \frac{\nu_{ji}}{Y_j}. \tag{4.43}$$

Moreover, for isotropic solids, there are only two independent coefficients. In fact, the only non-zero elements of the compliance and stiffness matrices can be expressed as [276][277]:

$$s_{11} = s_{22} = s_{33} = \frac{\mu(3\lambda + 2\mu)}{\lambda + \mu} \tag{4.44}$$

$$s_{12} = -\frac{\lambda}{\lambda + 2\mu} \tag{4.45}$$

$$s_{44} = s_{55} = s_{66} = \frac{\lambda}{2(\lambda + \mu)} \tag{4.46}$$

and

$$c_{11} = c_{22} = c_{33} = \lambda + 2\mu \tag{4.47}$$

$$c_{12} = c_{13} = c_{23} = \lambda \tag{4.48}$$

$$c_{44} = c_{55} = c_{66} = \mu \tag{4.49}$$

where λ and μ are the so-called *Lamé constants.*

In addition, the Poisson's coefficient defined in equation 4.42 can be expressed in terms of the Lamé constants as:

$$\nu_{ij} = \nu = \frac{\lambda}{2(\lambda + \mu)} \quad \forall i, j = 1, 2, 3. \tag{4.50}$$

In the simple experiment shown in Fig.4.2 a), a sample is acted upon by a stress in a certain direction and the resulting strain measured in the same direction. If we neglect the other two dimensions, *i.e.*, in the *unidimensional approach*, the compliance and stiffness matrices are diagonal and then[5], in view of equations 4.28 or 4.29) we have:

$$c_{ij} = s_{ij}^{-1}. \tag{4.51}$$

4.3.2 LINEAR VISCOSITY

So far, we have only considered the case where the forces (stresses) are non-dissipative. The opposite case is that of purely dissipative forces. In this case, the work done by the forces is completely converted into heat.

Let us consider a fluid set under the action of a non-homogeneous velocity field in the y direction. Although the velocity is directed along the $\hat{x}_2$ direction, each particle has also a component in the $\hat{x}_1$ direction because of thermal motion. Therefore, there

[5] Note that, in the unidimensional approach, the Poisson's coefficients are all zero. Therefore, (equation 4.50) $\lambda = 0$ and, from equations 4.46 and 4.49, the out-of-diagonal elements of the compliance and stiffness matrices are all zero. Moreover, in such a situation, equations 4.44 and 4.47 yield equation 4.51.

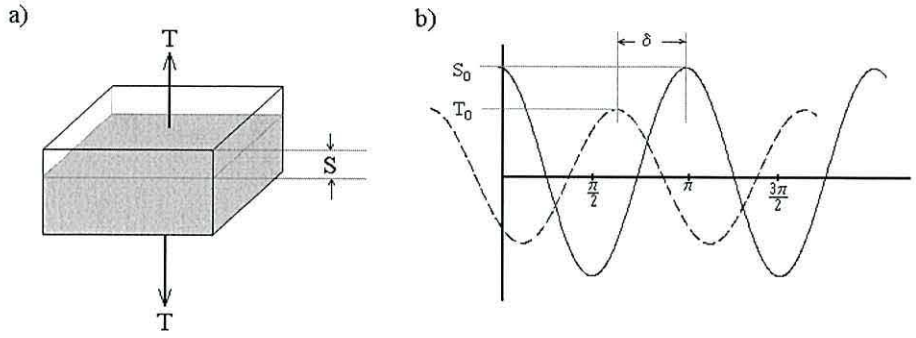

Figure 4.2: a) Representation of the stress and strain in a simple one-dimensional experiment. b) Stress-strain lag-in-phase in viscoelastic materials.

will be particles continuously crossing a certain plane π parallel to the y direction. In this situation, the particles crossing π from left to the right have higher momentum than those crossing the plane in the opposite direction. It has been experimentally found that, in the case of low velocities and incompressible fluids, *i.e.*, in the linear approximation:

$$\vec{p} = \eta \frac{\partial v_2}{\partial x_1} \tag{4.52}$$

where $\vec{p}$ is the momentum density per unit time across a plane $x = x_0$ and η is the so-called *viscosity*. Equation 4.52 is called *Newton's law of viscosity*.

Since the fluid on the right-hand side gains a momentum $\vec{p}$ the fluid on the right-hand side can be seen as acted on by a force. In section 4.1 we have seen that the value of a force per unit area is a stress and, since the force is the time derivative of momentum, equation 4.52 can be expressed as:

$$p = T_{12} \equiv T_2. \tag{4.53}$$

In the general case [277]:

$$\sigma_{ij} = 2\eta D_{ij} \tag{4.54}$$

$$T_{kk} = 3\left[-\tau(\rho, T) + \xi d_{kk}\right] \tag{4.55}$$

where τ is the thermodynamic pressure defined below (equation 4.61), ξ is the so-called *compressional viscosity* and the quantities T_{kk} and τ_{ij} are defined by the relations:

$$T_{ij} = \frac{1}{3}T_{kk}\delta_{ij} + \tau_{ij} \tag{4.56}$$

where D_{ij} are defined by:

$$d_{ij} = \frac{1}{3}d_{kk}\delta_{ij}D_{ij} \tag{4.57}$$

being:

$$d_{ij} = \frac{1}{2}\left(\frac{\partial v_i}{\partial R_j} + \frac{\partial v_j}{\partial R_i}\right). \tag{4.58}$$

When a material is at rest, at each point the stress components T_1, T_2 and T_3 are given by [279]:

$$\tau = -T_i \qquad \text{i=1, 2, 3} \tag{4.59}$$

where the so-called *thermodynamical pressure* $-\tau$ is what is usually understood by the term *pressure*.

In a dynamic situation the three stress components above do not equal each other so that the concept of pressure as defined above does not make sense. However, each normal stress component T_i can be separated into two parts:

$$T_i = T_i' + T_i'' \tag{4.60}$$

where the components T_i'' are consistent with a relation similar to equation 4.59 and the pressure is understood in the sense:

$$-\tau = T_i'' \qquad \text{i=1, 2, 3.} \tag{4.61}$$

4.3.3 Linear Viscoelasticity

In sections 4.3.1 and 4.3.2 pure (linear) elastic and pure (linear) viscous behaviour were treated. Real materials and polymers in particular do not conform to either of these two limiting cases. Two reasons for this are [280]:

1. When the deformations are not small, the stress-strain relations are more complex than the straight line predicted by the generalized Hooke's law (equation 4.36).

2. Similarly, when the deformation velocities are not small, the behaviour deviates from that predicted by Newton's law (equation 4.52).

Yet, when deformations and deformation rates are small, the mechanical behaviour may be a mixture of both elastic and viscous behaviours. In this case, the material is said to behave in a *viscoelastic* manner.

A viscoelastic solid may not be instantaneously deformed under the application of a constant force, as predicted by equation 4.36, but show a *retarded* response (*creep*) or even, at high temperatures and/or long times, flow as a fluid. On the other hand, a viscoelastic fluid, flowing on the application of a force may store some energy instead of dissipating it all, as predicted by equation 4.52 and recover to some extent when the force is released. Similarly, when a viscoelastic material is deformed, its stressed state follows a complicated time variation (*stress relaxation*). When a viscoelastic material shows a mixture of both linear elasticity and linear viscosity, it is said to be *linearly viscoelastic.* In addition, it is also an experimental fact that when a viscoelastic material is acted upon by an harmonic stress (strain), the resulting strain (stress) lags in phase by a certain angle δ (Fig.4.2 b)).

In attempting to describe these features, some models have been proposed which combine perfectly elastic (spring) and perfectly viscous (dashpot) elements. These

models behave as real polymers showing the above-mentioned features [281]. However, it is clear that such models are not satisfactory since they do not provide any connection between mechanical behaviour and the molecular processes involved.

Although some theoretical models have been developed to account for the viscoelastic properties of amorphous materials, semicrystalline materials (section 2.3) present additional difficulties. In fact, the mechanical behaviour is very sensitive to morphology, crystallinity and to the coupling between crystalline and amorphous regions [282]. On the other hand, molecular motions in the amorphous phase are constrained by surrounding crystalline regions in a manner that depends on crystallization conditions and/or subsequent thermal treatments [283]. Moreover, the mechanical and thermodynamical properties continue to change long after the polymer has solidified, because macromolecules in the solid state are still readjusting themselves towards the more stable state [58].

4.4 TIME RESPONSE

In a similar manner as we treated the time-dependent dielectric response in section 3.4, we can assume that the stress-strain proportionality holds providing that the elastic stiffness, c, is time-dependent, *i.e.*,

$$T(t) = c(t)S(t) \tag{4.62}$$

where the time dependence of the elastic constant can be separate into two terms:

$$c(t) = c_\infty + c_{ret} \tag{4.63}$$

where c_∞ and c_{ret} are the instantaneous and retarded responses respectively.

Under the described conditions, when a material is set under the action of a strain pulse (stress relaxation) of the form:

$$T(t) = T_0 \left(\Gamma(t - t_0) - \Gamma(t - t_0 - dt_0)\right) \tag{4.64}$$

the resulting stress will, by virtue of the superposition principle, be given by:

$$T(t) = c_\infty S(t)\Gamma(t-t_0) - c_{ret} S_0 f(t-t_0) + c_\infty S(t)\Gamma(t-t_0-dt_0) - c_{ret} S_0 f(t-t_0-dt_0). \tag{4.65}$$

Now, for short impulses (Dirac δ) we can write:

$$T(t) = c_\infty S(t) + c_{ret} \dot{f}(t - t_0) \tag{4.66}$$

where the term $(f(t - t_0) - f(t - t_0 - dt_0))\, dt_0$ has been approximated to the first term of its Taylor expansion. In addition, any function can be expressed as:

$$T(t) = c_\infty S(t) + c_{ret} \int_{-\infty}^{t} S(t_0)\phi(t - t_0) dt_0 \tag{4.67}$$

which, making the change $t - t_0 \rightarrow u$, transforms into:

$$T(t) = c_\infty S(t) + \int_0^\infty c_{ret} S(t - u)\phi(u) du \tag{4.68}$$

which, for the particular case of an harmonic excitation

$$S(t) = S_0 e^{\imath\omega t} \tag{4.69}$$

transforms into:

$$T(t) = \left[c_\infty + c_{ret} \int_0^\infty \phi(u) e^{-\imath\omega u} du\right] S(t). \tag{4.70}$$

Since the term in brackets in the equation 4.70 is a complex number, $\tilde{c}$, Hooke's relation (equation 4.36) holds for a complex stiffness $\tilde{c} = c'(\omega) - imathc''(\omega)$, *i.e.*:

$$T(\omega, t) = \tilde{c}(\omega, t) S(\omega, t). \tag{4.71}$$

Analogously, for an external applied stress (creep experiment):

$$S(\omega, t) = \tilde{s}(\omega, t) T(\omega, t) \tag{4.72}$$

where $\tilde{s}$ is the *complex compliance.*

The imaginary part of the modulus is a measure of the non-recoverable work done on the system and dissipated into heat. Multiplying by a complex quantity introduces a lag in phase (Fig.4.2), that is, the stress $T(\omega, t)$ in equation 4.71 can be written as:

$$T(t) = T_0 e^{\imath(\omega t + \delta)}. \tag{4.73}$$

By virtue of the mathematical identity:

$$\frac{e^{\imath(\omega t + \delta)}}{e^{\imath \omega t}} = \frac{e^{\imath \omega t} e^{\imath \delta}}{e^{\imath \omega t}} = e^{i\delta} = \cos\delta - \imath \sin\delta \tag{4.74}$$

we can write:

$$\frac{T}{S} = c' - ic'' \tag{4.75}$$

where:

$$c' = \left(\frac{T_0}{S_0}\right) \cos\delta \tag{4.76}$$

and

$$c'' = \left(\frac{T_0}{S_0}\right) \sin\delta \tag{4.77}$$

the so-called *storage* and *loss* moduli respectively. Their ratio:

$$\tan\delta = \frac{c''}{c'} \tag{4.78}$$

is called the *loss tangent*.

Since the above treatment is completely equivalent to that for the dielectric case, it follows that real and imaginary parts of the mechanical stiffness and compliance must obey the Kramers-Krönig relations (equations 3.67 and 3.68).

4.5 Acoustic Parameters

So far, we have considered that the magnitude of the stress (strain) is the same throughout the material. At frequencies close to the mechanical resonances where the two end surfaces of a sample are vibrating in anti-phase, this is a very rough approximation. This consideration leads us to the concept of strain (stress) propagation through materials, *i.e.*, sound waves. In addition, since both acoustic and mechanical properties account for the same physical principles, *i.e.*, the material response to a mechanical excitation, they are clearly related to each other. In the following sections expressions for some acoustical parameters will be introduced in terms of the mechanical parameters described in the previous sections.

4.5.1 Wave Propagation in a Linear Elastic Unbounded Media

For an isotropic and linearly elastic material, the stress tensor, T_{ij} can, in view of equations 4.33 and 4.36 and equations 4.47 to 4.49, be expressed as:

$$T_{ij} = \lambda\frac{\partial h_k}{\partial r_k}\delta_{ij} + \mu\left(\frac{\partial h_i}{\partial r_j} + \frac{\partial h_j}{\partial r_i}\right). \tag{4.79}$$

Therefore, the equation of motion (4.39) can be written as:

$$\rho\frac{d^2\vec{h}}{dt^2} = \mu\nabla^2\vec{h} + (\lambda+\mu)\vec{\nabla}\cdot(\vec{\nabla}\cdot\vec{h}). \tag{4.80}$$

Now, in the continuum approximation, $\vec{h}$ is differentiable and then, by virtue of the *Helmholtz theorem*, it can be expressed as the sum of a solenoidal vector, $\vec{h}_{sol}$, and an irrotational vector, $\vec{h}_{irr}$ which therefore obey the relations:

$$\vec{\nabla}\vec{h}_{sol} = 0 \tag{4.81}$$

and

$$\vec{\nabla}\times\vec{h}_{irr} = 0. \tag{4.82}$$

These two vectors give rise to two kinds of waves,

$$\rho\frac{d^2\vec{h}_{sol}}{dt^2} = \mu\nabla^2\vec{h} \tag{4.83}$$

which is the equation of a wave that propagates with velocity

$$v_{sol} = \sqrt{\frac{\mu}{\rho}} \tag{4.84}$$

and[6]

$$\rho\frac{d^2\vec{h}_{irr}}{dt^2} = (\lambda+2\mu)\nabla^2\vec{h} \tag{4.86}$$

which is the equation of a wave that propagates with velocity

$$v_{irr} = \sqrt{\frac{\lambda+2\mu}{\rho}} = \sqrt{\frac{c_{ii}}{\rho}}. \tag{4.87}$$

[6]Equation 4.86 was obtained after applying the vectorial identity:

$$\vec{\nabla}(\vec{\nabla}\vec{h}) = \nabla^2\vec{h} + \vec{\nabla}\times(\vec{\nabla}\times\vec{h}) \tag{4.85}$$

in equation 4.80 and considering that $\nabla\times\vec{h}_{irr} = \vec{0}$.

The two waves above are termed *transverse* (v_{sol}) and *longitudinal* (v_{irr}) waves.[7] In the longitudinal and transverse modes, the particle motion is respectively parallel and perpendicular to the direction of the propagation. For bounded solids, other propagation modes such as Rayleigh [284][285] and Lamb [286][287] modes can be present also.

4.5.2 Propagation of Transversal Waves in Viscoelastic Materials

If a stress function of the form $T(0,t) = T_0\ e^{\imath\omega t}$ is applied on the upper surface ($x = 0$) of an unbounded elastic solid as shown in Fig. 4.2 a), the time-dependence of the stress state at the surface $x = x'$ will be given by:

$$T(x',t) = T_0\ e^{\imath(\omega t - kx')} \tag{4.88}$$

where the *wave number* k is related to the wave length, Λ, and the propagation velocity, v, by the relations:

$$k = \frac{2\pi}{\Lambda} = \frac{\omega}{v}. \tag{4.89}$$

In addition, the propagation velocity is related to the mechanical modulus by equation 4.84. Thus, as a result of the complex character of the mechanical modulus, the propagation velocity and wave number have also a complex nature. Thus, introducing an imaginary term in the wave number:

$$\tilde{k} = k - \imath\alpha \tag{4.90}$$

equation 4.88 transforms into:

[7] Other terms such as *distortional* (transverse) and *dilational* (longitudinal) can be found in literature.

$$T(x',t) = T_0\ e^{\imath(\omega t-(k-\imath\alpha)x')} = T_0\ e^{\imath\omega t-(\imath k+\alpha)x'}. \tag{4.91}$$

where α is called the *acoustic attenuation* and $\Gamma = \imath k + \alpha$, the *attenuation constant.*

4.6 Thermo-Mechanical Properties of Polypropylene

Dynamic mechanical analysis (DMA, see section 7.2.2) is the most widely used technique for measuring the mechanical properties of viscoelastic materials. DMA experiments on polypropylene typically present three relaxation peaks. For the γ relaxation peak at around 220 K, the onset of small-scale chain motion in the amorphous portion of the polymer [288][289] as well as the combined effect of both local relaxation modes arising from the twisting of main chains in the amorphous phase and movement of crystal defects in the crystalline phase [283] have been proposed.

The β relaxation, 253 K, is attributed to the glass-transition [288][282]. For semicrystalline materials, it appears about 30 K lower than for amorphous materials due to the additional constraints placed on the mobility of polymer chains in the amorphous regions by the presence of crystallites [288]. In addition, the peak is broader in the semicrystalline case [290] suggesting a double transition involving the unconstrained regions of the amorphous phase and regions constrained by crystallites [291][283].

The α relaxation is usually located between 310 and 350 K. Its position varies with many factors (structure, density, etc.) [282]. It is known however that it requires the presence of a crystalline phase and has been attributed to the premelting and disordering within crystals [292] and can be increased by as much as 50 K by annealing for prolonged periods [289]. A relaxation of the amorphous phase due to constrained zones around crystallites [291], interlamellar shear processes [293] and diffusion of defects in the crystalline phase with a contribution of the amorphous phase around the crystallites [282] have also been suggested.

Two very-low-temperature relaxations at about 20 and 50 K have been reported by Sinnott [294] for low and high crystalline samples respectively who assigned them to the hindered rotations of pendant methyl groups in the amorphous (low crystalline) and crystalline (high crystalline) regions. This assignment was further confirmed by Nuclear Magnetic Resonance (NMR) methods [288][295].

A DMA spectrum of PP in the temperature range (-40-130)^{o}C is shown in Fig.9.8.

4.7 Polymeric Cellular Materials

A cellular material or foam is a two-phase structure in which a fluid (in man-made foams it is typically a gas) has been introduced through a continuous solid phase [15][280][296]. The mechanical response of a polymeric foam is determined by the properties of the polymer from which it is made as well as by its cellular structure.

The properties of polymeric materials (polypropylene) have been described in previous sections. The cellular structure and the paramenters used in its modelling are presented in this section.

One of the most relevant properties of a foam is the ratio between its density, ρ_f and the density of the solid phase, ρ_s,

$$\rho = \frac{\rho_f}{\rho_s} \tag{4.92}$$

which is known as *relative density* [280][15]. The volume fractions ϕ_g (sometimes referred to as *porosity*) and ϕ_s of the gas and the solid phases respectively are given by:

$$\phi_s = \frac{V_s}{V_t} = \approx \frac{\rho_f}{\rho_s} = \rho \tag{4.93}$$

$$\phi_g = \frac{V_g}{V_t} \approx 1 - \frac{\rho_f}{\rho_s} \tag{4.94}$$

where V_s and V_g are the volumes of the solid and gas phases respectively and V_t is the total volume.

It is clear that, as the relative density increases, the thickness of the cell walls increases with respect to the pore space. A value of $\rho \sim 0.3$ is usually taken as the upper limit between a foam and a material which must be viewed more like a solid with isolated pores [15].

Another important parameter associated with the cellular structure is the kind of cell (open or closed). In *open-cell* foams, the cells connect through open faces while in *closed-cell*, the walls are solid and all cells are sealed-off from their neighbours [15].

Other parameters are also of interest in the characterization of cellular structures and are relevant in their mechanical properties. Among the most relevant are the average cell size as well as the cell size distribution and dispersion, the average wall thickness and the anisotropy of the cellular structure [280][15].

Polymeric foams are usually found to be anisotropic due mainly to the cell shape anisotropy [297][14]. This anisotropy may result either as a consequence of the foaming process [280] or may be introduced *ad hoc* by a separate process, *e.g.*, biaxial stretching [298][299]. Anisotropy of the cellular structure influences the mechanical response more strongly than the cell size and cell size distribution and dipersion [15]. The anisotropy can be characterized by the so-called *shape anisotropy ratios*, defined as [300][297][15]:

$$R_{ki} = \frac{\bar{R}_k}{\bar{R}_i} \tag{4.95}$$

where $\bar{R}_k$ is the average cell size measured in the largest principal dimension.

It is worth mentioning that an anisotropy ratio $R_{ki} = 1.2$ may increase the stiffness in the $\vec{x}_k$ direction by a factor of two with respect to that in the $\vec{x}_i$ direction [15].

4.7.1 DEFORMATION MECHANISMS IN CELLULAR MATERIALS

A typical strain-stress curve of a closed-cell foam under a compressive ramp stress function is shown in Fig.4.3. It presents three clearly differentiated behaviour regimes.

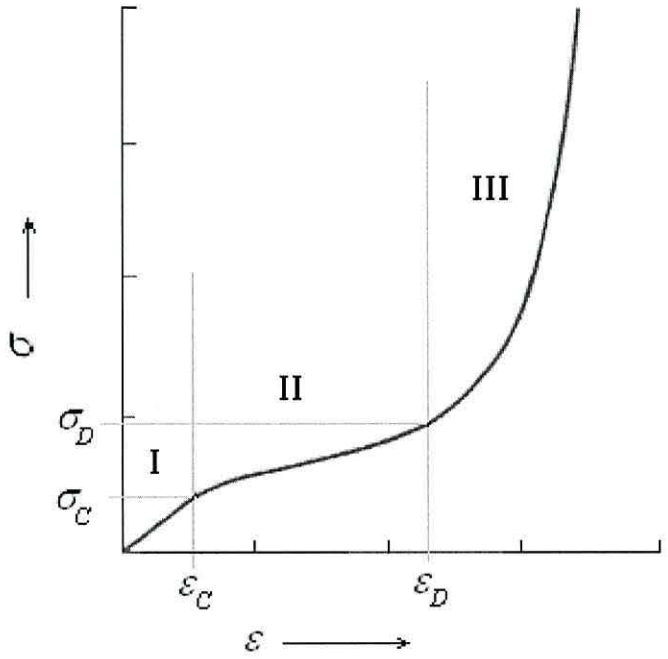

Figure 4.3: Typical strain-stress curve for a closed-cell polymer foam. The different regimes are shown in roman numbers, I) linear II) non-linear and III) densification. ϵ and σ represent the strain and stress respectively.

Linear Zone. Elastic Bending

At low values of the strain (typically around 3 to 5%), the response is linear. For closed-cell foams the involved mechanisms are cell wall bending (Fig.4.4 a)) [14][301][302][303] [304] and the expansion, contraction and the stretching of the faces that form the cell [14] [302][305][306][307][308][309]. In addition, if the enclosed gas does not diffuse out of the cells, it increases the foam stiffness [14][306][310][311][312][313][314].

Non-linear zone. Buckling

As the strain increases, the cellular structure collapses making further deformation depend mainly on the response of the gas enclosed. The elastic collapse of the foam is due to the elastic buckling of the cell walls (Fig.4.4 b)) [315][303][316][317][14][308][302][305] [318][311][312][313][314]. The stress and strain at which the collapse starts are called respectively *elastic collapse stress*, σ_c and *elastic collapse strain*, ϵ_c.

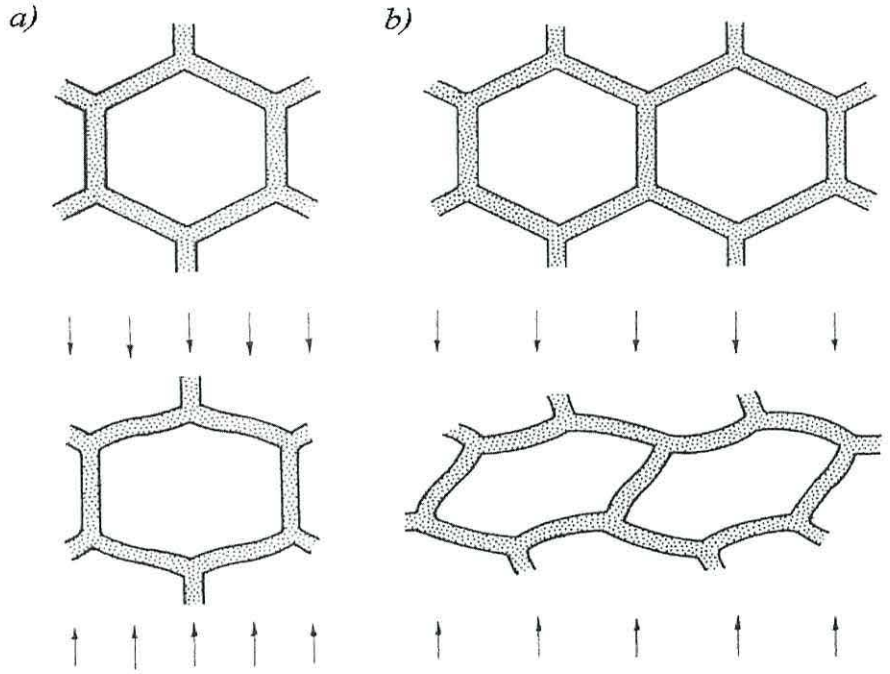

Figure 4.4: Two-dimensional representation of the cell deformation under a) elastic bending and b) elastic buckling. From [14].

Providing that there is no gas diffusion, the effect of the gas in the mechanical response of the foam can be estimated. For a sample that is compressed in a particular direction, the volume decreases from V^0 to:

$$V_1 = V^0 - V^0\epsilon. \tag{4.96}$$

On the other hand, the sample expands in the other two directions which implies an increase of volume given by:

$$V_2 = V^0 + V^0(\nu_{31}\epsilon + \nu_{32}\epsilon) \tag{4.97}$$

where ν_{i1} is the Poisson's coefficient defined in equation 4.42. Typically:

$$\nu_{31} = \nu_{32} \equiv \nu \tag{4.98}$$

so that we can write:

$$V_2 = V^0 + V^0(2\nu\epsilon). \tag{4.99}$$

Thus, the volume after compressing the sample is given by:

$$V = V^0 + V_1 + V_2 = V^0(1 - \epsilon(1 - 2\nu)) \tag{4.100}$$

and the volume occupied by the gas by:

$$V_g = V - V_s. \tag{4.101}$$

Now, assuming that the polymer is not compressed, the volume occupied by the solid is:

$$V_s \approx V\frac{\rho}{\rho_s}. \tag{4.102}$$

Therefore, we have, for the volume occupied by the gas:

$$V_g = V - V_s = V^0(1 - \epsilon(1 - 2\nu)) - \frac{\rho}{\rho_s} \tag{4.103}$$

and for the volume occupied by the gas at the initial state:

$$V_g^0 = V^0(1 - \frac{\rho}{\rho_s}). \tag{4.104}$$

Considering the gas as ideal, we can write, from equations 4.103 and 4.104:[8]

$$\frac{V_g^0}{V_g} = \frac{1 - \frac{\rho}{\rho_s}}{1 - \epsilon(1 - 2\nu) - \frac{\rho}{\rho_s}} = \frac{p}{p^0} \tag{4.105}$$

where p^0 and p are the gas pressures under uncompressed and compressed states re-

[8] Under compression, at all but high rates of strain ($\dot{\epsilon} > 100/s$), the gas can be supposed to be under isothermal conditions because it is is contact with the polymer whose thermal capacitance (see Table 2.5) is much higher than that of the gas [319]. An ideal gas under isothermal conditions follows Boyle's Law.

spectively.

Therefore, the pressure that the load must overcome is:

$$p' = p - p^0 = \frac{p^0\epsilon(1-2\nu)}{1-\frac{\rho}{\rho_s}-\epsilon(1-2\nu)} = \frac{p^0\epsilon(1-2\nu)}{\phi_g-\epsilon(1-2\nu)} \approx \frac{p^0\epsilon(1-2\nu)}{\phi_g-\epsilon}. \tag{4.106}$$

Hence, a representation of the stress, σ, versus the so-called *volumetric strain*, $\epsilon/(\phi_g-\epsilon)$, gives a straight line whose slope equals the so-called *effective pressure* of the gas, $p^0(1-2\nu)$. Finally, since p^0 is usually atmospheric pressure, the Poisson's coefficient can be calculated.

Densification

Finally, at high values of the strain, the sample eventually becomes highly compacted and the main part of the stress is sustained by the polymer itself [15]. Then, the slope of the curve (zone III in Fig.4.3) tends to the Young's modulus of the solid, Y_s, as the strain tends to unity. The so-called *densification strain*, ϵ_D, at which densification starts does not equal the porosity as it might seem. However, ϵ_D has been experimentally found to be given by [320]:

$$\epsilon_D = 1 - 1.4\left(\frac{\rho}{\rho_s}\right). \tag{4.107}$$

Chapter 5

PIEZOELECTRICITY

5.1 HISTORICAL OVERVIEW

Production of electric effects by pressure was first suggested by Becquerel (1788-1878) [321]. Previous work of Curie (J.) under the direction of Friedel on pyroelectricity laid the foundation for his further work together with his brother Pierre (1859-1906) with crystals of zinc blende, sodium chlorate, boracite, tourmaline, quartz, calamine, topaz, sugar and Rochelle salt (tartaric acid). By compressing a thin plate cut perpendicular to a binary axis in quartz or perpendicular to the ternary axis in tourmaline, onto the two faces of which two thin sheets of conductive materials were fastened, acquired equal but opposite polarity charges. The quantity of charge (measured with the help of a Kelvin electrometer) was proportional to the exerted pressure [322]. Thus the so-called *direct piezoelectric effect* had been discovered. Curie's results were presented at the Meeting of the Societe Mineralogique de France on 8 April 1880 [323] and at the Academie des Sciences during the Meeting of 24 August the same year [324]. They announced their discovery with the following words [325]:

> *Those crystals having one or more axes whose ends are unlike, that is to say hemihedral crystals with oblique faces, have the special physical property of giving rise to two electric poles of opposite signs at the extremities of these axes when they are subjected to a change in temperature: this is the*

phenomenon known under the name of pyroelectricity.

We have found a new method for the development of polar electricity in these same crystals, consisting in subjecting them to variations in pressure along their hemihedral axes.

A year after, Hankel [326][327] coined the term *piezoelectricity* and Lippman [328], from thermodynamic considerations, theoretically proved the so-called *converse* or *inverse piezoelectric effect*, namely, the mechanical deformation of crystals subjected to an electric field. The inverse effect was demonstrated experimentally by the Curie brothers [329][330] almost a year after Lippmann's suggestion.

In successive papers, the Curie brothers reported further experiments on quartz and tourmaline and suggested some laboratory experiments that could use the piezoelectric effect for measuring forces or pressures and high voltages. The most famous device, the *quartz piezoelectrique*, was used years later by Curie (M.) [331] in her later work on radioactivity.

During the following fifteen years, many physicists worked to interpret the piezoelectric effect and to construct an exact theory on the basis of thermodynamic principles. In 1893, Lord Kelvin developed an atomic model to describe the piezoelectric effect [332][333]. Kelvin estimated the experimentally observed magnitude of the piezoelectric effect of quartz by postulating that it results from the displacement of the centre of gravity of positive ions (detailed description of this model can be found in [334]). More accurate calculations were performed by Gibbs [335] for α-quartz and by Jaffe [336] for zinc blende in good agreement with experimental values.

Based on Kelvin's model, the phenomenology of piezoelectricity was improved by Duhem and Pockels [337]. However, it was Voigt (1850-1919) [338][339] who published the first complete and rigorous formulation of piezoelectricity and eight years later, in another publication on piezo and pyroelectricity [340], he introduced the term *tensor* into the vocabulary of mathematical physics.

In 1914, Langevin (1872-1946) commenced work on a method for detecting submerged enemy submarines using ultrasonic waves as suggested by Lord Rayleigh and Richardson two years before. In less than three years Langevin succeeded in obtaining adequate amplification using the piezoelectric properties of a quartz crystal clamped between steel electrodes [341]. Langevin's device was called the *Langevin Sandwich* by his group [342].

In 1921, Valasek [343] discovered ferroelectricity in an investigation on Rochelle salt. From observations of the piezoelectric properties of Rochelle-salt crystal plates used in underwater signalling, Cady noted some peculiarities in the electric behaviour in the neighbourhood of frequencies corresponding to mechanical resonances. He reported the first resonator in 1921 [344]. Two years later, Cady [345] and Pierce [346] independently of each other, used piezoelectric resonators for the frequency stabilization of high frequency oscillators. After Cady's work, studies of the crystal resonators in terms of mechanical parameters and electrical circuits were undertaken by Van Dyke [347], Dye [348] and Mason [349].

In the 1940's, piezoelectric properties of amorphous and polycrystalline materials predicted by Shubnikov were experimentally confirmed, among others, by Roberts [350] and von Hippel *et al.* [351]. These discoveries initiated a major research effort into the piezoelectric properties of ferroelectric ceramics and their applications. In the late 1940's, the phenomenological description of piezoelectric and other properties of ferroelectrics were developed by Ginzburg [352] and Devonshire [353].

In the early 1950's Jaffe *et al.* [354] discovered a strong piezoelectric effect in solid solutions of lead zirconate titanate (PZT). In 1950, Bazhenov [355] *et al.* observed piezoelectric effects in wood and in 1953 Yasuda *et al.* [356] reported electromechanical effects in bone. Quantitative analysis of the shear piezoelectricity of wood, bone and tendon was performed by Fukada [357] in 1955 and Fukada *et al.* [358] in 1957 respectively. After these preliminary studies many biopolymers have been shown to display shear piezoelectricity as shown in Table 5.1 [23].

		$-d_{31}$ (pCN^{-1})
Polysaccharides		
	wood	0.1
	ramie	0.2
Chitin		
	crab shell	0.2
	lobster apodem	1.5
Amilose		
	starch	2.0
Proteins		
	bone	0.2
	tendon	2.0
	skin	0.2
	wool	0.1
	horn	1.8

Table 5.1: Shear piezoelectric coefficients of biopolymers. From [23].

The early work in polymers, led to the finding of strong piezo- and pyroelectric properties of uniaxially-drawn and poled polyvinylidene fluoride (PVDF) in 1969 by Kaway [71] and Bergman *et al.* in 1971 [359]. Since then, piezoelectricity has been reported in several poled and drawn polymers. Some of them are listed in Table 5.2 [24].

A quasi-piezoelectric effect in non-polar, mechanically non-uniform electrets was theoretically predicted in the early 1970's [360][361]. This effect [362] as well as the pyroelectric effect [363] was soon observed in PP.

Some materials based on the above effect were developed afterwards. In the mid 1980's foamed PP films with high piezoelectric constants were invented in Finland (see Chapter 6). Layered sandwiches of polymers with different Young's moduli were developed in Poland in the mid 1990's [364][365] and have also been proved to show high piezoelectric constants. Around the same time, porous polytetrafluoroethylene (PTFE) with strong electret properties and high piezoelectric coefficients was developed in China [366] [367]. In the 1990's, the piezoelectric properties of metal electrode

	$-d_{31}$ (pCN^{-1})	k_{33}	p_3 $(\mu C/m^2K)$
PVDF	30	0.2	35
VDF/ TrFE	30	0.3	50
VDF/TeFE	30	0.25	35
VDCN/VAc	8	0.25	20
Nylon 11	4		5
PVC	0.3		1

Table 5.2: Piezo and pyroelectric properties of some synthetic polymers. From [24].

interfaces [368][369] and double layers located at interfaces [370] were studied by Lewis and coworkers.

5.2 THERMODYNAMIC RELATIONS AND PIEZOELECTRIC COEFFICIENTS

5.2.1 INTERNAL ENERGY

Using equations 3.23 and 4.38 the internal energy of a dielectric elastic material can be written:

$$dU = T_i dS_i + E_m dD_m - \theta d\sigma \qquad i = 1 \ldots 6 \; ; \; m = 1 \ldots 3 \tag{5.1}$$

where θ and σ are temperature and entropy respectively. For simplicity, we will consider the adiabatic and isothermal cases[1]. With this assumption:

$$dU = T_i dS_i + E_m dD_m \qquad i = 1 \ldots 6 \; ; \; m = 1 \ldots 3. \tag{5.2}$$

[1] The difference between adiabatic and isothermal constants have been shown to be small [371][28].

Other thermodynamic potentials are given in Table 5.3. Since dU is a perfect differential, we have from the Schwartz condition for exact differentials,

$$-h_{mi} = \left(\frac{\partial T_i}{\partial D_m}\right)_S = \left(\frac{\partial S_j}{\partial E_m}\right)_D . \tag{5.3}$$

Furthermore, the independent variables E_m and T_i can be expressed as a functions of their components as:

$$T_i = \left(\frac{\partial T_i}{\partial S_j}\right)_D dS_j + \left(\frac{\partial T_i}{\partial D_m}\right)_S dD_m \tag{5.4}$$

and

$$E_m = \left(\frac{\partial E_m}{\partial S_i}\right)_D dS_i + \left(\frac{\partial E_m}{\partial D_m}\right)_S dD_m. \tag{5.5}$$

Considering the coefficients defined in equations 5.3, the dielectric permittivity and elastic coefficients defined in equations 3.22 and 4.36 respectively, equations 5.4 and 5.5 above can be expressed as:

$$dT_i = c_{ij}^D dS_j - h_{im}^D dD_m \tag{5.6}$$

$$dE_m = -h_{mi}^D dS_i + \beta_{mi}^S dD_m. \tag{5.7}$$

Now, under linear approximation, T_i and E_m are homogeneous functions of the independent variables (S_j, D_m). Therefore, from Euler's theorem for homogeneous functions (see for instance [372]):

$$T_i = c_{ij}^D S_j - h_{im}^D D_m \tag{5.8}$$

$$E_m = -h_{mi}^D S_i - h_{im}^D D_m. \tag{5.9}$$

From the Gibbs function $G(T_i, E_m)$ (Table 5.3), it is possible to derive the piezoelectric equations equivalent to equations 5.8 and 5.9 with stress and electric field

Thermodynamic Potential	*Exact Differential*
Internal Energy $U(S_i, D_m)$	$dU = T_i dS_i + E_m dD_m$
Enthalphy $H(T_i, E_m)$	$dH = -S_i dT_i - D_m dE_m$
Elastic Enthalpy $H_{elas}(T_i, D_m)$	$dH_{elas} = -S_i dT_i + E_m dD_m$
Electric Enthalphy $H_{elec}(S_i, E_m)$	$dH_{elec} = T_i dS_i - D_m dE_m$
Gibbs Free Energy $G(T_i, E_m)$	$dG = -S_i dT_i - D_m dE_m$
Elastic Gibbs Free Energy $G_{elas}(T_i, D_m)$	$dG_{elas} = -S_i dT_i + E_m dD_m$
Electric Gibbs Free Energy $G_{elec}(S_i, E_m)$	$dG_{elec} = T_i dS_i - D_m dE_m$

Table 5.3: Exact differentials for different thermodynamic potentials.

components T_i and E_m. Hence,

$$d_{mi} = \left(\frac{\partial D_m}{\partial T_i}\right)_S = \left(\frac{\partial S_i}{\partial E_m}\right)_T \tag{5.10}$$

in terms of which, the linear piezoelectric equations are written as:

$$S_i = s_{ij}^E T_j + d_{mi} E_m \tag{5.11}$$

$$D_m = d_{mi} T_i + \varepsilon_{mk}^T E_k. \tag{5.12}$$

Finally, by choosing the appropriate thermodynamical potential in Table 5.3, the corresponding piezoelectric equations for the sets S, E and T, D are obtained, which are respectively given by:

$$T_i = c_{ij}^E S_j + e_{mi} E_m \tag{5.13}$$

$$D_m = e_{mi} T_i + \varepsilon_{mk}^T E_k \tag{5.14}$$

and:

$$S_i = s_{ij}^E T_j + g_{mi} E_m \tag{5.15}$$

$$E_m = -g_{mi} T_i + \beta_{mk}^T E_k \tag{5.16}$$

where:

$$g_{mi}^D = \left(-\frac{\partial E_m}{\partial T_i}\right)_D = \left(\frac{\partial S_i}{\partial D_m}\right)_T \tag{5.17}$$

$$e_{im}^S = \left(-\frac{\partial T_i}{\partial E_m}\right)_S = \left(\frac{\partial D_m}{\partial S_i}\right)_E . \tag{5.18}$$

5.3 Electromechanical Coupling Factors

The electromechanical coupling factor is a measure of the extension of the coupling between mechanical and electrical energy. The internal energy is given by equation 5.2 and, taking into account that U is an extensive function whose natural variables S and D are also extensive, then U is an homogeneous function of degree 1 so that, by virtue of Euler's theorem, U is given by:

$$U = \frac{1}{2} S_i T_i + \frac{1}{2} E_m D_m \qquad i = 1 \ldots 6 \; ; \; m = 1 \ldots 3. \tag{5.19}$$

Using equations 5.4 and 5.5 then leads to the expansion

$$U = \overbrace{\frac{1}{2} T_i s_{ij}^E T_j}^{U_{mechanical}} + \overbrace{\frac{1}{2} T_i d_{mi} E_m + \frac{1}{2} E_m d_{mi} T_i}^{U_{el-mec}} + \overbrace{\frac{1}{2} E_m \varepsilon_{mk}^T}^{U_{el}} . \tag{5.20}$$

The electromechanical factor is defined as:

$$k_{mi} = \frac{U_{el-mec}}{\sqrt{U_{el} U_{mec}}} = \frac{(E_m d_{mi} T_i)}{1/2 \sqrt{T_i s_{ij}^E E_m \varepsilon_{mk}^k}} . \tag{5.21}$$

Electromechanical coupling factors are much better than elastic, mechanical and

	$-d_{31}$ (pCN^{-1})	d_{33} (pCN^{-1})	k_{31}	k_{33}
$BaTiO_3$	79	190	0.21	0.49
PZT A	119	268	0.33	0.68
PZT B	234	480	0.39	0.72
$LiNbO_3$	85	6	0.02	0.17
$LiTaO_3$	3.0	5.7	0.07	0.14
$PbTiO_3$	7.4	47	0.052	0.35

Table 5.4: Typical values of piezoelectric properties of some piezoelectric ceramics and crystals [25].

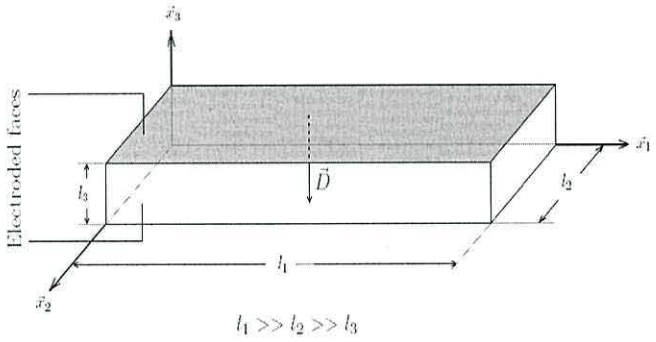

Figure 5.1: Resonator geometry and polarisation for the study of the resonance modes.

piezoelectric coefficients for characterizing the sample in power transduction. Electromechanical coupling factors and piezoelectric coefficients for typical piezoelectric polymers and ceramics are shown in Tables 5.2 and 5.4 respectively.

5.4 Piezoelectric Resonator

Electromechanical vibrations of piezoelectric bodies can be easily obtained under some approximations.

5.4.1 Thickness Mode

Given that $l_3 << l_2 < l_1$ (Fig. 5.1), the sample can be considered as mechanically clamped in the directions $\vec{x}_1$ and $\vec{x}_2$ and therefore, the strain tensor components (equation 4.33) are:

$$S_3 = \frac{\partial h_3}{\partial x_3} \tag{5.22}$$

$$S_i \approx 0 \qquad \forall i \neq 3. \tag{5.23}$$

In addition, by neglecting boundary effects, we can write:

$$D_i \approx 0 \qquad \forall i \neq 3 \tag{5.24}$$

and the non-vanishing component of the dielectric displacement in a dielectrically homogeneous medium is:

$$\frac{\partial D_3}{\partial x_3} = 0. \tag{5.25}$$

Under these conditions, equations 5.8 and 5.9 reduce to:

$$T_3 = c_{33} S_3 - h_{33} D_3 \tag{5.26}$$

$$E_3 = -h_{33} S_3 + \beta_{33} D_3. \tag{5.27}$$

On the other hand, the equation of motion (equation 4.39) and electromechanical coupling factor k_{33} (equation 5.21) are respectively:

$$\rho \frac{\partial^2 h_3}{\partial t^2} = \frac{\partial T_3}{\partial x_3} \tag{5.28}$$

and

$$k_{33} = \frac{d_{33}}{\sqrt{\varepsilon_{33}^T s_{33}^D}}. \tag{5.29}$$

From equations 5.22, 5.26 and 5.28 we can write:

$$\frac{\partial^2 h_3}{\partial t^2} = \frac{c_{33}^D}{\rho}\frac{\partial^2 h_3}{\partial x_3^2} \tag{5.30}$$

which, in the time-harmonic case

$$h_3(x_3, t) = \chi(x_3)e^{-\imath\omega t} \tag{5.31}$$

transforms into:

$$-\omega^2 \frac{\rho}{c_{33}^D}\chi = \frac{d^2\chi}{dx_3^2}. \tag{5.32}$$

The homogeneous solution of the equation above is given by:

$$\chi_3 = A' exp(\frac{\imath\omega x_3}{v_3}) + B' exp(-\frac{\imath\omega x_3}{v_3}) = A\cos\left(\frac{\omega x_3}{v_3}\right) + B\sin\left(\frac{\omega x_3}{v_3}\right) \tag{5.33}$$

where (see equation 4.87):

$$v_3 = \sqrt{\frac{c_{33}^D}{\rho}}. \tag{5.34}$$

is the sound velocity.

From equations 5.22, 5.31 and 5.34

$$S_3 = -\frac{\omega}{v_3}A\sin\left(\frac{\omega x_3}{v_3}\right) + \frac{\omega}{v_3}B\cos\left(\frac{\omega x_3}{v_3}\right) \tag{5.35}$$

which, when introduced into equation 5.26 gives:

$$T_3 = \frac{c_{33}^D\omega}{v_3}\left[B\cos\left(\frac{\omega x_3}{v_3}\right) - A\sin\left(\frac{\omega x_3}{v_3}\right)\right] - h_{33}D_3. \tag{5.36}$$

The boundary conditions for T_3 for a free resonator are given by:

$$T(x_3 = 0) = B\frac{c_{33}^D \omega}{v_3} - h_{33}D_3 = 0 \tag{5.37}$$

and then:

$$B = \frac{h_{33}D_3 v_3}{c_{33}^D \omega}. \tag{5.38}$$

Moreover:

$$T_3(x_3 = l_3) = \frac{c_{33}^D \omega}{v_3}\left[\left(\frac{h_{33}D_3}{\omega c_{33}^D}\right)\cos\left(\frac{\omega l_3}{v_3}\right) - A\sin\left(\frac{\omega l_3}{v_3}\right)\right] - h_{33}D_3 \tag{5.39}$$

$$= h_{33}D_3\cos\left(\frac{\omega l_3}{v_3}\right) - \frac{Ac_{33}^D}{v_3}\sin\left(\frac{\omega l_3}{v_3}\right) - h_{33}D_3 \tag{5.40}$$

from which:

$$A = \frac{v_3 h_{33}D_3}{\omega c_{33}^D}B\left[\frac{\cos\left(\frac{\omega l_3}{v_3}\right) - 1}{\sin\left(\frac{\omega l_3}{v_3}\right)}\right]. \tag{5.41}$$

From the trigonometric relation:

$$\frac{1 - \cos x}{\sin x} = \tan\left(\frac{x}{2}\right) \tag{5.42}$$

equation 5.41 can be written as:

$$A = -B\tan\left(\frac{\omega l_3}{2v_3}\right). \tag{5.43}$$

Introducing equation 5.43 into equations 5.33 and 5.35 gives respectively:

$$\chi_3 = -B\tan\left(\frac{\omega l_3}{2v_3}\right)\cos\left(\frac{\omega x_3}{v_3}\right) + B\sin\left(\frac{\omega x_3}{v_3}\right) \tag{5.44}$$

$$S_3 = \frac{B\omega}{v_3}\tan\left(\frac{\omega l_3}{2v_3}\right)\sin\left(\frac{\omega x_3}{v_3}\right) + \frac{B\omega}{v_3}\cos\left(\frac{\omega x_3}{v_3}\right). \tag{5.45}$$

From equations 5.27 and 5.45:

$$E_3 = \tilde{B}\tan\left(\frac{\omega l_3}{2v_3}\right)\sin\left(\frac{\omega x_3}{v_3}\right) + \tilde{B}\cos\left(\frac{\omega x_3}{v_3}\right) + \beta_{33}D_3 \tag{5.46}$$

where:

$$\tilde{B} = \frac{\omega h_{33}B}{v_3}. \tag{5.47}$$

The potential across the sample is given by:

$$V(x_3) = \int_0^{l_3} E_3 dx_3 = \int_0^{l_3} \tilde{B}\tan\left(\frac{\omega l_3}{2v_3}\right)\sin\left(\frac{\omega x_3}{v_3}\right) dx_3 \tag{5.48}$$

$$+ \tilde{B}\int_0^{l_3}\cos\left(\frac{\omega x_3}{v_3}\right) dx_3 + \beta_{33}l_3D_3 \tag{5.49}$$

which, upon considering equations 5.38, 5.42 and 5.21, can be written as:

$$V_3(x_3) = \frac{h_{33}D_3l_3}{c_{33}^D}\left[1 + \tan^2\left(\frac{\omega l_3}{2v_3}\right)\right] + \beta_{33}D_3l_3 \tag{5.50}$$

$$= D_3l_3\beta_{33}\left[1 - k_{33}^2\frac{1 + \left[\tan\left(\frac{\omega l_3}{2v}\right)\right]^2}{\frac{\omega l_3}{v_3}}\right] \tag{5.51}$$

where, it has been assumed that, close to the resonance:

$$\frac{\omega l_3}{v_3} \approx \frac{\pi}{2} \quad \text{and} \quad \sin\left(\frac{\omega l_3}{v_3}\right) \approx 1. \tag{5.52}$$

Finally, assuming that:

$$1 + \left[\tan\left(\frac{\omega l_3}{2v_3}\right)\right]^2 \approx 2\tan\left(\frac{\omega l_3}{2v_3}\right) \tag{5.53}$$

equation 5.51 can be written as:

$$V_3 = \beta_{33} D_3 l_3 \left[1 - k_{33}^2 \frac{\tan\left(\frac{\omega l_3}{2v_3}\right)}{\frac{\omega l_3}{2v_3}} \right]. \tag{5.54}$$

The current flowing through the sample is (equations 3.49-3.52):

$$I = A_{12} \frac{dD_3}{dt} \tag{5.55}$$

where $A_{12} = l_1 l_2$. In the case of an harmonic oscillation $D_3 = D_0 e^{\imath\omega t}$ the above expression transforms to:

$$I = \imath\omega A_{12} D_3. \tag{5.56}$$

Now, introducing the *clamped capacitance* and *dielectric permittivity* C_c and ϵ_{33}^S, *i.e.*, the capacitance and permittivity far below the resonance:

$$C_c = \frac{A_{12}\varepsilon_{33}^S}{l_3} \tag{5.57}$$

and since this is a one-dimensional electric problem, the dielectric impermeability β_{33} is given by:

$$\beta_{33} = \frac{E_3}{D_3} = \varepsilon_{33}^{-1} \tag{5.58}$$

so that:

$$C_c = \frac{A_{12}}{\beta_{33} l_3}. \tag{5.59}$$

Finally, the electric impedance Z (section 3.7) is:

$$Z = \frac{1}{\imath\omega C_c} \left[1 - k_{33}^2 \frac{\tan\left(\frac{\omega l_3}{2v_3}\right)}{\frac{\omega l_3}{2v_3}} \right]. \tag{5.60}$$

5.4.2 Length Mode

Since $l_1 >> l_2 >> l_3$ and therefore $A_{23} = l_2 l_3 << A_{13} = l_1 l_3 << A_{12} = l_1 l_2$ then, in a first approximation

$$T_i \approx 0 \qquad \forall i \neq 1. \tag{5.61}$$

For the length mode, equations 5.11 and 5.12 are therefore the most appropiate since they reduce to:

$$S_1 = s_{11}^E T_1 + d_{31} E_3 \tag{5.62}$$

and:

$$D_3 = d_{31} T_1 + \varepsilon_{33} E_3. \tag{5.63}$$

The equation of motion (equation 4.39) is for this case:

$$\frac{\partial^2 h_1}{\partial t^2} = \frac{1}{\rho} \frac{\partial T_1}{\partial x_1} \tag{5.64}$$

which, in conjunction with equation 5.62 and considering that $E_3 \neq f(x_1)$, gives:

$$\frac{\partial^2 h_1}{\partial t^2} = \frac{1}{\rho s_{11}^E} \frac{\partial S_1}{\partial x_1} = \left(v_1^E\right)^2 \frac{\partial S_1}{\partial x_1} \tag{5.65}$$

where:

$$v_1^E = \sqrt{\frac{1}{s_{11}\rho}}. \tag{5.66}$$

In the unidimensional approach here (see equation 4.51), the above equation can be written as:

$$v_1^E = \sqrt{\frac{c_{11}}{\rho}} = \sqrt{\frac{Y_1}{\rho}} \tag{5.67}$$

which is (see equation 4.87) the actual velocity of sound in length mode.

Now, for the harmonic oscillation,

$$h_1(x_1, t) = \chi_1 e^{i\omega t} \tag{5.68}$$

equation 5.65 transforms into:

$$\omega^2 \chi_1 = v_1^E \frac{d^2 \chi_1}{dx_1^2} \tag{5.69}$$

whose general solution is of the form:

$$h_1 = A \sin\left(\frac{\omega x_1}{v_1^E}\right) + B \cos\left(\frac{\omega x_1}{v_1^E}\right). \tag{5.70}$$

From equation 5.70 we deduce that:

$$S_1 = \frac{\partial \chi_1}{\partial x_1} = \frac{A\omega}{v_1^E} \cos\left(\frac{\omega x_1}{v_1^E}\right) - \frac{B\omega}{v_1^E} \sin\left(\frac{\omega x_1}{v_1^E}\right) \tag{5.71}$$

which, applied at the boundaries gives:

$$S_1(x_1 = 0) = \frac{A\omega}{v_1^E} = s_{11}^E \overbrace{T_1(x_1 = 0)}^{=0} + d_{31} \overbrace{E(x_1 = 0)}^{=E_3} = d_{31} E_3. \tag{5.72}$$

Hence,

$$A = \frac{v_1^E}{d_{31} E_3} \omega. \tag{5.73}$$

On the other surface:

$$S_1(x_1 = l_1) = \frac{A\omega}{v_1^E} \cos\left(\frac{\omega l_1}{v_1^E}\right) - \frac{B\omega}{v_1^E} \sin\left(\frac{\omega l_1}{v_1^E}\right) \tag{5.74}$$

from which, using equation 5.42:

$$B = -\frac{d_{31} E_3 v_1^E}{\omega} \tan\left(\frac{\omega l_1}{2 v_1^E}\right). \tag{5.75}$$

Substituing equation 5.73 and 5.75 into 5.72:

$$S_1 = d_{31}E_3\left[\cos\left(\frac{\omega x_1}{v_1^E}\right) + \tan\left(\frac{\omega l_1}{2v_1^E}\right)\sin\left(\frac{\omega x_1}{v_1^E}\right)\right] \tag{5.76}$$

which inserted into equation 5.62 gives:

$$T_1 = \frac{d_{31}E_3}{s_{11}^E}\left[\cos\left(\frac{\omega x_1}{v_1^E}\right) + \tan\left(\frac{\omega l_1}{2v_1^E}\right)\sin\left(\frac{\omega x_1}{v_1^E}\right)\right] - \frac{d_{31}}{s_{11}^E}E_3. \tag{5.77}$$

Introducing equation 5.77 into equation 5.63 we have:

$$D_3 = \frac{d_{31}^2E_3}{s_{11}^E}\left[\cos\left(\frac{\omega x_1}{v_1^E}\right) + \tan\left(\frac{\omega l_1}{2v_1^E}\right)\sin\left(\frac{\omega x_1}{v_1^E}\right) - 1\right] + \varepsilon_{33}^T E_3. \tag{5.78}$$

For an harmonic excitation $E_3 = E_0e^{\imath\omega t}$ we have:

$$\frac{dD_3}{dt} = \imath\omega E_3\varepsilon_{33}^T\left[\frac{d_{31}^2}{s_{11}^E\varepsilon_{33}^T}\left(\cos\left(\frac{\omega x_1}{v_1^E}\right) + \tan\left(\frac{\omega l_1}{2v_1^E}\right)\sin\left(\frac{\omega x_1}{v_1^E}\right) - 1\right) + 1\right] \tag{5.79}$$

so that the current flowing in the direction $\vec{x}_1$is given by:

$$I = \int_0^{l_2}\int_0^{l_1}\frac{dD_3}{dt}dx_1dx_2. \tag{5.80}$$

In view of equation 5.24 and considering equation 5.21 we can write

$$I = \imath\omega l_2E_3\varepsilon_{33}^T\left[\frac{k_{31}^2v_1^E}{\omega}\sin\left(\frac{\omega l_1}{v_1^E}\right)\left[1 + \left[\tan\left(\frac{\omega l_1}{2v_1^E}\right)\right]^2\right] - k_{31}^2 + 1\right] \tag{5.81}$$

where

$$k_{31} = \frac{d_{31}}{\sqrt{s_{11}^E\varepsilon_{33}^T}}. \tag{5.82}$$

Equation 5.81 close to the resonance (see equation ??) simplifies to:

$$I = \imath\omega l_2 E_3 \varepsilon_{33}^T \left[1 - k_{31}^2 + k_{31}^2 \frac{\tan\left(\frac{\omega l_1}{2v_1^E}\right)}{\left(\frac{\omega l_1}{2v_1^E}\right)} \right]. \tag{5.83}$$

In addition, the potential V_1 across the sample in the direction $\vec{x}_1$ is:

$$V_1 = \int_0^{l_1} E_3 dl_1 = \int_0^{l_1} E_0 e^{\imath\omega t} dl_1 = l_1 E_3 \tag{5.84}$$

so that the admittance Y_1 (section 3.7) is:

$$Y_1 = \frac{\imath\omega l_1 l_2 \varepsilon_{33}}{l_3} \left[1 - k_{31}^2 + k_{31}^2 \frac{\tan\left(\frac{\omega l_1}{2v_1^E}\right)}{\frac{\omega l_1}{2v_1^E}} \right]. \tag{5.85}$$

WIDTH MODE

In the width mode we have to deal with the coupling equations:

$$S_1 = 0 = s_{11}^E + s_{12}^E T_2 + d_{31} E_3 \tag{5.86}$$

$$S_2 = s_{21}^E s_{22}^E T_2 + d_{32} E_3 \tag{5.87}$$

$$D_3 = d_{31} T_1 + d_{32} T_2 + \varepsilon^T E_3. \tag{5.88}$$

From equation 5.86:

$$T_1 = -\frac{s_{11}^E T_2}{s_{11}^E} - \frac{d_{31} E_3}{s_{11}^E} \tag{5.89}$$

which, susbtituted into equation 5.87 gives:

$$S_2 = s_{21}^E \left[\left(-\frac{s_{12}^E}{s_{11}^E} T_2 \right) - \frac{d_{31}}{s_{11}^E} E_3 \right] + s_{22}^E T_2 + d_{32} E_3 \tag{5.90}$$

$$= T_2 \overbrace{\left(s_{22}^E - \frac{s_{21}^E s_{12}^E}{s_{11}^E} \right)}^{\Phi} + E_3 \overbrace{\left(d_{32} - \frac{d_{31} s_{21}^E}{s_{11}^E} = \right)}^{\Theta} = \Phi T_2 + \Theta E_3 \tag{5.91}$$

from which:

$$T_2 = \frac{1}{\Phi} - \frac{\Theta}{\Phi} E_3. \tag{5.92}$$

Analogously as in the previous cases, the equation of motion is written as[2]

$$\frac{\partial^2 h_2}{\partial t^2} = \frac{1}{\rho\Phi}\frac{\partial^2 h_2}{\partial x_2^2} = \tilde{v}_2^E \frac{\partial^2 h_2}{\partial x_2^2} \tag{5.93}$$

whose particular solution for an harmonic oscillation $h_2 = \chi_2 e^{i\omega t}$ and after applying the boundary conditions is given by

$$\chi_2 = \left[\Theta E_3 \sin\left(\frac{\omega x_2}{\tilde{v}_2^E}\right) - \Phi E_3 \tan\left(\frac{\omega l_2}{2\tilde{v}_2^E}\right)\cos\left(\frac{\omega x_2}{2\tilde{v}_2^E}\right)\right]\frac{\tilde{v}_2^E}{\omega} \tag{5.94}$$

from which

$$S_2 = \frac{\partial \chi_2}{\partial x_2} = \Theta E_3 \left[\cos\left(\frac{\omega x_2}{\tilde{v}_2^E}\right) + \tan\left(\frac{\omega l_2}{2\tilde{v}_2^E}\right)\cos\left(\frac{\omega x_2}{\tilde{v}_2^E}\right)\right]. \tag{5.95}$$

Upon substituting into equation 5.91 we obtain

$$T_2 = \frac{\Theta}{\Phi} E_3 \left[\cos\left(\frac{\omega x_2}{\tilde{v}_2^E}\right) + \tan\left(\frac{\omega l_2}{2\tilde{v}_2^E}\right)\sin\left(\frac{\omega x_2}{\tilde{v}_2^E}\right)\right] - \frac{\Theta}{\Phi} E_3. \tag{5.96}$$

Now, under the assumption that the resonances are well-spaced in frequency, we can take for the expression of T_1 that given by equation 5.77. Therefore, from equations 5.77, 5.88 and 5.96

$$D_3 = \frac{d_{31}^2 E_3}{s_{11}^E}\left[\cos\left(\frac{\omega x_1}{v_1^E}\right) + \tan\left(\frac{\omega l_1}{2v_1^E}\right)\sin\left(\frac{\omega x_1}{v_1^E}\right) - 1\right] +$$

$$+\frac{d_{32}\Theta}{\Phi} E_3 \left[\cos\left(\frac{\omega x_2}{\tilde{v}_2^E}\right) + \tan\left(\frac{\omega l_2}{2\tilde{v}_2^E}\right)\sin\left(\frac{\omega x_2}{\tilde{v}_2^E}\right) - 1\right] + \varepsilon_{33}^T E_3$$

[2]The symbol $\tilde{v}_2^E$ is used in analogy with the notation in the previous cases. However, it must be noted that $\tilde{v}_2^E$ is not the velocity of sound.

$$= \varepsilon_{33}^{T}\Big[k_{31}\Big(\cos(\frac{\omega x_1}{v_1^E}) + \tan(\frac{\omega l_1}{2v_1^E})\sin(\frac{\omega x_1}{v_1^E}) - 1\Big) + \\ + \frac{d_{32}\Theta}{\Phi}\left(\cos\left(\frac{\omega x_2}{\tilde{v}_2^E}\right) + \tan\left(\frac{\omega l_2}{2\tilde{v}_2^E}\right)\sin\left(\frac{\omega x_2}{\tilde{v}_2^E}\right) - 1\right) + 1\Big]. \tag{5.97}$$

The total current for an harmonic oscillation $E_3(x_3, t) = E_0 e^{\imath\omega t}$ is after solving the integral:

$$I = \int_0^{l_1}\int_0^{l_2}\frac{dD_3}{dt}dx_1dx_2 = \imath\omega\varepsilon_{33}^{T}E_3 l_1 l_2\left[1 - k_{31}^2 + k_{31}^2\frac{\tan\left(\frac{\omega l_1}{2v_1^E}\right)}{\frac{\omega v_1^E}{2v_1^E}}\right]\cdot$$

$$\cdot\left[1 - \tilde{k}_{32}^2 + k_{32}^2\frac{\tan\left(\frac{\omega l_2}{2\tilde{v}_2^E}\right)}{\frac{\omega l_2}{2\tilde{v}_2^E}}\right]$$

where:

$$\tilde{k}_{32} = \frac{k_{32}}{1 - k_{31}^2 + k_{31}^2\frac{\tan\left(\frac{\omega l_1}{2v_1^E}\right)}{\frac{\omega l_1}{2v_1^E}}} \tag{5.98}$$

and:

$$k_{32} = \frac{d_{32}}{\sqrt{s_{22}^E\varepsilon_{33}^T}}. \tag{5.99}$$

Under the assumption that $v_1^E \approx \tilde{v}_2^E$ then

$$\tilde{k}_{32} \approx \frac{k_{32}}{1 - k_{31}^2 + k_{31}^2\frac{\tan\left[\frac{l_1}{l_2}\left(\frac{\omega l_2}{2\tilde{v}_2^E}\right)\right]}{\frac{\omega l_1}{2v_1^E}}} \tag{5.100}$$

and, if

$$\frac{l_1}{l_2} \approx 8 \tag{5.101}$$

we can write

$$\tan\left[\frac{l_1}{l_2}\left(\frac{\omega l_2}{2\tilde{v}_2^E}\right)\right] \approx 0. \tag{5.102}$$

Then

$$\tilde{k}_{32} = \frac{k_{32}}{1 - k_{31}^2} \tag{5.103}$$

which, for low electromechanical coupling k_{31}, can be approximated to:

$$\tilde{k}_{32} \approx k_{32}. \tag{5.104}$$

Now, the potential across the sample can be taken from equation 5.54 and from equation 3.74, the complex capacitance of the sample can be written as:[3]

$$\tilde{C} = \imath\omega\tilde{C}^S \frac{\left[1 - k_{31}^2 + k_{31}^2 \frac{\tan A_1}{A_1}\right]\left[1 - \tilde{k}_{32}^2 + \tilde{k}_{32}^2 \frac{\tan A_2}{A_2}\right]}{1 - k_{33}^2 \frac{\tan A_3}{A_3}} \tag{5.106}$$

where:

$$A_i = \frac{\omega l_i}{2v_i^E} \qquad i = 1, 3 \tag{5.107}$$

$$A_2 = \frac{\omega l_2}{2\tilde{v}_2^E} \tag{5.108}$$

and $\tilde{C}^S$ is the so-called *clamped capacitance*, *i.e.*, the capacitance well below any resonance.

Mechanical resonance and antiresonance occur at the zeros of the susceptance, however, in the approximation of low mechanical losses, they are coincident with the poles of the admittance for length and width modes and the zero of the impedance for the thickness mode. Thus, the resonance and antiresonance frequencies, f_r and f_a, are

[3] We assume that ε_{33}^T and ε_{33}^S are interchangeable. In fact, their exact relation is [28]:

$$\varepsilon_{33}^S = \varepsilon_{33}^T \left(1 - k_{31}^2\right) \tag{5.105}$$

so that the approximation corresponds to the low electromechanical coupling case where $k_{31} \sim 0$.

given by:

$$f_r^1 = \frac{v_1}{2l_1} \tag{5.109}$$

$$f_r^2 = \frac{v_2}{2l_2} \tag{5.110}$$

and:

$$f_a^3 = \frac{v_3}{2l_3}. \tag{5.111}$$

The above treatment has been performed on the assumption of perfectly elastic material. However, the mechanical losses (viscoelastic character) of a material can be formally accounted for by the introduction of an imaginary term in the (complex) sound velocity (section 4.5.2).

5.4.3 One-Side Clamped Thickness-Mode Resonator

The one-side thickness-mode resonator parameters are very helpful when we are interested only in the thickness-mode properties. For a resonator clamped on one side, lateral vibrations are impeded. In addition, since the acoustic wavelength is four times the thickness, the antiresonance frequency is reduced by a factor of two by mechanical clamping [373], i.e.,

$$f_a = \frac{v_3}{4l_3}. \tag{5.112}$$

Chapter 6

Foamed Polypropylene Electromechanical Film (EMFi)

6.1 Introduction

Electromechanical films (EMFi) of foamed polypropylene were developed almost two decades ago by VTT Chemical Technology (Finland) [374][375]. Cellular PP films were created by high-pressure autoclave treatment of chalk-loaded ($CaCO_3$) PP which was subsequently extruded, cooled to the crystallization temperature, heated to the orientation temperature and biaxially oriented [298][299]. The resulting films have a three-layer structure so that the few micron thick surface layers are smooth and homogeneous, but the dominant, thicker mid-section is full of flat voids separated by leaf-like PP-layers [376][377] (see Fig.6.1).

A two-electrode system, where an array of point electrodes at ± 20-30kV is raised a few centimeters from the plate electrode was used to inject charges (corona poling) into the film surface [377]. The injected corona charge is located close to the surface ($\sim$ 1 μm) [8]. Large areas of film can be charged quickly, as the surface of a metal roller acts as a plate electrode [299]. Increasing the charging time above 2 s does not lead to a further increase in surface potential although longer times do not seem to cause destruction of the samples [376][299][378].

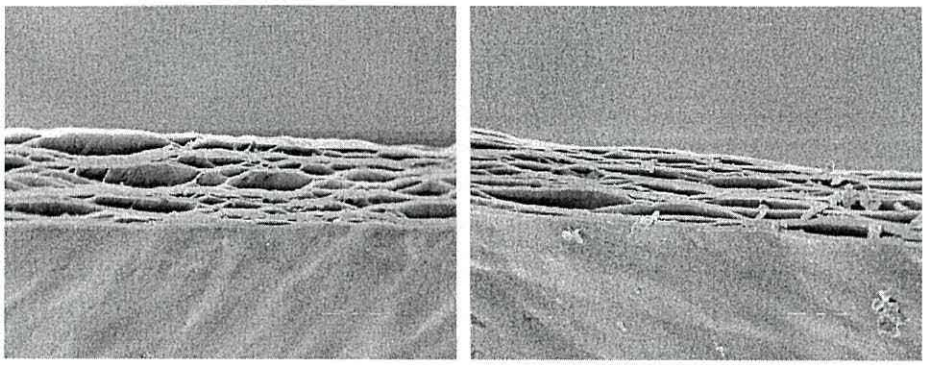

Figure 6.1: Cross-section SEM micrography of HS01 PP foam sample for the two edges in different directions. Magnification x 500. - 10 μm.

The permanent charge of the corona ions raises the surface potential of the film to about 2 kV for HS01 film [26][299]. During the charging process, the resulting internal electric fields (10-15 MV m^{-1}) cause Paschen breakdown of the gas in the voids as evidenced by the observation of electroluminescence inside the larger voids during charging [378][379]. Charges generated during these plasma discharges are trapped in the surface states on the internal PP layers forming macrodipoles [26]. Surface charge densities at the PP-air interfaces of about 690 μC m^{-2} [380][16], 890 μC m^{-2}[299] and 1000 μC m^{-2} [381] have been reported.

Corona-charging experiments with different gas atmospheres inside the voids confirmed the essential role of internal breakdown for obtaining the desired internal charge and the resulting piezoelectric effect [382][383]. Since small-molecule gases can quite easily diffuse through the thin polymer walls between the voids, the air in the cellular PP can be exchanged for other gases by use of pressure cycles. It was found that nitrogen (N_2) and nitrous oxide (N_2O) yielded the best results. These gases apparently lead to much higher breakdown strength in the voids which can therefore be charged to higher levels and piezoelectric d_{33} coefficients of around 790 pC N^{-1}, much higher than those after charging in air (see Table 6.1), can be obtained [382][383].

In addition to corona charging, electrode [384][385] and electron-beam charging [386] have also been reported. In the electrode charging method, only the mechanism for

Material Property	*Value*
Density ρ $(Kg\ m^{-3})$	330
Dielectric constant ε (at 10 KHz)	1.23
Dielectric loss tan δ (at 10 KHz)	0.001
LE coupling factors $k_{31} \sim k_{32}$	~ 0.018
TE coupling factor k_{33}	0.06
RE coupling factor k_p	0.024
Quasistatic piezoelectric coefficient d_{33} $(pC\ N^{-1})$	170-250
Dynamic piezoelectric coefficient d_{33} $(pC\ N^{-1})$	~ 140
Dynamic piezoelectric coefficient $d_{31} \sim d_{32}$ $(pC\ N^{-1})$	~ 2
Static inverse piezoelectric coefficient d_{33} $(m\ V^{-1})$	230 x 10^{-12}
Elastic compliance s_{11} $(m^2\ N^{-1})$	1.1 x 10^{-9}
Elastic compliance s_{22} $(m^2\ N^{-1})$	5.6 x 10^{-10}
Elastic stiffness c_{33} $(N\ m^{-2})$	2.2 x 10^6
Nominal thickness t_3 (μm)	70
Porosity (%)	33
Pyroelectric coefficient p_3 $(\mu C\ cm^{-2}\ K^{-1})$	0.25
Surface charge density at PP-Air interfaces σ_i $(\mu C\ m^{-2})$	690, 1000
Thermal diffusivity D $(m^2\ s^{-1})$	4.5 x10^{-8}
Thermal expansion α (K^{-1})	1.2 x 10^{-3}

Table 6.1: Material properties of HS01-type PP EMFi.

generating the near-surface charge is different. The high electric field across the film and the resulting internal breakdown are the same as with corona charging. Direct piezoelectric coefficients of around 280 pC N^{-1} have been reported [385] in DC voltage-charged samples (~10 kV) which are similar to those reported for corona-charged samples [26][299][377]. However, in electron-beam charged samples, only the voids in the irradiated region of the film are charged [384]. The obtained piezoelectic d_{33} coefficients are comparable and even higher than those of typical piezoelectric ceramics (Table 6.1).

EMFi is completed by coating the charged films with electrically conductive electrode layers either by vacuum evaporation, sputtering, screen-printing or aluminium foil lamination [376].

An external force applied normally to the film's surface will produce a change in the thickness of the air voids. The charges located on the polypropylene/void interfaces then move with respect to each other, and as a result, a mirror charge is generated on the electrodes leading to a direct piezoelectric coefficient d_{33} in the range (170-250 pC N^{-1}) [26][299][377]. The inverse piezoelectric effect (actuator model), *i.e.*, variation of the sample thickness as a result of an applied voltage has also been reported, and an actuator sensitivity constant of about 230 pm V^{-1} [380] confirming the expected reciprocity (see section 6.2).

The thermal stability of PP EMFi has been studied by charge-TSD (Thermally stimulated depolarisation) [387] and TSC [376]. The observed voltage/current reversal (around 60°C) has been attributed to the lower stability of near-surface homocharge in comparison with the heterocharge resulting from the breakdown process in the voids [387][299]. As a result of the charge detrapping, also observed in thermal-wave methods [265][27], thermal stability is limited to temperatures around 50°C [27]. Associated activation energies of 4.6 and (5.6-6.3) eV for homocharge and heterocharge detrapping has been suggested recently from photostimulated depolarisation experiments [388].

The pyroelectric response of PP EMFi has been studied by thermal-wave meth-

ods [27][387]. As a result of the low thermal expansion coefficient ($1.2x10^{-3}$ K^{-1})[27], a pyroelectric coefficient as low as 0.25 pC cm^{-2} K^{-1} [27][387] was found in PP EMFi. This value is around two orders of magnitude lower than those of the best ferroelectric polymers (see Table 5.2). Nevertheless, this is advantageous since it results in highly stable properties with temperature for temperatures below the depolarisation temperature (~50°C).

From measurements of the complex dielectric capacitance (dielectric constant) electromechanical coupling factors have been deduced to be 0.06 for the thickness resonance and 0.018 for length and width resonances [389][373][27] (see Table 6.1). In addition to electromechanical coupling factors, piezoelectric coefficients as well as mechanical parameters such as elastic modulus and sound velocity can be calculated from the resonance curves (see table 6.1).

In spite of the low depolarisation temperature, its low-price [376][377] and low processing requirements make PP EMFi attractive for many applications. In addition, samples of almost any shape and size can be obtained. Many applications have been reported [377]; EMFi has been used for monitoring the activity of laboratory animals [390][391], and human breath monitoring [392][393]. It is also useful for *on-line* monitoring of pressure distribution on the sole during walking or running as well as for floor sensors to be laminated under plastic, wooden or even ceramic and stone coatings [394]. The inverse effect has been applied for actuation of micromovements [395]. Flat loudspeakers have been investigated [396][397]. Active sound control has also been investigated [393]. Recently, characterisation of EMFi for air-borne ultrasound devices has been reported [398].

6.2 Physical Description of the Piezoelectric Behaviour of EMFi

In order to allow for the ready analysis of the electromechanical operation of EMFi, it is usually modelled [380][376][399][400][16][299] as a set of alternating parallel PP and air layers as shown in Fig.6.2 of thicknesses x_i^{PP} and x_j^{Air} respectively. It is further assumed that no volume charge exists and since surface charges on the opposite sides of each air layer originate from discharges in the air between them during poling, they are equal in magnitude and of opposite sign.

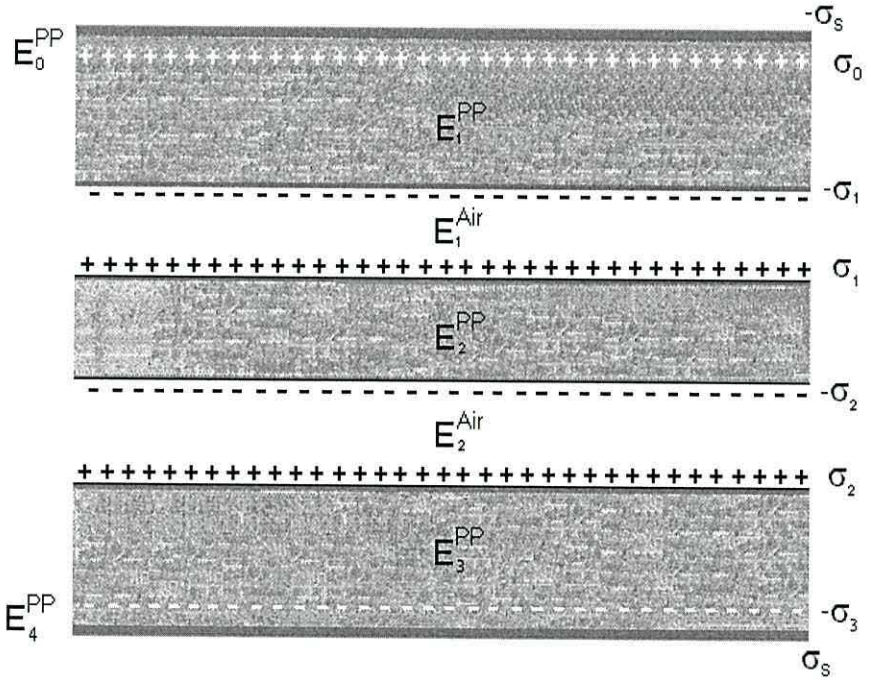

Figure 6.2: Simplified model of PP foamed EMFi cross-section. Modified from [16]

By applying Gauss' law to the surfaces containing the charge layers:

$$-\varepsilon E_0^{PP} + \varepsilon E_1^{PP} = -\sigma_0 \tag{6.1}$$

$$-\varepsilon E_1^{PP} + \varepsilon_0 E_1^{Air} = \sigma_1 \tag{6.2}$$

$$-\varepsilon_0 E_1^{Air} + \varepsilon E_2^{PP} = -\sigma_1 \tag{6.3}$$

$$-\varepsilon E_2^{PP} + \varepsilon_0 E_2^{Air} = \sigma_2 \tag{6.4}$$

$$-\varepsilon_0 E_2^{Air} + \varepsilon E_3^{PP} = -\sigma_2 \tag{6.5}$$

$$-\varepsilon E_3^{PP} + \varepsilon E_4^{PP} = \sigma_3. \tag{6.6}$$

From equations 6.2, 6.3, 6.4 and 6.5 we have:

$$E_i^{PP} \equiv E^{PP} = \frac{\varepsilon_0 E_1^{Air}}{\varepsilon} - \frac{\sigma_1}{\varepsilon}\ ; \qquad i = 1, 2, 3 \tag{6.7}$$

and, from equations 6.1 and 6.6 we can write respectively:

$$E_0^{PP} = E^{PP} + \frac{\sigma_0}{\varepsilon} \tag{6.8}$$

$$E_4^{PP} = E^{PP} + \frac{\sigma_3}{\varepsilon}. \tag{6.9}$$

On the other hand, from equations 6.2 and 6.3:

$$E_2^{Air} = E_1^{Air} + \frac{\sigma_2 - \sigma_1}{\varepsilon_0}. \tag{6.10}$$

Kirchhoff's law can now be written in terms of equations 6.7, 6.8, 6.9 and 6.10 as:

$$E_1^{Air}\left(\frac{X^{PP}\varepsilon_0}{\varepsilon} + X^{Air}\right) - \frac{\sigma_1}{\varepsilon}\left(X^{PP} + \frac{\varepsilon}{\epsilon_0}X^{Air}\right) + \tag{6.11}$$

$$+ \frac{x_0\sigma_0}{\varepsilon} + \frac{x_4\sigma_3}{\varepsilon} + \frac{\sigma_1 x_1^{Air}}{\varepsilon_0} + \frac{x_2^{Air}}{\varepsilon_0} + V = 0 \tag{6.12}$$

where:

$$X^{Air} = x_1^{Air} + x_2^{Air} \tag{6.13}$$

and:

$$X^{PP} = \sum_{i=0}^{4} x_i^{PP} \tag{6.14}$$

and V is the potential. From equation 6.12:

$$E_1^{Air} = \frac{\sigma_1}{\varepsilon_0} - \frac{\varepsilon \sum_{i=1}^{2} \sigma_i x_i^{Air} - \sigma_0 x_0^{PP} - \sigma_3 x_4^{PP} + \varepsilon V}{\varepsilon_0 \left(X^{PP} + \frac{\varepsilon}{\varepsilon_0} X^{Air} \right)} \tag{6.15}$$

which, introduced into equation 6.7 gives:

$$E^{PP} = \frac{\varepsilon \sum_{i=1}^{2} \sigma_i x_i^{Air} + \sigma_0 x_0^{PP} + \sigma_3 x_4^{PP} + \varepsilon V}{\varepsilon_0 \left(X^{PP} + \frac{\varepsilon}{\varepsilon_0} X^{Air} \right)}. \tag{6.16}$$

The above equations can be extended easily to the case of N PP layers by extending the sum:

$$E_i^{Air} = \frac{\sigma_i}{\varepsilon_0} - \frac{\varepsilon \sum_{i=1}^{N} \sigma_i x_i^{Air} - \sigma_0 x_0^{PP} - \sigma_{N+1} x_{N+2}^{PP} + \varepsilon V}{\varepsilon_0 \left(X^{PP} + \frac{\varepsilon}{\varepsilon_0} X^{Air} \right)} \tag{6.17}$$

which, when introduced into equation 6.7 gives:

$$E^{PP} = -\frac{\sum_{i=1}^{N} \sigma_i x_i^{Air} + \sigma_0 x_0^{PP} + \sigma_{N+1} x_{N+2}^{PP} + \varepsilon V}{\varepsilon_0 \left(X^{PP} + \frac{\varepsilon}{\varepsilon_0} X^{Air} \right)}. \tag{6.18}$$

In addition, applying Gauss' law to the upper electrode we have:

$$\sigma_s = -\varepsilon E_1^{PP} = -\varepsilon E^{PP}. \tag{6.19}$$

6.2.1 Sensor Model

In the sensor model, *i.e.*, the direct effect, the system works under short-circuit conditions $V = 0$. In addition, because of the great difference between Young's modulus for the polypropylene and the air layers we can assume that the total strain, S, under the applied stress, T, is mainly due to the thickness variation of the air layers. Therefore,

the electrode charge is controlled by this term *i.e.*:

$$\frac{\partial \sigma_s}{\partial X} = \frac{\partial \sigma_s}{\partial X^{Air}} \tag{6.20}$$

where:

$$X = X^{Air} + X^{PP}. \tag{6.21}$$

In addition, we can suppose that the thickness variation of each air layer is proportional to its original thickness, *i.e.*:

$$\frac{\partial x_i^{Air}}{\partial X^{Air}} = \frac{x_i^{Air}}{X^{Air}}. \tag{6.22}$$

With these assumptions and equations 6.19 and 6.18 we can write:

$$\frac{\partial \sigma_s}{\partial X} = \frac{\partial \sigma_s}{\partial X^{Air}} = -\frac{\varepsilon \sum_{i=1}^{N} \sigma_i x_i^{Air} \left(\frac{X^{PP}}{X^{Air}}\right) - \sigma_0 x_0^{PP} - \sigma_{N+1} x_{N+2}^{PP}}{\varepsilon_0 \left(X^{PP} + \frac{\varepsilon}{\varepsilon_0} X^{Air}\right)^2}. \tag{6.23}$$

According to equation 4.36, the strain, S, produced by the application of the applied stress, T, is, assuming that the strain is homogeneous throughout the sample, *i.e.*, far from the mechanical resonances, given by[1]:

$$\frac{\partial S}{\partial T} = \frac{1}{X}\frac{\partial X^{Air}}{\partial T} = \frac{1}{Y} \tag{6.24}$$

so that, the piezoelectric constant d_{33} in equation 5.10 can be expressed as:

$$d_{33} = \frac{\partial \sigma_s}{\partial T} = \frac{\partial \sigma_s}{\partial X^{Air}}\frac{\partial X^{Air}}{\partial T} \tag{6.25}$$

and therefore:

[1]Note that in the unidimensional approximation, Young's modulus and elastic stiffness are interchangeable terms.

$$d_{33} = \frac{\varepsilon X}{Y} \frac{\sum_{i=1}^{N} \sigma_i x_i^{Air} \left(\frac{X^{PP}}{X^{Air}}\right) - \sigma_0 x_0^{PP} - \sigma_{N+1} X_{N+2}^{PP}}{\varepsilon_0 \left(X^{PP} + \frac{\varepsilon}{\varepsilon_0} X^{Air}\right)^2}. \tag{6.26}$$

Since, as mentioned in section 6.1, in corona-charged samples surface charges are located around 1μm from the surfaces, the equation above simplifies to:

$$d_{33} = \frac{\varepsilon X}{Y} \frac{\sum_{i=1}^{N} \sigma_i x_i^{Air} \left(\frac{X^{PP}}{X^{Air}}\right)}{\varepsilon_0 \left(X^{PP} + \frac{\varepsilon}{\varepsilon_0} X^{Air}\right)^2}. \tag{6.27}$$

6.2.2 ACTUATOR MODEL

In order to obtain the expression for the piezoelectric coefficient in the actuator model, *i.e.*, the inverse effect, the relation between stress exerted over the i-th air layer as a result of the density charges on the two adjacent PP layers must be calculated. From Fig.6.3 we have:

$$dF = \frac{q\sigma dA}{4\pi\varepsilon_0 R^2} \cos\Psi = \frac{q\sigma dA}{4\pi\varepsilon_0} \frac{x_i}{(r^2 + x_i^2)^{3/2}} \tag{6.28}$$

so that the total force is:

$$F = \frac{q\sigma x_i}{4\pi\varepsilon_0} \int_S \frac{dA}{(r^2 + x_i^2)^{3/2}}. \tag{6.29}$$

In spherical coordinates equation 6.29 transforms into:

$$F = \frac{q\sigma x_i}{4\pi\varepsilon_0} \int_0^{2\pi} \int_0^a \frac{r dr}{(r^2 + x_i^2)^{3/2}}. \tag{6.30}$$

Upon making the variable change $u = r^2 + x_i^2$ we can now write:

$$F = \frac{q\sigma x_i}{4\pi\varepsilon_0} \int_0^{2\pi} \int_0^{a^2+x_i^2} \frac{2du}{u^{3/2}} = \frac{q\sigma}{2\varepsilon_0} \left(1 - \frac{x_i}{\sqrt{a^2 + x_i^2}}\right) \tag{6.31}$$

which, for an infinite layer, $a \to \infty$, simplifies to:

$$F = \frac{q\sigma}{2\varepsilon_0}. \tag{6.32}$$

Therefore, the total force exerted on the i-th layer of area S_i is given by:

$$T_i = \frac{-\sigma_i \sigma_i}{2\varepsilon_0}. \tag{6.33}$$

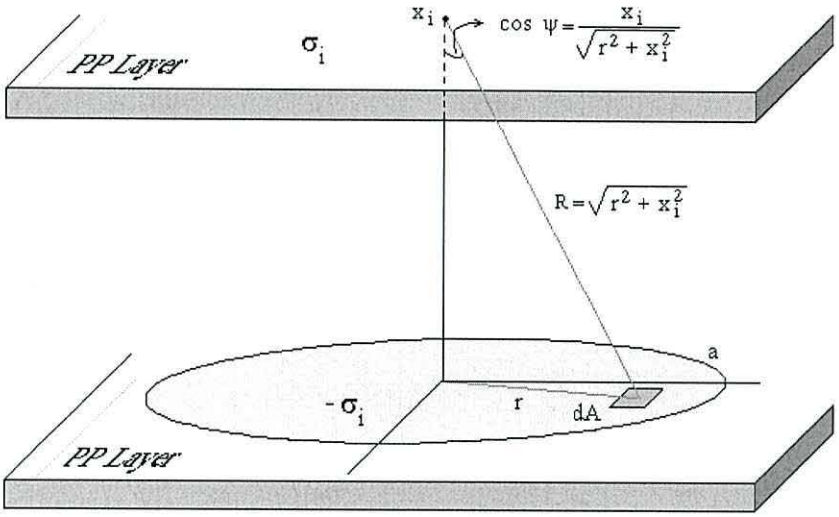

Figure 6.3: Geometry for determining the electric force between polypropylene layers.

On the other hand, in a first approximation, equation 6.17 can be written as:

$$\sigma_i = \varepsilon_0 E_i^{Air} \tag{6.34}$$

so that equation 6.33 becomes:

$$T_i = \frac{1}{2}\varepsilon_0 \left(E_i^{Air}\right)^2. \tag{6.35}$$

The piezoelectric coefficient for the inverse effect in equation 5.10 can thus be expressed as:

$$d_{33} = \frac{\partial S}{\partial E} = \frac{\partial S}{\partial T}\frac{\partial T}{\partial V}\frac{\partial V}{\partial E} = \frac{X}{Y}\frac{\partial T}{\partial V} \tag{6.36}$$

which, from equations 6.17 and 6.35, is:

$$d_{33} = \frac{\varepsilon X}{Y} \frac{\sum_{i=1}^{N} \sigma_i x_i^{Air} \left(\frac{X^{PP}}{X^{Air}}\right)}{\varepsilon_0 \left(X^{PP} + \frac{\varepsilon}{\varepsilon_0} X^{Air}\right)^2}. \tag{6.37}$$

From observation of equations 6.27 and 6.37 we can conclude that the EMFi works equally well in both directions, *i.e.*, as a sensor and as an actuator.

Chapter 7

Experimental Techniques

We have seen in chapters 3 and 4 that polymer structure plays an important role both in electrical and mechanical properties of polymers. With X-ray diffraction (section 7.1.3) and DSC (section 7.1.1) we can determine the crystalline phases of the polymer and their stability respectively, while with the aid of TMA and DMA (section 7.2) we determine the critical conditions (temperature and frequency) for the deblocking of the movement of chain segments or groups [401].

On the other hand, additives are also of considerable importance in the final properties of polymers. The percentage of additives present in a material can be determined using TGA (section 7.1.2). Some impurities however remain well above the polymer decomposition temperature or the maximum operating temperature of the TGA apparatus. EDX (Energy Dispersive X-ray Analysis), section 7.1.2, is used to determine the nature of these ashes.

Charge storage capabilities determine the use of polymers as electrets. Thermally stimulated depolarisation is a widely used technique for studying charge storage capabilities as well as the thermal stability of the injected charge. The TSC technique is described in section 7.7.

Piezoelectric materials are characterized by the coupling between their mechanical and electrical properties (Chapter 5). Determination of the piezoelectric coefficients, d_{3j}, will be described in section 7.4.1. Resonator parameters such as the velocity of

sound, v_i, the electromechanical coupling coefficients, k_{ij}, and resonance and antiresonance frequencies, f_r and f_a are determined from Dielectric Spectroscopy as we shall see in section 7.4.2.

Although most samples were pre-electroded and poled, for some it was necessary to deposit aluminium electrodes by evaporation. Electrode preparation and subsequent DC poling are described in section 7.3.1.

7.1 Characterization of the Raw Material (PP)

7.1.1 Differential Scanning Calorimetry (DSC)

DSC is a differential thermal technique that measures the energy necessary to establish a nearly zero temperature difference between a substance and an inert reference material, as the two specimens are subjected to identical temperature regimes in an enviroment that is heated or cooled at a controlled rate [402]. The DSC apparatus is shown schematically in Fig.7.1.

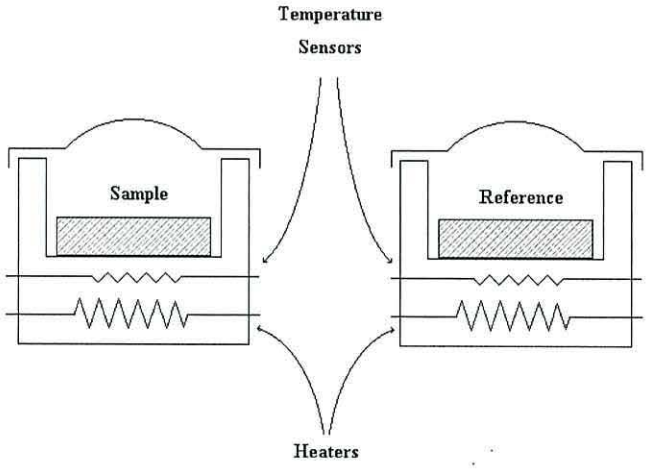

Figure 7.1: Schematic representation of a power-compensation DSC arrangement (modified from [17]).

The added heat, which is recorded as the temperature increases (*thermogram*), compensates for that lost or gained as a consequence of endothermic or exothermic reactions

occurring in the sample. The area under the thermogram is related to the enthalpy associated with these transitions [70][403].

Measurement of the melting behaviour is one of the major uses of DSC [70]. The heat evolved during melting can be measured directly from the DSC peak. Since the quantity of heat absorbed depends in principle on the degree of crystallinity, a DSC thermogram can be used to calculate the crystallinity of a sample from the ratio of the measured heat of melting the heat of melting of a perfectly crystalline polymer [404]. However, no perfectly crystalline polymer samples can be grown so the heat of melting is obtained by extrapolating values obtained from samples of different crystallinities [280].

The DSC experiments were performed with a DSC METTLER-30 under a nitrogen atmosphere[1]. Aluminium sample holders were used, an empty one working as the reference material.

In order to compare different samples of the same material, the thermal history effects were removed. Thermal history is deleted by applying a similar temperature program to all samples. In the first stage, the sample was heated from -40 to 220°C at a constant rate of 10°C min^{-1} (melting). The sample was kept at 200°C for 5 min and cooled to -40°C at 10°C min^{-1} (recrystallization). Finally, the sample was heated from -40 to 220°C at 10°C min^{-1} (melting).

From the first melting curve we gain information about the as-supplied material. In all cases, the melting point was taken from the minimum of the curve of enthalpy versus temperature and the degree of crystallinity was calculated from the ratio between the melting enthalpy of the sample and that of a 100% crystalline sample. The value of the melting enthalpy of a 100% crystalline sample was taken to be 190 J g^{-1} [405].

Shoulders associated with the main melting DCS peak due to the melting of small and imperfect spherulites [282] have been reported. Also, different crystalline systems may be involved in this phenomenon [406].

[1] N_2 is a very stable molecule due to triple bond formation. Dissociation percentage at 2000 K is in the order of $5 \cdot 10^{-5}$ [261].

7.1.2 Thermogravimetric Analysis (TGA) and Energy Dispersive X-Ray (EDX)

In thermo gravimetric analysis (TGA), the sample weight was measured as a function of temperature in the range (200 - 900)°C at a constant rate of 10°C min^{-1} with a precision of 10^{-3} g with a Perkin-Elmer TGA. The substances remaining up to 900°C, *e.g.*, inorganic additives were analysed using the EDX (Energy Diffraction X-Ray) technique, in which an electron beam is used to excite the external electrons of the atoms of the material. The energy of the X-Rays emitted by these electrons when they return to the ground state is measured. Since electronic transitions are unique for any kind of atom, the presence of different atoms is inferred.

7.1.3 Wide-Angle X-Ray Diffraction (WAXD)

The crystalline structure of non-poled, non-evaporated samples was also studied using wide angle X-ray diffraction. The experiments were performed with a Philips 1050/71 powder diffractometer with radiation corresponding to the K_α lines of copper (λ_1=1.54060 nm, λ_2=1.54439 nm). The experiments were performed in continuous mode for Bragg angles $5^o < 2\theta < 40^o$.

In order to look for possible preferential orientations, the experiments were performed with the large dimension (3.5 cm) in two perpendicular orientations.

The orientation of the crystalline phase was determined by the ratio of the intensities associated with the characteristic diffraction peaks for polypropylene.

7.2 Mechanical Characterization

The thermo-mechanical properties of PP EMFi were investigated using a *Perkin Elmer DMA 7*. The apparatus is shown schematically in Fig.7.2. The sample is located between two parallel plates in a temperature controlled furnace. DMA 7 incorporates a high precision motor with a force resolution of 1 mN [280]. The force applied is

transmitted to the upper plate while the lower plate is rigidly fixed. Determination of the instantaneous vertical position of the upper plated to a precision of 1 μm [280] is obtained using a linear variable differential transducer (LVDT).

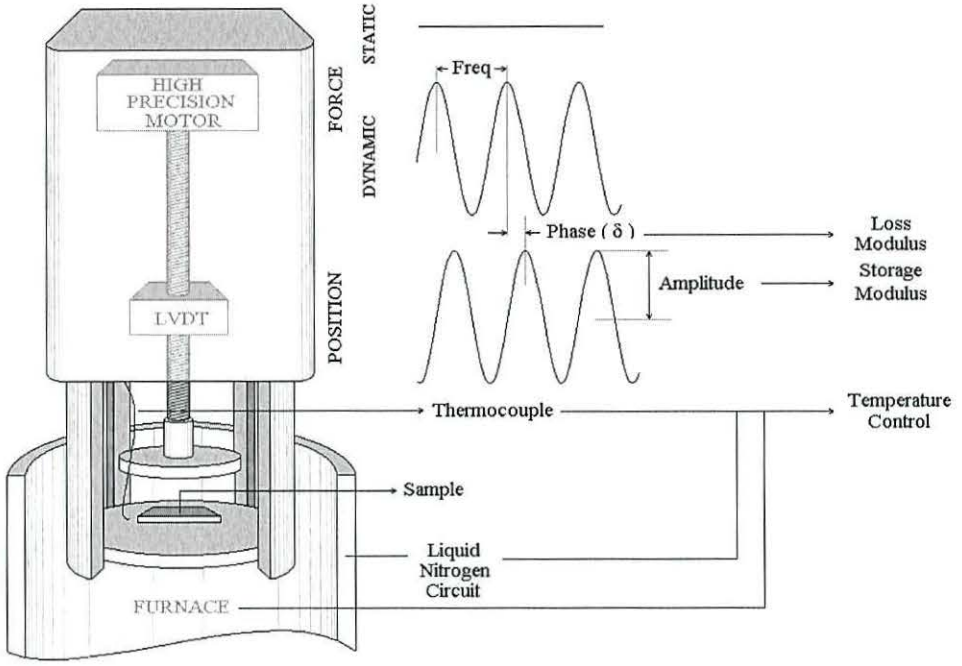

Figure 7.2: Experimental representation of the *Perkin Elmer DMA 7*.

The parallel-plate system together with the sample is located inside a computer-controlled furnace. The actual temperature is measured by a thermocouple located close to the sample. In addition, the oven incorporates a circuit for liquid nitrogen flow.

The applied mechanical stress (strain) in the DMA 7 as well as the oven temperature and liquid nitrogen flow is computer-controlled. Therefore, the DMA 7 allows for the implementation of temperature as well as stress (strain) programmes. Depending on the force and temperature programmes, different properties of the samples can be investigated.

The forces and the corresponding strains were, in all cases, applied and measured in the thickness direction since, as we will see in Chapter 6, the thickness-mode piezoelec-

tric coefficients are more interesting than those in lateral directions. All measurements were performed on unpoled samples 1 cm^2 in area.

7.2.1 Thermo-Mechanical Analysis. Thermal Expansion

In Chapter 6, it was mentioned that the main drawback of a polypropylene foam electret is its low thermal stability, which is limited to around 50°C. The thermal instability may be a consequence of the charge detrapping induced by temperature. However, we also pointed out in Chapter 6 that the piezoelectric character of the material strongly depends on the thickness of the air voids. Therefore, for completely characterizing the thermal instability, the effects of temperature on the cellular structure of the foam were also investigated. The effect of temperature on the cellular structure was studied by measuring the thermal expansion of the material in the thickness direction.

The thermal expansion was measured with a Perkin-Elmer DMA7 in the TMA mode. A sample 1 cm^2 in area was located between the parallel plates of the DMA7 inside the oven. A constant mechanical stress was applied and the temperature increased at a constant rate of 3°C min^{-1}. The thermal expansion coefficient was then calculated using equation 4.40. Thermal expansion measurements and thermal expansion coefficient calculations were performed for different applied mechanical stresses in the range (10-10^4) Pa.

The thermal expansion of solid polypropylene samples (1 cm^2 in area and 1.2 mm in thickness) was also measured in order to determine whether the changes in the foam thickness were due to changes in the cellular structure, in the polymer matrix or both.

Partial runs were performed in order to determine the reversibility of the thermal effects.

7.2.2 Strain-Stress and Creep-Recovery curves

Stress-strain (section 7.2.2) and creep-recovery (section 7.2.2) curves were studied by measuring the strain produced by the application of different ramp and step stress

functions respectively.

However, in both cases, the stress functions were superimposed on a low constant stress (100 Pa), large enough so as to ensure a good mechanical contact between the upper plate of the apparatus and the sample but small enough so as to neglect its effects on the sample.

Stress-strain curves as well as creep recovery were studied at different temperatures. In both cases the constant stress was applied at the pre-determined temperature and the thickness monitored until a stable value was reached (around 2 hours) after which the corresponding stress function was applied.

Strain-Stress Curves

Strain-Stress curves were obtained by applying the stress function shown in Fig.7.3 and recording continuously the thickness variation. The derivative of the applied stress with respect to the strain yields the Young's modulus. Strain-stress curves were measured at several temperatures in the range -30 to 80^{o}C.

Creep-Recovery

For the study of the creep and recovery properties, the sample was acted on by a square stress function of the form (Fig.7.4):

$$\sigma = \begin{cases} \sigma_r & \text{when } t < t_0 \\ \sigma_{max} & t_0 \leq t \leq t_{max} \\ \sigma_r & \text{when } t > t_{max} \end{cases} \tag{7.1}$$

The parameters that characterize the response curve (Fig.7.4) are [280]:

- $\epsilon_i = \epsilon(t_i)$ where t_i is the time at which $(d\epsilon/dt)$ reaches its maximum value.
- $\epsilon_{max} = \epsilon(t = t_{max})$ is the maximum strain.
- $\epsilon_r = \epsilon(t_{ir})$ where t_r is the time at which $d\epsilon/dt$ reaches its minimum value.

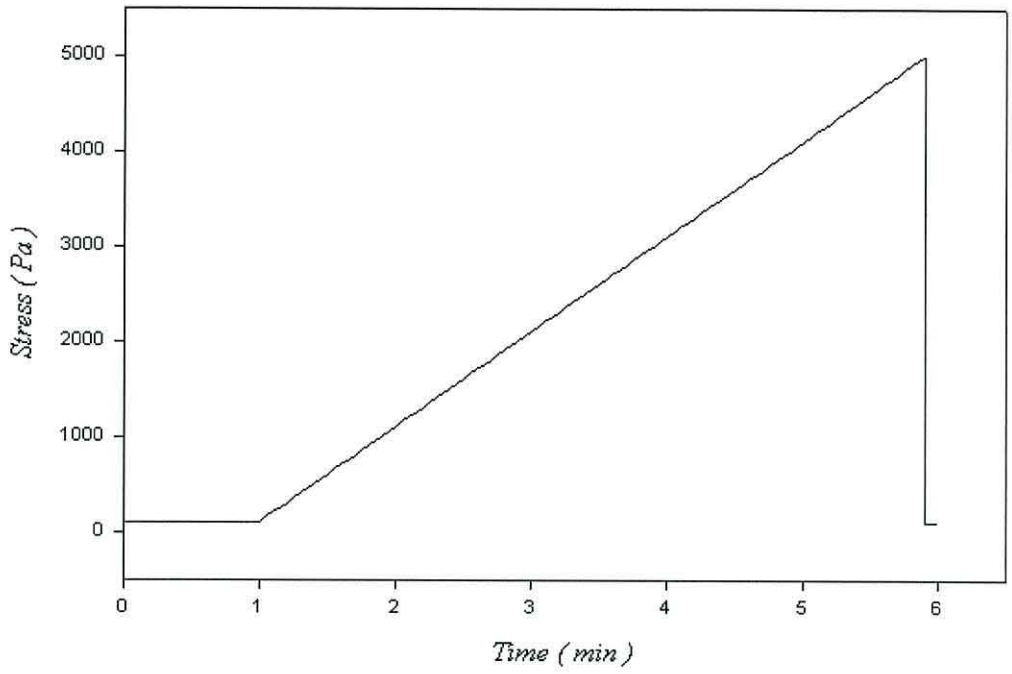

Figure 7.3: Applied stress function to obtain the stress-strain curves.

- $\epsilon_\infty = \epsilon(t = t_\infty)$ where t_∞ is the total time of the experiment.

All these parameters depend on the maximum stress and time ($\sigma_{max} = \sigma(t_{max})$) as well as on temperature. The influence of the mentioned parameters on the response curve was studied. In all cases, measurements for different values of the considered parameter (stress, time and temperature) were performed on different samples.

Dynamical Measurements

So far, a theoretical model for the relation between the microscopic structure and the viscoelastic behaviour has only been established for completely amorphous polymers [280]. In semicrystalline polymers however, the existence of different types of crystalline structures as well as the amorphous phase with their particular relaxation mechanisms (section 2.4) very much complicate their viscoelastic behaviour [407]. The use of phenomenological models is then required for studying the viscoelastic behaviour of semicrystalline polymers.

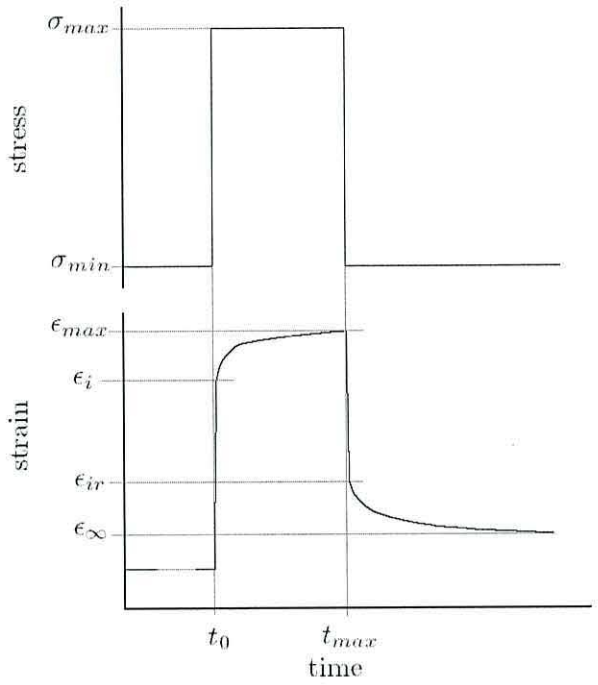

Figure 7.4: Stress function and typical response curve in a creep-recovery experiment.

In chapter 4, we saw that some mechanical coefficients, *e.g.*, Young's modulus, have a complex character for viscoelastic materials (equation 4.65). We also saw that for harmonic excitations (one dimensional case), the complex nature of the corresponding coefficient (the viscoelastic character of the material) leads to a lag in the phase of the resulting strain (stress) with respect to the applied stress (strain) that can be studied with the help of the real and imaginary parts of the corresponding coefficient (equations 4.76 and 4.77) or the loss tangent (equation 4.78).

Dynamic experiments were performed using the Perkin-Elmer DMA7 (described in section 7.2) in DMA mode. A sinusoidal stress (strain) was applied to the sample and the resulting strain (stress) continuously monitored as the temperature was linearly increased from -40 to 130°C at a constant rate of 5°C min^{-1}. All measurements were performed at 1Hz.

7.3 Electrical Characterization

7.3.1 Sample Poling and Electrode Evaporation

In addition to the pre-electroded and pre-poled[2] samples, VTT Chemical Technology also supplied non-poled, non-electroded samples. To prepare these latter samples for measurements it was necessary to furnish them with electrodes and to pole them by DC-voltage charging in order to impart an EMFi character to the films. Aluminium electrodes were deposited by evaporation through a shadow mask under a vacuum of 10^{-5} Pa.

To define the electrode area, circular shadow masks, 1 cm in diameter were used. In order to estimate the increase in sample temperature during the evaporation process, the system was also provided with a thermocouple located near the mask. The total time required to complete the evaporation process was about 5 min. The temperature measured near the mask reached a maximum of around 45^{o}C.

Due to the low density of the material, the contact between the back evaporated electrode and the plane electrode of the corona poling system was very poor with perhaps no contact. This enhanced the production of sparks which destroyed the evaporated electrode. Therefore a DC-voltage method was used to perform the poling, in which aluminium evaporated samples were located between two electrodes inside a Pyrex glass container and connected to a high voltage supply (0-10) KV as shown in Fig.7.5. Polarisation at potentials higher than 8 KV was not possible due to breakdown of the sample. The breakdown was usually observed at the edges of the evaporated electrodes as shown in Fig.7.6.

For polarization at high temperatures, the Pyrex glass was located inside a temperature controlled oven (shown in Fig.7.14). From capacitance measurements at different temperatures (sections 7.2 and 11.2) we conclude that thermal equilibrium is attained after heating for about 2 hours. Therefore, the samples were kept at the pre-determined

[2]Positively corona poled.

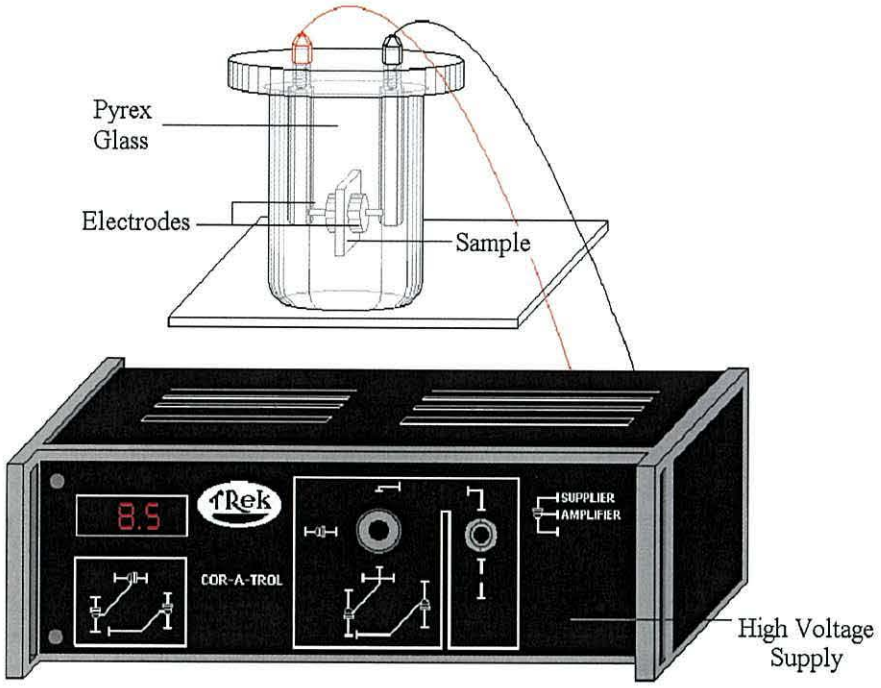

Figure 7.5: Experimental setup for DC-voltage poling.

temperature for this time after which, the voltage was applied for 2 min. Finally, the samples were allowed to cool to room temperature for 24 hours. In DC-voltage polarization, homocharge injection from electrodes may take place [8] in addition to heterocharge deposition arising from ionisation of the gas in the foam.

7.3.2 Thermally Stimulated Currents (TSC)

For the thermally stimulated current (TSC) experiments, a polarised sample was placed on a heating plate and its electrodes short-circuited (short-circuit TSC) through a programmable electrometer (Keithley model 617). In order to minimize the temperature gradient through the sample it was located in a vacuum chamber evacuated to 10^{-5} Pa.

Four heaters and a thermocouple inside the heating plate allowed for precise temperature control and measurement. The temperature was increased at a constant rate (3^{o}C min^{-1}) using a programmable temperature controller (Eurotherm) connected to both the heaters and the thermocouple. The accuracy in temperature measurement

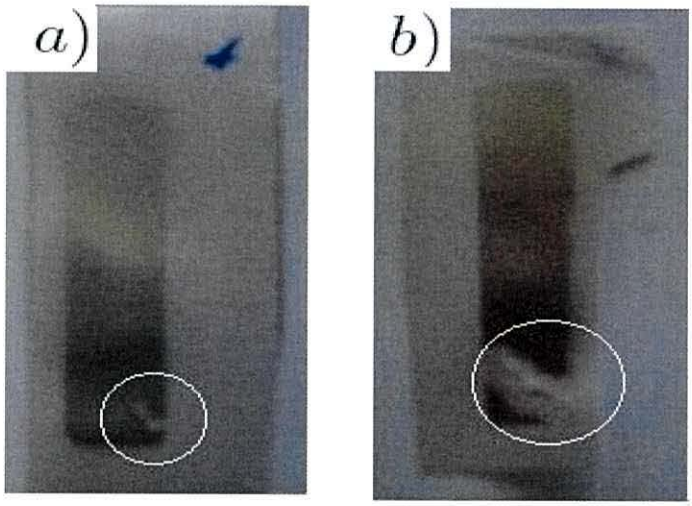

Figure 7.6: a) Initiation of breakdown at the electrode edge. b) Complete breakdown. The electrode covers only part of the sample.

was 0.1°C. The Eurotherm and the electrometer were connected to a computer through the serial and GPIB port respectively. A MATLAB® program was written in order to facilitate computer-device communication and data acquisition.

Good thermal and electrical contacts were provided by pressing the sample using a small screw-driven aluminium plate (1mm thick) contacting the upper electrode of the sample. A diagram of the system is presented in Fig.7.7.

The foamed nature of the material introduces an additional complexity in TSC measurements. Firstly, low thermal conductivity is expected. Consequently, it was necessary to determine the temperature difference between top and bottom surfaces of the sample prior to TSC measurements. In addition to the thermocouple inside the heating plate, therefore, another thermocouple in contact with the top surface was incorporated as shown in Fig.7.8 a).

A TSC run under the same conditions as those described above was performed and the temperatures given by the two thermocouples measured. The temperatures were plotted against each other (Fig.7.9) from which it is seen that the temperature gradient through the sample is small. Therefore, currents ascribed to temperature gradients are

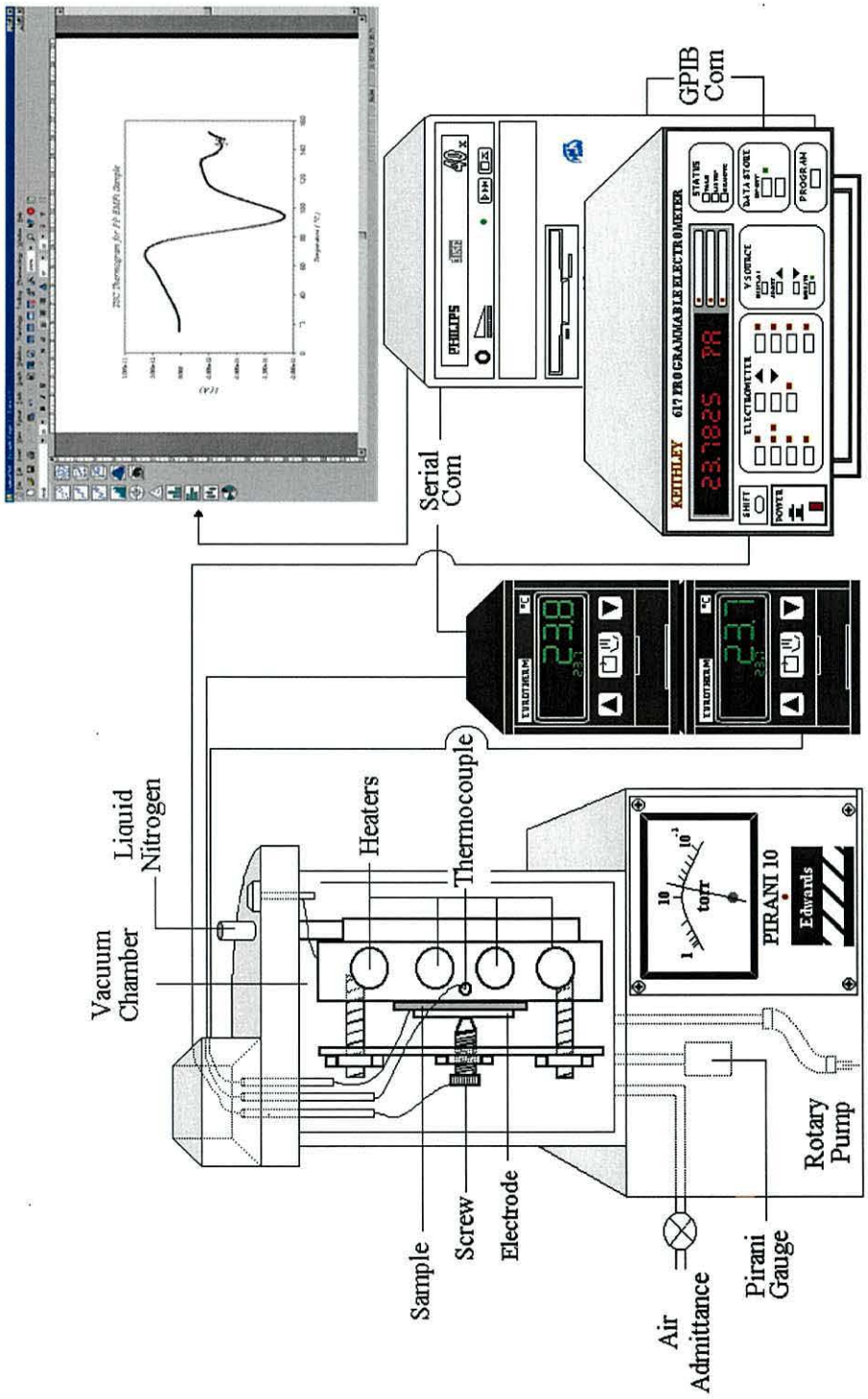

Figure 7.7: Experimental setup for TSC experiments.

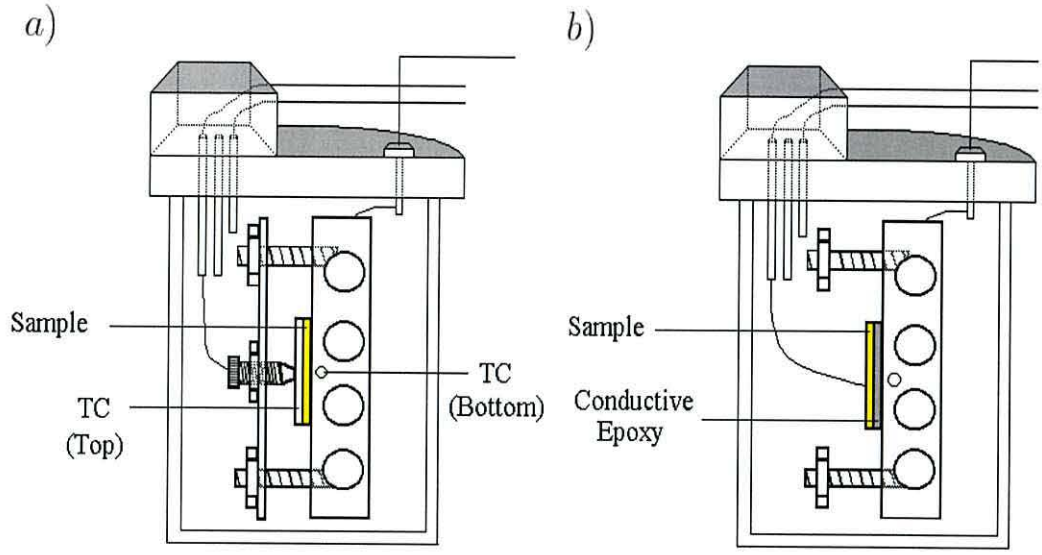

Figure 7.8: Detailed view of the sample holder for a) thermal gradient determination and b) low pressure measurements.

likely to be sufficiently small to ignore.

In addition to the low thermal conductivity, the foamed nature of the samples results in a low Young's modulus and therefore, possible effects arising from contraction of the sample as a result of the applied pressure were also considered. To investigate this possibility, samples were glued to the heating plate using a thin layer of a two-part conductive epoxy and connected to the electrometer using a 20 μm diameter aluminium wire as shown in Fig.7.8 b).

7.4 Piezoelectric Properties

7.4.1 Piezoelectric Coefficients

The piezoelectric d_{33} coefficient of the foam was obtained using a Pennebaker Model 8000 Piezo d_{33} Tester and an AC voltmeter. For this measurement an electroded sample was located on a metallic vibrating (50 Hz) base. A high-precision screw provided a static controlled-stress short-circuit. As a result of the piezoelectric character of the

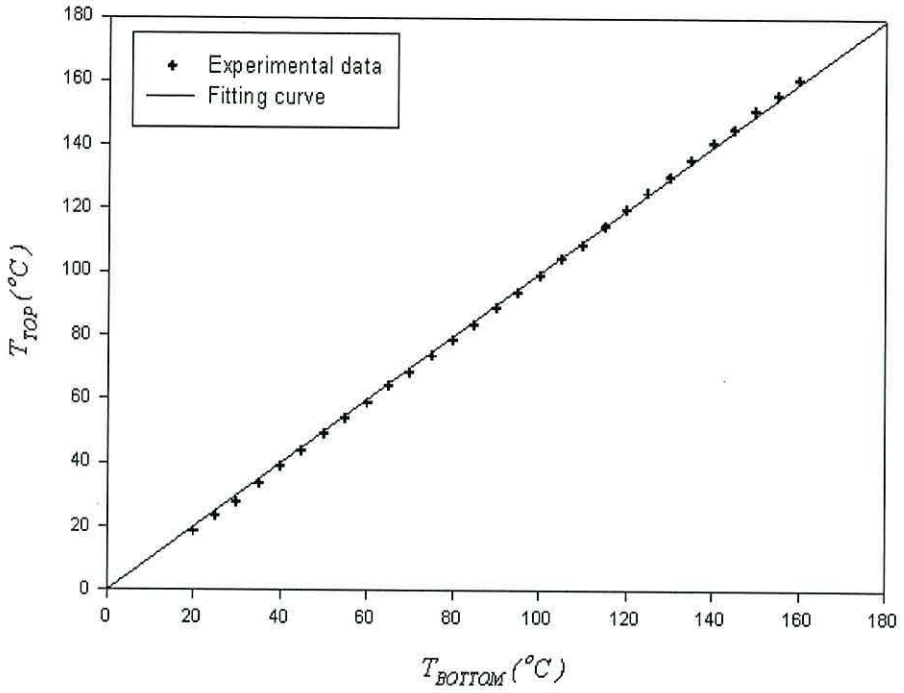

Figure 7.9: Measured temperatures on top and bottom thermocouples in a TSC ramp. Heating rate 3°C min^{-1}.

film, the applied mechanical stress causes an AC voltage to develop across the sample. This voltage was measured with an AC voltmeter connected to the Piezo d_{33} Tester as shown in Fig.7.10. Previous calibration with the aid of a ceramic of known piezoelectric d_{33} coefficient (101 pC N^{-1}) resulted in a voltmeter reading (in mV) that was equal to the value of the d_{33} coefficient (in pC N^{-1}).

Due to the foamed character of the material, it shows a noticeable creep after the application of the static stress. Therefore, a time decaying reading was observed (Fig.7.11). After 20 s, the rate of decay was relatively slow. In addition, this value was observed not to vary after successive measurements, so it was taken as the d_{33} value.

The effect of the annealing temperature as well as the polarisation voltage on the piezoelectric d_{33} coefficient was investigated. For temperature measurements, the sample was heated at a constant rate of 3°C min^{-1} up to the desired temperature and then allowed to cool to room temperature over a period of 24 hours after which the

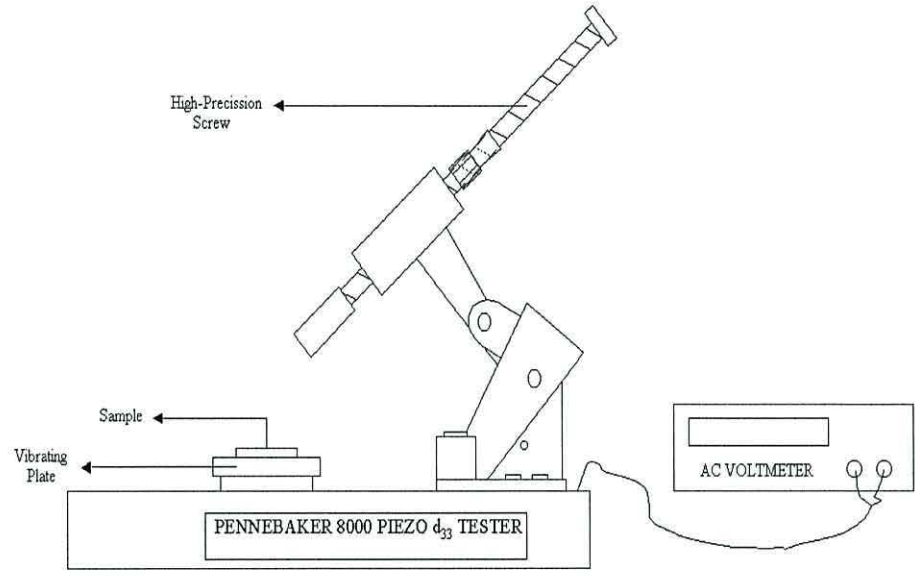

Figure 7.10: Schematic representation of Pennebaker Model 8000 Piezo d_{33}.

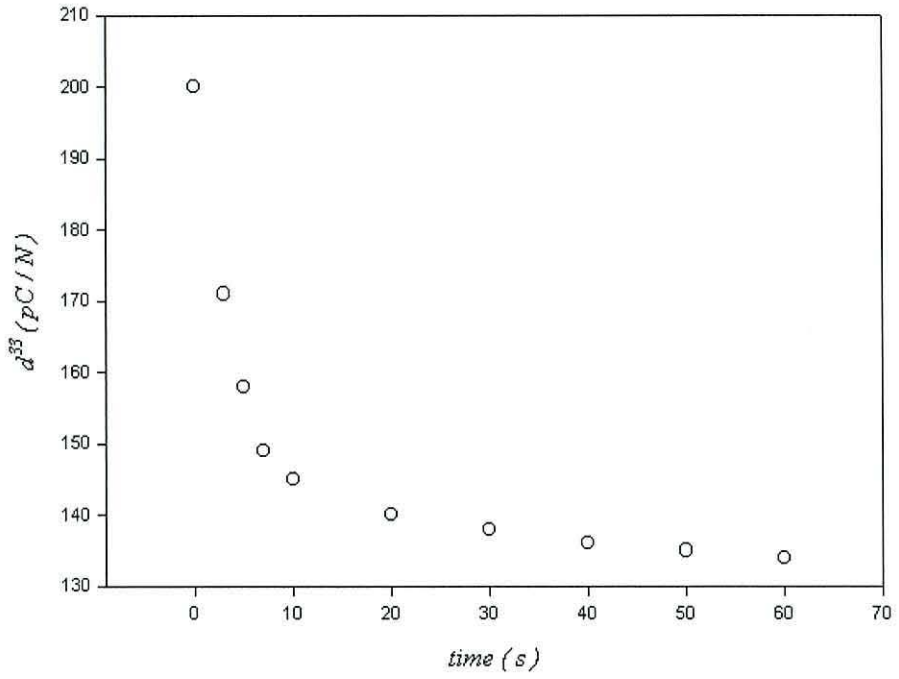

Figure 7.11: Time variation of the piezoelectric d_{33} coefficient.

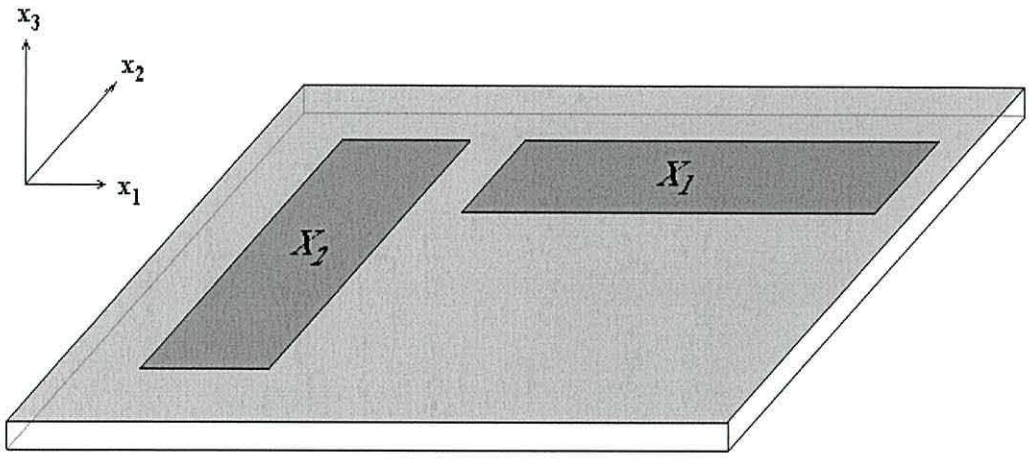

Figure 7.12: Geometry of PP foam for d_{31} and d_{32} measurements. The dimensions of the shown areas are (4x0.4)cm.

piezoelectric coefficient was measured.

Figure 7.13 is a diagram of the apparatus used for determining d_{31} and d_{32}. A standard capacitor, C, of nominal capacitance 10 nF ($\sim$ three orders of magnitude greater than that of the sample, C_S) was connected in parallel with the sample. An external controllable stress perpendicular to the thickness direction was applied by the addition of weights (100 g) to samples X_1 and X_2 (see Fig.7.12).

The voltage developed across the direction $\vec{x}_3$ was then measured with a Gould Digital Storage Oscilloscope (DSO) model 4050. The equivalent capacitance seen by the oscilloscope is given by:

$$C_{eq} = C_S + C = \frac{Q_T}{V} \tag{7.2}$$

where Q_T is the total developed charge. The charge on the capacitor satisfies the equation:

$$C = \frac{Q_C}{V} \tag{7.3}$$

and since $C >> C_S$,

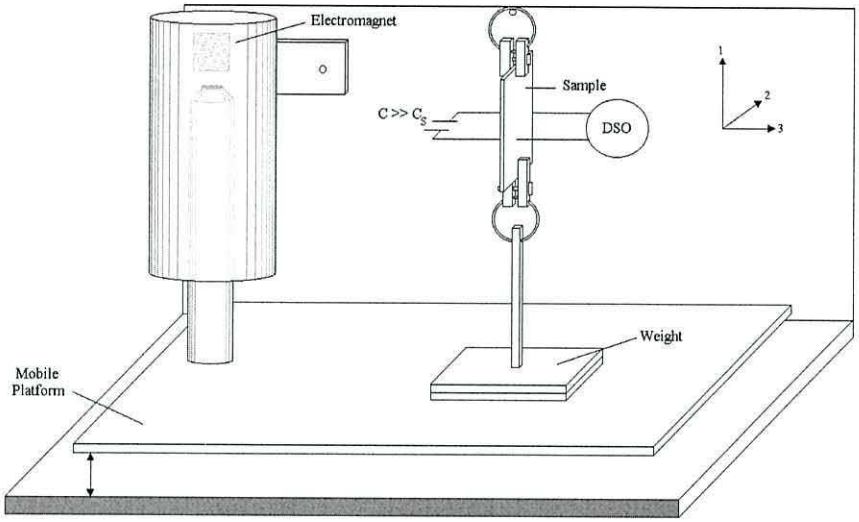

Figure 7.13: Experimental setup for the determination of d_{31} measurements.

$$Q_T \approx Q_C \approx CV. \tag{7.4}$$

The d_{31} coefficient for an applied stress T_1 can be expressed as:

$$d_{31} = \frac{D_3}{T_1} = \frac{CV/A_{12}}{F/A_{23}} = \frac{CVl_3}{mgl_1} \tag{7.5}$$

where F is the applied force and

$$A_{ij} = l_i l_j. \tag{7.6}$$

From the d_{33} and d_{31} coefficients it is usual to define the so-called *hydrostatic coefficient* d_h as[3] [30]:

$$d_h = 2d_{31} + d_{33} \tag{7.7}$$

which indicates the goodness of a piezoelectric material for hydrostatic applications.

[3] Note that usually $d_{31} \sim d_{32}$ and then, $d_h \sim 2d_{31} + d_{33}$.

7.4.2 Resonator Parameters

Atmospheric Pressure

The measurement of the complex capacitance and estimation of the resonator parameters for different pressures and different temperatures will be described in this section. For free-resonator mode measurements at atmospheric pressure, the sample was located in a temperature controlled oven and connected to a Hewlett Packard 4284-A precision LCR meter as shown in Fig.7.14. The real and imaginary parts of the complex capacitance were measured in the frequency range (10 KHz -1 MHz) with an accuracy of $\pm$ 0.05%.

The experimental values of the real and imaginary parts of the complex capacitance were fitted to the theoretical expression given in equation 5.106. Due to the complexity of these expressions, a standard least-squares fitting was not possible. On the contrary, the theoretical expression for the complex capacitance was separated into its real and imaginary parts with the help of the MATLAB® symbolic calculus toolbox. The resulting functions were then plotted over the experimental data and the theoretical parameters, thicknesses, sound velocity, acoustic absorption and electromechanical coupling coefficient as well as the low-frequency values of C' and C'' varied until a good fit was obtained. A difference of around 5% in any of the resonator parameters was sufficient to distinguish between the resuting curves.

The plotting of experimental data as well as theoretical curves was performed with the help of a MATLAB ® guided user interface specially developed for this purpose (Fig.7.15). The MATLAB ® program created for the separation of the complex capacitance was attached to the interface.

As a preliminary step, the complex capacitance of a non-polarised sample was measured at room temperature. Real and imaginary parts of the complex capacitance were observed not to vary noticeably with frequency as shown in Fig.10.1 and therefore were considered as having constant values for each sample.

Free-resonator parameters were also obtained at different temperatures ranging from

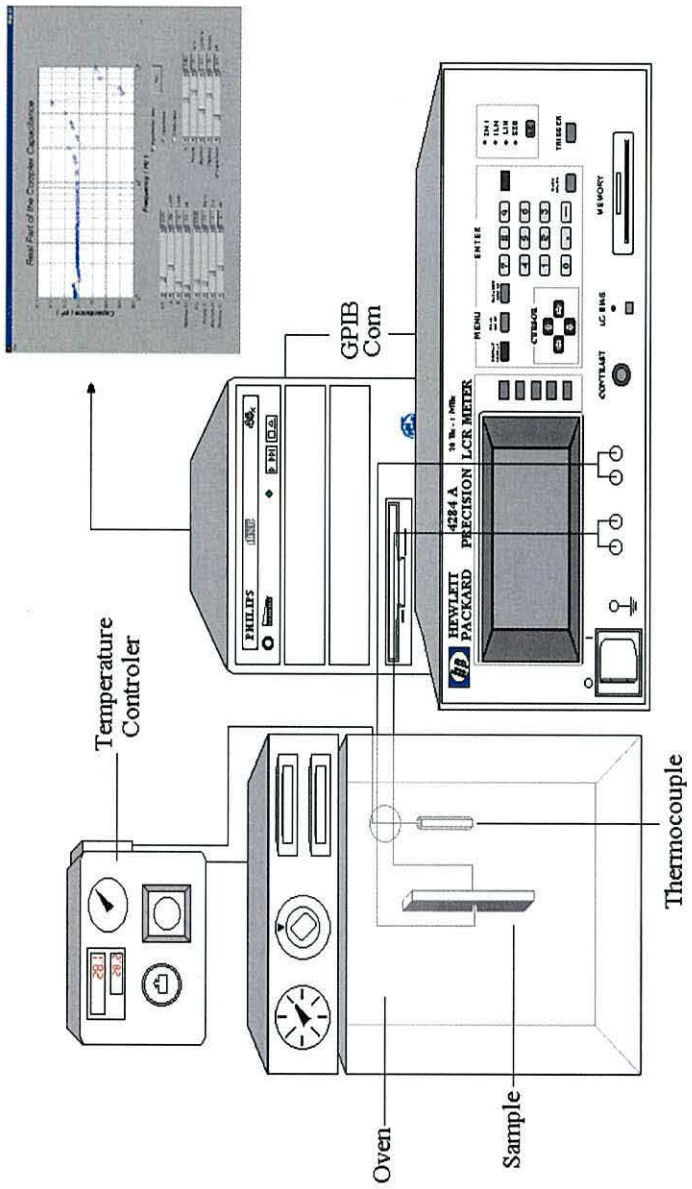

Figure 7.14: Experimental setup for (free-resonator) dielectric spectroscopy measurements at different temperatures.

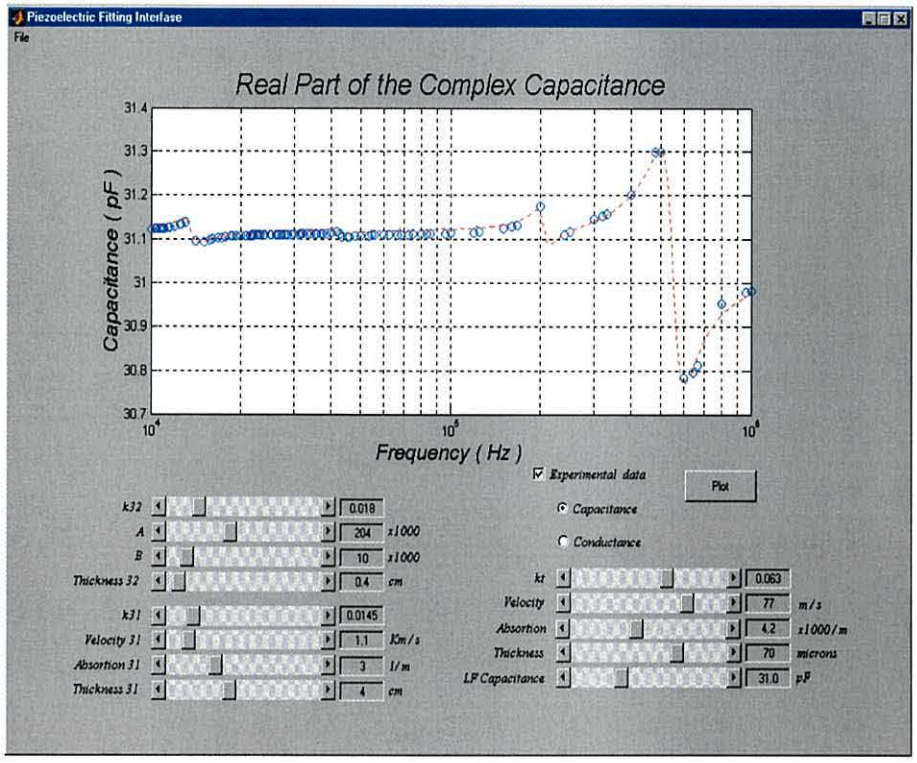

Figure 7.15: MATLAB ® guided user interface developed for determination of the resonator parameters.

$\sim$ 20 to 80°C at intervals of 10°C. The sample was heated up to the pre-determined temperature and the complex capacitance measured at intervals of 15 min until the difference between two consecutive measurements was negligible both for the real and the imaginary parts of the complex capacitance. The time required was found to be around 2 hours after which the sample was supposed to be at thermal equilibrium. After each measurement the sample was allowed to cool to room temperature for 24 hours and the complex capacitance re-measured.

Pressure

Since PP EMFi has a closed cell structure, a rather slow diffusion of the air out of the voids when the films is under vacuum is expected. Therefore, evacuation time may have a considerable effect on the properties of the samples. This effect was investigated by measuring the sample capacitance as a function of time under a vacuum of 10^{-5} Pa. In

this case, the sample was freely suspended inside a vacuum chamber.

7.4.3 One-Side Clamped Resonator Mode

For the one-side clamped resonator measurements the sample was heated by contact to a heater plate located inside a vacuum chamber as shown in Fig.7.9 b). Because of the gluing, the lateral displacements (directions $\vec{x}_1$ and $\vec{x}_2$) were impeded. The experimental data were fitted by the corresponding theoretically derived expression (section 5.4.3). A MATLAB® guided user interface similar to that shown in Fig.7.15 was developed in order to carry out the fitting process. The pressure was decreased to 10^{-5} Pa in order to ensure a sufficiently small difference between the temperature of the sample and that of the heaters.

Chapter 8

Characterisation of the Raw Material

The PP foam investigated in this work was obtained as a gift from VTT Chemical Technology (Tampere, Finland). No information was given on either its physico-chemical properties, composition, morphology or structure. In this chapter are reported a series of measurements to characterise these properties of the foam.

8.1 Differential Scanning Calorimetry (DSC)

The experimental DSC thermograms for both electroded, poled and non-electroded, non-poled samples are presented in Fig.8.1.

From Fig.8.1 we can see that the melting process starts at around 50°C and extends to 170°C revealing a wide range of spherulite size. The phenomenon at low temperatures is called premelting and is the melting of small and imperfect spherulites as mentioned in section 4.6.

As stated in section 7.1.1, in order to remove thermal history effects, the samples were subjected to a predetermined thermal program. Firstly, the samples were heated at a constant rate of 10°C min^{-1} up to 220°C and then, beyond the melting point. The first (endothermal) peak reflects the melting of the polymer. After that, the samples were cooled to 20°C. The second (exothermal) peak reflects the recrystallisation of

the polymer as the temperature decreased. Finally, the heating process was repeated and the third (endothermal) peak recorded. This peak was compared to the data (extrapolated) for a 100% crystalline polypropylene subjected to the same thermal treatment as explained in section 7.1.1.

From the DSC melting peak a degree of crystallinity of about 50% was calculated[1] for both electroded and non-electroded samples. This indicates that the polymer is stereo-regular (see section 2.3.1). Moreover, the high melting point indicates that polypropylene is crystallized in the isotatic conformation (see Table 2.5). The thermogram does not present shoulders or complex peaks which seems to indicate that there is only one crystalline system involved [406].

8.2 Thermogravimetric Analysis (TGA) and Energy Dispersive X-Ray (EDX)

The TGA for a both non-electroded, non-poled sample and a poled sample, whose electrodes were removed using NaOH, are shown in Fig.8.2.

The main decrease in Fig.8.2 a) starts at 400°C and is due to polymer decomposition. From Fig.8.2 a) we can see that the remaining mass in the case of the sample treated with NaOH is $\sim$ 1% higher than that for the non-electroded one suggesting that the electrodes were glued rather than evaporated onto the polymer. The presence of epoxy (epoxy is a resin with a high decomposition temperature) used in fixing the electrode deposition may be the reason for the observed difference in the residual mass.

The step starting at 500°C in both samples is probably related to the reaction[2]:

$$CaCO_3 \rightarrow CaO + CO_2. \tag{8.1}$$

The initial amount of $CaCO_3$ calculated from the TGA curves is also shown in Fig.

[1]The crystallinity was calculated by the DSC apparatus.
[2]Pertier and Duval [408] report a temperature of 660°C for this reaction.

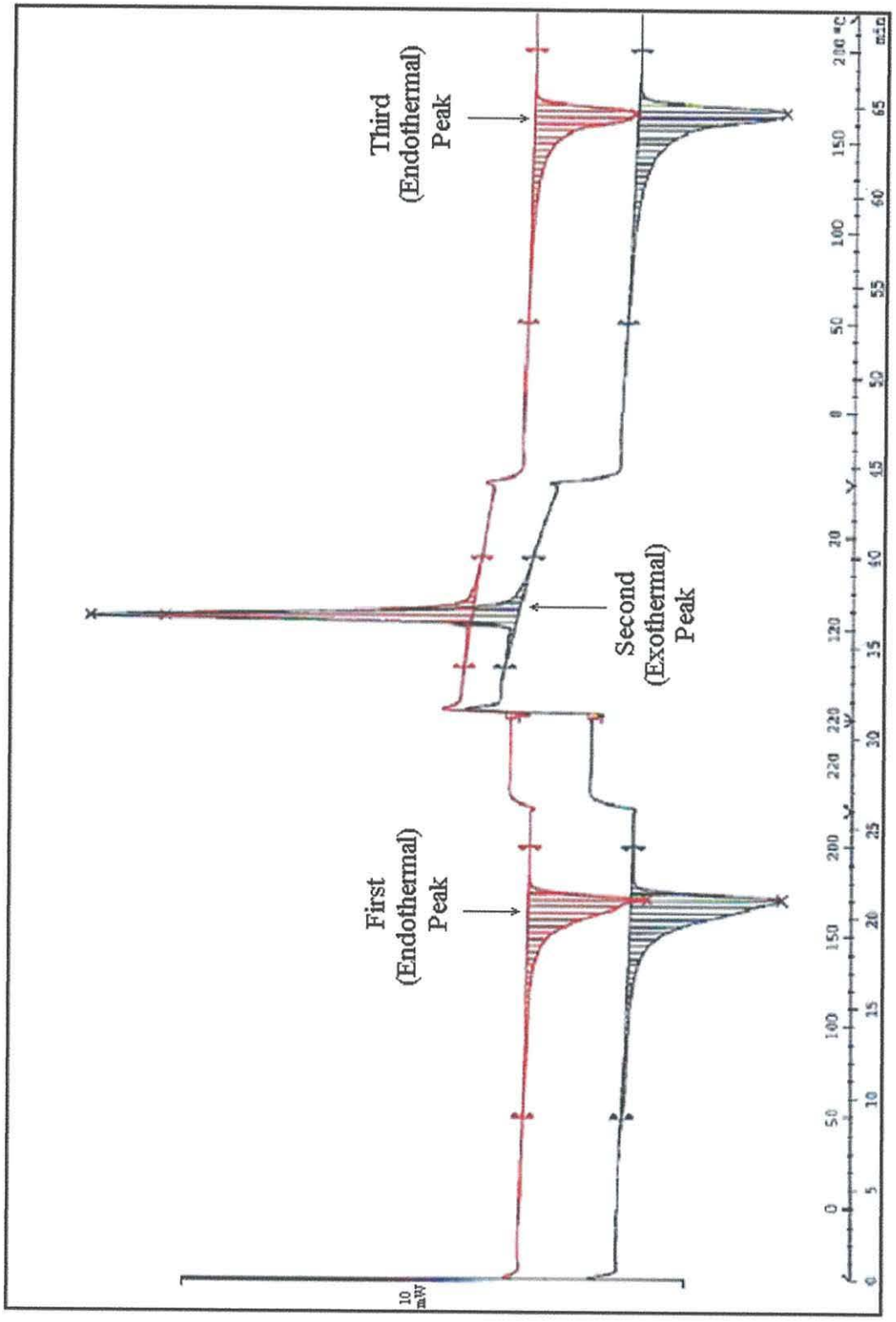

Figure 8.1: Experimental DSC thermogram of electroded, poled (black curve) and non-electroded non-poled (red curve) samples.

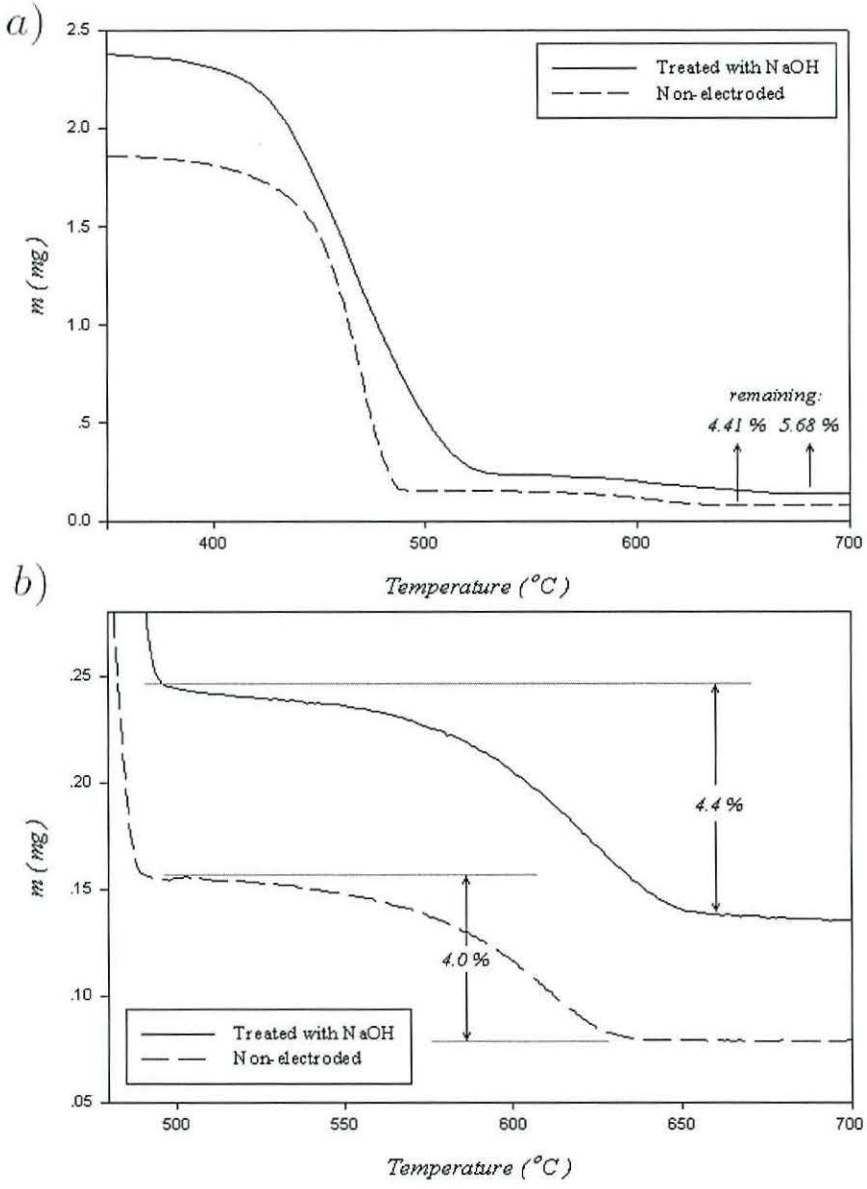

Figure 8.2: TGA for non-poled, non-electroded and NaOH treated samples. a) Total run showing the evaporation of the polymer as well as the remaining percentage of the initial mass after heating at 900°C. b) Mass loss associated with calcium carbonate decomposition together with the calculated percentage of the loss.

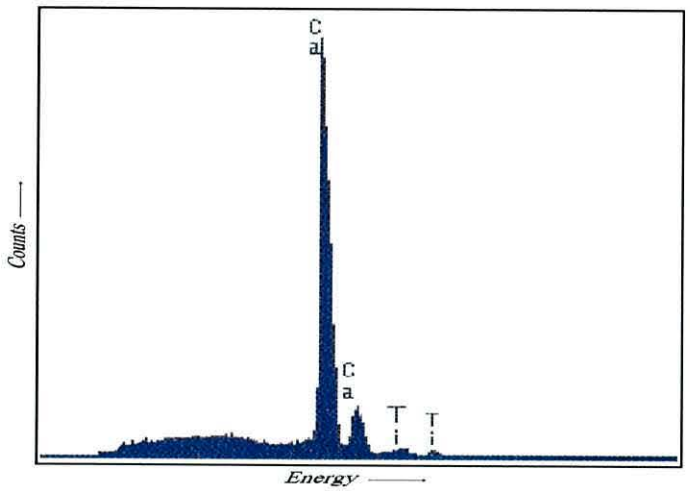

Figure 8.3: EDX Spectrum of the ashes of non poled, non evaporated polypropylene foam after thermal treatment at 900°C. Two peaks are present for each element, associated with the K_α and K_β transitions.

8.2 b). In view of the high decomposition temperature of the $CaCO_3$, which is higher than that of the polymer, we infer that it was not introduced as a foaming agent but as a filler.

The residual calcium was detected using the EDX technique. Figure 8.3 shows two peaks corresponding to calcium and two smaller peaks that correspond to titanium. Two peaks appear for each element which are associated with the K_α and K_β transitions. The larger peak in both cases are associated with K_α transition. Calcium appears in the sample as $CaCO_3$ while titanium may be either residual catalyst from the polymerisation reaction or as TiO_2, a widely used whitener (pure polypropylene is transparent while polypropylene foam is white).

8.3 WIDE ANGLE X-RAY DIFFRACTION (WAXD)

The WAXD revealed the existence of two main peaks corresponding to the planes (110) and (040) (Fig.8.3) which correspond to the monoclinic system [273] (see section 2.5).

Peak intensities as well as their ratio at different temperatures are presented in Table 8.1 where X_1 and X_2 refer to samples with their major dimension in directions

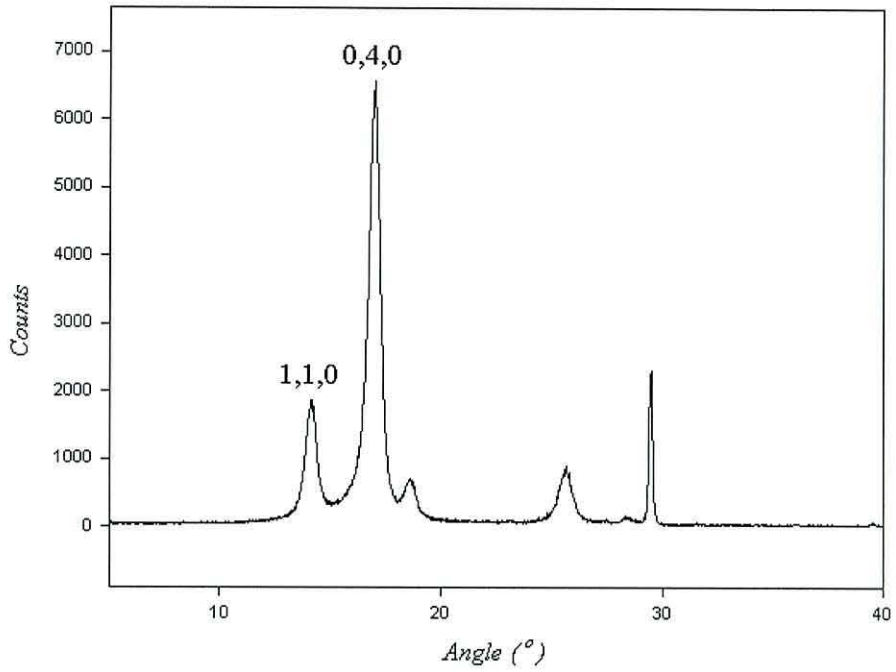

Figure 8.4: WAXD spectrum of foamed polypropylene.

$\vec{x}_1$ and $\vec{x}_2$ respectively as mentioned in section 7.1.3.

In isotropic polypropylene, the ratio I_{040}/I_{110}=0.54 [409] whereas in the foam the ratio is much higher, 3.15 $\pm$ 0.15, suggesting a high orientation in the latter [410].

From Table 8.1 we see that anneal temperatures below 80°C have little effect on the crystalline phase. The results preclude the premelting of imperfect spherulites since these, due to their imperfect structure, probably do not contribute to the diffraction peaks but rather to the much broader background.

The ratios I_{040}/I_{110} suggest that polymer molecules display a high in-plane orientation. However, the similar values obtained in the X_1 and X_2 samples indicate that there is no preferred orientation, consistent with the biaxial stretching of the film.

I/T	$X_1(20)$	$X_2(20)$	$X_1(50)$	$X_2(50)$	$X_1(80)$	$X_2(80)$
I_{040}	4591	3442	4803	3814	4592	4588
I_{110}	1398	1111	1513	1230	1461	1461
I_{040}/I_{110}	3.284	3.098	3.168	3.100	3.14	3.14

Table 8.1: Relative intensity of the two main peaks at room temperature before and after thermal treatment at 20, 50 and 80°C.

8.4 Thickness Distribution

As explained in section 7.2, the DMA7 apparatus allowed us to measure the sample thickness under a preset compressive mechanical stress. For these measurements an initial static load of 100 Pa was applied in order to ensure a good mechanical contact between the upper plate and the sample.

This allowed us to compare the initial thicknesses under the same stress at room temperature. The obtained initial thicknesses as well as the mean value are presented in Fig.8.4. The average thickness was found to be 67 μm with a standard deviation of 2.7 μm. This value is in good agreement with the value of 70 μm reported by the manufacturer.

8.5 Characterisation of the Cellular Structure

The cellular structure was characterized in terms of the average cell size in the three spatial directions.

SEM micrographs of samples X_1 and X_2 (see Fig.7.12) were subdivided by drawing equidistant, parallel lines in the considered direction [411] as shown in Fig.8.5. The number of cells crossed by a particular line was determined and the average size, $< L >$ calculated as:

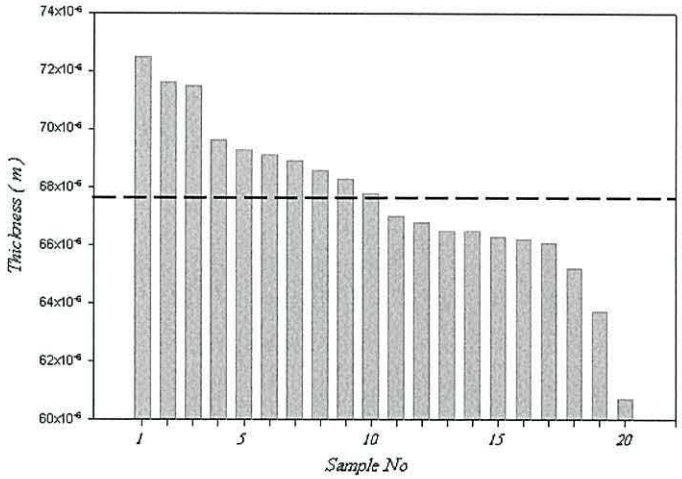

Figure 8.5: Thicknesses of the samples utilised in mechanical measurements and the average thickness value.

$$< L >= \frac{L_t}{N} \tag{8.2}$$

where L_t and N are the length of the line and the number of cells crossed respectively.

Due to the low rigidity of the material, it was technically difficult to mount samples accurately in one orientation making it difficult to obtain completely perpendicular cross-section SEM micrographs. Hence, the thickness appears distorted in SEM micrographs. As a consequence, we were not able to determine the sample thickness accurately. As we saw in the previous section, a total thickness of $\sim$ 70 μm can be supposed for all samples.

In addition, the thickness of the polymer layers is not small compared to the thickness of the air layer. As a consequence, equation 8.2 cannot be used without making an appreciable error in the determination of cell size in thickness direction, $\vec{x}_3$.

A total of six SEM micrographs (taken from different samples) covering a total length of 230 μm were analysed (three for X_1: p_{11}, p_{12}, p_{13} and three for X_2: p_{12}, p_{22}, p_{23}, where the first number labels the micrograph and the second, the direction). The obtained number of cells, N, as well as the average value, $< N >$ and the averaged dimension, $< L >$, for each picture are shown in Table 8.2.

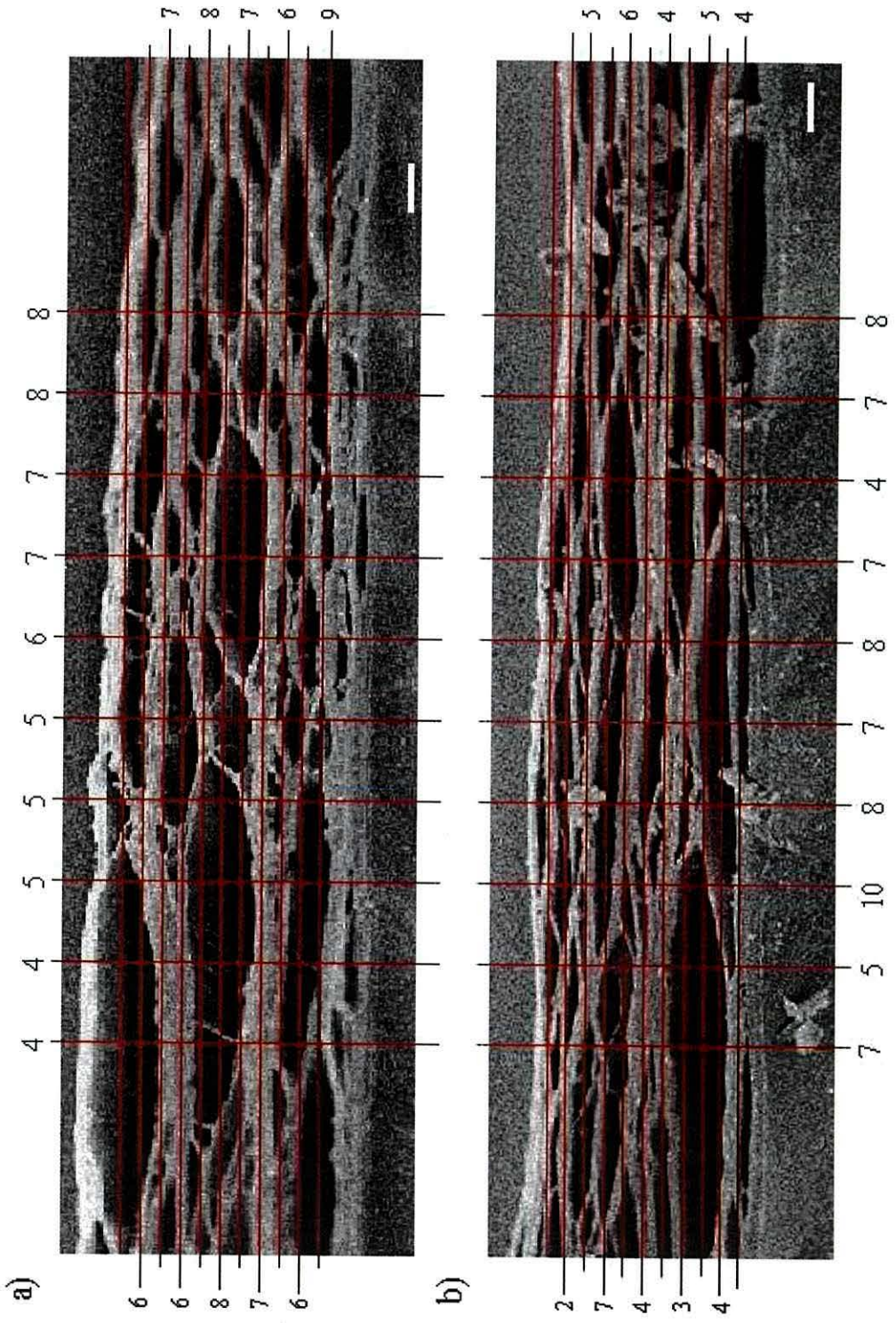

Figure 8.6: Division for cell size determination for sample 1 in a) $\vec{x}_1$ and b) $\vec{x}_2$ directions. Bar is 10 μm.

X1				*X2*			*X3*				
p_{11}	p_{12}	p_{13}	p_{21}	p_{22}	p_{23}	p_{11}	p_{12}	p_{13}	p_{21}	p_{22}	p_{23}
6	8	8	2	5	7	4	6	8	7	6	5
7	6	6	5	6	3	4	5	8	5	8	4
6	8	9	7	6	6	5	7	4	10	8	7
8	7	7	6	6	4	5	7	7	8	7	4
8	9	5	4	5	3	6	5	8	7	7	5
7	10	8	4	4	4	7	5	9	8	7	7
6	9	8	3	5	0	7	7	8	7	6	6
6	9	4	5	4	5	7	7	8	4	8	6
7	8	7	4	4	2	8	5	6	7	7	7
9	6	8	4	5	4	8	6	7	8	7	4
$< N >$											
7	8	7	4.4	5	3.78	5.9	6	6.54	7.1	7.18	5.66
$< L > (\mu m)$											
32.63				55.16				6.93			

Table 8.2: Averaged number of cells, $< N >$ and lengths, $< L >$ in the three spatial directions.

From the values in Table 8.2 the following anisotropy ratios (section 4.7) were calculated:

$$R_{12} = 1.69 \tag{8.3}$$

$$R_{13} = 7.96 \tag{8.4}$$

$$R_{23} = 4.71. \tag{8.5}$$

Measuring the thickness of air and polypropylene directly on SEM micrographs assuming a total thickness of 70 μm yielded estimated values for the total thickness of the air and polypropylene layers of 42.3 μm and 27.7 μm respectively for sample sample X_1, *i.e.*, $\rho_f^1 \sim 347$ Kg m^{-3}) and 35.4 μm and 34.6 μm for sample X_2, *i.e.*, $\rho_f^2 \sim 437$ Kg m^{-3}. These values yielded an average density of $\rho_f \sim 392$ Kg m^{-3}. However, capacitance measurements (see section 10.1) yielded thicknesses of 46 μm and 24 μm for air and polypropylene layers respectively which correspond to $\rho_f \sim 330$ Kg m^{-3}.

Figure 8.7 shows a detail of the SEM micrograph. As readily observed, the average cell wall thickness in the directions $\vec{x}_1$ and $\vec{x}_2$ is less than 1 μm, and therefore, much lower than that in the thickness direction $\vec{x}_3$. It can also be seen that several PP layers are stuck together. This suggests that the gas can easily leak from some voids either during the fabrication and/or during the preparation for SEM micrographs as shown in Fig.8.8. This would also explain the relatively high densities estimated from direct observation of the SEM pictures.

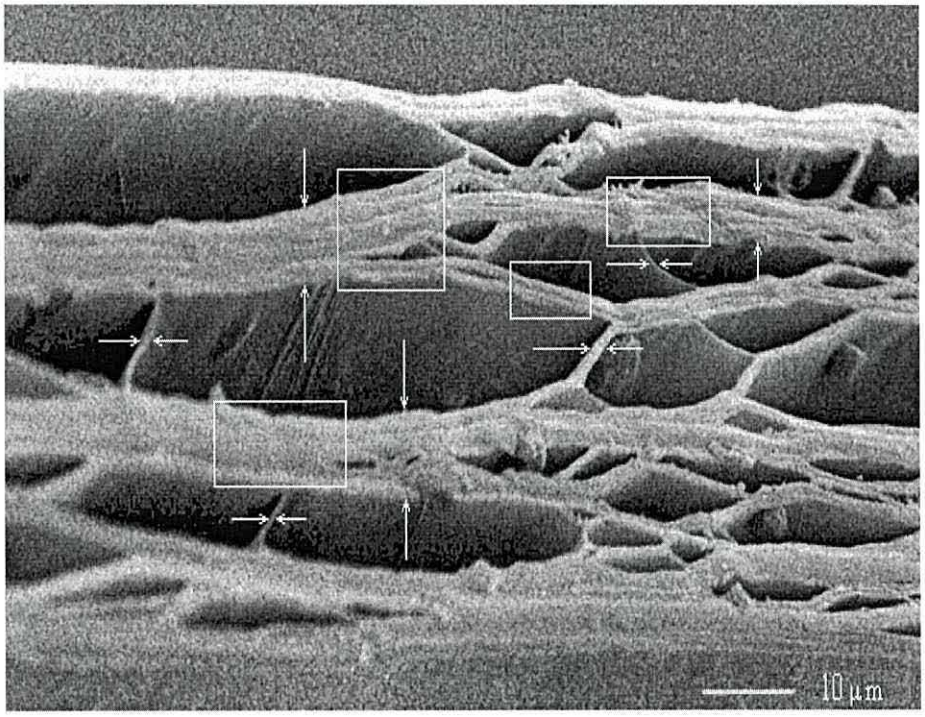

Figure 8.7: Detail of a SEM picture showing the difference in cell wall thickness in lateral and thickness directions. Also stressed is the presence of various PP layers stuck together.

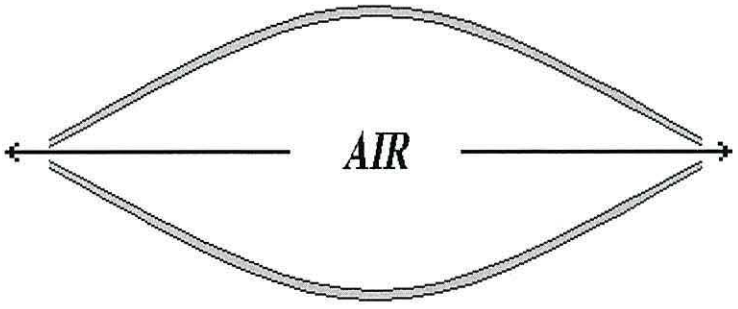

Figure 8.8: Proposed mechanism for the leakage of the gas out of the voids.

8.6 SUMMARY

The physico-chemical properties of the foamed polypropylene were studied using different techniques such as DSC, TGA, EDX, WAXD, DMA and SEM.

The raw material was found to be isotactic PP with a degree of crystallinity around 50% and a wide distribution in the spherulite sizes. Evidence of melting was found at temperatures as low as 50°C corresponding to the melting of spherulites of smaller sizes. The bigger spherulites are crystallized in the monoclinic system, highly oriented in the plane and neither melt nor undergo a phase transition at least for temperatures below 80°C.

The presence of some additives such as $CaCO_3$ (around 4%), and probably TiO_2 was detected. In addition, in the electroded samples we also detected the presence of some additives with high decomposition temperature, *e.g.*, epoxy probably used for attaching the electrodes although the evidence on this point is not clear.

SEM micrograph analysis revealed plane-to-thickness anisotropy characterised by anisotropy ratios as high as 8 and 4.7 and in-plane anisotropy characterised by an anisotropy ratio of 1.7.

SEM micrographs also revealed that the thicknesses of cell walls in the in-plane directions are much thinner than those in the thickness direction. The micrographs also showed a series of PP layers stuck together suggesting that during the fabrication of the foam and/or during the handling for the required preparation of samples for SEM microscopy, the gas leaked out of some voids either to other voids or out of the sample. We propose that the leaking occurs in voids with holes in the lateral cell walls, *i.e.*, in open-cell voids.

Chapter 9

Mechanical Characterization

To understand fully the electromechanical properties of electroactive PP foam it is necessary first of all to establish the mechanical properties of the material. This chapter reports the results of a detailed investigation of the mechanical properties covering the temperature range -30 to 140°C, in which the electrical and piezoelectric properties of the foam are likely to be utilised

9.1 Thermal Expansion

The thermal stability of the PP foam was studied as described in section 7.2.1. The observed strain values and the calculated thermal expansion coefficients (equation 4.40) for different values of the static mechanical stress are shown in Figs.9.1 and 9.2 respectively.

As shown in Fig.9.1, even for low values of the applied stress (<10 Pa) the sample is clearly unstable at temperatures above 60°C. The large strain values in Fig.9.1 indicate that contraction is mainly due to a decrease in the thickness of individual cells.

From Fig.9.2 it can be seen that increasing the mechanical stress both increases the rate of contraction in the temperature range (20-100)°C and decreases the temperature at which it reaches its maximum value. Hence, increasing mechanical stress decreases the thermal stability of the material.

In order to investigate the reversibility of the processes involved in the contraction,

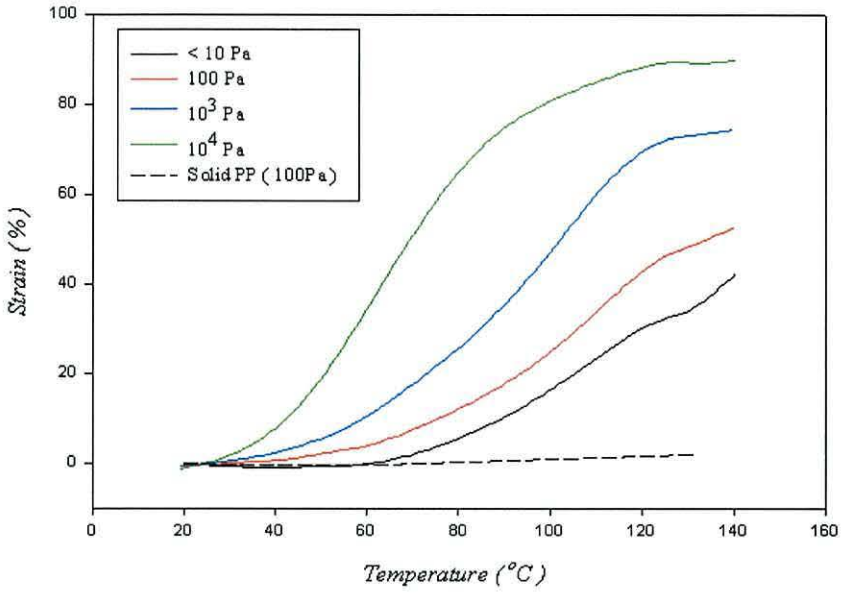

Figure 9.1: Decrease in thickness of foam samples as a function of temperature for different static loads. The change is expressed as a percentage of the original thickness (strain). Also shown is the result for a solid PP sample. Heating rate 3°C min^{-1}.

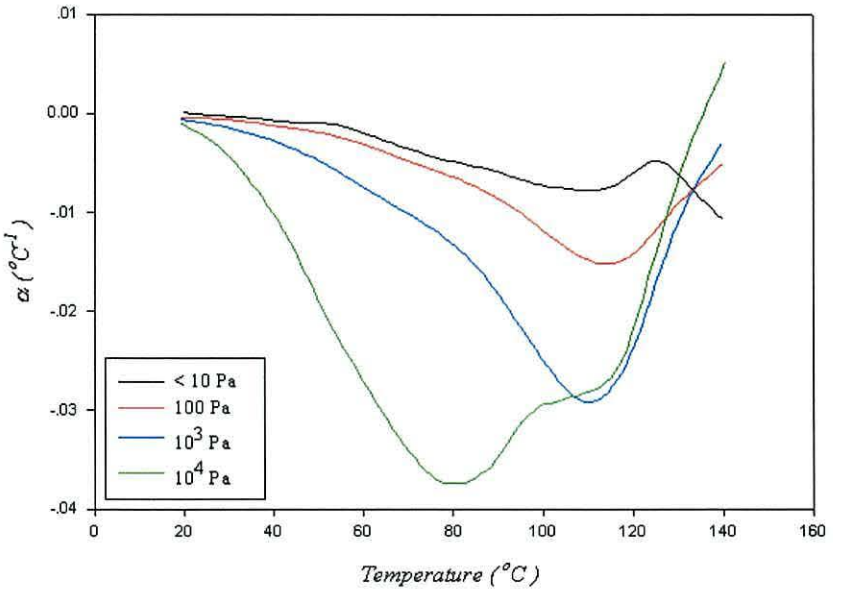

Figure 9.2: Thermal expansion coefficients derived from Fig.9.1.

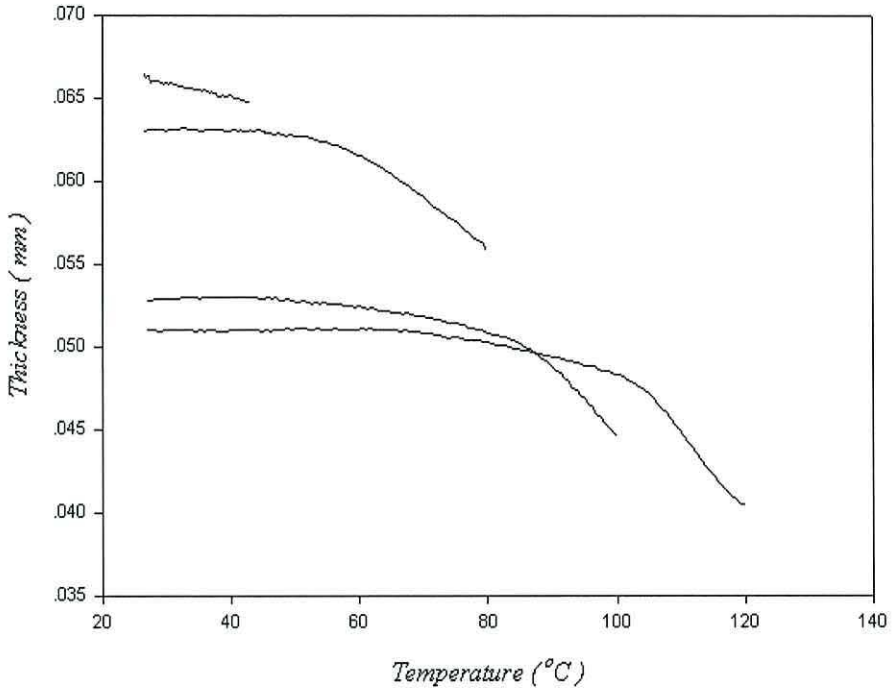

Figure 9.3: Thickness variation of a polypropylene foam sample in partial TMA experiments. Succesive runs to higher temperature show that up to 80°C sample contraction is irreversible. Applied mechanical stress 100 Pa. Heating rate 3°C min^{-1}.

a partial experiment under a compressive load of 100 Pa was performed. The thermal stability was measured up to a predetermined temperature. After heating, the sample was inmediately cooled to room temperature and the next run performed to a higher temperature. The thickness variations are shown in Fig.9.3 from which we see that the contraction is irreversible for temperatures below 80-100°C while it is almost completely reversible at higher temperatures. This supports the interpretation of the data in Figs.9.1 and 9.2 that the cellular structure in the foam begins to collapse at relatively low temperatures even under modest mechanical load. Above about 100°C, the response is dominated by the polymer itself.

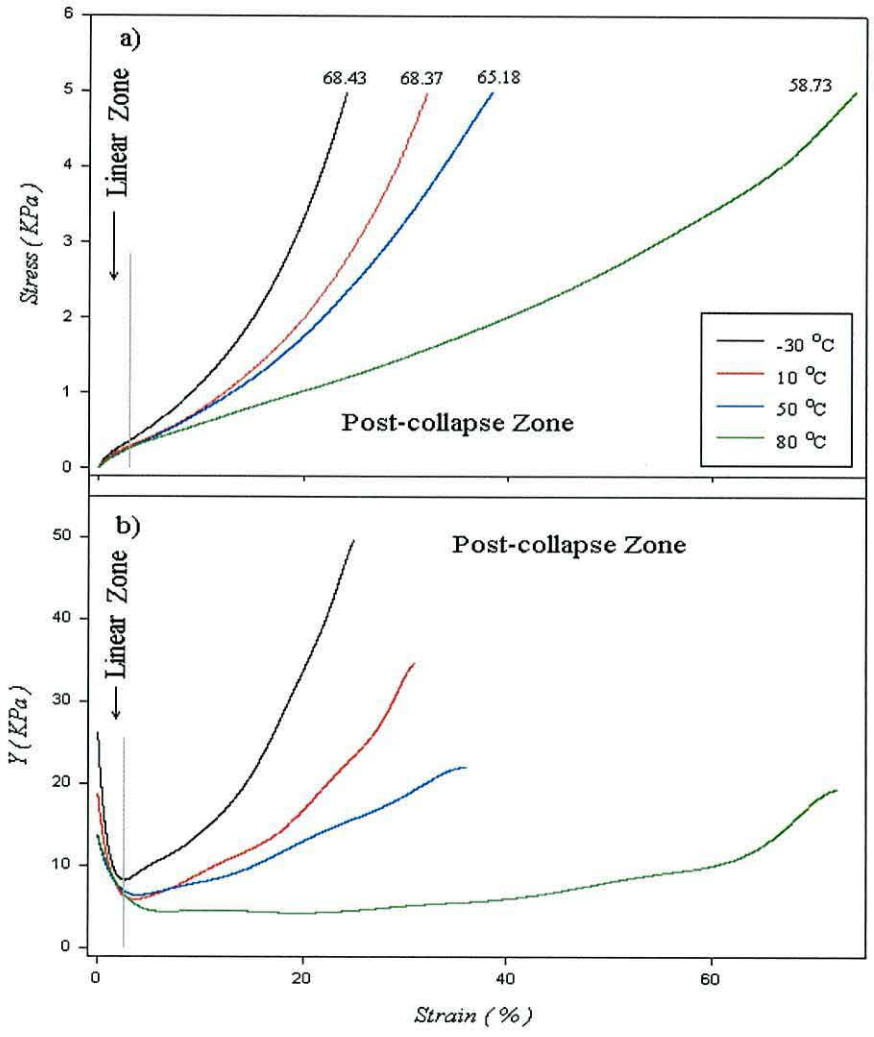

Figure 9.4: a) Strain-stress curves at different temperatures and b) Young's modulus calculated from the curves in a). The initial thicknesses (in μm) are also indicated.

9.2 Stress-Strain Curves

Stress-strain curves were obtained at different temperatures as described in section 7.2.2 and are presented in Fig.9.4 a). The calculated thickness Young's moduli, Y_3, are shown in Fig.9.4 b). Two zones can be distinguished in these figures, *viz*, linear and post-collapse zones. As we mentioned in section 4.7.1 for strain values up to around 3%, the response is dominated mainly by the bending of the cell walls (linear zone). For higher strain values, the structure collapses so that the enclosed air dominates the mechanical response (post-collapse zone).

The obtained values of the Young's moduli, are unusually low for closed-cell polymeric foams [280][14][1] especially for high density foams.

In the linear zone, Young's modulus very strongly depends on the cellular structure, *i.e.*, on the shape of the cells. Moreover, Young's modulus is lower in the direction perpendicular to that of maximum elongation of cells and decreases with increasing anisotropy ratio (section 4.7.1). The low Young's moduli obtained then reflect the high plane-to-thickness anisotropy reported in section 8.5.

In the post-collapse zone, Young's modulus depends mainly on the response of the enclosed gas. The low Young's moduli in this zone suggest high values of the Poisson's coefficients (equation 4.42), ν_{31} and ν_{32} and/or a significant loss of gas.

In Fig.9.5 we present the stress versus the volumetric strain (equation 4.106) obtained from data in Fig.9.4 a) together with the fitting curves under the assumption that the samples were closed-cell.

From the fitting process, average Poisson's coefficients[2] $\bar{\nu} > 0.4$. were obtained for temperatures in the range (-30 to 50)°C. Such high values are difficult to accept. First of all, they would result in lateral expansions that could be detected even with the naked eye. Experimentally, lateral expansion as a result of compression in thickness was not observed at all. On the other hand, in view of equation 4.43 and assuming that we are in the elastic regime, the Poisson's coefficient ν_{31} is given by:

[1] Typical values are around three orders of magnituide greater.

[2] Here we assume that, in a first approximation $\nu_{31} \approx \nu_{32} = \bar{\nu}$.

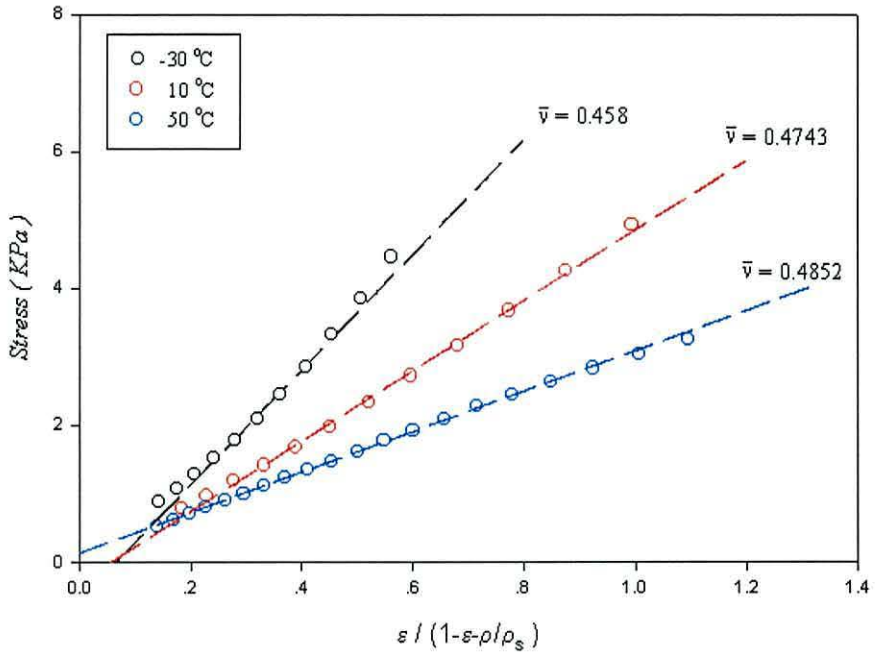

Figure 9.5: Representation of the stress versus the volumetric strain $\epsilon/(\phi - \epsilon)$.

$$\nu_{13} = \frac{Y_1}{Y_3}\nu_{31} \tag{9.1}$$

where Y_1 is the Young's modulus measured in direction $\vec{x}_1$. Introducing $\nu_{31} = 0.4$ into expression 9.1, and considering that, due to the cellular structure, Y_1 is much higher than Y_3, gives a Poisson's coefficient ν_{13} close to, if not higher than, unity. Consequently, we must accept that an important loss of gas takes place even on the relatively short timescale of the present experiments. Air diffusion in closed-cell polymeric foams at such short times is usually neglected [280][14]. Therefore, the results presented here indicate that the PP foam behaves as an open-cell foam or, at least, as partially open. As we saw in section 8.5 the cell wall thicknesses in the lateral directions, $\vec{x}_1$ and $\vec{x}_2$ are around 1 μm or less. Therefore, as a result of the increasing pressure exerted by the air as the stress increases, some walls may break or gas can leak out between the leaflets of the laminated in-plane walls. Thus, not only can air out of the cells but also, out of the sample (see Fig.8.8).

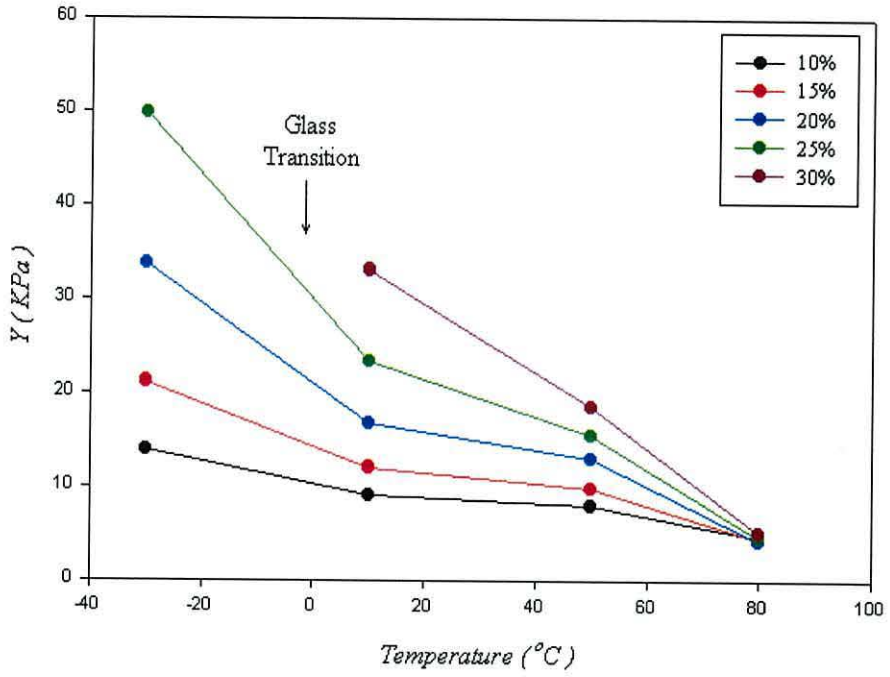

Figure 9.6: Representation of Young's modulus as a function of temperature for sample strained at different values.

The effect of temperature on Young's modulus is clearly seen in Fig.9.6, where the variation of Young's modulus in Fig.9.4 b) with temperature is plotted for different values of the strain. From Fig.9.6 we see that Young's modulus decreases with temperature in the considered temperature range for all strain values. In addition, there is a relatively high decrease of the Young's modulus above -30°C. This reflects the glass transition of polypropylene (∼-20°C) (see Table 2.5). Also from Fig.9.6 we see that, above 50°C, Young's modulus decreases with temperature at a higher rate than it does in the range (10-50)°C, especially for low strain values. This may be due to a decrease in Young's modulus for the polypropylene or an increase of its porosity enhancing the diffusion of gas out of the sample.

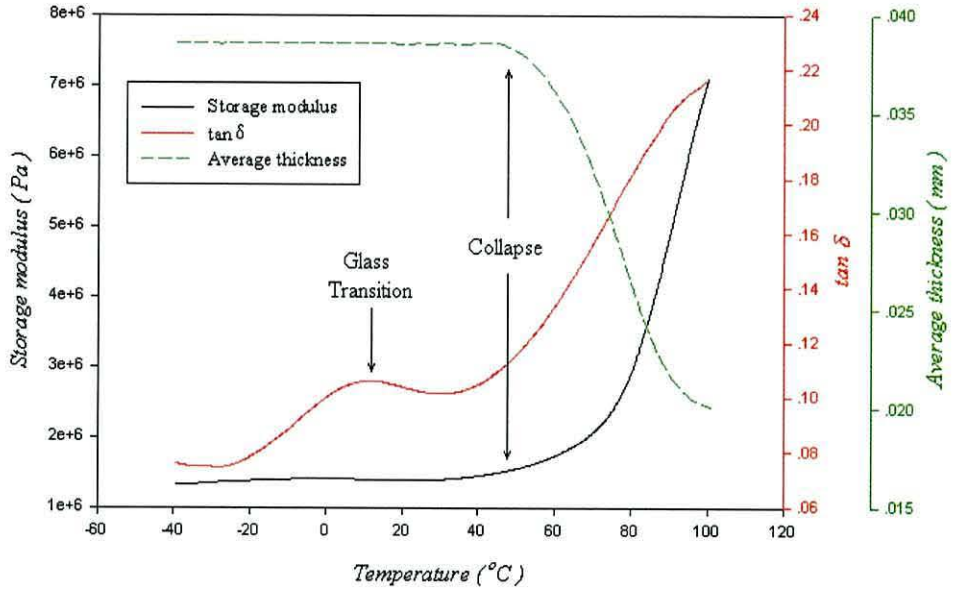

Figure 9.7: Storage modulus and mechanical loss tangent for a polypropylene foam sample subjected to a static stress of 10^4 Pa and a dynamic stress of 4000 Pa. Also shown are the mean positions of the probe (average thickness).

9.3 DYNAMICAL-MECHANICAL ANALYSIS (DMA)

The storage modulus and mechanical loss tangent, (equations 4.76 and 4.78), of the polypropylene foam were measured as described in section 7.2.2. The results are shown in Fig.9.7. For comparison we also measured the corresponding parameters for a solid polypropylene sample (Fig.9.8).

The storage modulus at temperatures below 40°C in Fig.9.7 is around 1.2 MPa, and thus, more than two orders of magnitude greater than values extracted from stress-strain curves presented in section 9.2. The applied static stress (10^4 Pa) produced a compression of around 40% as suggested by the value of the initial thickness (~37 μm). As a consequence, the dynamic strain arising from the superimposed dynamic stress (4000 Pa), from which storage modulus and mechanical loss tangent were calculated, corresponded to that of a compressed sample. As density increases, the effect of polypropylene becomes more important in the mechanical response of the foam (section

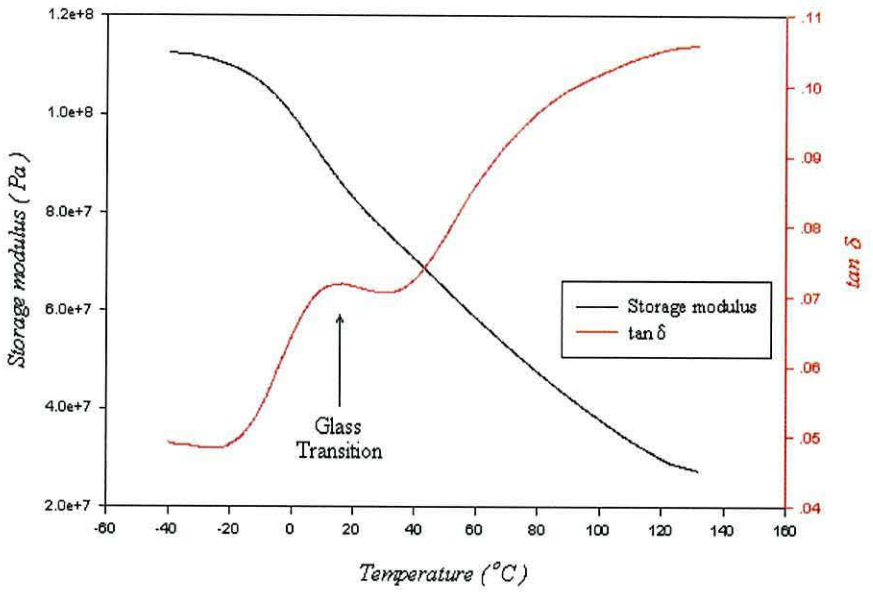

Figure 9.8: Storage modulus and mechanical loss tangent for a solid polypropylene sample subjected to a static stress of 10^4 Pa and a dynamic stress of 4000 Pa.

4.7.1) a fact that is reflected in the increase of the storage modulus.

The maximum in the mechanical loss tangent observed at about 10°C in Figs.9.7 and 9.8 is associated with the glass transition of the polypropylene [410].

The average thickness suggests that for temperatures above 40°C the cellular structure starts collapsing. Hence, the foam tends towards the behaviour of solid polypropylene above 40°C with the storage modulus increasing towards that of the solid polypropylene.

Young's modulus of the PP foam has been measured by several authors using a range of different techniques. For example, fitting capacitance data measured around the piezoelectric thickness resonance ($\sim$ 600 KHz) with the theoretical expression (equation 5.106) yields values around 2.2 MPa [27][373]. Measurements of the mean amplitude of the thickness vibration resulting from the application of alternating voltages (13.64 Hz) yielded Young's modulus of about 0.95 MPa [399][16][381] and about 0.89 MPa for DC voltages [380][299].

In all the experiments above, samples deformed less than 10 nm which corresponds

to strain values less than 1.5×10^{-4}%. For such small compressions, the response is dominated by the cell wall bending. The corresponding Young's modulus is then expected to be much higher than that at higher strain values as indicated in section 9.2 (Fig.9.4 b)).

In addition, the strain-stress curves here correspond to very low frequency measurements (Fig.7.3) and it is known that Young's modulus decreases with with decreasing frequency [412].

A Young's modulus of 1.5 MPa has been reported from measurements of the (dynamic) piezoelectric d_{33} coefficient in the sensor configuration (direct effect). The d_{33} coefficient was measured under the application of a dynamic stress (10 Hz) of $\sim$ 6300 Pa superimposed on a static stress of 0.1 MPa [299]. This result is in good agreement with the storage modulus presented in Fig.9.7.

It must be mentioned here though, that there are some factors that make it difficult to accurately measure Young's modulus from piezoelectric measurements. To begin with, not all voids are electroactive. Only those with thicknesses within a certain range fullfil the conditions for Paschen breakdown, thus becoming electroactive. On the other hand, for piezoelectric measurements samples must be electroded and poled. Irreversible compressions as a result of occasional stresses suffered by the material during electrode deposition and/or poling processes would lead to an increase in the sample stiffness.

Young's modulus of PP foam has also been calculated from mechanical measurements, *i.e.*, from the measured stress established (5 seconds) after compressing the sample to a predetermined strain [299][399][16]. From these mesurements, a constant Young's modulus of 0.9 MPa was obtained in the strain range (0-20)%. Considering that Young's modulus is constant over this range and assuming that PP layers do not compress, the d_{33} coefficient (equation 6.27) must increase by around 6% with increasing strain from 0 to 20%. However, the same authors report a decrease of d_{33} with increasing static stress (increasing strain). Such a decrease has also been observed by us, as mentioned in section 7.4.1 (Fig.7.11). Unfortunately, the initial thicknesses of the

samples were not reported by the authors. Therefore, it remains unknown whether the experiments were performed on previously compressed samples (probably as a result of the set up). The high Young's modulus obtained suggests that this was probably the case.

9.4 Creep and Recovery

Creep-recovery curves, (section 7.2.2) measured at 10°C for different values of the maximum stress, σ_{max}, are presented in Fig.9.9 a) from which we can see that, as a result of the compressive stress, the sample contracts rapidly up to relatively high strain values (instantaneous creep). Following the instantaneous response, the strain increases at much lower rate (retarded creep). After the stress is released, the sample recovers rapidly at first (instantaneous recovery), but then more slowly (retarded recovery) until a stationary value of the strain is reached (remanent strain).

In Fig.9.9 b) is plotted the time derivative of the strains in Fig.9.9 a) from which it is seen that instantaneous strain and recovery take around 15 s to complete. This is however due to the time constant of the DMA7 apparatus [413] and cannot be ascribed to any property of the foam.

An instantaneous strain of about 25% (for a maximum stress of 5000 Pa) corresponds to a decrease in thickness of around 17 μm. Since this value nearly corresponds to that of the total thickness of the PP (24 μm, see section 9.2), the instantaneous strain must be mainly due to the contraction of the voids rather than of the cell walls. Viscous flow of polypropylene seems to be more related with the retarded response.

In Fig.9.10 the values of ϵ_i and ϵ_{max} in Fig.9.9 a), are plotted as a function of the stress. Also plotted is the stress-strain curve obtained for a ramp stress function at 10°C (Fig.9.4 a)). From Fig.9.10 we see that there is good agreement between the two for strain values up to $\sim$ 25%. We also show two strain-stress pairs obtained from capacitance measurements (see section 10.1). These points lie close to the other curves and show good agreement with the mechanical measurements for strain values up to

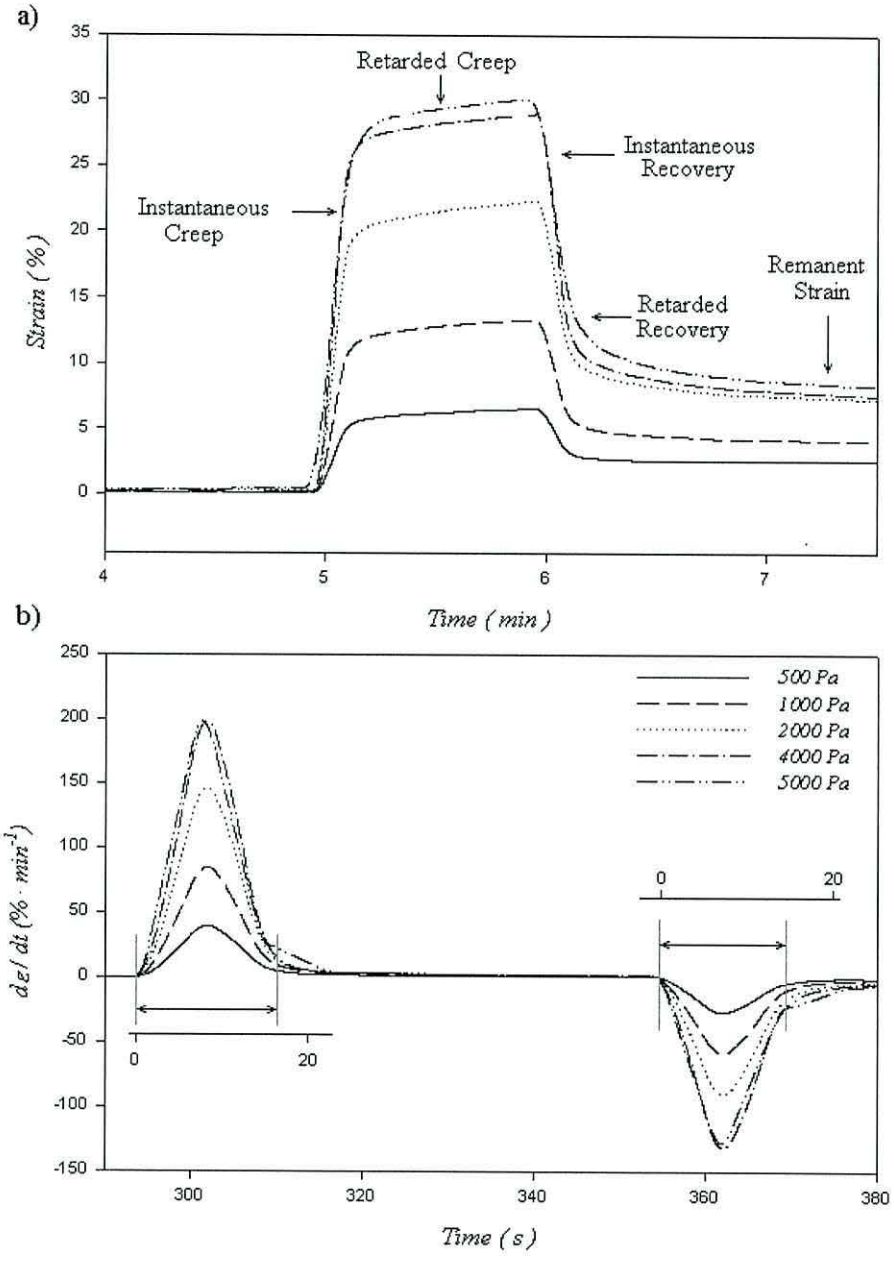

Figure 9.9: Creep-recovery curves for different values of the stress. a) Time response of the strain to a step increase/decrease in stress. b) Time rate of change of the strain.

15%.

From Fig.9.9 a) we can see that, the retarded and remanent strain increase as the maximum stress increases. This supports the idea that the retarded response is due to the viscous flow of the polymer. Hence, since viscous flow is irreversible, the recovery (remanent strain) of the cellular structure after releasing the stress decreases (increases) with increasing viscous flow of the polymer, and hence with increase in the retarded strain.

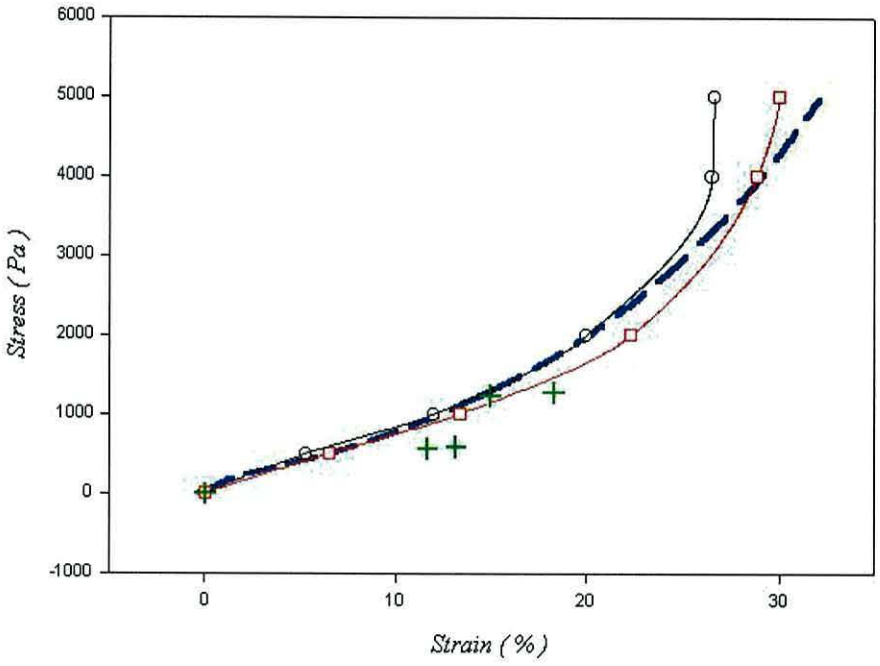

Figure 9.10: Variation of (o) ϵ_i, (□) ϵ_{max}, with strain obtained from a creep experiment at 10°C plotted together with the Matlab® interpolation curves (solid lines) and the stress-strain curve (- -) obtained from a ramp stress function at 10°C. Also plotted (+) are the stress-strain points obtained from capacitance measurements (see section 10.1)

The effect of the time duration of the stress, $t' = t_{max} - t_0$ on the creep-recovery ($\sigma_{max} = 10^4$ Pa) behaviour was also studied and is shown in Fig.9.11 for different values of t'.

In Fig.9.11, retarded, ϵ_r, and maximum, ϵ_{max}, strains do not depend to any significant extent on t' for $t >$ 1 min. In contrast, the remanent strain, ϵ_∞, strongly

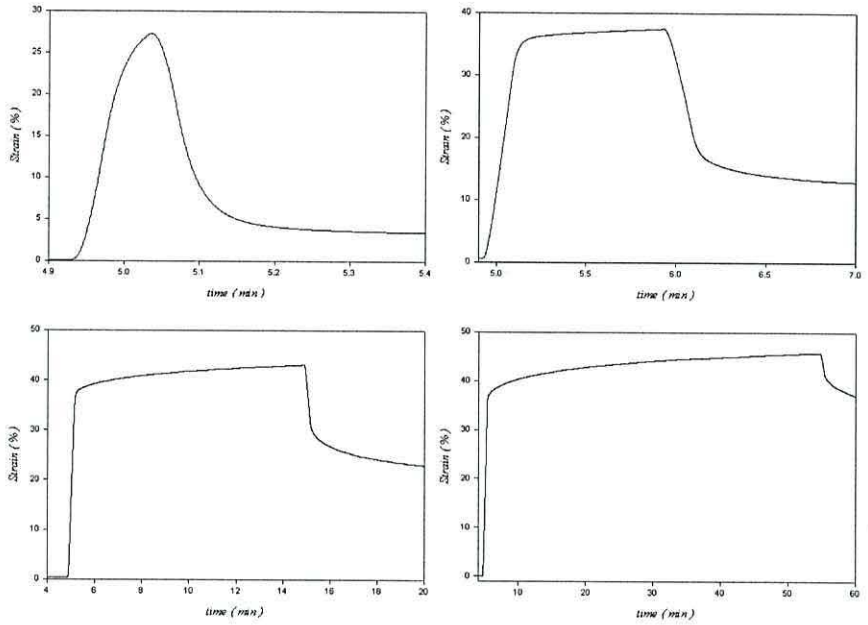

Figure 9.11: Creep-recovery curves for stresses prolonged for different times. Maximum stress 10^4 Pa.

increases with increasing t'. It seems, therefore, that in response to an applied stress, the solid phase is reversibly deformed and air diffuses out of the cells. When the stress is removed, the cellular structure tends to recover and the gas leaks back into the cells. When the stress is applied for long times, polymer flow (see section 4.3.2) is more extensive leading to the observed increase in the remanent strain.

Finally we investigated the effect of temperature on the creep-recovery response ($\sigma_{max} = 10^4$ Pa). The results are shown in Fig.9.12. For temperatures below 50°C the retarded strain is $\sim$ 6%, above 50°C, $\sim$ 9% and at 80°C $\sim$ 15%. Also from Fig.9.12 we can see that the instantaneous strain increases with temperature, especially at 80°C. This increase is in good agreement with the observed decrease of the Young's modulus presented in Fig.9.4 b).

From Fig.9.12, the remanent strain, ϵ_∞, increases with increasing temperature and the increase is especially rapid above $\sim$ 60°C. As temperature increases, molecular motions are less impeded so that the polymer can flow more easily. The observed increase in the retarded reponse with temperature explains the observed increase of the

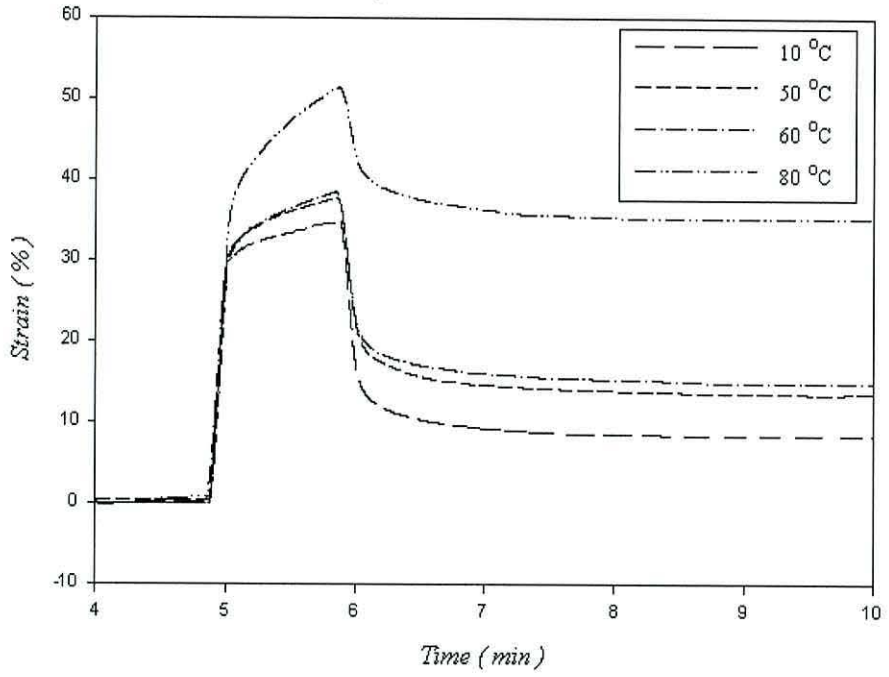

Figure 9.12: Creep-recovery curves at different temperatures. Maximum stress 10^4 Pa. Recovery time 4 minutes.

remanent strain.

9.5 SUMMARY

The mechanical stability of PP foam subjected to low compressive loads is limited to temperatures below $\sim 60^{o}$C. For higher temperatures a significant reduction in thickness was observed as a result of the collapse of the cellular structure. Upon increasing the compressive stress these effect were seen at lower temperatures.

As a result of gas leakage, the Young's modulus calculated from strain-stress curves is low when compared to the usual values obtained for closed-cell materials. The Young's modulus was observed to decrease with temperature especially above -30^{o}C (Fig.9.6), below the glass transition of the polymer, and above 50^{o}C. The latter probably reflects the decrease of the Young's modulus of the polypropylene and/or the increase of the porosity which would facilitate the diffusion of gas out of the foam.

The dynamic Young's modulus measured under a large static compressive stress was found to be around two orders of magnitude higher than those determined from strain-stress curves. Under large compressive stress, the material density increases leading to an increase in the Young's modulus. At temperatures higher than 40^{o}C the cellular structure starts to collapse. Consequently, Young's modulus for the foam begins to increase towards that of solid polypropylene.

The creep response of the foam showed two separated zones. After applying the stress, most of the gas leaks out of the sample leading to strain values up to $\sim$ 30% (5000 Pa). The curve obtained by plotting the instantaneous strain versus the maximum applied stress at 10^{o}C very closely resembles the strain-stress curve at 10^{o}C for strain values up to 25%. Capacitance measurements also give similar strain-stress relations for strain values up to 15%.

After gas leakage, the viscous character of the polymer becomes noticeable. Viscous flow was found to increase both with increasing time of applicaction of stress and with temperature. Since polymer flow leads to irreversible deformations in the cellular structure, the remanent strain increases with increasing time of application of the stress and with increasing temperature.

Chapter 10

Electrical Characterization

In this chapter we report the basic dielectric data, dielectric constant and losses obtained from samples of PP foam. Such data is essential for determining the resonator parameters from the electromechanical measurement reported in Chapter 11. Further, the results of thermally stimulated depolarisation measurements are reported and discussed in relation to the mechanical properties presented in Chapter 9. From these combined results a foundation is established for interpreting the thermal instability effect.

10.1 Dielectric Measurements

The complex capacitance of a non-poled sample was measured over the frequency range (10^4-10^6) Hz. The results are presented in Fig.10.1 from which it is seen that both real and imaginary parts of the capacitance are constant in the considered frequency range. The sample used in this measurement was furnished with circular electrodes 10 mm in diameter as explained in section 7.3.1. Assuming a film thickness of 70 μm (section 8.4) the effective relative permittivity is estimated to be ε_f=1.24.

As we saw in section 8.5 the cell walls in directions $\vec{x}_1$ and $\vec{x}_2$ are much thinner than in directions $\vec{x}_3$. Therefore, the foam can be visualised as a two layer system as depicted in Fig.10.2. Hence, the capacitance of the foam, C_f, will be given by:

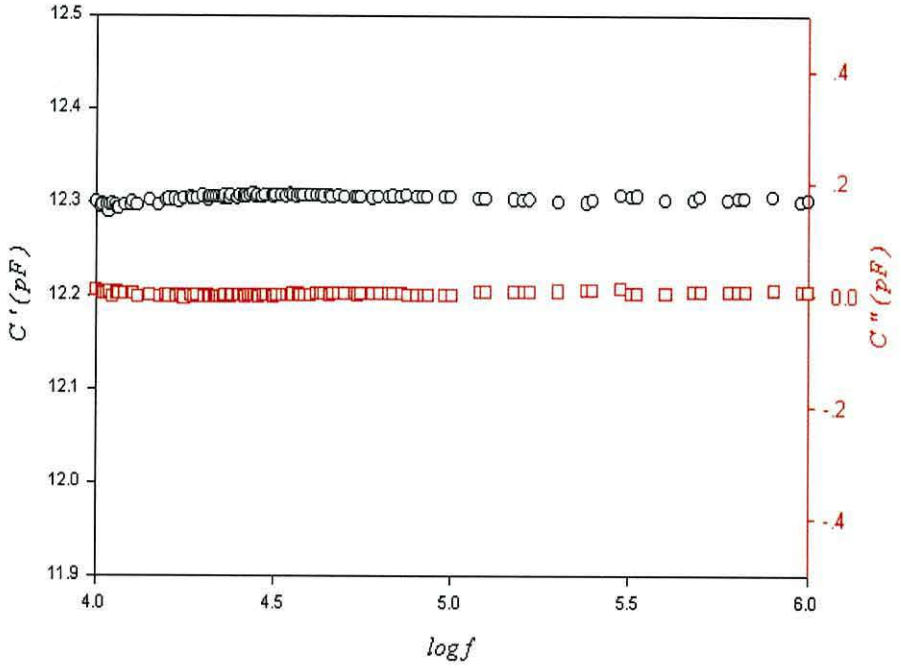

Figure 10.1: Real (o) and imaginary (□) parts of the complex capacitance of non-poled PP foam. Area 0.758 cm^2.

$$\frac{d_f}{A\varepsilon_f\varepsilon_0} = C_f^{-1} = (C_{AIR})^{-1} + (C_{PP})^{-1} = \frac{d_{AIR}}{A\varepsilon_{AIR}\varepsilon_0} + \frac{d_{PP}}{A\varepsilon_{PP}\varepsilon_0}$$

$$= \frac{1}{\varepsilon_0 A}\left(\frac{d_f - d_{PP}}{\varepsilon_{AIR}} + \frac{d_{PP}}{\varepsilon_{PP}}\right) \tag{10.1}$$

where A is the area, d, the thickness and ε, the relative permittivity.

Now, taking $\varepsilon_{AIR} \sim 1$ we have:

$$\varepsilon_f^{-1} = 1 + (\varepsilon_{PP}^{-1} - 1)\frac{d_{PP}}{d_f} \tag{10.2}$$

which, in view of equation 4.93, transforms into:

$$\varepsilon_f^{-1} = 1 + (\varepsilon_{PP}^{-1} - 1)\frac{\rho_f}{\rho_{PP}}. \tag{10.3}$$

Taking the measured value $\varepsilon_f = 1.24$ together with the relative permittivity, $\epsilon_{PP} = 2.2$ and density, $\rho_{PP} = 910$ Kg m^{-3}, of solid polypropylene (see Table 2.5) and using equation 10.3, the foam density, ρ_f is estimated to be 326 Kg m^{-3} which is close to that (330 Kg m^{-3}) reported by the supplier [414][376][387]. This value yields thicknesses of 45.5 and 24.5 μm for the air and the polypropylene layers respectively.

Equation 10.3 relates the relative permittivity of the foam to its density. On the other hand, for an uncompressed sample we have

$$d_{AIR} + d_{PP} \sim= 70\ \mu m. \tag{10.4}$$

and, assuming that the polypropylene layer does not compress, we can assume that

$$d_{PP} \sim 24\ \mu m \sim Constant. \tag{10.5}$$

Using equations 10.3, 10.4 and 10.5 with the capacitance data taken under different compressive loads we can calculate therefore the strain at different applied stresses (Young's modulus).

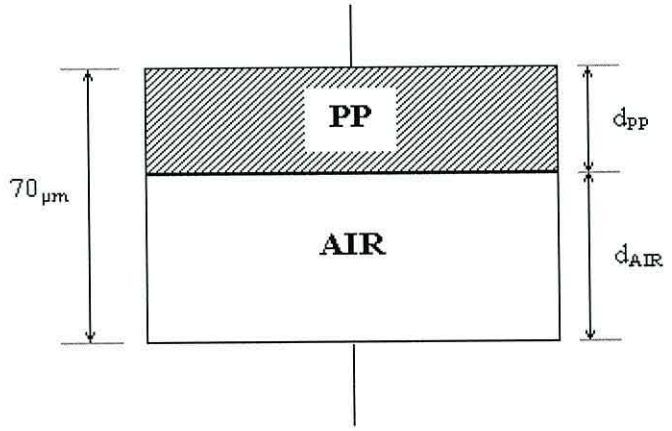

Figure 10.2: Schematic representation of the sample for capacitance measurements.

A non-poled sample with evaporated electrodes 10 mm in diameter was glued to a metallic background using conductive epoxy and stressed by manually locating different

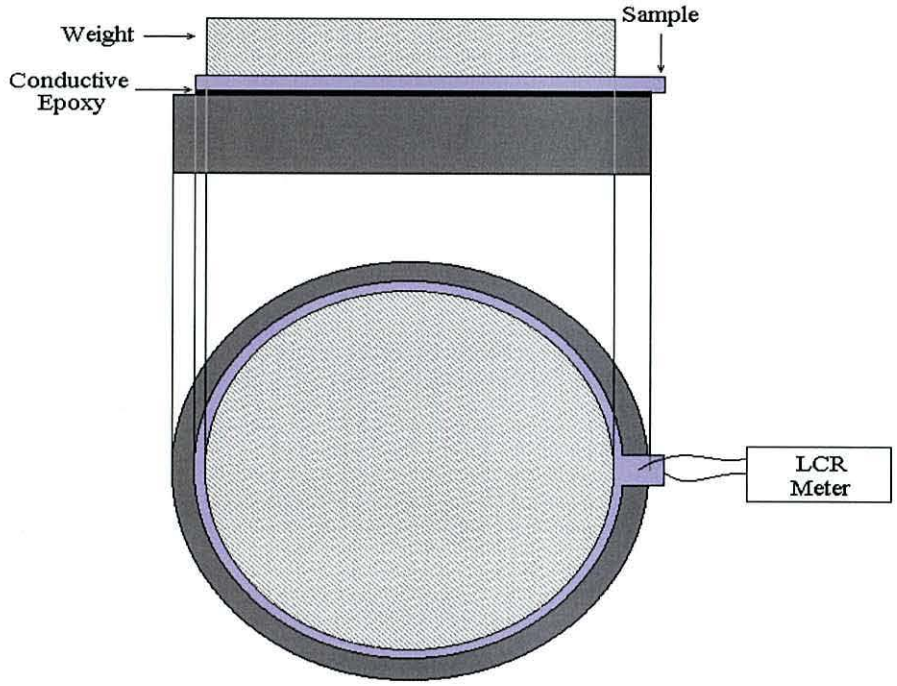

Figure 10.3: Schematic representation of the setup for measuring the capacitance under different compresive stresses.

weights at the upper surface. The capacitance was measured using a Hewlett Packard 4284A precision LCR meter (Fig.10.3).

In Fig.10.4 we present the variation of the capacitance after the application of two different mechanical stresses. The density calculated from the capacitance data of the sample under no load conditions assuming a total thickness of 70 μm was very much higher than that reported by the supplier. Probably, the sample was irreversibly compressed during the gluing. Thus, in Table 10.1 we present the measured capacitance and the relative permittivities, densities and strains calculated assuming values of 60 and 70 μm for the initial thickness of the sample. The strain-stress data were presented in Fig.9.10 in Chapter 9.

Stress (Pa)	0		510			1340		
Capacitance (pF)	14.5		16.8			18		
Thickness (μm)/Parameter	ε	ρ ($Kg\ m^{-3}$)	ε	ρ ($Kg\ m^{-3}$)	*Strain* (%)	ε	ρ ($Kg\ m^{-3}$)	*Strain* (%)
60	1.25	336.1	1.45	518.5	13.7	1.55	595	18.37
70	1.46	526.4	1.69	682.8	11.8	1.81	748.46	15.7

Table 10.1: Measured capacitance and calculated dielectric permittivities, densities and strains for a sample subjected to different stresses assuming two different values of the total thickness. Area=0.785 cm^2.

10.1.1 EFFECT OF VACCUM

The effect of vacuum on the capacitance was also investigated on two corona poled samples X_1 and X_2 (see Fig.7.12). The samples were freely suspended inside a chamber and the capacitance measured at atmospheric pressure.

These samples were provided with electrodes by the supplier. No information was given about the process of electrode deposition. It seems however that the electrodes were not evaporated but otherwise deposited on the material surfaces[1]. Therefore, irreversible compression during electrode deposition cannot be discounted. From the capacitance data in Fig.10.5 at atmospheric presure (1), we calculated the densities ρ_f^1 and ρ_f^2 of samples X_1 and X_2 respectively as well as the average density $\bar{\rho}_f$ and the density ratio, $\rho_f^{12} = \rho_f^1/\rho_f^2$ assuming a total thickness of 60 μm and 70 μm. The results are presented in Table 10.2.

Regardless of the absolute value of the density, it can be seen in Table 10.2 that ρ_f^1 is lower than ρ_f^2 resulting in density ratios of 1.88 and 1.38 for 60 and 70 μm thick films respectively. The density ratio reflects the in-plane anisotropy of the cellular structure ($R_{21} \sim 1.7$).

After making the measurements at atmospheric pressure, the chamber was evacuated

[1] We noted that the electrodes on the samples provided by the supplier were more stable than those evaporated onto a sample. Also treatment with NaOH showed that the required time for removing the evaporated electrodes was much lower than in the other case.

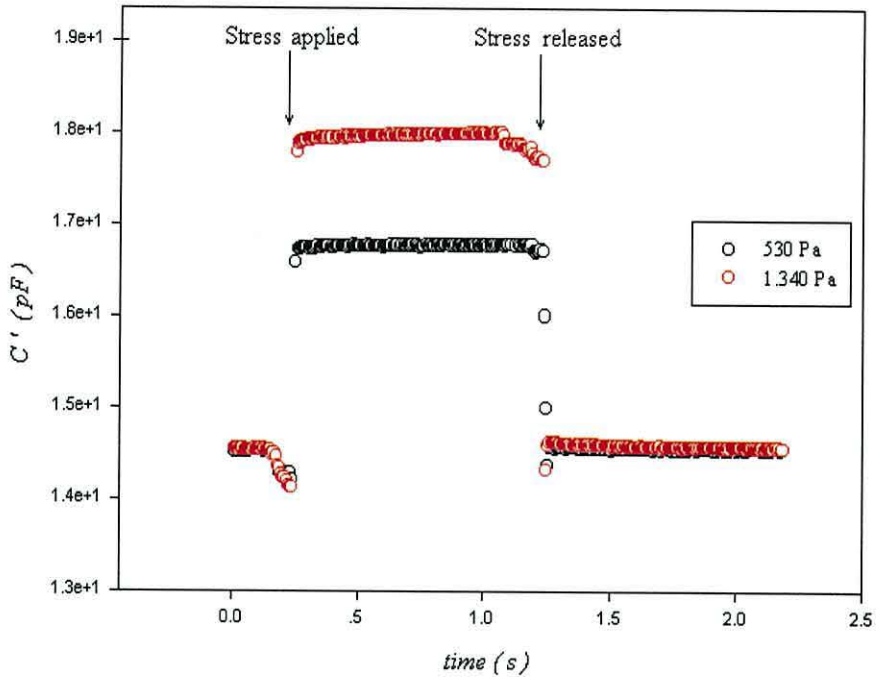

Figure 10.4: Change in capacitance upon applying and removing two different stresses under atmospheric conditions. Frequency 10 KHz. Area 0.785 cm^2

and the capacitance recorded at different stages until a constant value was obtained. The results are shown in Fig.10.5. In the first $\sim$ 10 s or so, the capacitance rapidly decreases by about 25% until it reaches a minimum. This corresponds to an increase in thickness due to the expansion of the sample subjected to a pressure gradient.

Subsequently, the capacitance slowly increased until a stable value was obtained after $\sim$ 55 hours. This slow increase results from the contraction of the sample as the gas diffuses out of the sample. After $\sim$ 55 hours, the pressures inside and outside the sample equilibrate, the contraction finishes and the capacitance displays a stationary value.

During the first $\sim$ 5s or so after vacuum release starts, the samples contract as a result of the pressure exerted by the incoming air. This contraction is accompanied by the observed decrease in capacitance. The pressure gradient drives the air diffusion into the sample. As the gas diffuses into the sample, the foam expands and the subsequent

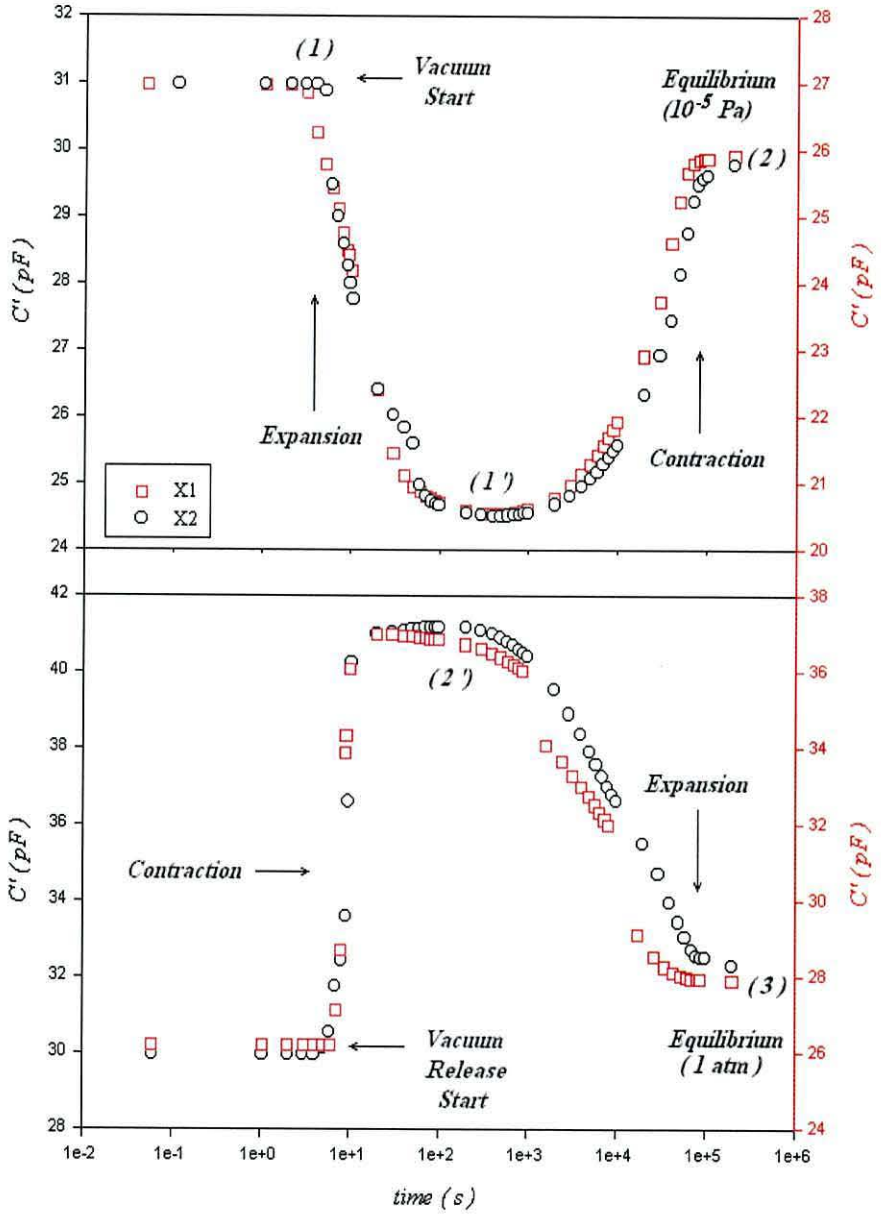

Figure 10.5: Temporal variation of the capacitance during chamber evacuation for (o) X_1 and (o) X_2 samples. Area 1.6 cm^2. Frequency 10 KHz.

Thickness (μm)	ρ_f^1 ($Kg\ m^{-3}$)	ρ_f^2 ($Kg\ m^{-3}$)	$\bar{\rho}_f$ ($Kg\ m^{-3}$)	ρ_f^{21}
60	211	398	304	1.88
70	419	580	500	1.38

Table 10.2: Calculated densities for samples X_1 and X_2 for two values of the total thickness. Also shown are the averaged densities and density ratios.

increase in capacitance is observed. When the pressure inside and outside the sample equilibrates, the sample once again displays a stable capacitance.

The mentioned contraction and expansion expressed in terms of the corresponding strain values, calculated from the capacitance values at different stages of the vacuum process in Fig.10.5, are presented in Table 10.3.

Thickness/Strain	(1′)		(2)		(2′)		(3)	
(μm)/(%)	X_1	X_2	X_1	X_2	X_1	X_2	X_1	X_2
60	−27.7	−16.42	−3.3	−2.5	23.60	19.26	3.12	3.5
70	−23.7	−14.07	−2.8	−2.1	20.24	16.50	2.67	3.0

Table 10.3: Calculated strains at the different stages of the vacuum process in Fig.10.5 for samples X_1 and X_2 calculated assuming 60 and 70 μm for the initial thickness. The strains are calculated taking (1) as the reference state.

The high strain values shown in Table 10.3 and the slow recovery afterwards suggest the presence of some closed cells, in contrast with the results in Chapter 9.

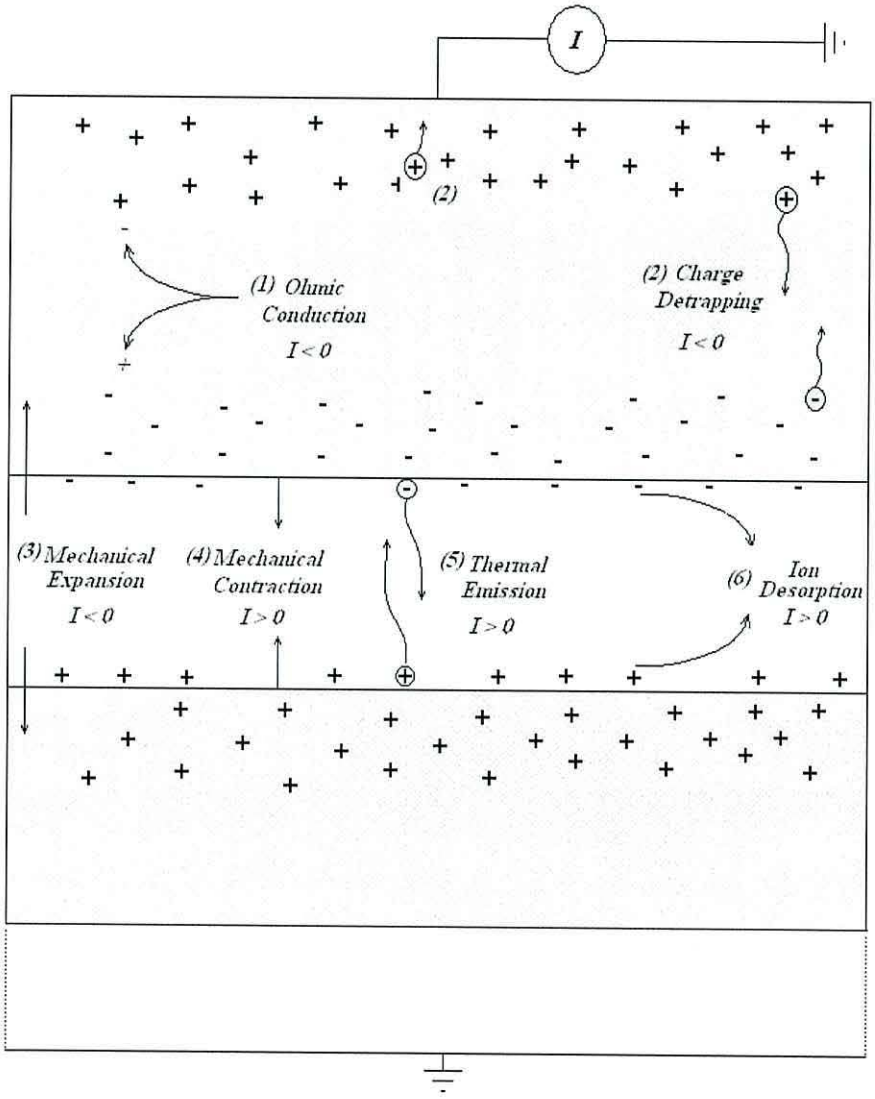

Figure 10.6: Possible processes responsible for thermally stimulated currents in a positive corona poled sample. Also indicated is the sign of the current.

10.2 Thermally Stimulated Currents (TSC)

Thermally stimulated currents (TSC) performed on corona charged samples were obtained as described in section 7.3.2. The several possible processes giving rise to thermally stimulated currents are presented in Fig.10.6.

Ohmic conduction, (1), represents the movement of intrinsic charge carriers through the polymer in the electric field generated by the trapped charges, as the conductivity of the polymer increases.

As the temperature increases, the (thermal) energy of the trapped charges increases. When this energy equals the energy of the trap, the charges can move (2), giving rise to an electric current.

A contraction or an expansion of the thickness of the air layers, processes (3) and (4), modify the electric field inside the sample and then, the charges generated on the electrodes with the subsequent electric current.

The thermal emission (5) is the movement of charges on surfaces state through the air in the electric field generated by the trapped charges. This ionic species on surfaces states may also desorb from the surface and return into the gas phase, process (6), producing a current of the same sign as that in process (5).

10.2.1 Effect of the Stress

The TSC currents obtained for high and low mechanical stress are presented in Fig.10.7 from which we see that under low stress conditions, no measurable current is observed below 60°C. For the clamped sample, on the other hand, a positive-going current is observed at temperatures as low as 20°C. This is in good agreement with the TMA results in section 9.1 where we saw that increasing the stress results in a decrease of the thermal stability of the sample. Therefore, we propose that the positive-going current in Fig.10.7 a) is due to the mechanical compression of the sample rather than to charge detrapping.

Since we have measured the thermal contraction, $l_3(T)$ (Fig.9.1) we can estimate

the thermally stimulated current arising from that contraction [2]. This current will be given by:

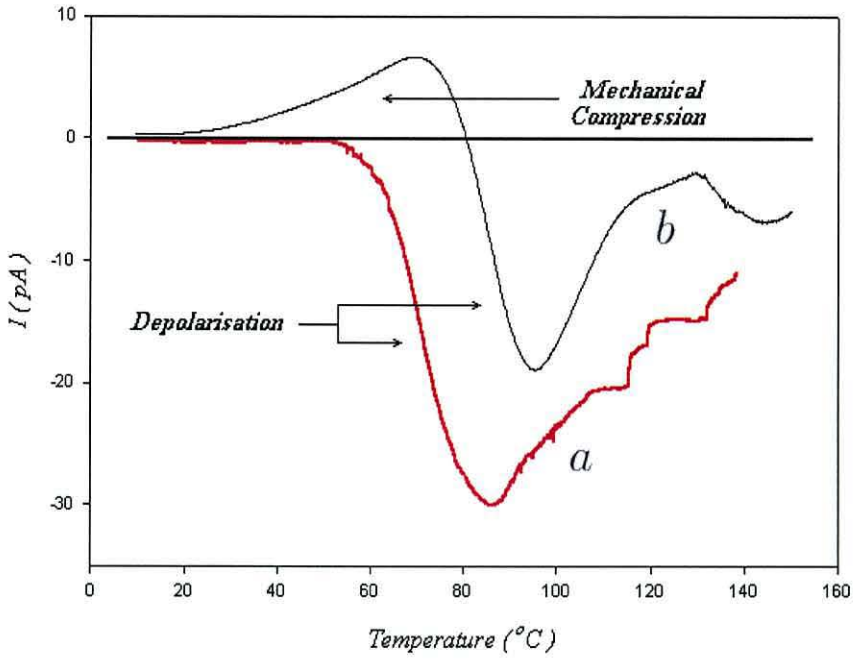

Figure 10.7: TSC runs for corona charged samples (a) free film and (b) under mechanical stress. Heating rate 3°C min^{-1}. Area $\sim$ 1 cm^2.

$$I = \frac{dQ}{dt} = A\frac{d\sigma_s}{dt} = A\frac{d\sigma_s}{dX_{AIR}}\frac{dX_{AIR}}{dT}\frac{dT}{dt}. \tag{10.6}$$

The first term in equation 10.6, A, is the sample area ($\sim$ 1 cm^2). The second term is the derivative of the charge density induced on the electrodes, σ_s (see Fig.6.2) with respect to the sample thickness. It can be theoretically obtained from equation 6.23. The third is the thermal contraction of the sample and can be obtained by fitting the curve of thickness versus temperature under a mechanical stress of 1000 Pa (Fig.9.1) to a polynomial whose coefficients are given in Fig.10.8 a). This curve was then differentiated (MATLAB® symbolic calculus toolbox) to yield d_{AIR}/dT. The last

[2] Although we cannot measure the applied stress during the TSC experiment, we can estimate the strain from capacitance measurements prior to and after the contraction. Such a procedure yielded a final thickness of 40 μm a similar value to that under a compression of 1000 Pa (9.1).

term in equation 10.6 is the heating rate, $3^oC\ min^{-1}$ ($0.05^oC\ s^{-1}$).

Figure 10.8 b) shows the current calculated from equation 10.6 plotted against temperature in the range (20-60)^{o}C for a value of $\sigma_i = 300\ \mu C\ m^{-2}$ for the charge density at the polypropylene-air interfaces. Also shown in Fig.10.8 b) is the measured current. It can be seen that reasonably good agreement is found between the measured and the calculated curves. The value assumed for σ_i is however more than two times lower than those reported by other authors [399][15][381].

Given that the foam contracts under mechanical stress, it may be assumed that the foam will tend to expand under vacuum and indeed Fig.10.5 confirms this. However, the data presented in Fig.10.5 also shows that gas can diffuse out of the foam at a pressure of 10^{-5} Pa and takes $\sim$ 55 hours to come to a new equilibrium. This allowed us to perform TSC measurements under non-equilibrium conditions.

As temperature increases, the enclosed gas should expand, leading to an expansion of the foam. However, as we saw in Chapter 9, the material contracts with temperature even for low compressive loads. The results shown in Fig.10.5 suggest that it is possible to reduce the ambient pressure without decreasing very much the pressure inside the voids. This will facilitate the expansion of the enclosed gas with increasing temperature.

A TSC run was performed under non-equilibrium conditions, *i.e.*, between stages (1) and (2) in Fig.10.5. The obtained currents are presented in Fig.10.9. In this case, the low temperature currents are negative. This is readily explained by expansion of the sample as a result of the expansion of the enclosed gas. The current peak associated with the depolarisation appears, as in the previous cases (Fig.10.7), around 90^{o}C.

A partial TSC experiment under high mechanical load applied, was performed in order to investigate the reversibility of the processes occuring as a result of the heating. A clamped sample (Fig.7.8 a)) was heated at a constant rate of $3^oC\ min^{-1}$ up to the predetermined temperature and rapidly cooled with the help of liquid nitrogen after each run. The final temperature was increased in steps of 10^{o}C after each run.

From Fig.10.10 we can see that the processes responsible for the observed thermal

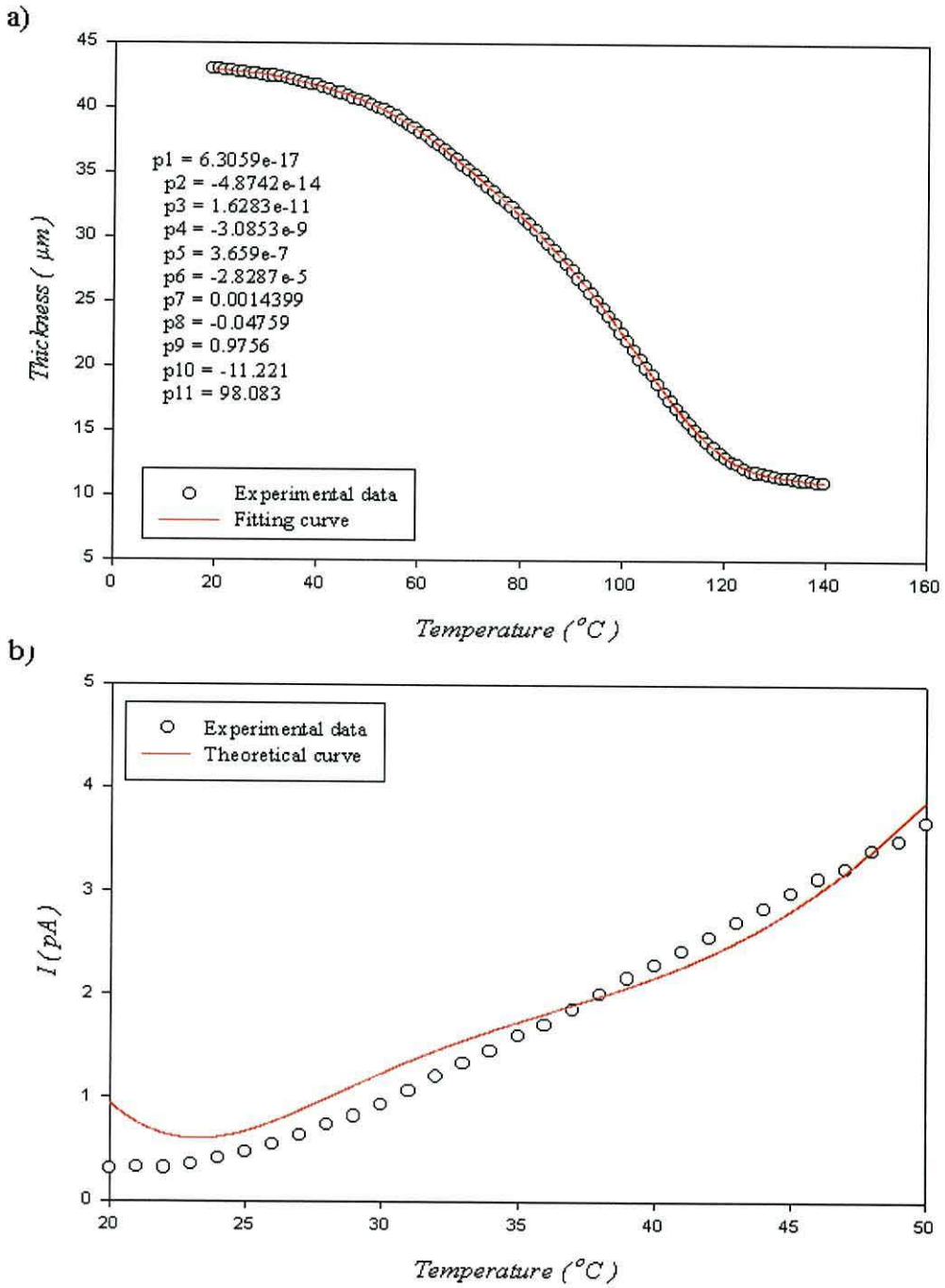

Figure 10.8: a) Measured (o) and fitted (-) b) Experimental (-) and theoretical (o) curves of thermally stimulated current under a compressive stress of around 1000 Pa.

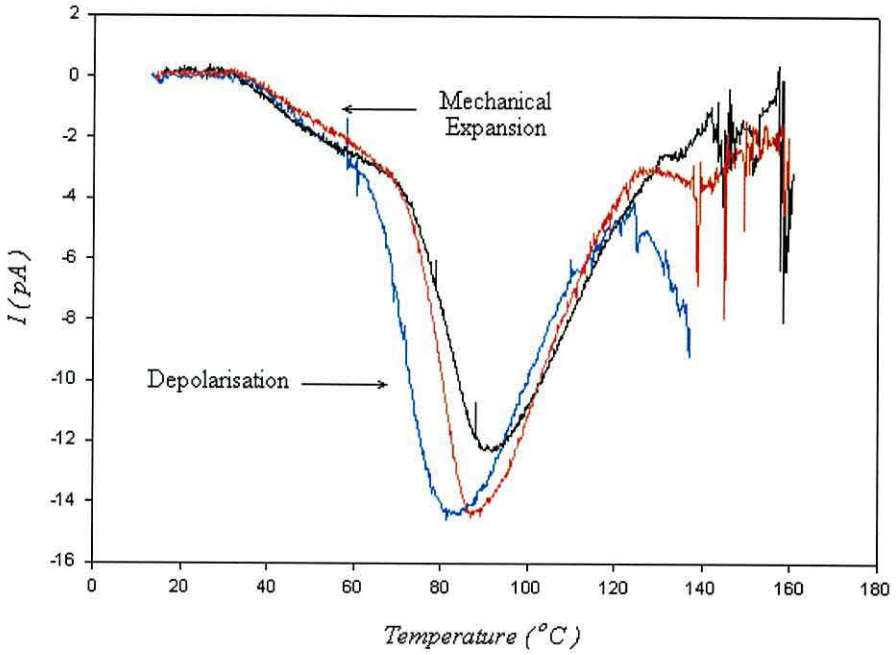

Figure 10.9: TSC runs for samples under non-equilibrium conditions. Heating rate 3°C. Area 1 cm^2.

currents are irreversible. At low temperatures (up to 60°C) the results are in good agreement with the irreversible contractions reported in Fig.9.3. From Fig.10.10, the negative-going current is also irreversible as expected for charge detrapping or ohmic conduction processes.

10.2.2 Effect of the Polarisation Voltage

Finally, the effect of the polarisation voltage was also investigated. The samples were DC polarised at room temperature for 1 minute at different voltages (section 7.3.1). After poling, the d_{33} coefficient was measured (section 11.1) and a TSC run performed in the range (10-140)°C. The obtained TSC plots are presented in Fig.10.11 from which we see that the maximum negative currents do not linearly increase with the polarisation voltage. There is a noticeable increase between 4 and 5 KV and between 6 and 7 KV. These may reflect the distribution in thickness of individual voids and/or the fact that

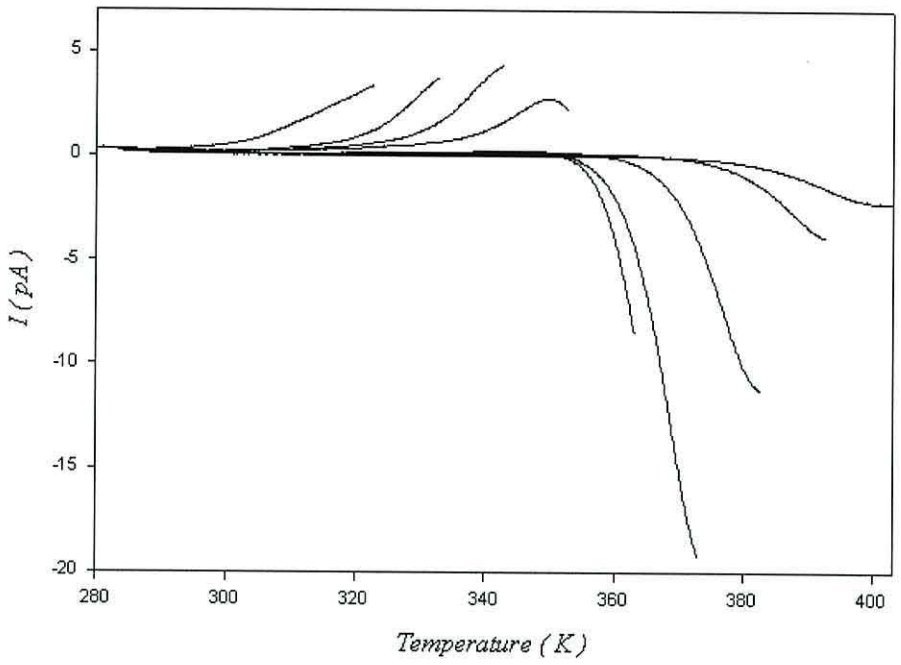

Figure 10.10: Partial TSC runs of corona charged samples. Heating rate 3°C min^{-1}. Area 1 cm^2.

the discharge current (and therefore the deposited charge at the PP-air interfaces) does not linearly depend on the voltage.

A change in slope occurs in the positive-going part of the TSC spectrum above $\sim$ 60°C. The reason could be that these experiments were performed under moderate mechanical stress. Thus, TSC curves resemble, at low temperatures, that of the thermal expansion coefficient at low mechanical stress (10 Pa) in Fig.9.2 and presented here in Fig.10.12 with the arrow indicated.

10.3 Activation Energies

As mentioned above, in curve a) in Fig.10.7, only the depolarisation of the sample is observed. From this curve, the activation energy associated with this phenomenon was determined using the so-called *initial rise method.* In this method, the first part of the thermally stimulated current can be approximated by the equation [415][416][217]:

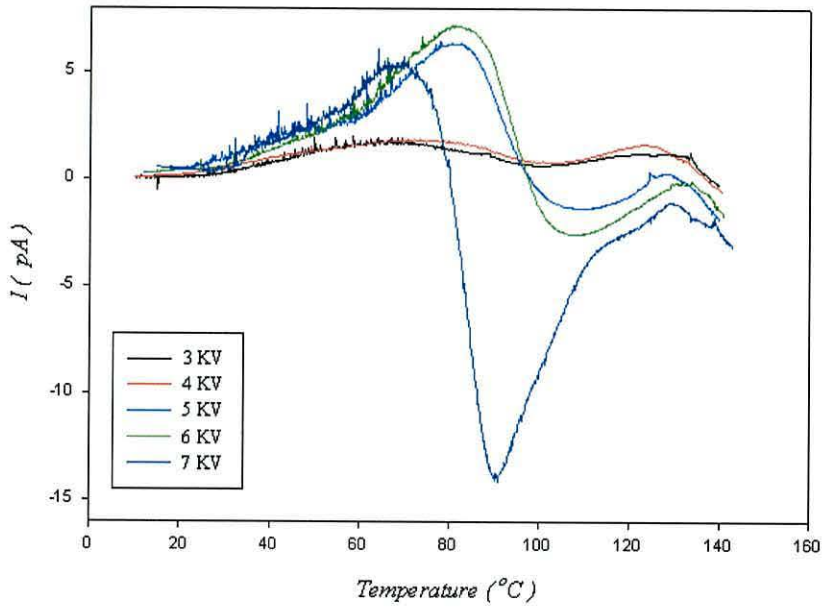

Figure 10.11: TSC plots obtained for samples DC polarised at different voltages. Area 0.785 cm^2. Heating rate 3°C min^{-1}.

$$I = I_0 exp\left(\frac{-E_a}{k_B T}\right) \tag{10.7}$$

where E_a is the activation energy, T the temperature in Kelvin and k_B Boltzmann's constant. Thus, plotting $ln\ I$ versus T should yield a straight line whose slope gives the activation energy E_a. The fitting (least squares) curve presented in Fig.10.13 yielded a value of E_a=2.04 eV. This value is around two times higher than the activation energy for ohmic conduction in polypropylene [5][270][417] and very close to the activation energy associated with detrapping of negative ($\sim$ 2 eV) and positive ($\sim$ 1.7 eV) corona deposited charges (mechanism (2) in Fig.10.6) [270].

The initial rise method in conjunction with thermal cleaning was used to calculate the activation energies associated with the material depolarisation, *i.e.*, in the temperature range (90-130)°C in Fig.10.10. The results are presented in Fig.10.14. The initial rise method yielded values in the range (4.5-3.51) eV for the main negative peak.

These values are in contrast with the value of $\sim$ 2 eV found from the fitting in

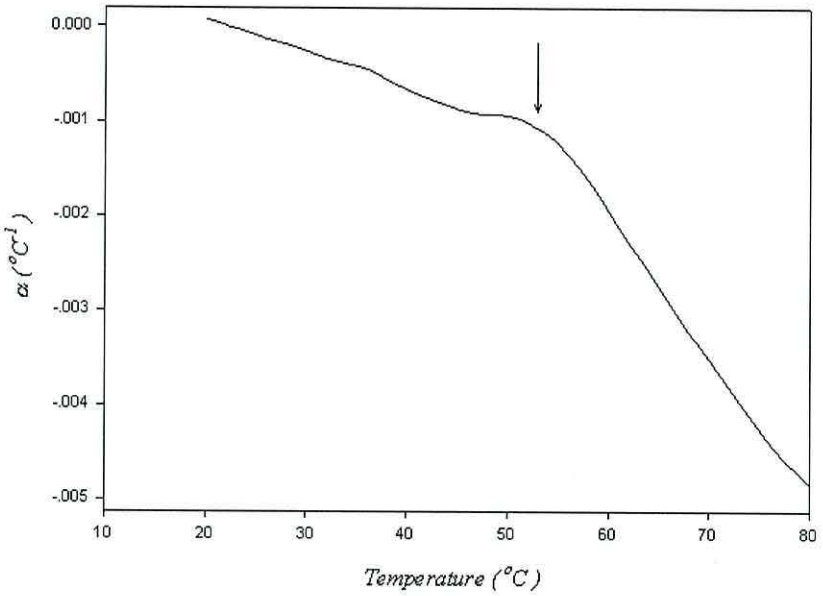

Figure 10.12: Thermal expansion coefficient of a PP foam under a mechanical stress of 10 Pa. Area 1 cm^2. Heating rate 3°C min^{-1}. Arrow stresses the temperature.

Fig.10.13. In addition, the activation energies do not increase in the successive sweeps suggesting that those early sweeps may be affected by the collapse of the cellular structure.

Initial parts of the curves in the temperature range (50-90)°C in Fig.10.10 do not follow an exponential dependence with T^{-1} and therefore, they are not activated processes.

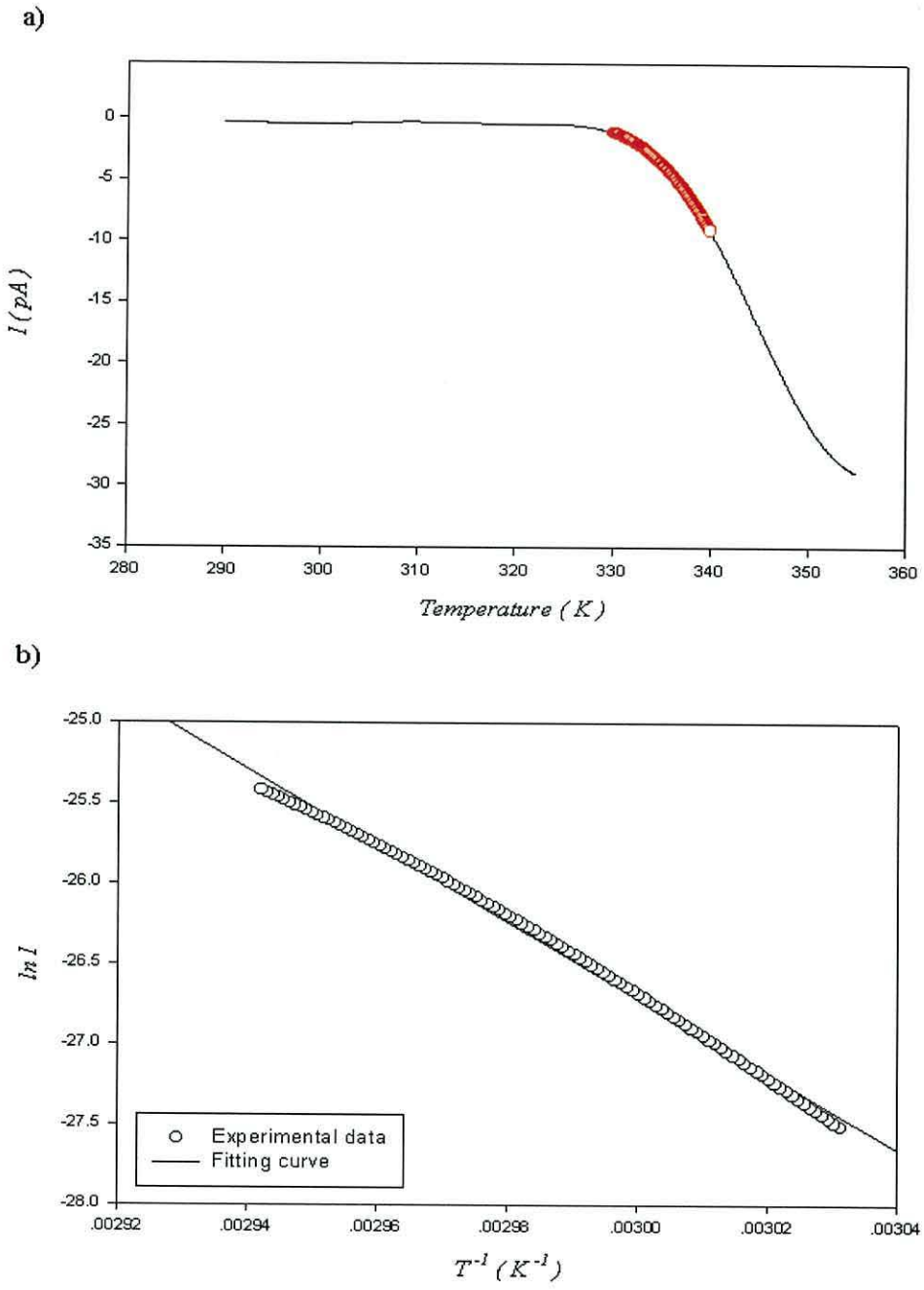

Figure 10.13: a) Part of the curve b) in Fig.10.7 (o) used for determining the activation energy. b) Arhenius plot for the initial rise of curve in a).

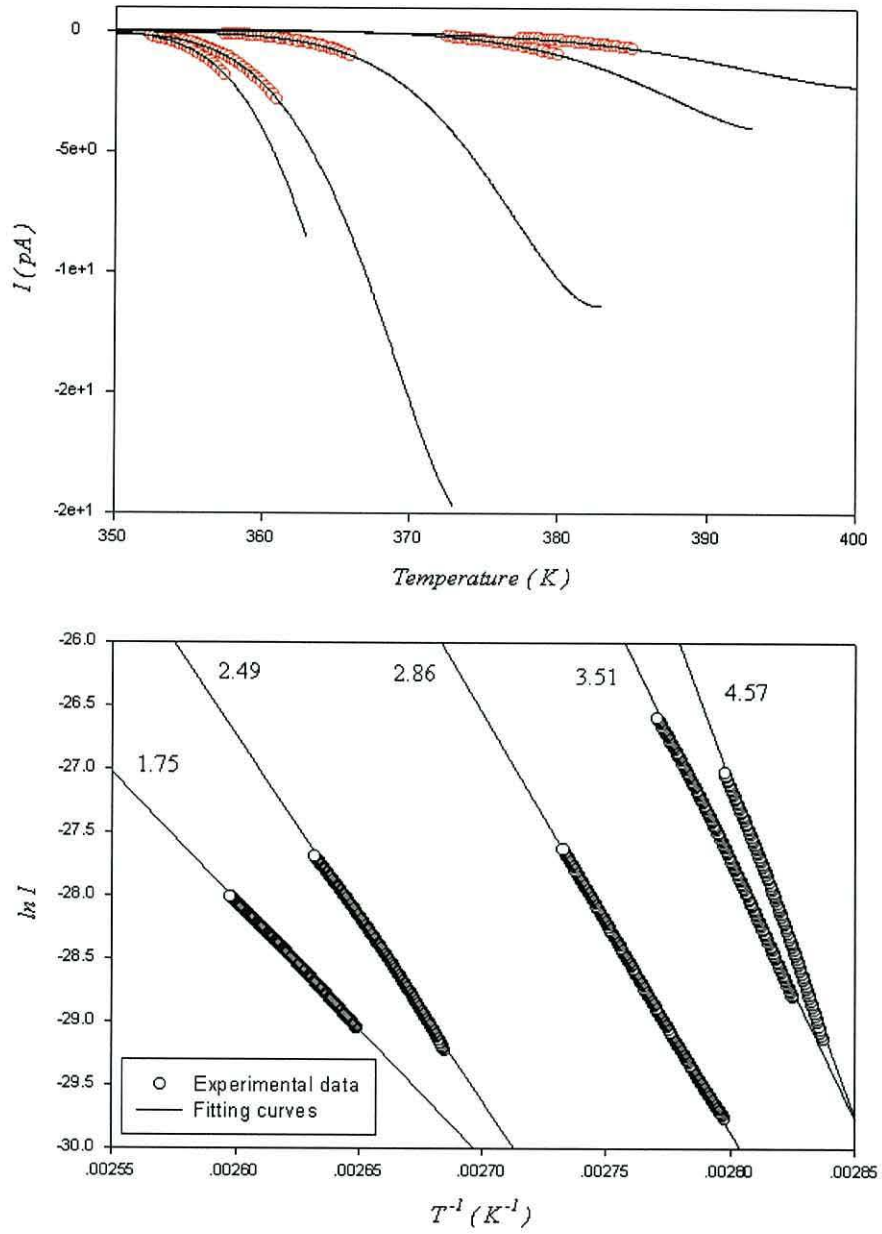

Figure 10.14: a) Thermal negative-going currents obtained in the thermal cleaning (-) and the initial rise current used for determining the activation energy (o). Area 1 cm^2. Heating rate 3°C min^{-1}. b) Arhenius plots for the initial rise of curves in a). Also shown are the obtained activation energies (in eV).

10.4 SUMMARY

The density of PP was calculated from capacitance measurements on a non-poled, evaporated sample using a two layer approach to represent the material and assuming a value of 70 μm for the thickness of the samples. The values obtained were reasonably similar to those provided by the supplier considering the simplicity of the approach.

However, for the samples electroded by the supplier, the densities were found to be very high if a thickness of 70 μm is considered. Therefore, it must be considered that at some stage in the handling (poling, electrode deposition, gluing, etc.) of the foam a compression of $\sim$15% may well have occurred.

By comparing samples oriented with major dimension in directions $\vec{x}_1$ and $\vec{x}_2$ we conclude that the difference in density in these two directions is appreciable and results from the anisotropy of the cellular structure.

All these data will be of special importance for obtaining Young's moduli from the resonances curves as we will see in Chapter 11.

The same approach was used to calculate the variation in density under compressive stresses. Assuming that the polypropylene layers do not compress we determined the compression of the voids. Hence, two sets of strain-stress data were obtained. In Chapter 9 we saw that these data lie close to the mechanically measured strain-stress curves (Chapter 9).

The effect of vacuum on the structure of the PP foam was also investigated from capacitance data. Quasi-instantaneous expansions and contractions of the foam were recorded as a result of the decrease and increase of the pressure outside the sample with respect to the pressure of the enclosed gas suggesting the presence of close cells.

Slow responses ascribed to the diffusion out and into the sample driven by the pressure gradient were also observed. The low diffusion rates allowed us to induce thermal expansions as a result of the thermal expansion of the enclosed gas.

The mentioned expansion produced a negative-going thermally stimulated current starting at low temperatures. In good agreement is the positive-going current when

the sample is compressed. When no stress is applied and the sample is in equilibrium, only the peak associated with depolarisation is present. From the TSC current under such conditions, the initial rise method yielded an activation energy of ~ 2 eV, which suggests that the material depolarisation is due to the detrapping of charges stored in the polypropylene layers.

Chapter 11

Piezoelectric Characterization

In this chapter we present the results obtained in the study of the piezoelectric properties of PP foam. The effect of sample orientation, *i.e.*, cellular structure, ambient pressure and temperature on the piezoelectric character is investigated and an explanation of the results provided based on the material properties described in Chapters 8, 9 and 10.

11.1 Piezoelectric Strain Coefficients

The piezoelectric d_{ij} coefficients defined in equation 5.10 are very helpful in providing a measure of the goodness of piezoelectric materials as sensors since they give the charge density developed at the electrodes, *i.e.*, under open-circuit conditions, the voltage across the sample in direction $\vec{x}_i$ per unit of stress applied in direction $\vec{x}_j$.

11.1.1 Length and Width Piezoelectric Coefficients, d_{31} and d_{32}

The piezoelectric d_{31} and d_{32} coefficients were measured as described in section 7.4.1 for samples X_1 and X_2 respectively. The experimental data together with the fitting curves (equation 7.5) used for calculating d_{31} and d_{32} are shown in Fig.11.1. The fitting process yielded the values d_{31} =-1.56 pC N^{-1} and d_{32} =-1.49 pC N^{-1} which are identical

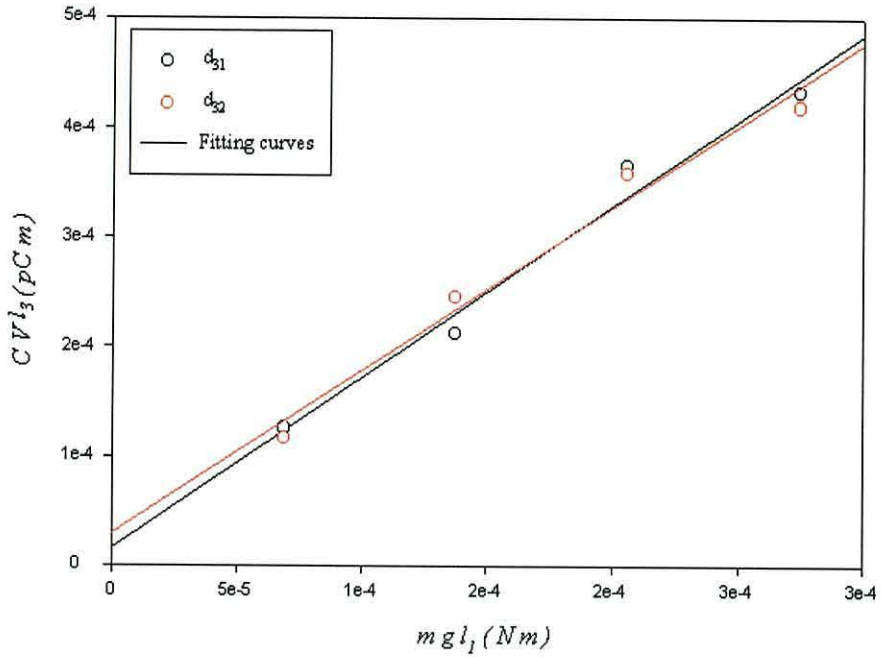

Figure 11.1: Experimental data and fitting curves used for determining the piezoelectric d_{31} (o) and d_{32} (o) coefficients.

within experimental error. The minus sign reflects the fact that an extensional stress in lateral directions ($\vec{x}_1$ or $\vec{x}_2$) produces a contraction in the thickness ($\vec{x}_3$).

Low values for d_{31} and d_{32} were expected since they reflect the anisotropy of the cellular structure, characterised by the anisotropy ratios, R_{13} and R_{23} (section 8.5). Due to this anisotropy, the Young's moduli in directions $\vec{x}_1$ and $\vec{x}_2$ are higher than in the thickness direction. Therefore, a high stress is necessary to induce an appreciable lateral expansion. In addition, also as a result of the anisotropy (R_{13} and R_{23}), the foam displays negligible Poisson's moduli ν_{31} and ν_{32}. In consequence, even appreciable elongations in lateral directions will lead to little contraction in thickness and therefore, to small charge density on the electrodes.

It should be noted, though, that Young's moduli in the lateral directions, Y_1 and Y_2, may be influenced by the presence of the electrodes. The obtained coefficients are, therefore, difficult to correlate with the foam properties.

11.1.2 Thickness Piezoelectric Coefficient d_{33}

As already mentioned, the most interesting piezoelectric property of the PP foam is the magnitude of the piezoelectric d_{33} coefficient that can be attained after poling, which determines the efficacy of the material as a thickness-mode sensor. Hence, it is important to study the variation of this coefficient with temperature to determine the temperature range in which the material can be used satisfactorily. A direct measurement of d_{33} at different temperatures was technically impossible in this work. However, we measured d_{33} at room temperature after heating the sample at different temperatures.

A corona-poled sample was mounted on a heating plate as in TSC measurements and a moderate stress applied in order to ensure a good contact between the sample and the plate as shown in Fig.7.8 a). The temperature was increased to a predetermined value at a constant rate of 3°C min^{-1}. Upon reaching the required temperature, the sample was immediately cooled to room temperature and the coefficient measured as explained in section 7.4.1. The results obtained are presented in Fig.11.2.

The piezoelectric d_{33} coefficient at room temperature (140 pC N^{-1}) combined with the low values of d_{31} and d_{32} give a high value for the piezoelectric hydrostatic coefficient d_h ~137 pC N^{-1} (equation 7.7) suggesting that the material would be very good for hydrostatic applications.

As we can see in Fig.11.2, the piezoelectric coefficient remains constant up to 40°C but decreases thereafter. Between 40 and 60°C the decrease is small and is related to sample contraction. The main decrease occurs in the range 60 to 80°C. This decrease is in good agreement with the depolarisation of the material as indicated by the TSC curves in Fig.10.7. However, as we saw in section 9.1, the foam irreversibly compresses for temperatures above ~60°C for moderate static stress. After an irreversible contraction and the subsequent loss of cellular character, an increase in Young's modulus is expected. This increase in Young's modulus after heating to temperatures above ~ 60°C may also contribute to the observed decrease of d_{33}.

A similar dependence on the depolarisation temperature of the pyroelectric coeffi-

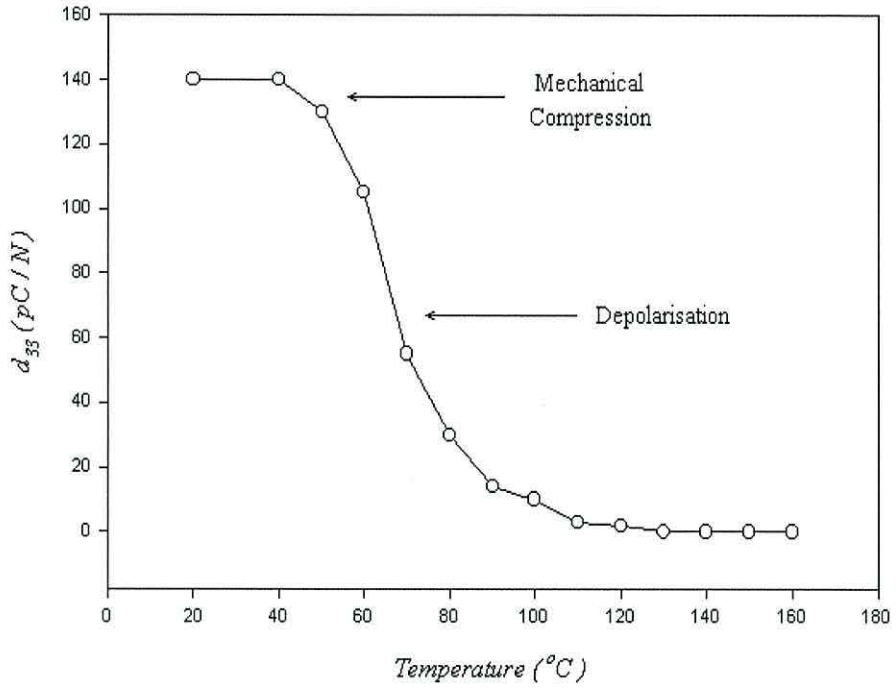

Figure 11.2: Variation of the piezoelectric d_{33} coefficient measured at room temperature but plotted as a function of the previously applied temperature.

cient has been reported [27].

The piezoelectric d_{33} coefficient was also measured as a function of the polarisation voltage. Samples with evaporated electrodes 10 mm in diameter were DC polarized as described in section 7.3.1 at different voltages from 2 to 7 KV and the piezoelectric d_{33} coefficient measured. The experimental results are presented in Fig.11.3 from which we see that a minimum voltage ~4-5 KV is required to obtain an appreciable piezoelectric effect. Moreover, the piezoelectric coefficient increases rapidly with the polarisation voltage for voltages around 6-7 KV in good agreement with the TSC curves shown in Fig.10.11.

It is worth noting that the piezoelectric coefficient seems not to tend to a limiting value. Poling voltages of around 8 KV were not achievable due to the breakdown of the foam (see Fig.7.6). Therefore, increasing the electric strength of the material would lead to higher polarisation voltages and to higher d_{33} coefficients.

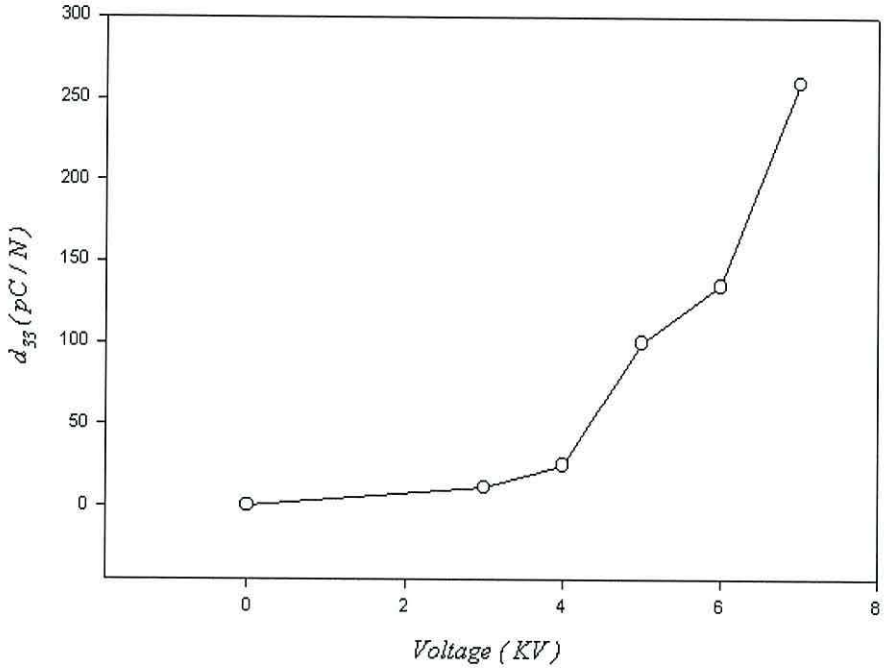

Figure 11.3: Variation of the piezoelectric d_{33} coefficient as a function of the polarisation voltage.

11.2 Resonator Parameters

The complex capacitance of a piezoelectric material measured at a particular signal frequency is determined by the mechanical (velocity, v, and acoustic attenuation, α), electrical (dielectric permittivity, ε) and electromechanical (electromechanical coupling coefficients, k_{ij}) properties of the material.

Therefore, in principle, all the parameters can be obtained by fitting the theoretically predicted behaviour (equation 5.106) to the experimental data obtained close to the mechanical resonances. The magnitudes of these parameters are of great interest if the electromechanical properties are to be fully characterised.

When used as a resonator, the amplitude of the thickness vibration is less than $\sim$ 10 nm for voltages up to 450 V [380] corresponding to strains less than $\sim$ 1.5x10^{-2}%. For the particular sample geometry used here (0.4 x 4 cm^2), in the frequency range 10^4-10^6 Hz piezoelectric length, width and thickness resonances occur. Therefore, from

an analysis of these resonances we can extract information on the mechanical and electromechanical properties of the material at levels of strain and frequencies that are not accessible by other techniques such as TMA and DMA presented in Chapter 8.

To this end, the real, C', and imaginary, C", parts of the complex capacitance were measured in the frequency range (10^4-10^6) Hz and the theoretically predicted capacitance curve fitted to the data, for samples X_1 and X_2, as described in section 7.4.2. The capacitance data and fitting curves are presented in Fig.11.4 where we can see the length, width and thickness resonances in order of increasing frequency. Other small resonances in the frequency range (30-100 KHz) correspond to higher harmonics of the length resonance. These higher harmonics are missing in the experimental data due to the high acoustic damping of the polymer [27].

The resonator parameters extracted from the fitting are presented in Table 11.1. From the velocities in Table 11.1 and from the densities presented in Table 10.2, the corresponding Young's moduli (equation 5.66) were calculated and are presented in Table 11.2. Young's moduli of the PP foam calculated from resonance curves have already been reported by Neugschwandtner *et al* [26][27] assuming a constant density equal to the value provided by the supplier (330 Kg m^{-3}) for samples X_1 and X_2 and a total thickness of 70 μm. However, as we saw in the previous chapter, there is an important relation between the density and the orientation of the sample (cellular structure). In addition, for the pre-electroded samples used here, taking 70 μm for the total thickness leads to density values of 419 and 580 Kg m^{-3} for samples X_1 and X_2 (see Table 10.2), which are much higher than 330 Kg m^{-3}.

The Young's modulus, Y_1, was expected to be higher than Y_2 because of the higher density of the latter. However, from Table 11.1 we see that Y_2 is 1.6 to 2.2 times higher than Y_1. As mentioned above, at low strains, the cellular structure and the polymer itself determine the mechanical response of the foam. Since the molecular structure of the polypropylene is the same in the two directions (section 8.3) we assume that the difference observed in the mechanical response can be completely assigned to the

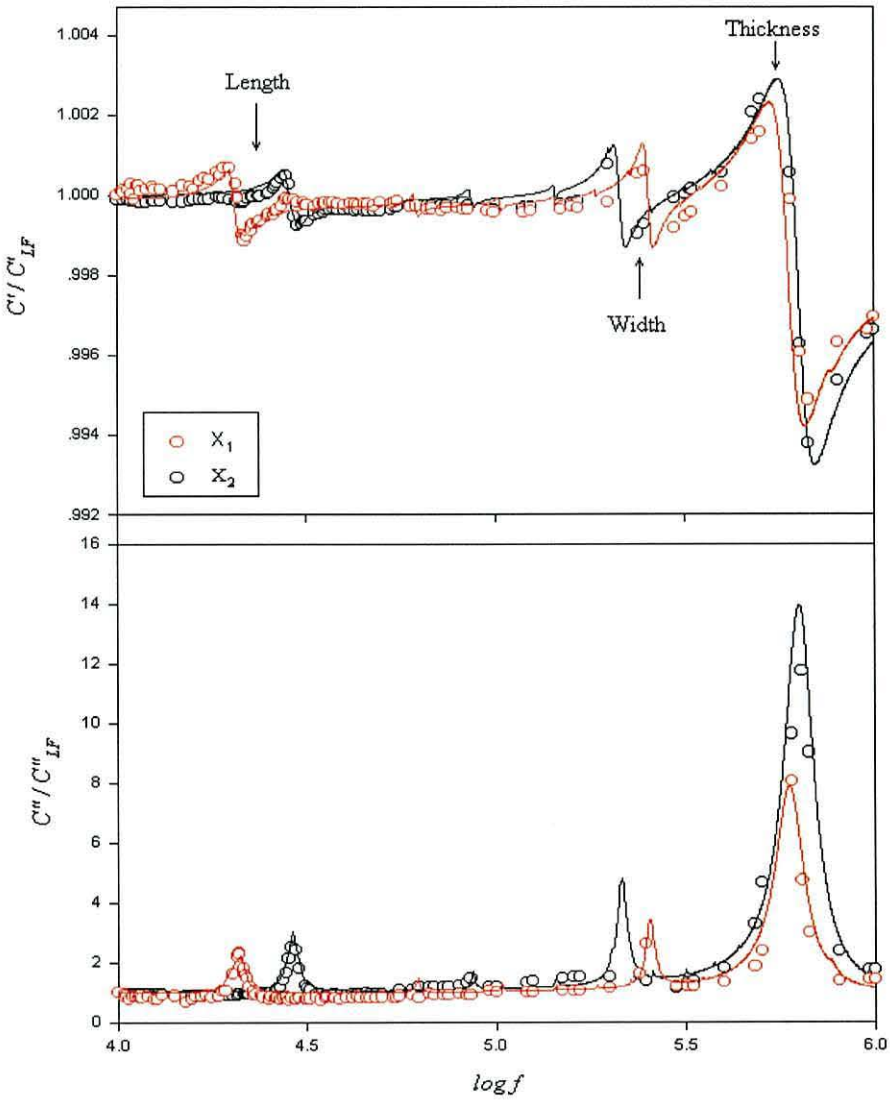

Figure 11.4: Experimental data and fitting curves of the normalized real and imaginary parts of the complex capacitance for samples (o) X_1 and (o) X_2. C'_{LF} was $\sim$ 27 and $\sim$ 31 pF for X_1 and X_2 respectively. C''_{LF} was $\sim$ 0.025 pF in both cases.

	Length			*Width*	*Thickness*			
	k_{31}	v_1 $(Km\ s^{-1})$	α_1 (m^{-1})	k_{32}	k_{33}	v_3 $(m\ s^{-1})$ $(60\ \mu m)$	$(70\ \mu m)$	α_3 $(10^3\ m^{-1})$
X_1	0.015	1.78	3.5	0.0158	0.05	68.5	80	3.8
X_2	0.018	2.3	4	0.0165	0.05	74.57	87	4

Table 11.1: Calculated resonator parameters for length, width and thickness resonances for samples X_1 and X_2.

	X_1		X_2		*Strain – Stress*
Thickness (μm)	Y_1 (MPa)	Y_3 (MPa)	Y_2 (MPa)	Y_3 (MPa)	Y_3 KPa
60	668.3	0.99	2105.4	2.21	
70	1327.5	2.682	3068.2	4.390	5 – 35

Table 11.2: Calculated Young's moduli from the resonance curves for samples X_1 and X_2. Also shown is the range of values obtained from strain-stress curves directly measured using TMA technique (Fig.9.4). Values reported by other authors for the mechanical compliances and stiffness are given in Table 6.1 [26][27].

cellular structure. Thus, we see that an anisotropy ratio $R_{21} = 1.6$ results in a similar Young's modulus ratio. The high values of the Young's moduli, Y_1 and Y_2, however, suggest that the mechanical response of the foam in $\vec{x}_1$ and $\vec{x}_2$ directions is very much influenced by the polymer (via the anisotropy in the cell walls thickness) as well as by the electrodes which may partially mask the effect of the cellular structure.

From Table 11.2 we see that the calculated Young's modulus in the thickness direction, Y_3, is 0.99 to 2.682 MPa for sample X_1 and 2.21 to 4.390 MPa for sample X_2. These values are around three orders of magnitude greater than those obtained from strain-stress, creep-recovery curves (Chapter 9) and capacitance measurements (Chapter 10) as would be expected for a mechanical response dominated by cell wall bending at high frequencies. We also see that a variation of 15% in the estimate of initial sample thickness, leads to variations of ~100% in the calculated Young's modulus. The values

extracted from the resonance curves may then be seen as rough estimations rather than as exact values.

For this reason, it is difficult to establish a quantitative relation between cellular structure and Young's modulus. However, the differences observed between Y_3 for X_1 and X_2 samples do, in our opinion, reflect actual differences in the cellular structure (R_{13} and R_{23}).

From the electromechanical coupling factors in Table 11.1, Young's moduli in Table 11.2 and dielectric permittivities, calculated from the capacitance values (27 and 31 pF for samples X_1 and X_2 respectively) using equation 10.3, we can obtain the piezoelectric d_{ij} coefficients using the equations 5.29, 5.82 and 5.99. The calculated permittivities and d_{ij} coefficients are shown in Table 11.3

Thickness (μm)	X_1 ε	d_{31} ($pC\ N^{-1}$)	d_{33} ($pC\ N^{-1}$)	X_2 ε	d_{32} ($pC\ N^{-1}$)	d_{33} ($pC\ N^{-1}$)
60	1.14	1.84	159	1.31	1.33	114
70	1.33	1.41	104	1.53	1.19	87

Table 11.3: Calculated relative dielectric permittivities and piezoelectric d_{ij} coefficients from data in Tables 11.1 and 11.2.

The d_{33} coefficients calculated here are in general lower than those directly measured (section 11.1.2), which reflects the higher Young's modulus, Y_3, of the material at high frequency and low strain. However, the difference is much smaller than would be expected from the three orders of magnitude difference in Y_3 arising from the two techniques. Therefore, it seems that the static stress applied to the material in the direct determination of d_{33} compresses the foam sufficiently for the Young's modulus to increase to the same order of magnitude as those presented in Table 11.2.

Parameter	*(1)*	*(2)*	*(3)*
k_{33}	0.05	0.065	0.05
f_a (MHz)	0.56	0.39	0.62
α_3 $(10^3\ m^{-1})$	3.8	3.2	3.5

Table 11.4: Resonator parameters at different stages of the vacuum treatment for X_1 and X_2 samples.

11.2.1 Effect of Pressure

When a foamed material is set into vibration, the vibration propagates through the solid phase as well as through the air. In order to investigate the effect of the gas and solid phases, the resonator parameters of sample X_2 were calculated at a) atmospheric pressure, b) at equilibrium at 10^{-5} Pa and c) at atmospheric pressure after vacuum exposure (stages (1)), (2) and (3) respectively in Fig.10.5). The experimental data and fitting curves are shown in Fig.11.5 and the resonator parameters presented in Table 11.4.

In this case, it is convenient to present the antiresonance frequency, f_a, defined in equation 5.111 instead of the velocity, v_3.

As we can see from the values in Table 11.4, f_a decreases by around 30% under vacuum while at atmospheric pressure after the vacuum treatment, f_a increases by around 9%. From Table 10.3 we see that sample X_2 expands by around (2.1-2.5)% after equilibrating at 10^{-5} Pa. Since f_a is inversely proportional to double the sample thickness, the observed decrease in f_a under vacuum cannot be completely attributed to expansion of the sample. On the other hand, when the sample expands, the voids tend to a more spherical shape and, as we saw above (Fig.11.4), this results in a higher f_a. Therefore, the decrease of f_a observed under vacuum must be attributed to a decrease of the sound velocity due to a decrease in the Young's modulus of the gas phase, consistent with a reduced pressure in the cells.

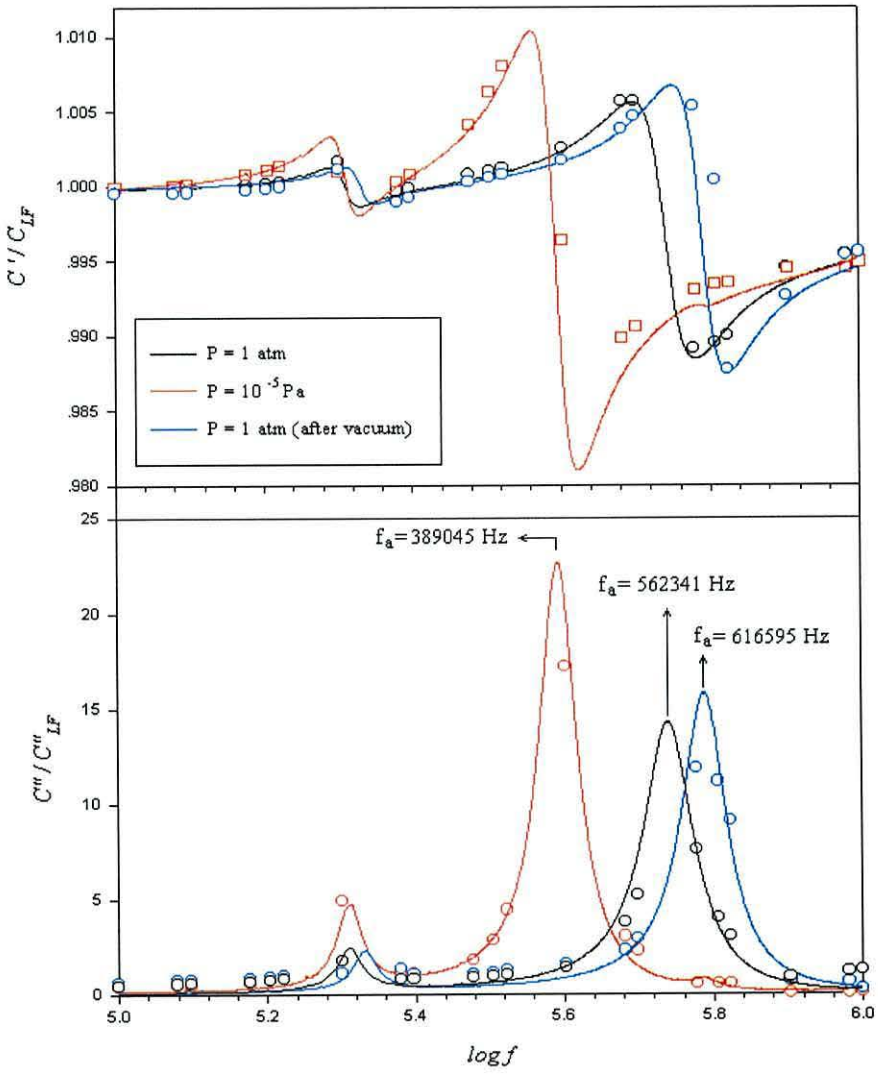

Figure 11.5: Normalized experimental data and fitting curves for the real and imaginary parts of the complex capacitance at atmospheric pressure, at equilibrium at 10^{-5} Pa and at atmospheric pressure after vacuum (stages (1), (2) and (3) respectively in Fig.10.5).

From Table 10.3 we see that the strain state of the sample at stage (3) with respect to the stage (1) is, for sample X_2, between 3.0 and 3.5%. Since, as mentioned above, f_a is inversely proportional to double the thickness, the reduction in thickness accounts for the increase in f_a at atmospheric pressure after vacuum exposure.

The acoustic attenuation, α_3, decreases by around 15% at low pressure due to the decrease of air pressure. Therefore, we estimate that the air accounts for some 15% of the mechancial losses of the foam with the greater part of the mechanical losses associated with the polymer. At atmospheric pressure after vacuum exposure, α_3 increases. However, the original value is not reached probably due to incomplete recovery of the gas pressure in the cells.

11.2.2 Effect of Temperature

As we have seen, the behaviour of the piezoelectric foam close to its mechancial resonances is very sensitive to the cellular structure. Therefore, a study of the variation of the various parameters (sound velocities, resonances and antiresonance frequencies, and acoustic attenuation) with temperature should be very helpful for understanding the thermal instability of the cellular structure. In addition, electromechanical coupling factors k_{ij} also depend on the polarisation of the material, *i.e.*, the charge density at the air-polypropylene interfaces. Therefore, their thermal properties may give some information about charge stability.

Free Resonator

The capacitance of a freely suspended sample, X_2, was measured as described in section 7.4.2 and the resonator parameters estimated at different temperatures and at room temperature after heating. The experimental data and the fitting curves are presented in Figs.11.6 and 11.7 and the calculated parameters in Tables 11.5 and 11.6 respectively. Again, we use resonance frequency, f_r^1 (defined in equation 5.109) instead of velocities for the length mode.

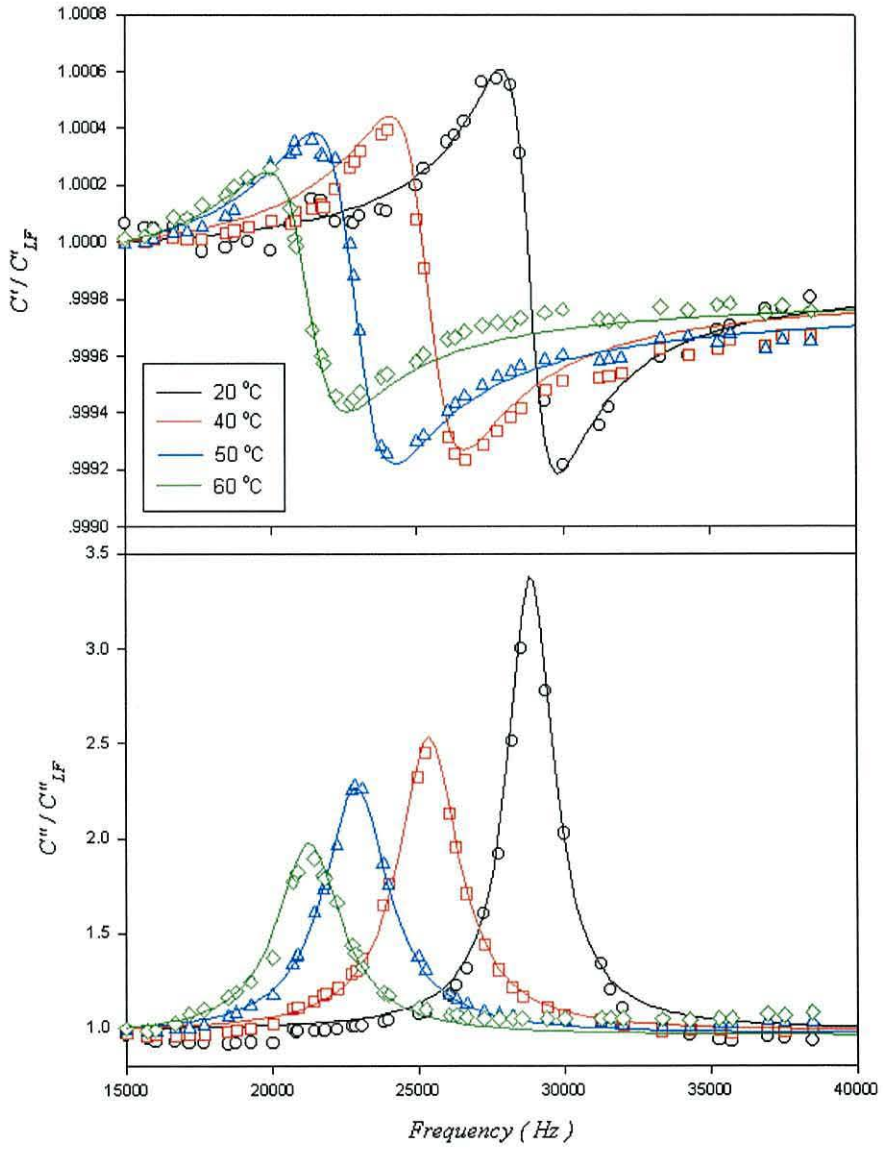

Figure 11.6: Normalized real and imaginary parts of the complex capacitance around the length mode resonance of sample X_2 together with the calculated curves at different temperatures. ∘ 20°C; □ 40°C; △ 50°C; ◇ 60°C.

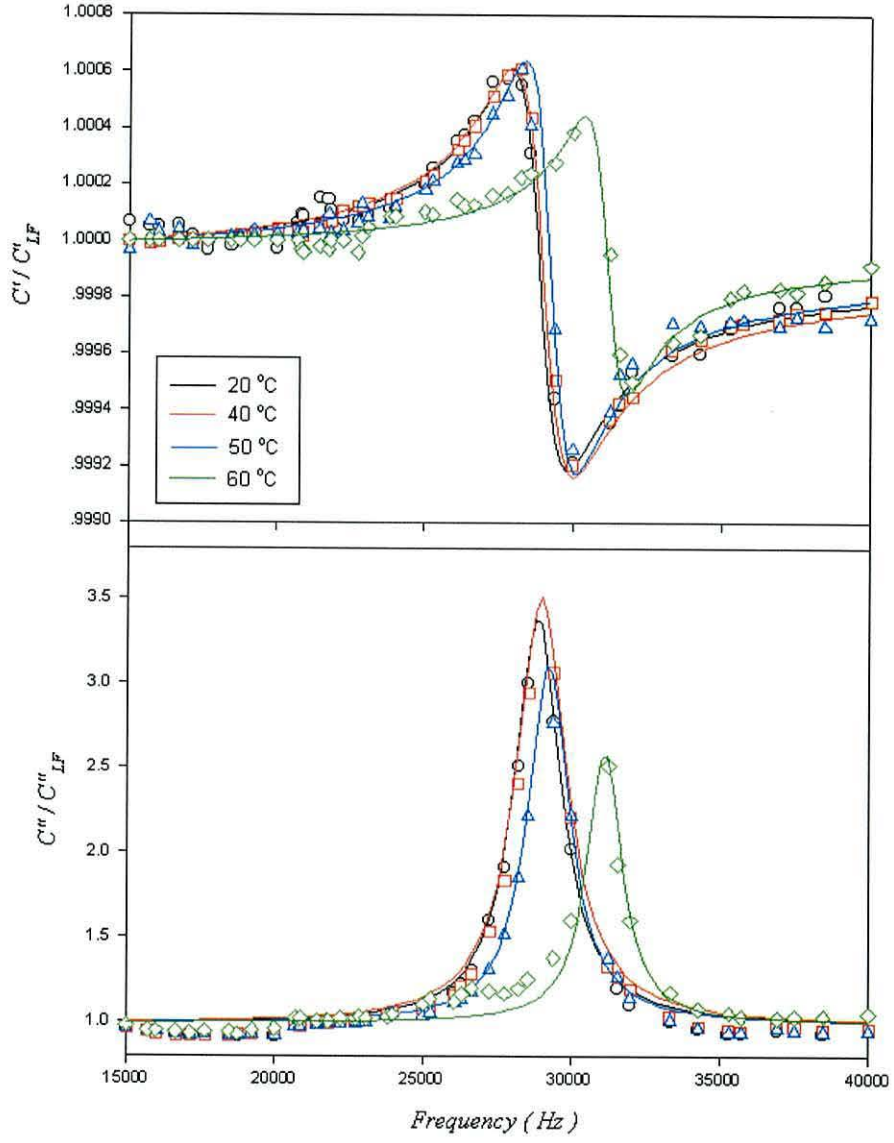

Figure 11.7: Normalized real and imaginary parts of the complex capacitance around the length mode resonance of sample X_2 together with the calculated curves at room temperature after annealing at different temperatures. ○ 20°C; □ 40°C; △ 50°C; ◇ 60°C.

T (^oC)	*Electromechanical Coupling Factor*		*Resonance Frequency*	*Sound Velocity* [a)]	*Acoustic Attenuation*	
	k_{31}	k_{33}	f_r^1 (MHz)	v_3 ($m\ s^{-1}$)	α_1 (m^{-1})	α_3 ($10^3\ m^{-1}$)
20	0.018	0.050	0.29	87	3	4
40	0.0120	0.052	0.27	77	3.9	5.1
50	0.0122	0.062	0.24	69	4.7	7.3
60	0.009	0.054	0.22	66	5.01	7.7

Table 11.5: Resonator parameters as a function of temperature calculated from curve fitting to the data in Fig.11.6. [a)] A total thickness of 70 μm was assumed to obtain the sound velocities, v_3.

T (^oC)	*Electromechanical Coupling Factor*		*Sound Velocity* [a)]		*Acoustic Attenuation*	
	k_{31}	k_{33}	f_r^1 (MHz)	v_3 ($m\ s^{-1}$)	α_1 (m^{-1})	α_3 ($10^3\ m^{-1}$)
40	0.012	0.050	0.28	86	2.8	4
50	0.012	0.050	0.28	86	2.3	4
60	0.0075	0.037	0.32	85	1.8	3.3

Table 11.6: Resonator parameters at room temperature after heating to different temperatures. Values were obtained from curve fitting to the data in Fig.11.7.[a)] A total thickness of 70 μm was assumed to obtain the sound velocities, v_3.

Thickness (μm)	*Assumed Density* ($Kg\ m^{-3}$)	Y_1 (GPa) $20°C$	$40°C$	$50°C$	$60°C$
60	398	2.105	1.806	1.51	1.29
70	580	3.068	2.656	2.205	1.879

Table 11.7: Young's modulus, Y_1, obtained from the resonance frequencies at different temperatures.

From Table 11.5, we see that the length mode resonance frequency, f_r^1 decreases by around 20% from 20 to 60°C. Now, f_r^1 depends on the length, l as $1/2l$ (equation 5.109). Therefore, a length expansion of ~15% (0.6 cm) is necessary to explain the observed decrease in f_r^1 in terms of an expansion of the material in length direction. Such an expansion, which could be detected by direct observation, was not observed at all.

Therefore, it seems that the observed decreases in f_r^1 must be attributed to either an increase of density or a decrease in the Young's modulus of the foam. An increase in the density would result from compression of the foam. However, from results presented in Chapter 9, we know that, at moderate stress (here the sample is freely suspended), the sample thickness hardly changes. Therefore, we propose that an appreciable decrease of the Young's modulus, Y_1 is responsible for the observed behaviour.

The decrease of Y_1 can be estimated assuming a constant density and length (4cm) values.

One-side Clamped Resonator

The effect of temperature on a clamped thickness-mode resonator was also investigated. Since the available frequencies were limited by the LCR Meter, poor resolution was attained in the free resonator measurements. In order to achieve better resolution we should go down in frequency. The sample thickness cannot be modified to the extent needed to decrease f_a sufficiently as to get a better resolution. For a one-side clamped

Parameter	$T\ (^oC)$			
	-20	20	50	70
k_{33}	0.071	0.074	0.078	0.043
$f_a^3\ (MHz)$	0.25	0.23	0.21	0.19
$\alpha_3\ (10^3\ m^{-1})$	1.9	2.7	5.1	5.9

Table 11.8: Resonator parameters for a clamped sample at different temperatures.

Parameter	$T\ (^oC)$			
	40	50	60	70
k_{33}	0.074	0.073	0.073	0.043
$f_a^3\ (MHz)$	0.255	0.255	0.266	0.270
$\alpha_3\ (10^3\ m^{-1})$	3.0	3.0	3.0	2.8

Table 11.9: Resonator parameters for a clamped sample at room temperature for samples heated to different temperatures.

resonator, f_a decreases by 50% with respect to the free resonator (see equations 5.111 and ??). This fact was used to measure the effect of temperature with more resolution.

The capacitance of the resonator was measured as described in section 7.4.3. The experimental data as well as the curve fits at and after annealing at different temperatures are shown in Figures 11.8 and 11.9 respectively and the corresponding parameters presented in Tables 11.8 and 11.9.

The calculated Young's moduli at different temperatures are presented in Table 11.7. The observed decrease of Y_1 should lead to an increase of k_{31} (equation 5.82), which was not observed. The reason for this is not clear, but it seems that it is probably because the piezoelectric length resonances were too small for the curve fit to pick up.

At room temperature, after heating up to 50°C, Y_1 recovers its original value and so

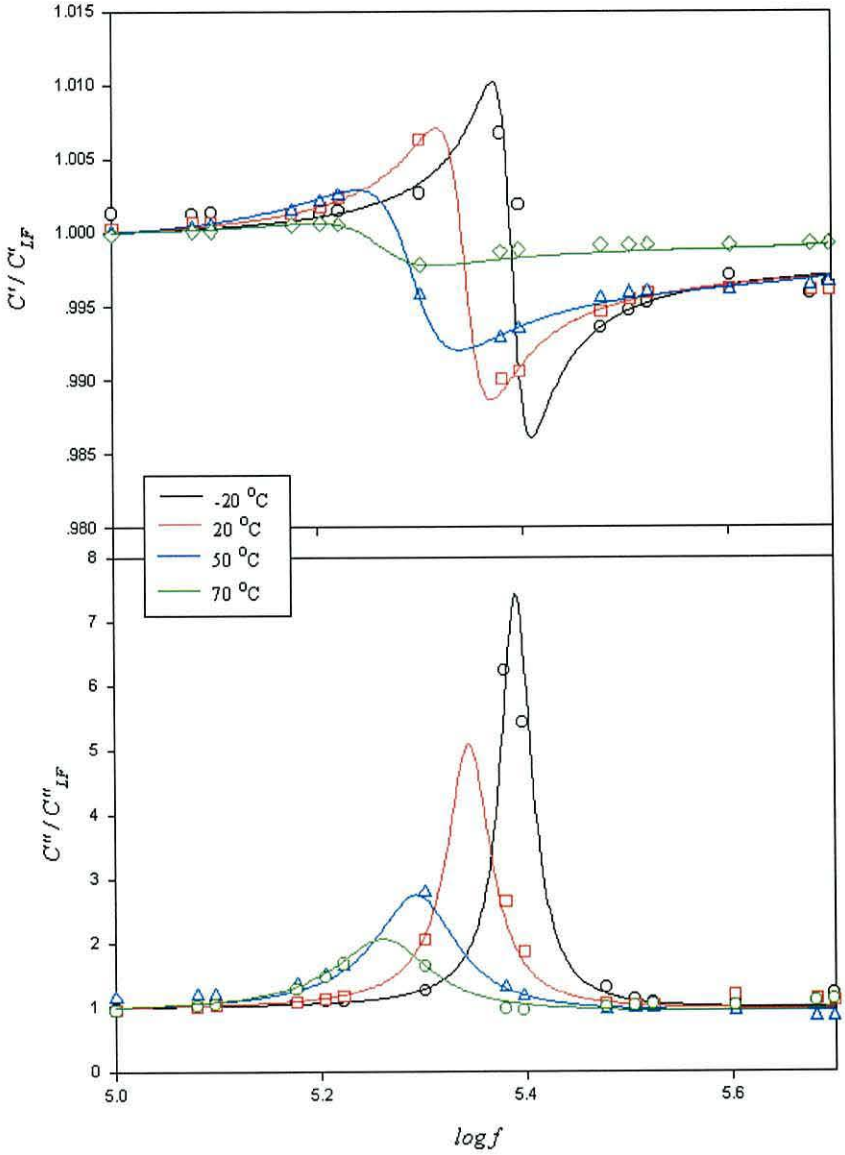

Figure 11.8: Normalized real and imaginary parts of the complex capacitance around the thickness resonance together with the calculated curves at different temperatures. ○ -20°C; □ 20°C; △ 50°C; ◇ 70°C.

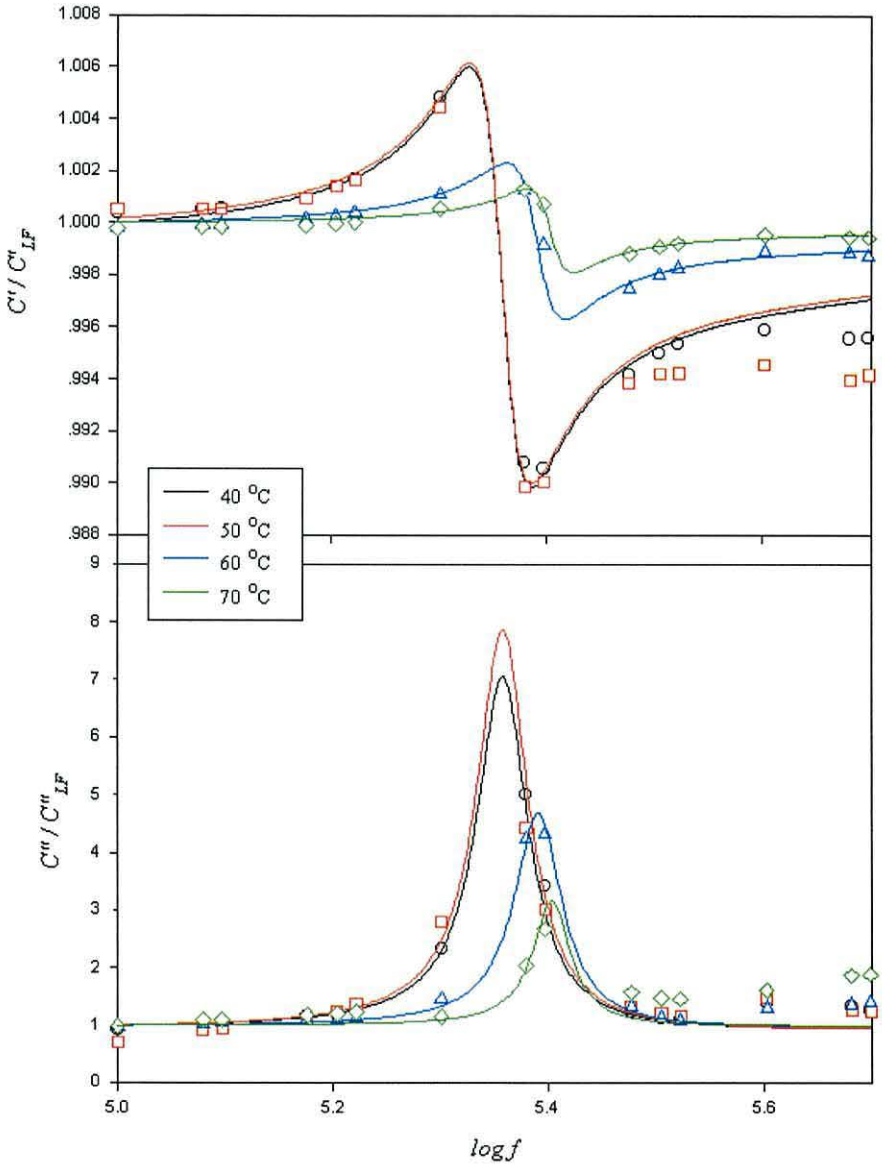

Figure 11.9: Normalized real and imaginary parts of the complex capacitance around the thickness resonance together with the calculated curves after annealing at different temperatures. ∘ 40°C; □ 50°C ; △ 60°C ; ◇ 70°C .

does the resonance frequency. However, heating to 60°C causes an irreversible change and f_r^1 increases by $\sim$ 8%. As we saw in section 9.1 at low static load, the sample is thermally unstable above $\sim$ 60°C and the foam starts compressing. As a consequence, the Young's modulus Y_1 increases leading to the observed increase in f_r^1. This is also in good agreement with the observed decrease in the acoustic attenuation after heating. However, as the sample contracts, the density increases and f_r^1 decreases. Therefore, an estimation of Y_1 after heating at 60°C would not be possible.

The effect of temperature on the thickness-mode resonator both for free and clamped resonators, is similar to that in length-mode and the reason is thought to be the same as that given for the length mode.

However, in the thickness mode, the resonances were more visible and the increase in k_{33} with increasing temperatures was observed for temperatures up to 50°C as expected from the decrease of the Young's modulus Y_3. However, at 60°C, k_{33} decreases by $\sim$ 13% with respect to the value at 50°C (free resonator) and by $\sim$ 25% at 70°C (clamped resonator). This decrease suggests that the sample depolarised for temperatures above $\sim$ 60°C, in good agreement with the TSC results observed for samples at zero stress (Fig.10.7b)).

These results demonstrated clearly that the cellular structure of the foam is unstable above $\sim 60^oC$.

11.3 SUMMARY

The piezoelectric d_{31}, d_{32} and d_{33} coefficients were measured at room temperature. The values obtained were in good agreement with those expected from the cellular structure. As a result of the particular cellular structure of the foam, the material exhibits a hydrostatic piezoelectric coefficient, d_h, which is close to d_{33}.

However, d_{33} drastically decreases when the samples are heated to temperatures above $\sim$ 60°C. Charge detrapping is thought to account for most of the observed decrease. However, part of the observed decrease of d_{33} may reflect the decrease in sample

stiffness due to irreversible thermal contraction.

From an analysis of the behaviour of the foam near to its piezoelectric resonances, we were able to extract information about the mechanical and electrical properties of the material. Thus, from the resonator parameters obtained for samples cut in different orientations and at different ambient pressures we determined the importance of the cellular structure and of the different phases, polypropylene and air, in the mechanical properties of the PP foam.

Similar Young's moduli Y_1, Y_2 were calculated from samples oriented in two different directions which may reflect the effect of the supra-structure and / or the effect of the metallic electrode. However, the different Young's moduli, Y_3, calculated from samples oriented in those directions, suggest that the cellular structure has a measurable influence on the mechanical properties of the foam. In both directions the thickness Young's modulus, Y_3, was more than three orders of magnitude larger than those obtained from direct observations where the low frequency stresses applied produced high strains.

The effect of temperature on the resonator character of the foam was also investigated. The analysis of the resonator parameters calculated at different temperatures and at room temperature after heating to different temperatures led us to propose that the Young's modulus of the foam decreases with temperature due to a decrease in the Young's modulus of the polypropylene for temperatures up to $\sim 50°C$. For higher temperatures, the foam is thermally unstable and irreversibly compresses. The decrease of the electromechanical coupling factor k_{33} at temperatures above $\sim 60°C$ suggests that the sample depolarises at around this temperature, in good agreement with the TSC curves taken under similar conditions.

Chapter 12

Conclusions and Future Work

12.1 Conclusions

This thesis reports an investigation of the thermal instability of PP electromechanical film (EMFi) based on an extensive study of the properties of the raw material (PP) and its cellular structure, and the effects of these on the mechanical, electrical and piezoelectric properties of the material. This is the first time that such an integrated, comprehensive study has been reported.

Firstly, we investigated the physico-chemical properties of the raw material (PP) using different techniques such as DSC, TGA, EDX and WAXD. The results obtained showed that the polypropylene forming the foam is a highly (in-plane) oriented 50% crystalline isotatic polypropylene with a wide distribution of spherulite size and loaded with $\sim 4\%$ of $CaCO_3$.

The analysis of SEM micrographs of the cross-section in perpendicular directions, $\vec{x}_1$ and $\vec{x}_2$, revealed both plane-to-thickness and in-plane anisotropy of the cellular structure. This anisotropy was quantified by the corresponding anisotropy ratios $R_{13} \sim 8$ and $R_{23} \sim 4.7$. Analysis of SEM micrographs, also yielded, assuming a total thickness of 70 μm, estimated values of $\sim$ 42.3 μm and 27.7 μm for the total thicknesses of air and polypropylene layers respectively for orientation $\vec{x}_1$ ($\rho = 347$ Kg m^{-3}) and 35.4 μm and 34.6 μm ($\rho = 437$ Kg m^{-3}) for orientation $\vec{x}_2$. The estimated densities, ρ, were

higher than that reported by the manufacturer (330 Kg m^{-3}).

Cross-section SEM micrographs also showed thick laminated cell walls in the thickness direction in comparison with those in lateral directions due probably to the collapse of individual voids. Such collapse may be due to leaking of the gas out of the sample due to compressions suffered by the foam during fabrication or during the required preparation of the samples for SEM microscopy.

The mechanical properties of non-poled foam in the thickness direction were studied using TMA and DMA techniques. From TMA experiments we directly measured the initial thicknesses of the utilised samples. We found an average thickness of 67 μm in good agreement with the value reported by the supplier (70 μm).

Under moderate static pre-compressions, the recorded strain-stress curves yielded unusually low thickness Young's modulus in comparison to the usual values found in literature for closed-cell foams. Although a low Young's modulus was expected for the particular cellular structure, *i.e.*, cells elongated in lateral directions, detailed calculation suggests also the importance of gas leakage out of the foam, *i.e.*, the partially open-cell character of the foam must be considered when explain the obtained Young's moduli.

The thermal stability of the mechanical properties of the foam was also investigated using TMA technique. We found that it is limited to temperatures around 60°C for low static mechanical loads. Above $\sim$ 60°C, irreversible compression was recorded. The high values obtained for the thermal expansion coefficients indicated that the contraction is mainly due to collapse of the voids. Also, we found that the thermal stability decreases with increase in the statically applied mechanical stress.

Pre-compressions at around 10^4 Pa, bring the sample to the densification regime. In good agreement, the storage modulus (Young's modulus) obtained using DMA measurements for pre-compressed samples was found, for temperatures below $\sim$ 40°C, to be around two orders of magnitude higher than those obtained using TMA. Above $\sim$ 40°C, the sample collapses and consequently, the storage modulus of the foam tends

towards that of solid polypropylene.

The strain-stress data extracted from the creep response curves of the foam under different step-stress functions at room temperature were found to lie close to the strain-stress curves confirming the low stiffness of the material in the thickness mode.

The creep-recovery curves obtained using the TMA technique indicate that, for long times and/or high temperatures, the viscous character of the polymer becomes important. Under such experimental conditions, the irreversible flow of the polymer leads to an irreversible compression of the foam and then, to a poor recovery after releasing the applied stress.

A two-layer model was used to estimate the total thickness of polypropylene and air layers from capacitance data. Using a circular sample (and thus not oriented in any particular direction) and assuming a total thickness of 70 μm, we obtained a total thickness of around 45.5 μm and 24.5 μm respectively for the air and PP layers in very good agreement with the values given by the manufacturer.

Using the two-layer model for the data obtained under different mechanical applied stress we calculated two sets of strain-stress data in reasonable agreement with those directly measured by using mechanical analysis techniques. This confirms, once again, the low stiffness of the material in the thickness direction.

The same procedure yielded unacceptably high densities for pre-electroded and poled samples if a total thickness of 70 μm was assumed. Assuming a total thickness of 60 μm gave however, more realistic density values. This probably reflects, again, the irreversible compression of the foam during electrode or poling processes. In consequence, an actual thickness between 60 μm and 70 μm was assumed for the foam.

From capacitance measurements, we also investigated the effect of ambient pressure on freely suspended pre-electroded and poled samples. Quasi-instantaneous expansion and contractions were recorded arising from the decrease and increase of the pressure, suggesting the presence of closed cells in the foam. Slow ($\sim$ 55 hours) gas diffusion out of and into the sample, driven by the difference in pressure inside and outside the foam,

was also observed.

Because of the low diffusion rates, the external pressure could be decreased without decreasing very much the pressure of the enclosed gas facilitating the thermal expansion of the enclosed gas. Such expansion produced negative-going thermally stimulated currents. In good agreement are the positive-going currents observed when the sample was compressed.

When the sample is free of stress and in equilibrium, the TSC runs only display the depolarisation of the sample starting at $\sim 60^{o}$C due to charge detrapping as suggested by the activation energy ($\sim$ 2 eV) calculated using the initial rise method.

As a result of the plane-to-thickness anisotropy of the cellular structure, the high orientation of the polymer and the effect of the electrodes, the pre-electroded samples display low piezoelectric d_{31} and d_{32} coefficients ($\sim$ -1.5 pC N^{-1}) in comparison with the thickness-mode, d_{33}, coefficient ($\sim$ 140 pC N^{-1}). Consequently, the material exhibits good properties for hydrostatic applications.

The piezoelectric coefficient, d_{33}, increases with increasing DC poling voltage at a rate which is especially high above 6 KV. Values of d_{33} as high as 250 pC N^{-1} were obtained after DC-voltage poling at 7 KV while poling at higher voltages was not possible due to the electrical failure of the foam.

However, the d_{33} value, displayed by the foam at room temperature after heating, drastically decreases after heating above $\sim 60^{o}$C, due mainly to the depolarisation of the material, as suggested by the TSC curves.

The decrease of the resonance and antiresonance frequencies with increasing temperature indicates that the Young's modulus of the foam decreases due to the decrease of the Young's modulus of the polypropylene. For temperatures above 60°C, the observed increase in the resonance and antiresonance frequencies measured at room temperature after heating suggests that the foam irreversibly compresses, in good agreement with the irreversible thermal contraction observed using TMA. Also in good agreement is the observed increase of the electromechanical coupling factor k_{33} for temperatures up

to 60°C and the decrease at room temperature for higher heating temperatures. The observed decrease of the electromechanical coupling factor k_{33} for temperatures above 60°C also reflects the depolarisation of the material observed in the TSC experiments.

12.2 Future Work

The results presented in this work reveal the usefulness of additional experimental work which would clarify some aspects of the electromechanical character of the cellular polypropylene.

In the following we give some examples of future work that may generate new results that increase our understanding about both the piezoelectric effect in porous materials and the thermal instability of the cellular polypropylene film.

It would be very helpful, in the understanding of the deformation process, to obtain SEM micrographs of the same zone of the sample before and after applying different compressive loads or after applying the same stress for different times or temperatures. Also SEM micrographs after heating to different temperatures would, by comparison, throw some light into the still not clear deformation mechanisms.

Capacitance data measured with greater frequency resolution in the range (10^4-10^6) Hz would produce more accurate curve fits and then more exact resonator parameters. With this available, the effect, not only of temperature, but also of the pre-compression on the piezoelectric properties of the material could be described in terms of precise values of the properties involved.

The highly accurate stress and strain determination provided by the standard apparatus utilized for mechanical properties, such as the DMA-7 Perkin-Elmer used in this work, the highly sensitive electrometers available, *e.g.*, Keithley 617 programmable electrometer, and impedance bridges suggest that the simultaneous use of all these technical facilities would provide a good method for an accurate electromechanical characterization of materials.

The historical overview in Chapters 2, 3 and 5 have drawn on the texts and papers listed below. References cited from these sources are included in the main reference list.

POLYMERS

Bolker, I, *Natural and Synthetic Polymers. An Introduction.* Marcel Dekker Inc, New York, (1974)

Ulrich, H, *Introduction to Industrial Polymers*, Hanser Publishers, (1982)

Eirich, K.F.(Editor), *Science and Technology of Rubber*, Academic Press, (1978)

Bovey, F. and Winslow, F (Editors). *Macromolecules. An Introduction to Polymer Science.* Academic Press, (1979)

M.P. Stevens, *Polymer Chemistry. An Introduction*, Oxford University Press, (1990)

Borchart, H.J. J. Chem Educ., **33**, 103, (1956)

Elias, H.G. *Macromolecules. Vol 1, Structures and Properties.* Plenum Press, (1977)

Tess, R. and Poehlein, W.(Editors) *Applied Polymer Science*, American Chemical Society, Washington, D.C., (1985)

DIELECTRICS

Hilczar, B. and Maleki, J. *Electrets*, Elsevier, (1986)

Ku, C.C. and Liepins, R. *Electrical Properties of Polymers. Chemical Principles*, Hanser Publishers, (1987)

Elliot, R.S. IEEE Trans. microwave theory and techniques, **36**, 806, (1988)

Böttcher, C.J.F. *Theory of Electric polarization*, Vol. 1, Elsevier, (1978)

Multhaupt, R.G. IEEE Trans. Electr. Insul., **EI-22**, 531, (1987)

Moore, A.D. *Electrostatics and its Applications*, John Wiley & Sons, (1973)

PIEZOELECTRICITY

Zelenka, Z. *Piezoelectric Resonators and their Applications*, Academic, Prage, (1986)

Cady, W.G. *Piezoelectricity*, McGraw-Hill, (1946)

Mason, W.P. *Piezoelectric Crystal and their Applications to Ultrasonics*, D. van Nostrand, (1956)

Taylor, G.W., Gagnepain, J.J, Meeker, T.R., Nakamura, T. and Shuvanov, L.A. (Editors), *Piezoelectricity*, Gordon and Breach Science Publishers, (1985)

Fukada, E. IEEE Trans. Ultrason. Ferroelectr. & Freq. Contr., **47**, 1277, (2000)

References

[1] Cowie, J. *Polymers: Chemistry & Physics of Modern Materials.* Blakie Academic & Professional, (1991).

[2] Keller, A. *J. Polym. Sci.* **39**, 151 (1959).

[3] Bunn, C. W. *Chemical Crystallography.* Oxford University Press, London & New York, (1946).

[4] Natta, G. and Corradini, P. *Nuovo Cim., Suppl.* **15**(10), 9 (1960). In reference [101].

[5] Das-Gupta, D. K. and Joyner, K. *J. Phys. D: Appl. Phys.* **9**, 2041 (1976).

[6] Dissado, L. A. and Fothergill, J. C. *Electrical Degradation and Breakdown in Polymers.* Peter Peregrinus Ltd., (1992).

[7] Krause, G., Meurer, D., and Klee, D. *IEEE Trans. Dielec. & Electr. Insul.* **24**(3), 419 (1989).

[8] Sessler, G. M. *Topics in Applied Physics Vol. 33. Electrets.* Springer-Verlag, (1980). Editor.

[9] Sessler, G. M. and West, J. E.

[10] Collins, R. E. *Proc. IREE* **34**, 381 (1973).

[11] Hilczer, B. and Malecki, J. *Electrets.* Elsevier, (1986).

[12] Sessler, G. M. and West, J. E. *J. Appl. Phys.* **43**, 922 (1972).

[13] Creswell, R. A., Perlman, M. M., and Kabayama, M. A. *Dielectric Properties of Polymers.* Plenum Press (1972). Edited by F. E. Karasz.

[14] Gibson, L. and Ahsby, M. *Proc. R. Soc. London A* **382**, 43 (1982).

[15] Paajanen, M., Välimäki, H., and Lekkala, J. *10th International Symposium on Electrets* , 735 (1999).

[16] Pope, M. I. *Differential Thermal Analysis.* Heyden & Son Ltd., (1977).

[17] Billmeyer, W. *Textbook of Polymer Science.* John Wiley & Sons, (1984).

[18] Tess, R. and Poehlein, W. *Applied Polymer Science.* American Chemical Society, Washington, D.C, (1985). (Ed.).

[19] Elias, H. G. *Macromolecules Vol.1, Structures and Properties.* Plenum Press, (1977).

[20] Brandrup, J. and Immergut, E. *Polymer Handbook.* John Wiley & Sons, (1960). (Editor).

[21] Gibson, J. and Ashby, F. *Cellular Solids. Structure and Properties.* Cambridge University Press, (1997).

[22] Rabuffi, M. and Picci, G. *IEEE Trans. Plasma Sci.* **30**(5), 1939 (2002).

[23] Fukada, E. *IEEE Trans. Ultrason. Ferrelectr. & Freq. Contr.* **47**(6), 1277 (2000).

[24] Furukawa, T. *IEEE Trans. Dielec. & Electr. Insul.* **24**(3), 375 (1989).

[25] Moulson, A. J. and Herbert, J. M. *Electroceramics.* Chapman & Hall, (1990).

[26] Neugschwandtner, G. S., Schwödiauer, R., Bauer-Gogonea, S., Paajanen, M., and Lekkala, J. *J. Appl. Phys.* **89**(8), 4503 (2001).

[27] Neugschwandtner, G. S., Schwödiauer, R., Bauer-Gogonea, S., Paajanen, M., and Lekkala, J. *J. Appl. Phys.* **89**(8), 4503 (2001).

[28] Berlincourt, D. A., Curran, D. R., and Jaffe, H. *Piezoelectric and Piezomagnetic Materials and Their Function in Transducers. In Physical Acoustics.* Academic Press (1964). Edited by W. P. Mason.

[29] Zelenka, J. *Piezoelectric Resonators and their Applications.* Academia, Prage, (1986).

[30] Marín-Franch, P. *Evaluation of PTCa PEKK Composite Sensors for Acoustic Emission Detection.* PhD thesis, School of Informatics, University of Wales, Bangor, (2002).

[31] James, L. K. *Nobel Laurates in Chemistry: 1901-1992.* American Chemical Society and Chemical Heritage Foundation (1994). Editor.

[32] Munk, P. *Introduction to Macromolecular Science.* John Wiley & Sons, (1989).

[33] Wolf, R. *Rubber World* **10**, 64 (1964).

[34] *National Historic Chemical Landmarks. Am. Chem. Soc.* (2001).

[35] Faraday, M. *Q. J. Sci.* **21**, 19 (1826).

[36] Harries, C. *Ber. Dtsch. Chem. Ges.* **37**, 2708 (1904).

[37] Eirich, K. F. *Science and Technology of Rubber.* Academic Press, (1978). (Editor).

[38] Williams, G. *Proc. R. Soc. London* **10**, 516 (1860).

[39] Bolker, I. *Natural and Synthetic Polymers. An Introduction.* Marcel Dekker Inc, New York, (1974).

[40] Hooke, R. *Micrographia.* London, (1665). Reprinted by New-York -Weinheim, 1961.

[41] Mauskopf, S. H. *Dictionary of Scientific Biography*, volume 2. Charles Scribner's Sons, New York, (1970).

[42] Ulrich, H. *Introduction to Industrial Polymers.* Hanser Publishers, (1982).

[43] Berthelot, M. *Bull. Soc. Chim. France* **6**, 294 (1866).

[44] Baekeland, L. *J. Ind. Eng. Chem.* **1**, 149 (1909).

[45] Staudinger, H. *Ber. Dtsch. Chem. Ges.* **B53**, 1073 (1920).

[46] Graham, T. *Phil. Trans. Roy. Soc. London* **A151**, 183 (1861).

[47] Olby, R. *J. Chem. Educ.* **47**(3), 168 (1970).

[48] Mark, H. *J. Polym. Sci.* , 1 (1965).

[49] Katz, I. *Naturwissenschaften* **13**, 410 (1925).

[50] Sponsler, O. *J. Gen. Physiol.* **9**, 677 (1926).

[51] Sponsler, O. and Dore, W. *Colloid Symposium Monograph Vol IV*, 174. Chemical Cataloge Co. (1926).

[52] Meyer, K. and Mark, H. *Ber. Dtsch. Chem. Ges.* **61B**, 1936 (1928).

[53] Staudinger, H. *Ber. Dtsch. Chem. Ges* **61B**, 2427 (1928).

[54] Svedberg, T. and Rinde, H. *J. Am. Chem. Soc.* **46**, 2677 (1924).

[55] Svedberg, T. and Fahraeus, R. *J. Am. Chem. Soc.* **48**, 430 (1926).

[56] Carothers, W. *J. Am. Chem. Soc.* **51**, 2548 (1929).

[57] Carothers, W. *Chem. Rev.* **8**, 353 (1931).

[58] Bovey, F. and Winslow, F. *Macromolecules. An Introduction to Polymer Science.* Academic Press, (1979). Editors.

[59] Flory, J. *J. Am. Chem. Soc.* **59**, 241 (1937).

[60] Khun, W. *Ber. Dtsch. Chem. Ges.* **65**, 1503 (1930).

[61] Ziegler, K., Gellert, H. G., Martin, H., Nagel, K., and Schneider, J. *Just. Liebigs Ann. der Chim.* **589**, 91 (1954).

[62] Natta, G., Pino, P., Corradini, P., Danusso, F., Mantica, E., Mazzanti, G., and Moraglio, G. *J. Am. Chem. Soc.* **77**, 1708 (1955).

[63] Natta, G. *J. Polym. Sci.* **XVI**, 143 (1955).

[64] Jaccodine, R. *Nature* **176**, 305 (1955).

[65] Chatelier, H. L. *Bull. Soc. Franc. Mineral.* **10**, 204 (1887).

[66] Chatelier, H. L. *Z. Phys. Chem.* **1**, 396 (1887).

[67] Borchardt, H. J. *J. Chem. Educ.* **33**, 103 (1956).

[68] Watson, E. S., O'Neil, M. J., Justin, J., and Brenner, N. *Anal. Chem.* **36** (1964).

[69] Stevens, M. P. *Polymer Chemistry. An Introduction.* Oxford University Press, (1990).

[70] Loft, B. C. *J. Polym. Sci. Polym. Symposium* **49**, 127 (1975).

[71] Kaway, N. *Japan J. Appl. Phys.* **8**, 975 (1969).

[72] Nakamura, K. and Wada, Y. *J. Polym. Sci. Polymer Chem. Ed.* **16**, 3039 (1971).

[73] Gennes, P. D. *J. Chem. Phys.* **55**(2), 572 (1972).

[74] Klein, J. *Nature* **271**(12), 143 (1978).

[75] Shirakawa, H., Louis, E., MacDiarmid, A., Chiang, C., and Heeger, A. *J. Chem. Soc. Chem. Commun.* , 578 (1977).

[76] Young, R. *Introduction to Polymers.* Chapman and Hall, (1983).

[77] Das-Gupta, D. *IEEE Trans. Dielec. & Electr. Insul.* **8**(1), 6 (2001).

[78] London, F. *Z. Phys.* **63**, 245 (1930). In reference [163], page 127.

[79] der Waals, J. D. V. PhD thesis, Leiden (holland), (1890). English translation by Threlfall and Adair, *Phisical Memoires **1**, 333, (1891).* In reference [163] page 127.

[80] Curtis, H. and Barnes, N. *Invitation to Biology.* Worth Publishers, (1994).

[81] Gennes, P. D. *Scaling Concepts in Polymer Physics.* Cornell University Press, (1979).

[82] Hanks, P. *The New Oxford Dictionary of English.* Clarendon Press, Oxford, (1998). Chief Editor.

[83] Peterlin, A. *J. Polym. Sci.* **C9**, 61 (1965).

[84] Nishikawa, S. and Ono, S. *Proc. Math. & Phys. Soc. Tokyo* **7**, 131 (1913). In reference [27].

[85] Schildknecht, C. *Ind. Eng. Chem.* **40**, 708 (1948).

[86] Schlesinger, H. and Leeper, H. *J. Polym. Sci.* **XI**(3), 203 (1953).

[87] Fisher, A. *Z. Naturforsch.* **12a**, 753 (1957). In reference [72].

[88] Keller, A. *Philos. Mag.* **2**(8), 1171 (1957).

[89] Till, P. *J. Polym. Sci.* **25**(106), 301 (1957).

[90] Das-Gupta, D. *IEEE Electr. Insul. Magazine* **10**, 5 (1994).

[91] Bunn, C. and Alcock, T. *Trans. Faraday Soc.* **41**, 317 (1945).

[92] K. Hermann, O. G. and Abitz, K. *Z. Physik. Chem.* **B10**, 371 (1930). In reference [72].

[93] K. Hermann, O. G. and Abitz, K. *Biochem. Z.* **228**, 409 (1930). In reference [72].

[94] Bunn, C. *Proc. Roy. Soc.* **A180**, 82 (1942).

[95] Mark, H. *J. Phys. Chem.* **44**, 764 (1940).

[96] Storks, K. *J. Am. Chem. Soc.* **60**, 1753 (1938).

[97] Flory, J. *J. Am. Chem. Soc.* **84**, 2857 (1962).

[98] Geil, P., F.R., Anderson, Wunderlich, B., and Arakawa, T. *J. Polym. Sci.* **A2**, 3707 (1964).

[99] Bailey, R. T., North, A., and Pethrick, R. A. *Molecular Motion in High Polymers.* Oxford Science Publications, (1981).

[100] Varga, J. *Crystallization, Melting and Supermolecular Structure of Isotactic Polypropylene. In Polypropylene: Structure, Blends and Composites. Edited by J. Karger-Kocsis.* Chapman and Hall, (1995).

[101] Wunderlich, B. *Macromolecular Physics. Vol 2.* Academic Press, New York, (1980).

[102] Young, R. J. and Lovell, P. A. *Introduction to Polymers.* Cambridge University Press, (1983).

[103] Audren, P. and Ronach, D. *J. Appl. Phys.* **60**, 946 (1986).

[104] Willbourn, A. H. *Trans. Faraday Soc.* **54**, 717 (1958).

[105] Sinnott, K. M. *J. Appl. Phys.* **37**, 3385 (1966).

[106] Hoofmann, J. D., Williams, G., and Passaglia, E. *J. Polym. Sci.* **C14**, 173 (1966).

[107] Stehling, F. C. and Mandelkern, L. *Macromolecules* **3**, 242 (1970).

[108] Natta, G., Corradini, P., and Cesari, M. *Atti dell Áccademia Nazionale dei Lincei Rendiconti* **21**, 365 (1956). In reference [402], page 5.

[109] Natta, G., Corradini, P., and Ganis, P. *J. Polym. Sci.* **58**, 1191 (1962).

[110] Turnes-Jones, A., Aizlewood, J. M., and Beckett, D. R. *Makromolekulare Chemie* **75**, 134 (1964).

[111] Morrow, D. R. and Newman, B. A. *J. Appl. Phys.* **39**, 4944 (1968).

[112] Cheng, S. Z. D., Janimak, J. J., and Rodríguez, J. *Crystalline Structures of Polypropylene Homo- and Copolymers in Polypropylene. In Polypropylene: Structure Blends and Composites. Edited by J. Karger-Kocsis.* Chapman and Hall, (1995).

[113] Ramby, B., Morehead, F., and Walter, N. *J. Polym. Sci.* **44**, 349 (1960).

[114] Kowalewski, T. and Galeski, A. *J. Appl. Polym. Sci.* **32**, 2919 (1986).

[115] Mitsuishi, K., Ueno, S., Kodana, S., and Kawasaki, H. *J. Appl. Polym. Sci.* **43**, 2043 (1991).

[116] Rybnikar, F. *J. Appl. Polym. Sci.* **27**, 1479 (1982).

[117] Menczel, J. and Varga, J. *J. Therm. Anal.* **28**, 161 (1983).

[118] Kip, A. F. *Fundamentals of Electricity and Magnetism.* McGraw-Hill Book Company, Inc., (1962).

[119] Moore, A. D. *Electrostatics and its Applications.* John Wiley & Sons, (1973).

[120] Kuhfeld, A. W. *IEEE Engin. Med. & Bio.* **January/February**.

[121] Gilbert, W. *De Magnete.* London, (1600). An English translation from the Latin was published by Mottlelay in 1893.

[122] Kelly, S. *Dictionary of Scientific Biography*, volume 5. Charles Scribner's Sons, New York, (1970).

[123] Multhaupt, R. G. *IEEE Trans. Dielec. & Electr. Insul.* **26**(1), 85 (1991).

[124] Gray, S. *Phil. Trans. Roy. Soc. London* **37**, 285 (1732).

[125] Eguchi, M. *Proc. Phys. Math. Soc. Jap. Ser. 3* **1**, 326 (1919).

[126] Eguchi, M. *Phil. Mag.* **49**, 178 (1925).

[127] Wilcke, J. C. *K. Svenka Vetenskaps Academiens Handlingar* **23**, 206 (1762).

[128] Wilcke, J. C. *K. Svenka Vetenskaps Academiens Handlingar* **23**, 245 (1762).

[129] Elliot, E. *Polymers and People: An Informal History.* Chemical Heritage Foundation (www.chemheritage.org/EducationalServices/Polymers+People), (2000).

[130] Heilbron, J. L. *Dictionary of Scientific Biography*, volume 1. Charles Scribner's Sons, New York, (1970).

[131] von Laue, M. *History of Physics.* Academic Press, Inc., (1950).

[132] Coulomb, C. A. *Histoire de l'Académie Royale des Sciences* , 569 (1785).

[133] Poisson, S. S. D. *Bull. Soc. Philomanthique* **3**, 388 (1813).

[134] Ampere, A. M. *Ann. Chimie et Physique* **15**, 59 (1820).

[135] Poisson, S. D. *Mém. Acad. Sci., Paris. Ser. 2* **5**, 247 (1824).

[136] Faraday, M. *Phil. Trans. Roy. Soc. London* **142**, 25 (1852).

[137] Slater, C. J. *Electromagnetism.* McGraw-Hill, Inc., (1947).

[138] Mossotti, O. F. *Bibl. Univ. Modena* **6**, 193 (1847). In references [153] page 22 and [163] page 2.

[139] Clausius, R. *Die Mechanische Wärmetheorie. Vol. 2.* Vieweg Verlag, Braunschweich, (1879).

[140] Matteucci, C. *Ann. Chim. Phys.* **27**, 133 (1849).

[141] Kohlrausch, R. *Ann. Phys.Chem.* **91**, 56 (1854).

[142] Kohlrausch, R. *Ann. Phys. Chem.* **91**, 179 (1854).

[143] Hedvig, P. *Dielectric Spectroscopy of Polymers.* Adam Hilger Ltd., (1977).

[144] Maxwell, J. (1856). Read to the Cambridge Philosophical Society on December 10, 1855 and February 11, 1856. Reprinted in *Scientific Papers*, Vol I, London: Cambridge University Press, 1890.

[145] Maxwell, J. C. *A Treatise on Electricity and Magnetism. Vol I.* Dover, (1954).

[146] Wagner, K. W. *Archiv für Electrotechnik 2* , 371 (1914).

[147] Sillars, R. W. *IEE Journal* **80**, 378 (1937).

[148] Siemens, W. *Poggendorf Annalen de Physik und Chemie* **125**, 137 (1864).

[149] Maxwell, J. *Phil. Trans. Roy. Soc. London* **155**, 459 (1865).

[150] Pellat, H. *Annales de Chimie et de Physique* **18**, 150 (1899).

[151] Pellat, H. *Journal de Physique* **9**, 313 (1900).

[152] Hertz, H. *Ann. Phys.* **31**, 421 (1887).

[153] Drude, P. *Z. Phys.* **23**, 267 (1897).

[154] von Schweidler, E. *Ann. Phys.* **4**(24), 711 (1913).

[155] Wagner, K. W. *Ann. Phys.* **4**(40), 817 (1913).

[156] Debye, P. *Ber. D. Phys. Ges.* **15**, 777 (1913). *Collected Papers*, Interscience, New York 1954.

[157] Stokes, G. *Trans. Cambridge Phil. Soc.* **9**, 8 (1951).

[158] Ku, C. C. and Liepins, R. *Electrical Properties of Polymers.* Hanser Verlag, (1987).

[159] Heaviside, O. *Phil. Trans. Roy. Soc. London* **155**, 459 (1865).

[160] Fukada, E. *IEEE Trans. Ultrason., Ferroelectr. and Freq. Contr.* **47**(6), 1277 (2000).

[161] Kelvin, W. T. L. *Reprints of Papers on Electrostatics and Magnetism.* MacMillan and Co., (1872).

[162] Maxwell, J. C. *A Treatise on Electricity and Magnetism. Vol II.* Dover, (1954).

[163] Lorentz, H. A. *Proc. Roy. Acad. Amsterdam* , 254 (1902).

[164] Mazur, P. and Nijboer, B. R. A. *Physica* **19**, 971 (1953). In reference [163] page 59.

[165] Mazur, P. *Advances in Chem. Phys.* **1**, 310 (1958). In reference [163] page 59.

[166] Groot, S. R. and Vlieger, J. *Physica* **31**, 125 (1965). In reference [163] page 59.

[167] Böttcher, C. J. F. *Theory of Electric Polarization. Vol. I.* Elsevier, (1973).

[168] Ashcroft, N. W. and Mermin, N. D. *Solid State Physics.* Holt, Rinehart and Winston, (1976).

[169] Lorrain, P. and Corson, D. R. *Campos y Ondas Electromagnéticas.* Selecciones Científicas, (1972). In Spanish.

[170] Joncher, A. *Dielectric Relaxations in Solids.* Chelsea Dielectric Press, (1983).

[171] Landau, L. D. and Lifshitz, E. M. *Electrodynamics of Continuous Media.* Pergamon Press, (1960).

[172] Jackson, J. D. *Classical Electrodynamics.* John Wiley & Sons, Inc., (1963).

[173] Maxwell, J. C. *Phil. Trans. Roy. Soc. London* **158**, 643 (1868). In reference [163] page 2.

[174] Lorenz, L. *Ann. Phys. Chem.* **11**, 70 (1880). In references [153] page 22 and [163] page 2.

[175] Lorentz, H. A. *Ann. Phys.* **9**, 641 (1880).

[176] Debye, P. *Phys. Z* **13**, 97 (1912). In references [153] page 23 and [163] page 3.

[177] Langevin, P. *J. Phys.* **4**(4), 678 (1905). In reference [163] page 163.

[178] Langevin, P. *Ann. Chim. Phys.* **5**(8), 70 (1905). In reference [163] page 163.

[179] Joncher, A. K. *IEEE Trans. Dielec. & Electr. Insul.* **27**(3), 407 (1992).

[180] Onsager, L. *J. Am. Chem. Soc.* **58**, 1486 (1936).

[181] Fröhlich, H. *Theory of Dielectrics. Dielectric Constant and Loss.* Clarendon Press, (1958).

[182] Scholte, T. G. PhD thesis, Leiden, (1950). In reference [163] page 137.

[183] Kramers, H. A. *Collected Sci. Papers.* North-Holland, Amsterdam, (1956).

[184] Kronig, R. *J. Opt. Soc. Am.* **12**, 547 (1926).

[185] Curie, J. *Ann. Phys. Chem., Paris* **18**, 208 (1889). In reference.

[186] Taylor, D. M. and Lewis, T. J. *J. Phys. D: Appl. Phys.* **4**, 1346 (1971).

[187] Kirkwood, J. G. *J. Chem. Phys.* **7**, 911 (1939).

[188] Albella-Martin, J. M. and Martinez-Duart, J. M. *Física de Dieléctricos. Aplicación a los Materiales y Dispositivos Electrónicos.* Boixareu Editores, (1984).

[189] Kittel, C. *Introducción a la Física de Estado Sólido.* Editorial Reverté S.A., (1993).

[190] Frenkel, J. *Phys. Rev.* **37**, 1276 (1931).

[191] Das-Gupta, D. K. *J. Electrostatics* **51-52**, 160 (2001).

[192] Wannier, G. H. *Phys. Rev.* **52**, 191 (1937).

[193] Adamec, V. and Calderwood, J. H. *J. Phys. D: Appl. Phys* **11**, 781 (1978).

[194] Ieda, M. *IEEE Trans. Dielec. & Electr. Insul.* **EI-19**(3), 162 (1984).

[195] Das-Gupta, D. K. *IEEE Trans. Dielec. & Electr. Insul.* **8**(1), 6 (2001).

[196] Cole, K. S. and Cole, R. H. *J. Chem. Phys.* **9**, 341 (1941).

[197] Böttcher, C. J. F. and Bordewijk, P. *Theory of Electric Polarization. Vol. II.* Elsevier, (1978).

[198] Cole, R. H. *J. Chem. Phys.* **23**, 493 (1955).

[199] Davidson, D. W. and Cole, R. H. *J. Chem. Phys.* **18**, 1417 (1950).

[200] Davidson, D. W. and Cole, R. H. *J. Chem. Phys.* **19**, 1484 (1951).

[201] Havriliak, S. and Negami, S. *J. Polym. Sci.* **C14**, 99 (1966).

[202] Fuoss, R. M. and Kirkwood, J. G. *J. Am. Chem. Soc.* **63**, 385 (1941).

[203] Joncher, A. K. *Colloid Polym. Sci.* **253**, 231 (1975). In reference [175] page 115.

[204] Joncher, A. *IEEE Elec. Insul. Mag.* **6**(2), 16 (1990). Stated in Editor's note.

[205] Dissado, L. A. *Phys. Scripta* **T1**, 110 (1982). In reference [175] page 369.

[206] Dissado, L. A. and Hill, R. M. *Proc. Roy. Soc. London* **A390**, 131 (1983).

[207] Dissado, L. A. *Chem. Phys.* **91**, 183 (1984).

[208] Dissado, L. A. and Hill, R. M. *J. Chem. Soc. Faraday Trans. 2* **80**, 291 (1984).

[209] Bloch, F. *Z. Physik* **52**, 555 (1928).

[210] Anderson, P. W. *Phys. Rev.* **109**, 1492 (1958).

[211] Mott, N. F. *Phil. Mag.* **13**, 689 (1966).

[212] Mott, N. F. *Advances in Physics* **16**, 49 (1967).

[213] Cohen, M. H., Fritzsche, H., and Ovshinsky, S. R. *Phys. Rev. Lett.* **22**, 1065 (1969).

[214] Lewis, T. J. *IEEE 7th International Conference on Solid Dielectrics, Eindhoven, Nederlands* , 223 (2001).

[215] Meunier, M., Quirke, N., and Aslanides, A. *Conference on Electrical Insulation and Dielectric Phenomena* , 21 (2000).

[216] Fowler, J. F. *Proc. R. Soc. London* **A236**, 464 (1956).

[217] Creswell, R. A. and Perlman, M. M. *J. Appl. Phys.* **41**(6), 2365 (1970).

[218] Perlman, M. M. *J. Electroch. Soc.* **119**, 892 (1972).

[219] Das-Gupta, D. K. *IEEE Trans. Dielec. & Electr. Insul.* **27**(5), 909 (1992).

[220] Fuhrmann, H. *J. Electrostatics* **4**, 109 (1978).

[221] Rodehed, C. and andU.W. Gedde, A. G. *IEEE Trans. Dielec. & Electr. Insul.* **25**, 1066 (1990).

[222] Haridoss, S. and Perlman, M. M. *J. Appl. Phys.* **55**(5), 1332 (1984).

[223] Baba, A. and Ikezaki, K. *Appl. Phys. Lett.* **40**(12), 1027 (1982).

[224] Das-Gupta, D. K. *IEEE Trans. Dielec. & Electr. Insul.* **4**(2), 149 (1997).

[225] Malecki, J. *9th International Symposium on Electrets* , 110 (1996).

[226] Gemant, A. *Phil. Mag.* **20**, 929 (1935).

[227] van Turnhout, J. *Thermally Stimulated Discharge of Polymer Electrets.* Elsevier, Amsterdam, (1975).

[228] Sessler, G. M. and West, J. E. *Appl. Phys. Lett.* **17**, 507 (1970).

[229] Sessler, G. M. and West, J. E. *J. Electrostatics* **1**, 111 (1975).

[230] Gross, B., Sessler, G. M., and West, J. E. *J. Appl. Phys.* **45**, 2841 (1974).

[231] Perlman, M. M. *Appl. Phys. Lett.* **24**, 579 (1974).

[232] Carlson, C. F. *US Patent 2.588.699* (1952). In reference [3] page 30.

[233] Tyler, R. W., Webb, J. H., and York, W. C. *J. Appl. Phys.* **26**, 61 (1955).

[234] Sawa, G., Lee, D. C., and Ieda, M. *Jap. J. Appl. Phys.* **14**, 643 (1975). In reference [3] page 30.

[235] Starr, W. T. and Steffens, H. *IEEE Electr. Insul. Magazine* , 41 (1988).

[236] von Seggern, H. *J. Appl. Phys.* **50**(4), 2817 (1979).

[237] Shahin, M. M. *J. Appl. Opt.* **Suppl. 3**, 106 (1969). In reference [3] page 30.

[238] Perlman, M. M., Kao, K. J., and Bamji, S. *The Effect of Corona Generated Excited Molecules on Surface Potential Decay in Polyethylene. In Charge Storage, Charge Transport and Electrostatics with their Applications.* Elsevier Sci. Publishing company, Amsterdam (1979). Edited by Y. Yada, M. M. Perlman and H. Kokado.

[239] Vance, D. W. *1970 Ann. Rep. Conf. Electr. Insul. & Dielectr. Phenom.* , 1 (1971).

[240] Carlson, D. and Wiles, D. *Canad. J. Chem.* **48**, 2397 (1970).

[241] Ziyu, L., Guanghui, C., and Welfang, J. *Conference Record of 1986 IEEE Int. Symp. Elect. Insul.* , 343 (1986).

[242] Blaise, P., Carlsson, D. J., and Wiles, D. M. *J. Polym. Sci.* **A-1**(10), 1077 (1972).

[243] Perlman, M. M. and Reedyk, C. W. *J. Electroch. Soc.* **115**, 45 (1968).

[244] Lewis, T. J. *IEEE Elect. Insul. Mag.* **17**(4), 6 (2001).

[245] Ieda, M., Mizutami, T., and Ikeda, S. *IEEE Trans. Dielec. & Electr. Insul.* **EI-21**(3), 301 (1986).

[246] Mizutami, T. and Ieda, M. *IEEE Trans. Dielec. & Electr. Insul.* **EI-21**(6), 833 (1986).

[247] Iida, K., Kim, J. S., Nakamura, S., and Sawa, G. *IEEE Trans. Dielec. & Electr. Insul.* **27**(2), 391 (1992).

[248] Vanderschueren, J. and Linkens, A. *J. Appl. Phys.* **49**, 4195 (1978).

[249] Seanor, D. A. *J. Polym. Sci.A-2* **6**, 463 (1968).

[250] Saito, S., Sasabe, H., Nakajima, T., and Yada, K. *J. Polym. Sci. A-2* **6**, 1297 (1968).

[251] Wintle, H. J. *IEEE Trans. Dielec. & Electr. Insul.* **6**(1), 1 (1999).

[252] McCubbin, W. L. *J. Polym. Sci.* **C9**(30), 181 (1970).

[253] Kryszewski, M. *J. Polym. Sci. Polym. Symposium* **50**, 359 (1975).

[254] Hirsch, J. and Martin, E. *J. Appl. Phys.* **43**, 1001 (1972).

[255] Less, K. J. and Wilson, E. G. *J. Phys. C: Sol. Stat. Phys.* **6**, 3110 (1973).

[256] Lowell, J. *J. Phys. D: Appl. Phys.* **23**, 205 (1990).

[257] Swan, D. W. *J. Appl. Phys.* **48**, 5051 (1967).

[258] Lewis, T. J. and Taylor, D. M. *J. Phys. D: Appl. Phys.* **5**, 1664 (1972).

[259] Chand, S. and Mehendru, P. C. *J. Phys. D: Appl. Phys.* **19**, 857 (1986).

[260] Karanja, P. and Nath, R. *IEEE Trans. Dielec. & Electr. Insul.* **1**(2), 213 (1994).

[261] Ríos, E. G. *Química Inorgánica.* Editorial Reverté, (1994). In Spanish.

[262] Joumha, A. and Reboul, J. P. *8 th International Symposium on Electrets* , 517 (1994).

[263] Anderson, E. W. and McCall, D. W. *J. Polym. Sci.* **31**, 241 (1958).

[264] Curtis, A. J. *J. Chem. Phys.* **36**, 3500 (1962).

[265] de Haan, P. H., van Turnhout, J., and Wapenaar, K. E. D. *Proc. of the 5 th International Symposium on Electrets* , 756 (1985).

[266] von Seggern, H. *J. Appl. Phys.* **52**(4), 4086 (1981).

[267] Yang, G. M. *J. Phys. D: Appl. Phys.* **25**, 690 (1993).

[268] Singh, R., Keller, J. M., and Datt, S. *Proceedings 6th Internatinal Symposium on Electrets* , 313 (1988).

[269] Datt, S. C., Baghel, R. S., and Singh, R. *Proceedings 6th International Symposium on Electrets* , 246 (1988).

[270] Motyl, E. *J. Electrostatics* **30**, 57 (1993).

[271] Krause, G., Meurer, D., and Klee, D. *Proc. 6 th International Symposium on Electrets* , 92 (1988).

[272] Krause, G., Möller, K., and Meurer, D. *IEEE Trans. Dielec. & Electr. Insul.* **24**(2), 215 (1989).

[273] Nath, R. and Perlman, M. *IEEE Trans. Dielec. & Electr. Insul.* **24**(3), 409 (1989).

[274] Baba, A. and Ikezaki, K. *J. Appl. Phys.* **72**, 2057 (1992).

[275] Ikezaki, K., Yagishita, A., and Yamanouchi, H. *8 th International Symposium on Electrets* , 428 (1994).

[276] Love, A. E. H. *A Treatise on the Mathematical Theory of Elasticity.* Dover, New York, (1944).

[277] Thurston, R. N. *Wave Propagation in Fluids and Normal Solids. In Physical Acoustics.* Academic Press (1964). Edited by W. P. Mason.

[278] Murnagham, F. D. *Finite Deformation of an eleastic body.* Wiley, (1951).

[279] Hansen, A. H. *Fluids Mechanics.* Wiley, New York, (1967).

[280] Rodríguez-Pérez, M. A. *Propiedades Térmicas y Mecánicas de Espumas de Poliolefinas.* PhD thesis. University of Valladolid (Spain), (1998).

[281] Rosen, S. L. *Fundamental Principles of Polymeric Materials.* J. Wiley, New York, (1982).

[282] Jourdan, C., Cavaille, Y., and Pérez, J. *J. Polym. Sci. Polym. Phys. Ed.* **27**, 2361 (1989).

[283] Inamura, I., Ochiai, H., and Yamamura, H. *J. Polym. Sci. Polym. Phys. Ed.* **12**, 2267 (1974).

[284] Rayleigh, J. W. S. *Proc. Math. Soc. London* **17** (1887).

[285] Rayleigh, J. W. S. *Scientific Papers. Vol. 2.* Cambridge University Press, (1900).

[286] Lamb, H. *Phil. Trans. Roy. Soc. London* **A203**, 1 (1904).

[287] Lamb, H. *Proc. Roy. Soc. London* **A93**, 114 (1917).

[288] Sauer, J. A., Wall, R. A., Fuschillo, N., and Woodward, A. *J. Appl. Phys.* **29**(10), 1385 (1958).

[289] Turley, S. G. and Keskkula, H. *J. Polym. Sci.* **C14**, 69 (1966).

[290] Boyd, R. H. *Polym. Eng. Sci.* **19**, 1010 (1979).

[291] Wada, Y. and Hotta, Y. *J. Polym. Sci.* **C23**, 583 (1968).

[292] Muus, L. T., McCrum, N. G., and McGrew, F. C. *SPE J.* **15**, 368 (1959). In reference [293].

[293] McCrum, N. G. *Polym. Lett.* **2**, 167 (1964).

[294] Sinnott, K. M. *SPE Trans* **2**, 65 (1962). In reference [293].

[295] Slichter, W. P. and Mandell, E. R. *J. Appl. Phys.* **29**, 1438 (1958).

[296] Berna, J. L. *Revista de Plasticos Modernos* **435**, 289 (1992).

[297] Cowin, S. *J. Materials Science* **26**, 5155 (1991).

[298] Sämäläinen, M. K. and Parviainen, J. K. *Rev. Sci. Intrum.* **67**, 1598 (1996).

[299] Paajanen, M., Välimäki, H., and Lekkala, J. *J. Electrostatics* **48**, 192 (2000).

[300] Rodríguez-Pérez, M. A., Alonso, O., Duijsens, A., and de Saja, J. A. *J. Polym. Sci., Phys. Ed.* **36**, 2587 (1998).

[301] Ko, W. L. *J. Cellular Plastics* **1**, 217 (1965).

[302] Patel, M. and Finnie, I. *J. Mater.* **5**, 909 (1970).

[303] Menges, G. and Knipschild, F. *Polym. Eng. Sci.* **15**, 623 (1975).

[304] Warren, W. and Kraynik, A. *J. Appl. Mech.* **55**, 341 (1988).

[305] Gent, A. and Thomas, A. *J. Appl. Polym. Sci.* **1**, 107 (1959).

[306] Gent, A. and Thomas, A. *Rubber Chem. Tech.* **36**, 597 (1963). In reference [284] page 266.

[307] Lederman, J. *J. Appl. Polym. Sci.* **15**, 693 (1971).

[308] Christensen, R. *J. Mech. Phys. Solids* **34**, 563 (1986). In reference [111] page 183.

[309] Green, D. *J. Amer. Chem. Society* **68**, 403 (1985).

[310] Skochdopole, R. and Rubens, L. *J. Cellular Plastics* **1**, 91 (1965).

[311] M.Fátima and Fortes, M. *J. Matter. Sci. Lett.* **12**, 1408 (1993).

[312] Wegner, L. and Gibson, L. *Acta Metall. Mater.* **43**, 1651 (1995).

[313] Mackenzie, R. *Acoustic Bulletin* **March/April**, 29 (1994). In reference [284] page 263.

[314] Weaire, D. and Fortes, M. *Advances in Physics* **43**, 685 (1984).

[315] P. Barma, M. R. and Salovey, R. *J. Appl. Phys.* **49**, 4985 (1978).

[316] Chan, R. and Nakamura, M. *J. Cell. Plast.* **5**, 112 (1969).

[317] Mantonis, V. *Soc. Plast. Eng. J.* **September**, 1024 (1964). In reference [111] page 198.

[318] Mills, N. *Low density cellular plastics: Physical Basis of Behaviour.* Chapman and Hall, (1994). Edited by N. C. Hilyard and A. Cunnungham.

[319] Zhang, J. and Ashby, M. *CPGS Thesis.* Cambridge, UK, (1988).

[320] Maiti, S., Ashby, M., and Gibson, L. *Acta Metall.* **32**, 1963 (1984).

[321] Becquerel, A. C. *Bull. Soc. Philomath. Paris. Ser 3* **7**, 149 (1820).

[322] Wyari, J. *Dictionary of Scientific Biography, Vol.3.* Charles Scribner's Sons, New York, (1970).

[323] Curie, J. and Curie, P. *Bull. Soc. Min. de France* **3**(4), 90 (1880).

[324] Curie, J. and Curie, P. *C. R. Acad. Sc. Paris* **91**, 383 (1880).

[325] Cady, W. G. *Piezoelectricity.* McGraw-Hill Book Company, Inc, (1946).

[326] Hankel, W. G. *Abh. Sächs* **12**, 457 (1881).

[327] Hankel, W. G. *Ber. Sächs* **33**, 52 (1881).

[328] Lippman, G. *C. R. Acad. Sc. Paris* **92**, 1049 (1881).

[329] Curie, J. and Curie, P. *C. R. Acad. Sc. Paris* **93**, 1137 (1881).

[330] Curie, J. and Curie, P. *C. R. Acad. Sc. Paris* **94** (1882).

[331] Curie, M. S. *Traité de Radioacivité.* Gauthiers Villars, Paris, (1910).

[332] Kelvin, L. *Phil. Mag.* **36**, 331 (1893).

[333] Kelvin, L. *Baltimore Lectures on Molecular Dynamics and The Wave Theory of Light.* Cambridge University Press, London, (1904).

[334] Heising, R. A. *Quartz Crystals for Electrical Circuits*, chapter Quartz Crystals Applications. Van Nostrand, New York (1946).

[335] Gibbs, R. E. *Proc. Roy. Soc. London* **A110**, 443 (1926).

[336] Jaffe, H. *Phys. Rev.* **66**, 357 (1944).

[337] Ballato, A. *1996 IEEE Ultrasonics Symposium* , 575 (1996).

[338] Voigt, W. *Abh. Gött.* **36**, 1 (1890).

[339] Voigt, W. *Lerhbuch de Kristallphysik.* B. G. Teubner, Lipzig, Berlin, (1910).

[340] Voigt, W. *Ann. Phys.* **66**, 1030 (1898).

[341] Langevin, A. *Presses Universitaires de France. Paris* (1942).

[342] Weil-Brunschvicg, A. R. *Dictionary of Scientific Biography, Vol.3.* Charles Scribner's Sons, New York, (1970).

[343] Valasek, J. *Phys. Rev.* **17**, 475 (1921).

[344] Cady, W. G. *Phys. Rev.* **17**, 531 (1921).

[345] Cady, W. G. *Phys. Rev.* **21**, 371 (1923).

[346] Pierce, G. W. *Proc. Amer. Acad. Sci.* **59**, 81 (1923).

[347] Dyke, K. S. V. *Phys. Rev.* **25**, 895 (1925).

[348] Dye, D. W. *Proc. Phil. Soc.* **38**, 329 (1926).

[349] Mason, W. P. *Bell. Syst. Techn. Journ.* **22**, 178 (1943).

[350] Roberts, S. *Phys. Rev.* **71**, 890 (1947).

[351] von Hippel, A., Breckenridge, R. G., Chesley, G., and Tisza, L. *Ind. Eng. Chem.* **38**, 1097 (1946).

[352] Ginzburg, V. L. *Zh. Eksptl i Teoret Fiz.* **19**, 36 (1949).

[353] Devonshire, A. F. *Phil. Mag.* **40**, 1040 (1949).

[354] Jaffe, B., Roth, R. S., and Marzullo, S. J. *J. Appl. Phys.* **25**, 809 (1954).

[355] Bazhenov, V. A. and Konstantinova, V. P. *Doklady Akad. Nauk SSSR* **71**, 283 (1950).

[356] Yasuda, I., Nagayama, H., Kato, T., Hara, O., Okada, K., Noguchi, K., and Sata, T. *J. Kioto Med. Soc.* **4**, 395 (1953).

[357] Fukada, E. *J. Phys. Soc. Japan.* **10**, 149 (1955).

[358] Fukada, E. and Yasuda, I. *J. Phys. Soc. Japan* **12**, 1158 (1957).

[359] Bergman, J. G., McFee, J. H., and Grane, G. R. *Appl. Phys. Lett.* **18**, 203 (1971).

[360] Hayakawa, R. and Wada, Y. *Advances in Polymer Science* **11**, 1 (1973).

[361] Hayakawa, R. and Wada, Y. *Reports on Progress Polymer Physics in Japan* **19**, 321 (1976).

[362] Dreyfus, G. and Lewiner, J. *Piezoelectricity Induced by Charge Injection in Thin Polymer Films. Electrets.* The Electrochemical Society (1973). Edited by M. M. Perlman.

[363] Crosnier, J. J., Michelson, F., Dreyfus, G., and Lewiner, J. *J. Appl. Phys.* **47**, 4798 (1976).

[364] Kacprzyk, R., Motyl, E., Gajewski, J. B., and Pasternak, A. *J. Electrostatics* **35**, 161 (1995).

[365] Kacprzyk, R., Dobrucki, A., and Gajewski, J. B. *J. Electrostatics* **39**, 33 (1997).

[366] Xia, Z., Jian, J., Zhang, Y., Cao, Y., and Wang, Z. *IEEE Annual Report, Conference on Electrical Insulation and Dielectric Phenomena* , 471 (1997).

[367] Künstler, W., Xia, Z., Weinhold, T., Puncher, A., and Gerhard-Multhaupt, R. *Appl. Phys. A* **70**, 5 (2000).

[368] Lewis, T. J., Llewenllyn, J. P., and van der Sluijs, M. J. *IEEE Proc. A* **140**, 385 (1993).

[369] Lewis, T. J., Llewenllyn, J. P., and van der Sluijs, M. J. *J. Colloid Interface Sci.* **162**, 381 (1994).

[370] Lewis, T. J. *Proc. 8 th International Symposium on Electrets* , 3 (1994).

[371] Mason, W. P. *Piezoelectric Crystals and Their Applications to Ultrasonics.* D. Van Nostrand Company, Inc., (1950).

[372] Zemansky, M. W. and Dittman, R. H. *Heat and Thermodynamics.* McGraw-Hill, (1981).

[373] Schwödiauer, R., Neugschwandtner, G. S., Vieytes, M., Bauer-Gogonea, S., Bauer, S., Hillenbrand, J., Kressmann, R., Sessler, G. M., Paajanen, M., and Lekkala, J. *Appl. Phys. Lett.* **77**, 3827 (2000).

[374] Kirjavainen, K. *U. S. Patent No. 4.654.546.* (1987). In reference [391].

[375] Savolainen, A. and Kirjavainen, J. *J. Macromol. Sci.-Chem.* **A26**, 583 (1989).

[376] Paajanen, M., Lekkala, J., and Kirjavainen, K. *Sensors & Actuators* **84**, 95 (2000).

[377] Lekkala, J. and Paajanen, M. *IEEE 10 th International Symposium on Electrets* , 743 (1999).

[378] Wegener, M., Paajanen, M., Wirges, W., and Gerhard-Mulhaupt, R. *IEEE 11th Int. Symp. Electrets* , 54 (2002).

[379] Bauer, S., Bauer-Gogonea, S., Dansachmüller, M., Hoislbauer, H., Lindner, M., and Schwödiauer, R. *IEEE 11 th International Symposium on Electrets* , 50 (2002).

[380] Peltonen, J., Paajanen, M., and Lekkala, J. *J. Appl. Phys.* **88**(8), 4789 (2000).

[381] Sessler, G. M. and Hillenbrand, J. *Appl. Phys. Lett.* **75**(21), 3405 (1999).

[382] Paajanen, M., Wegener, M., and Gerhard-Multhaupt, R. *J. Phys. D: Appl. Phys.* **34**, 2482 (2001).

[383] Paajanen, M., Wegener, M., and Gerhard-Multhaupt, R. *Annual Report, Conference on Electrical Insulation & Dielectric Phenomena* , 24 (2001).

[384] Lindner, M., Bauer-Gogonea, S., Bauer, S., Paajanen, M., and Raukola, J. *J. Appl. Phys.* **91**, 5283 (2002).

[385] Gerhard-Multhaupt, R., Wegenwe, M., Wirges, W., Giacometti, J. A., Altafim, R. A. C., Santos, L. F., Faria, R. M., and Paajanen, M. *Annual Report, Conference on Electrical Insulation and Dielectric Phenomena* , 299 (2002).

[386] Paajanen, M., Lekkala, J., and Välimäki, H. *IEEE Trans. Dielec. & Electr. Insul.* **8**(4), 629 (2001).

[387] van Turnhout, J., Staal, R. E., Wübbenhorst, W., and de Haan, P. H. *Proc. 10 th Internatinal Symposium on Electrets* , 785 (1999).

[388] Mellinger, A., Camacho, F., and Gerhard-Multhaupt, R. *Appl. Phys. Lett.* **82**(2), 254 (2003).

[389] Schwödiauer, R., Neugschwandtner, G. S., Schrattbauer, K., Lindner, M., Vieytes, M., Bauer-Gogonea, S., and Bauer, S. *IEEE Trans. Dielec. & Electr. Insul.* **7**, 578 (2000).

[390] Räisänen, L., Pohjanvirta, R., Unkila, M., and Touomisto, J. *Pharm. & Toxic.* **70**(3), 230 (1992).

[391] Heikkinen, L. M., Panula, H. E., Lyyra, T., Olkkonen, H., Kiviranta, J., Nevalainen, T., and Helminen, H. J. *Scandinavian Journal of Laboratory Animal Science* **24**, 85 (1997).

[392] Siivola, J., Leinonen, K., and Räisänen, L. *Medical & Biological Engineering and Computing* **31**, 634 (1993).

[393] Alametsä, J., Värri, A., Koivuluoma, M., and Barna, L. *2th Open ECG Workshop 'Integration of the ECG into the EHR & Interoperability of ECG Device Systems', Berlin* (2004).

[394] Lekkala, J., Poramo, R., Nyholm, K., and Kaikkonen, T. *Medical & Biological Engineering & Computating* **34**(Suppl. 1, Part 1) (1996).

[395] Hämäläinen, M. K., Parviainen, J. K., and Jaaskelainen, T. *Rev. Scientific Intruments* **67**, 1598 (1996).

[396] Antilla, M., Muurinen, T., Linjama, J., and Nikänen, H. *Proc., Active 97, Budapest* , 607 (1997).

[397] Lekkala, J. *Industrial Horizons* **December**, 12 (1997).

[398] Hoislbauer, H., Schwödiauer, R., Bauer-Gogonea, S., and Bauer, S. *11 th International Symposium on Electrets* , 58 (2002).

[399] Paajanen, M., Välimäki, H., and Lekkala, J. *J. Electrostatics* **48**, 193 (2000).

[400] Hillenbrand, J. and Sessler, G. M. *IEEE Trans. Dielec. & Electr. Insul.* **7**(4), 537 (2000).

[401] Monasse, B. and Haudin, J. M. *Molecular Structure of Polypropylene Homo and Copolymers. In Polypropylene: Structure, Blends and Composites. Edited by J. Karger-Kocsis.* Chapman and Hall, (1995).

[402] Mackenzy, R. C. *Basic Principles and Historical Development. In Differential Thermal Analysis. Vol. 1. Fundamental Aspects.* Academic Press, (1970).

[403] Skoog, D. A. *Principles of Instrumental Analiysis.* Saunders College Publishing, (1985).

[404] Ke, B. *J. Polym. Sci.* **42**, 15 (1960).

[405] Wunderlich, B. *Macromolecular Physics. Vol 3.* Academic Press, New York, (1980).

[406] Mucha, M. *J. Polym. Sci. Polym. Symposium* **69**, 78 (1981).

[407] Perena, J. M. *J. Appl. Polym. Sci.* **27**, 687 (1982).

[408] Peltier, S. and Duval, C. *Anal. Chim. Acta* **1**, 345 (1947).

[409] Addink, R. *Polymer* **2**, 185 (1961).

[410] Diez-Guitierrez, S. *Estudio de la Homogeneidad de Discos Inyectados de Talco de Composites PP-Talco Mediante Análisis Mecánico Dinámico.* Master thesis. University of Valladolid. Spain, (1998).

[411] *ASTM D3576, Annual Book of ASTM Standards, Vol 8.02.* (1994).

[412] Corsaro, R. D. and Sperling, L. *Sound and Vibration Damping with Polymers.* American Chemical Society, Washington, DC, (1990).

[413] Rodríguez-Pérez, M. A. *Personal communication* .

[414] Kressmann, R., Sessler, G. M., and Günther, P. *IEEE Trans. Dielec. & Electr. Insul.* **3**(5), 607 (1996).

[415] Garlick, G. and Gibson, A. *Proc. Roy. Soc. London* **A 60**, 574 (1948).

[416] Hino, T. *IEEE Trans. Dielec. & Electr. Insul.* **EI-15**(3), 301 (1980).

[417] Tavakoli, M. and Hirsch, J. *J. Phys. D: Appl. Phys.* **21**(3), 454 (1988).

Publications

- **Evaluation of PTCa/PEKK Composites for Acoustic Emission Detection.** P. Marin-Franch, T. Martin, O. Fernández-Pérez, D.L. Tunnicliffe and D.K. Das-Gupta, *IEEE Transactions on Dielectrics & Electrical Insulation*, **11**(1) 50,(2004).

- **Effect of Temperature on Electroactive Films of Cellular Polypropylene.** O. Fernández and D.M. Taylor. *Proccedings of the 2004 International Conference on Solid Dielectrics*, Toulouse, France, **2**, 784,(2004).

- **Thermal Instability of Electroactive Polypropylene Films**. O. Fernández and D.M. Taylor. *2004 Annual Report Conference on Electrical Insulation & Dielectric Phenomena*, Boulder, USA, 489,(2004).

- **Thermal Instability of Electromechanical Films of Cellular Polypropylene.** D.M. Taylor and O. Fernández, *IEEE Transactions on Dielectrics & Electrical Insulation*, (submitted).